HARD-CORE BOSONS IN PHASE DIAGRAMS OF 2D LATTICE GAUGE THEORIES AND BOSONIZATION OF DIRAC FERMIONS

Dissertation

SEBASTIÁN FELIPE MANTILLA SERRANO

Max-Planck-Institut für Physik komplexer Systeme

Institut für Theoretische Physik
Fakultät Physik
Technische Universität Dresden

Dresden, Deutschland
Juni 2022

HARD-CORE BOSONS IN PHASE DIAGRAMS OF 2D LATTICE GAUGE THEORIES AND BOSONIZATION OF DIRAC FERMIONS

Dissertation

zur Erlagung des akademischen Grades
Doctor in Philosophy (Ph.D.)
vorlegt dem Bereich Mathematik und Naturwissenschaften

von

SEBASTIÁN FELIPE MANTILLA SERRANO

geboren am 5 Mai 1993 in Bogotá, Kolumbien

Prof. Dr. Inti A. N. Sodemann V.
Prof. Dr. Roderich Moessner

Max-Planck-Institut für Physik komplexer Systeme

Institut für Theoretische Physik
Fakultät Physik
Technische Universität Dresden

Dresden, Deutschland
Juni 2022

Eingereicht am 26.07.2022.

Gutachter:
- Prof. Dr. Jan Carl Budich.
- Prof. Dr. Roderich Moessner.
- Prof. Dr. Inti Sodemann.

Verteidigt am 19.01.2023.

I do not know what I may appear to the world, but to myself I seem to have been only like a boy playing on the sea-shore, and diverting myself in now and then finding a smoother pebble or a prettier shell than ordinary, whilst the great ocean of truth lay all undiscovered before me.

— Sir Isaac Newton. [SM20]

If I were forced to sum up in one sentence what the Copenhagen interpretation says to me, it would be "Shut up and calculate!" But I won't shut up. I would rather celebrate the strangeness of quantum theory than deny it, because I believe it still has interesting things to teach us about how certain powerful but flawed verbal and mental tools we once took for granted continue to infect our thinking in subtly hidden ways. Mathematics must therefore remain an essential element of the knowledge and abilities which we have to teach, of the culture we have to transmit, to the next generation.

— N. David Mermin. [Mer89]

Dedicated to my loved ones.

ABSTRACT

Hard-core bosons are versatile and useful in describing several physical systems due to their one-to-one mapping with spin-1/2 operators. We propose two frameworks where hard-core boson mapping not only reduces the complexity of the original problem, but also captures important features of the physcs of the original system that would have implied high-computational procedures with not much profound insight in the mechanisms behind its behavior.

The first case study comprising part i is an approach to the description of the phases 2D Lattice Gauge Theories, the Quantum 6-Vertex Model and the Quantum Dimer Model using one fluctuating electric string as an 1D precursor of the whole 2D systems[HAMS19]. Both models and consequently the string are described by the Rokhsar-Kivelson Hamiltonian with parameter v measuring the competition of potential versus kinetic terms. The string can be mapped one-to-one onto a 1D system of hard-core bosons that can be solved exactly for the Quantum 6-Vertex Model, and offers footprints of the phase diagram of the Quantum Dimer Model in the region close to the Rokhsar-Kivelson point $v = 1$, especially when $|v| \leq 1$.

The second case study we have discussed in part ii is an extension of higher-dimensional bosonization techniques in Landau Fermi liquids to the case of nodal semimetals where the Fermi surface shrinks to a point, so the description of particle-hole interactions as fluctuations of the Fermi surface is not available [MS20]. Additionaly, we focus our analysis on the $\mathbf{Q} = 0$ sector where the electron and the hole have opposite momenta $\pm\mathbf{k}$, so they are mapped into a hard-core boson located at a site $\mathbf{k}$ in the reciprocal lattice. To test our extension we calculate nonperturbative corrections to the optical conductivity of 2D Dirac fermions with electron-electron interactins described as a Coulomb potential, obtaining results consistent to the literature and the experimental reports where corrections are small even in strong coupling regimes.

Part iii discusses further ideas derived from parts i and ii, including a brief discussion on addressing the weak coupling instability in bilayer graphene using the bosonization extension that offers a picture of hard-core bosons describing $\mathbf{Q} = 0$ excitons that undergo a Bose-Einstein condensation resulting in a ground state adiabatically disconnected from the noninteracting case.

PUBLICATIONS

Some ideas and figures have appeared previously in the following publications:

[HAMS19] Herzog-Arbeitman, J., Mantilla, S. and Sodemann, I., 2019. Solving the quantum dimer and six-vertex models one electric field line at a time. Physical Review B, **99**(24), p.245108.
DOI: `https://doi.org/10.1103/PhysRevB.99.245108`

[MS20] Mantilla, S. and Sodemann, I., 2020. Bosonization of the $\mathbf{Q} = 0$ continuum of Dirac fermions. Physical Review B, 102(12), p.121103.
DOI: `https://doi.org/10.1103/PhysRevB.102.121103`

Further publications not covered in this thesis:

[BR+22] Benavides-Riveros, C.L., Chen, L., Mantilla, S. and Pittalis, S., 2022. Excitations of Quantum Many-Body Systems via Purified Ensembles. arXiv preprint arXiv:2201.10974.
DOI: `https://doi.org/10.48550/arXiv.2201.10974`

> *Science is the search for truth - it is not a game in which one tries to beat his opponent, to do harm to others. We need to have the spirit of science in international affairs, to make the conduct of international affairs the effort to find the right solution, the just solution of international problems, not the effort by each nation to get the better of other nations, to do harm to them when it is possible.*
>
> — Linus Pauling [PH58]

ACKNOWLEDGMENTS

As a young physics student with experience in high-energy and particle physics, doing research in condensed matter is a project I was delaying since I began studying physics enchanted, due to my passion for music, by the concept of phonons, and their role in thermal properties of materials. During my B.Sc. and M.Sc. studies, condensed matter left footprints: my first approach to graphene as a tabletop system to explore high-energy phenomena, the electroweak symmetry breaking by the Higgs mechanism, originated in superconductivity; or the application of Bogoliubov transformations studying the Hawking radiation in black holes.

For the previous motivations, I do not have enough words of gratitude to my advisor, Prof. Dr. Inti Sodemann, for having supervised my Ph.D. He taught me not only different technical procedures to address physical problems in this thesis but also made me realize the researcher I want to be. Furthermore, his advice and patience in reaching high-quality research made me a better physicist. Additionally, in Prof. Sodemann's group, I had enriching discussions with Dr. Prof. Falko Pientka, Jun Yong Khoo, Peng Rao, Oles Matsyshyn, and Nikolaos Stefanidis that helped me to realize and solve different issues I had during my research.

I am also enormously grateful to Prof. Dr. Roderich Moessner for his support as the head of the Condensed Matter Division of MPIPKS. Thanks to him, I was fortunate to do my Ph.D. at the institute. His permanent support, especially during the hard times of the pandemic, is why I achieved this goal. Being part of his department is an honor for me. Similarly, I would like to thank Paul McClarty, the coordinator of the IMPRS, for his effort in organizing seminars, retreats, schools, and many other events that contributed to my knowledge of contemporary physics.

Additionally, I want to highlight the work team efficiency and human quality of the institute's workers: Visitors' Program, HR department, cafeteria, IT department, German teachers, and the administrative staff. They were ready to solve any issue I might have during these years. Es war sehr schön, mit euch mein Deutsch üben zu können. Ich habe genauso viel gelernt, wie während des Unterrichts.

Lastly, regarding the organizations that have supported me during my Ph.D., I want to thank TUD and Würzburg-Dresden Cluster **ct.qmat**. TUD let me take many lectures with excellent professors and improve my teaching skills, and of course, for issuing the Ph.D. title together with MPIPKS. Würzburg-Dresden Cluster **ct.qmat** has also influenced me strongly by letting me attend events organized by them that take care of students' improvement and self-esteem.

Among the people who contributed to my formation, I feel gratitude and admiration for Jonah Herzog-Arbeitman. Working with him in my first research project[HAMS19] was joyful and insightful in every chat we had. As a result, I have beautiful memories from that time beginning my Ph.D. Besides, special people such as Snehasish Nandy, Tanay Nag, Renato Alves Dantas, Daniele Trapin, Fran Peña-Benítez, Piotr Surowka, Nicolás Morales Durán, among others, made my first days in the Ph.D. easier thanks to their friendship. Especially Sourav Manna and Piotr Witkowski, with whom I enjoyed long chats about our research.

I thank Aidan Wastiaux, who has been available every time I need to talk to someone; thanks for giving me your advice in difficult moments. Peng Rao has influenced me in many different ways. He is not only a rigorous scientist who honestly cares about the details but also a friend who never hesitates to show his well-argued opinion on science and life matters. As well, I can consider Luis Colmenarez, my brother. Beyond his inspiring diligence and organization at work, he also considerably shaped my appreciation of science and society. Those long chats about physics are some of the things I will miss the most. Gracias por siempre haber estado en todo momento que necesitaba a un amigo, este logro también es tuyo, mi pana.

Moreover, MPIPKS, TUD, and **ct**.qmat gave me the chance to meet with researchers that have contributed to my formation, such as Madelynn Nayga, Yi-Ping Huang, Benedikt Placke, Friederike Metz, Nicolás Moreno, Adisorn Panasawatwong, Dominik Hahn, Soumi Dutta, Rafael Flores, Aniket Patra, Heiko Burau, Santanu Dey, Nicolò Beato, Robin Schäfer, among too many others. During coffee breaks and journal clubs, they have taught me uncountably. The student community of MPIPKS is a network of support that showed its actual value in 2020 when I needed to meet all of them.

This rich atmosphere also allowed me to meet Carlos Benavides-Riveros, who I consider my second advisor during the second half of my Ph.D. Endless discussions about physics taking care of understanding the details have shaped my way of addressing new frameworks outside my comfort zone. Especially his lack of fear in attacking new problems is just a source of inspiration to me. Gracias por tu apoyo y tus consejos.

I want to do a special mention of Laura Baez and Andrés Schlief. Not only the joyful chats about numerical methods or non-Fermi liquids, but especially your unique perspective opened to me new scenarios. Pasar tantos momentos juntos son de los más hermosos recuerdos que me quedan de estos años, no tengo cómo agradecerles.

I cannot continue without recognizing the permanent advice of my former supervisor, Prof. Dr. Roberto Martínez, at Universidad Nacional de Colombia. I am glad he still takes his time to give me recommendations on different life and work matters. Also, Prof. Dr. José Robel Arenas encouraged me to study quantum many-body physics during his lectures on gravitation, so this thesis is part of his inspiring work. Finally, I would like to express my gratitude to Prof. Ángel Miguel Ardila, Prof. Karen Fonseca, Prof. José Jairo Giraldo, Prof. William Herrera, Prof. José Daniel Muñoz, Prof. Julio Evelio Rodríguez, Prof. Fredy Ochoa, Prof. Herbert Vinck, and Prof. Carlos Leonardo Viviescas, among many other faculty members that contributed to paving my path in physics.

Among my fellow students during my B.Sc. and M.Sc. studies, I want to mention Daniel Padilla González; there has been no doubt or query in physics I needed to do that was not successfully solved when he gave me his support. No alcanzarán las cervezas para agradecer tanto apoyo, parcero. Similarly, Jenny Martinez, Santiago Rueda, Juan Mauricio Valencia, and Juan Sebastián Valbuena have been endless sources of inspiration and support; since we met for the first time at the Faculty until today, I have learned from you the fruits when diligence and talent come together.

I recognize Freddy T. Payoma too. Thanks for inviting me as a lecturer in the Workshop on Basic Science at Universidad Nacional Abierta y a Distancia and for being permanent support despite the distance and encouraging me to go ahead in science outreach. Likewise, my old friends David Camilo Latorre and Brian Numpaque were a constant support to me in the most difficult moments of my doctorate. Gracias por su permanente compañía durante tantos años a pesar de estar tan lejos.

Of course, I would like to thank my family and loved ones, my parents, Luis Omar Mantilla and Deipsy Omed Serrano, and my brother Santiago Mantilla Serrano. They have never failed in giving me their unconditional support and innumerable sacrifices to make this Ph.D. possible. Finally, I thank Julián Calderón, my partner, best friend, confidant, and inspiration, for his ongoing care and love. I know being engaged with a scientist might be difficult, but this is another reason to appreciate even more that you have been next to me. Gracias por todo.

Last but never least, I want to mention my emotional support in Dresden during these years. Daian Simoné Hernández, Saúl González, Claudia, Víctor Ledesma, Aleix Martínez, María and Thomas Kordt, Manuel Martínez, Eneddyn Molina, Camilo Guillén among many other lovely people, you made of this city my home. Vielen Dank an alle.

CONTENTS

1 Introduction 1
  1.1 Quantum link models and fluctuating electric strings 2
  1.2 Bosonization of Particle-hole excitations in 2D Dirac fermions 7
  1.3 Structure of the document 11

I Quantum link models and fluctuating electric strings

2 A Brief Introduction to Lattice Gauge Theories 15
  2.1 Continuous formulation of U(1) gauge theories 15
    2.1.1 Gauge field equations 16
    2.1.2 Gauss' law as generator of the gauge transformations 18
  2.2 U(1) gauge theories on a lattice 19
    2.2.1 Gauge field Hamiltonian 20
    2.2.2 Cylindrical algebra from LGT 20
    2.2.3 Generator of gauge transformations 21
  2.3 Abelian Quantum Link Model 22
    2.3.1 Quantum Link Models (QLMs) with S = 1/2 23
    2.3.2 't Hooft operators and winding number sectors 24
    2.3.3 Construction of the QLM Hamiltonian 26
  2.4 Conclusions 28
3 Electric string in Q6VM as a XXZ chain 29
  3.1 Realization of the Q6VM in the $S = 1/2$ QLM 31
  3.2 Mapping the electric string to the XXZ chain 32
  3.3 Phases of the electric string from the XXZ chain 33
    3.3.1 $v > 1$: FM insulator 34
    3.3.2 $v = 1$: RK point 36
    3.3.3 $-1 < v < 1$: Gapless phase 36
    3.3.4 $v \leq -1$: KT transition and AFM insulator 37
  3.4 Numerical approach: Drude Weight and system size effects 38
  3.5 Summary and Discussion 40
4 Electric line in the QDM as a hard-core boson two-leg ladder 41
  4.1 Realization of the QDM in the $S = 1/2$ QLM 42
  4.2 Construction of an electric string in the QDM 43
  4.3 Mapping the electric string in QDM to a two-leg ladder 45
    4.3.1 QLM in a triangular lattice 45
    4.3.2 From the triangular lattice to the two-leg ladder 45
    4.3.3 Construction of the 1D bosonic Hamiltonian 46
  4.4 Phases of the electric string from the bosonic two-leg ladder 48
    4.4.1 Left Hand Side (LHS) of the Rokhsar-Kivelson (RK) point: Charge Density Wave (CDW) states 48

4.4.2 Right Hand Side (RHS) of the RK point: phase-separated states 50
4.5 Numerical approach: Drude Weight and system size effects 51
4.6 Summary and Discussion 52

II Bosonization of particle-hole excitations in 2D Dirac fermions

5 Graphene in a nutshell 57
5.1 Origin of the hexagonal structure 57
5.1.1 Hybrid orbitals in C 58
5.1.2 Honeycomb lattice 60
5.2 Tight-binding approach 61
5.2.1 Hopping and overlapping matrices in Nearest Neighbor (NN) approximation 62
5.2.2 Dispersion relation for π electrons 62
5.3 Effective 2D Dirac Fermion Hamiltonian 64
5.4 Electron-electron interactions 65
6 Bosonization of the $Q = 0$ continuum of Dirac Fermions 67
6.1 Effective Hamiltonian and Hilbert space 69
6.2 Effective Heisenberg Hamiltonian 70
6.3 Quadratic Bosonic Hamiltonian 71
6.4 Connection to diagramatic perturbation theory 73
6.5 Parametrization of the reciprocal space 74
6.5.1 Coordinate transformation 74
6.5.2 Polar parametrization 75
6.5.3 Angular momentum channels 75
6.6 Discussion and Summary 76
7 Non-perturbative corrections to the Optical Conductivity of 2D Dirac Fermions 77
7.1 Optical Conductivity 79
7.1.1 Bosonized current operator and susceptibility 79
7.1.2 Susceptibility in terms of the eigenstates 80
7.1.3 Regularization of the Lehman representation 81
7.2 Numerical approach: IR regularization and system size effects 82
7.2.1 Discretization size dependence 82
7.2.2 Dependence on the IR cutoff 83
7.2.3 Comparison of numerical results with corrections from first order perturbation theory 84
7.2.4 Optical conductivity for several coupling constants 85
7.3 Discussion and Summary 86

III Weak coupling instability, New Perspectives & Conclusions

8 Weak coupling instability in bilayer graphene from a bosonization picture 91
8.1 Band structure of Bernal-stacked bilayer graphene 92
8.2 Generalization of the effective Hamiltonian of graphene 93

    - 8.2.1 Density of states in monolayer and bilayer graphene 94
    - 8.2.2 Projection onto $Q = 0$ sector and effective Heisenberg pseudospin Hamiltonian 95
    - 8.2.3 Zeeman vortex coordinates and HCB operators 95
    - 8.2.4 Bogoliubov-Valatin basis 97
  - 8.3 Interaction potentials 97
  - 8.4 BCS instability in pseudospin picture 99
  - 8.5 Numerical procedure 101
    - 8.5.1 Numerical BCS instability 101
    - 8.5.2 Functional form of the instability 101
    - 8.5.3 Comparison to the instability from BCS theory 105
  - 8.6 Conclusions 105
- 9 Conclusions 107

IV Appendices

- A Yang & Yang's expressions of ground state energy of XXZ Chain using Bethe Ansatz 115
  - A.1 Bethe Ansatz 115
  - A.2 Explicit formulas for $f(\Delta, 0)$ 116
- B Kadanoff-Baym (KB) self-consistent Hartree-Fock (SCHF) approximation 119
  - B.1 Details of connection to perturbation theory 119
    - B.1.1 Bare and dressed fermion propagators 119
    - B.1.2 Bethe-Salpeter ladder 120
    - B.1.3 Particle-hole propagator and comparison to HP boson propagator 121
- C Optical Conductivity from Pseudospin precession 123
  - C.1 Minimal coupling and band (electron-hole) basis 123
  - C.2 Equations of motion of charge and pseudospin densities 124
  - C.3 Optical Conductivity from Fermi-Dirac distributions at finite temperature 124
- D Momentum space reparametrization 127
  - D.1 General coordinate transformations on the continuum limit 127
  - D.2 Polar re-discretization 129
  - D.3 Angular momentum channels 130
  - D.4 Selection of the radial parametrization 130

Bibliography 133

LIST OF FIGURES

Figure 1.1 Electric string connecting two defects in a square lattice in a $S = 1/2$ QLM in the Gauss' law sector. 2
Figure 1.2 Ice rules: Representation of the location of protons in water ice. 3
Figure 1.4 2D pyrochlore XXZ Heisenberg model as Quantum 6-Vertex Model (Q6VM). 4
Figure 1.3 Q6VM from the water ice. 4
Figure 1.5 Candidate phase diagram of the Quantum Dimer Model (QDM). 5
Figure 1.6 Background configuration for the electric string in QDM. 6
Figure 1.7 Phase diagram of the electric string in Q6VM. 7
Figure 1.8 Low-energy band and pseudospin pictures of monolayer graphene. 8
Figure 1.9 Shell of validity for bosonization in any dimension. 8
Figure 1.10 Shear sound in Fermi liquids. 9
Figure 1.11 Exciton operators. 10
Figure 1.12 Absorbance and sheet conductivity of graphene. 10
Figure 2.1 2D square lattice labelling rule and plaquette operators. 19
Figure 2.2 Cylindrical limit from QLM. 21
Figure 2.3 Link and plaquette operators in the $S = 1/2$ QLM. 24
Figure 2.4 Dual of the electric field. 24
Figure 2.5 't Hooft operators. 25
Figure 2.6 Example of an electric field line with a flippable plaquette. 27
Figure 3.1 Ices rules: Pictorical representation of the location of protons in water ice and their displacement vectors. 29
Figure 3.2 Q6VM as a 2D description of water/spin ice. 30
Figure 3.3 Equivalence between the ice rules and $\hat{Q}_{\mathbf{r}} = 0$. 31
Figure 3.4 Two dynamically-connected states of an electric string and mapping to a 1D system. 32
Figure 3.5 Exact phase diagram of the electric string from the XXZ chain at $M = 0$. 34
Figure 3.6 Electric string in Q6VM in the Ferromagnetic (FM) phase $1 < v$. 35
Figure 3.7 Electric string in Q6VM in the gapless phase $-1 < v < 1$. 37
Figure 3.8 Electric string in Q6VM in the Antiferromagnetic (AFM) phase $v < -1$. 38
Figure 3.9 Two lowest energy levels vs. v in Q6VM. 39

Figure 3.10 Phase diagram at $M = 0$ and Drude weight in the Q6VM. 40
Figure 4.1 Background configuration for the electric string in QDM. 41
Figure 4.2 The dimer resonance process in the QLM. 42
Figure 4.3 Vertices consistent with $Q_{\mathbf{r}} = 2(-1)^{x+y}$. 43
Figure 4.4 Construction of an electric string on the staggered vacuum of QDM. 44
Figure 4.5 Successive states of an open string under the action of the RK Hamiltonian (4.2). 46
Figure 4.6 Electric string in QDM in the CDW phase $V < t$. 48
Figure 4.7 Two lowest energy levels vs. V/t in QDM. 49
Figure 4.8 Electric string in QDM in the FM phase $t < V$. 50
Figure 4.9 Two lowest energy levels vs. v for each k momentum sector. 52
Figure 5.1 Carbon electronic configuration. 58
Figure 5.2 Hybrid atomic orbitals. 59
Figure 5.3 Direct and reciprocal lattice of the honeycomb. 60
Figure 5.4 Band structure of graphene 63
Figure 5.5 Log-shaped Dirac cone. 66
Figure 6.1 particle-hole excitations (PHEs) in an usual Fermi liquid 67
Figure 6.2 PHEs in a non-doped nodal semimetal. 68
Figure 6.3 Creation of an electron-hole pair in $\mathbf{Q} = 0$ sector as the flipping of a pseudospin on a vortex configuration. 69
Figure 6.4 Exciton creation and annihilation operators. 71
Figure 6.5 Particle-hole operator by Kadanoff-Baym (KB) Self-Consistent Hartree-Fock (SCHF) resummation. 73
Figure 6.6 Coordinate systems in the reciprocal space. 75
Figure 6.7 Zeeman vortex in the polar lattice. 76
Figure 7.1 PHE in the Dirac cone. 77
Figure 7.2 Self-energy and vertex corrections to the conductivity $\sigma(\omega)$. 78
Figure 7.3 System size effects on $\tilde{\sigma}(\omega)$. 83
Figure 7.4 Infrared (IR) cutoff effects on $\tilde{\sigma}(\omega)$ in the thermodynamic limit. 83
Figure 7.5 Perturbative effects of the IR cutoff on $\sigma(\omega)/C\alpha$. 84
Figure 7.6 Corrections to the optical conductivity for different couplings α with $M \to \infty$ and $\mathcal{K}_{\mathrm{IR}}/\mathcal{K} = 10^{-4}$. 85
Figure 7.7 Detail of the Renormalization Group (RG) running of $\tilde{\sigma}(\omega)$ for small α. 87
Figure 8.1 Lattice of bilayer graphene. 92
Figure 8.2 Band structure of bilayer graphene. 93
Figure 8.3 Monolayer and bilayer graphene in the pseudospin picture. 94

Figure 8.4 Electron-electron interaction potentials. 99
Figure 8.5 Unstable mode in bilayer graphene with Gaussian-like potential. 102
Figure 8.6 Unstable mode in bilayer graphene with Coulomb-like potential. 102
Figure 8.7 Coefficients $C^{\ell}(a_{\text{eff}}, r)$ and $G^{\ell}(a_{\text{eff}}, r)$ for Gaussian potential. 103
Figure 8.8 Coefficients $C^{\ell}(a_{\text{eff}}, r)$ and $G^{\ell}(a_{\text{eff}}, r)$ for Coulomb potential. 104
Figure 8.9 Power-law parameters for Gaussian and Coulomb potentials. 104
Figure 8.10 *Zeeman vortex in bilayer graphene*: Similarly to monolayer graphene, the kinetic term can be expressed as a Zeeman term involving the pseudospin $\mathbf{s_k}$ coupled to a 2-folded Zeeman vortex. 105
Figure 9.1 Possible phase diagrams of the QDM. 108
Figure 9.2 Fluctuating electric string in the QLM. 108
Figure 9.3 Phase diagram and Drude weight of the electric string. 109
Figure 9.4 Bosonization of PHEs of gapless fermions. 110
Figure 9.5 Weak coupling instability in bilayer graphene due to Gaussian electron-electron interaction. 111
Figure B.1 Dressed propagator as a Dyson series. 120
Figure B.2 Bethe-Salpeter ladder of the self-consistent Hartree-Fock approximation. 121
Figure C.1 Optical conductivity vs. energy for graphene at finite temperature with noninteracting electrons. 125
Figure D.1 Coordinate systems in the reciprocal space. 127
Figure D.2 Reconfiguration of the momentum lattice. 129
Figure D.3 First sample of numerical results using different radial parametrizations. 131
Figure D.4 Second sample of numerical results using different radial parametrizations. 132

LIST OF TABLES

Table 7.1 Detail of the RG running of $\tilde{\sigma}(\omega)$ for small α. 86

ABBREVIATIONS

AFM	Antiferromagnetic
BCS	Bardeen-Cooper-Schrieffer
BV	Bogoliubov-Valatin
CB	Conduction band
CDW	Charge Density Wave
DMRG	Density Matrix Renormalization Group
DOF	degrees-of-freedom
DP	Dirac Point
EPR	Einstein-Podolsky-Rosen
FCC	Face-Centered Cubic
FM	Ferromagnetic
HCB	Hard-core Boson
HF	Hartree-Fock
HP	Holstein-Primakov
IR	Infrared
JW	Jordan-Wigner
KB	Kadanoff-Baym
KT	Kosterlitz-Thouless
LGT	Lattice Gauge Theory
LHS	Left Hand Side
NN	Nearest Neighbor
PHE	particle-hole excitation
Q6VM	Quantum 6-Vertex Model
QCD	Quantum Chromodynamics
QDM	Quantum Dimer Model
QED	Quantum Electrodynamics
QLM	Quantum Link Model
RG	Renormalization Group
RHS	Right Hand Side
RK	Rokhsar-Kivelson
RPA	Random Phase Approximation
RVB	Resonant Valence Bond
SCHF	Self-Consistent Hartree-Fock
UV	Ultraviolet
VB	Valence band

1

INTRODUCTION

> *The measure of greatness in a scientific idea is the extent to which it stimulates thought and opens up new lines of research.*
>
> — Paul A. M. Dirac [Dir72]

The many-body behavior of particles constituting matter is mainly dictated by their statistics. According to Particle Data Group review [Zyl+20], the universe is composed by a set of fermions and bosons with a finite number of flavors. The lowest-energy modes relevant to condensed matter research are the electron and the photon manifesting as electromagnetic electron interactions (usually Coulomb repulsions). The different atomic arrangements in materials offer structured environments where electrons can exhibit a large class of collective behaviors, going from the well-known Fermi gas and Landau Fermi liquid[AGD12], passing through the Bardeen-Cooper-Schrieffer (BCS) superconductors [BCS57] and semimetals[Kat12], to the Resonant Valence Bond (RVB) and spin ice states[Fra13]. However, approaching these problems might imply enormous computational resources because of the exponential growth of the Hilbert spaces involved. So, it is required to reduce the difficulty by doing sensible mappings of the relevant degrees-of-freedom (DOF) of the original systems onto simpler ones that still keep the low-energy behavior.

Some of these mappings can be done using *Hard-core Bosons (HCBs)*[Fra13; CS16]. First implemented in the problem of superfluid Helium II in a lattice model, HCBs have the following commutation relations[MM56; MM57]:

$$[b_i, b_j] = [b_i^\dagger, b_j^\dagger] = 0, \quad [b_i, b_j^\dagger] = \delta_{ij}(1 - 2n_i), \tag{1.1}$$

where the bosons fulfill the *hard-core constraint*, i. e., $n_i = b_i^\dagger b_i$ only takes values 0 and 1, This constraint can be obtained from a strongly interacting bosonic system described by the Hamiltonian

$$H_{\mathrm{HCB}} = \sum -t(b_i^\dagger b_{i+1} + h.c.) + U n_i(n_i - 1), \tag{1.2}$$

with $U \to \infty$ projecting out multiply occupied sites. This kind of interaction have been experimentally implemented in ultracold atoms as a tunable contact potential [BDZ08; Par+04; Chi+10]. This is also found in *composite bosons*, where an even number of fermions form a bound state and the Pauli exclusion is mapped into the hard-core constraint [CS16].

The main interest we have in HCBs in this work comes from their exact one-to-one mapping with spin-1/2 operators[MM56; MM57]. We have employed the HCB mapping in the frameworks of Lattice Gauge Theories (LGTs), more specifically in 2D Quantum Link Models (QLMs) [Hor81; OR90] discussed in part i, and in a new bosonization framework for interacting particle-hole excitations (PHEs), or excitons, in nodal semimetals in part ii [Fuc+10; Li+12; Goe11], where excitons emerged as HCBs allow to reexpress the fermionic Hamiltonian as quadratic in HCB picture. The implementation of such a mapping not only yields more viable strategies to address the problems outlined above, but also gives a new picture where the fluctuations of the string in a 2D QLMs, or the PHEs in nodal semimetals, can be easily understood as scalar particles fulfilling the hard-core constraint $n_i = \{0, 1\}$ as discussed below. The following sections present a brief discussion about QLMs and bosonization of PHEs with special focus in 2D systems, and the problems we address implementing HCBs in a straightforward way.

1.1 QUANTUM LINK MODELS AND FLUCTUATING ELECTRIC STRINGS

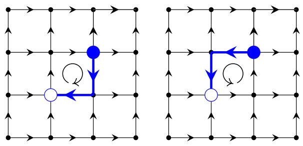
(a) (b)

Figure 1.1: *Electric string connecting two defects in a square lattice in a $S = 1/2$ QLM in the Gauss' law sector*. The string γ is embedded in a lattice where $Q_{\mathbf{r}} = 0$ except at the defects $Q_{\partial\gamma} = \pm 2$. (a) and (b) are the two states $|\circlearrowleft\rangle$ *and* $|\circlearrowright\rangle$ *states of flippable plaquettes in QLM.*

The first framework we address in this work consists in the description of the phases of an *electric string* parametrized along a directed path γ, as shown in FIG. 1.1, connecting two charges $Q_{\partial\gamma}$ at the boundaries of γ called *defects* for reasons discussed below, by mapping of the string onto a 1D HCB chain [HAMS19]. The string is embedded in a square lattice where each site is assigned with a quantum number $Q_{\mathbf{r}}$ counting the number of ingoing and outgoing electric lines $E_{\mathbf{r},\ell}$ along the four links $(\mathbf{r}, \ell)$ connecting each site with its Nearest Neighbors (NNs) (see FIG. 1.1). The background configuration of $Q_{\mathbf{r}}$ is determined by two rules: $Q_{\mathbf{r}} = 0$ for every lattice site, case shown in FIG. 1.1 and called *Gauss' law sector* [IM14]; and $Q_{\mathbf{r}} = \pm 2$, with positive and negative signs forming a checkerboard lattice (a site in sublattice A or B is assigned with $+2$ or -2, respectively). Hence, the sources $Q_{\partial\gamma}$ are defect where the rules are violated (depicted as fat dots in FIG. 1.1).

The previous problem is one type of LGT, quantum mechanical lattice models with local conservation laws suited to simulate the physical vacuum of our universe [Kog79], and also give rise to unconventional phases of matter [Fra13; Wen04]. LGTs consist on placing the matter fields at the sites $\mathbf{r}$ of a lattice, and the segments joining the sites $\mathbf{r}$ and $\mathbf{r} + \boldsymbol{\ell}$ (where ℓ are the primitive lattice vectors) are oriented links $(\mathbf{r}, \ell)$ with quantum numbers $n_{\mathbf{r},\ell} \in \mathbb{Z}$ counting the *number of electric field lines* $E_{\mathbf{r},\ell} |n_{\mathbf{r},\ell}\rangle = n_{\mathbf{r},\ell} |n_{\mathbf{r},\ell}\rangle$ along the link. At each site we can define a charge $Q_{\mathbf{r}}$ determined by the difference between the ingoing and outgoing links touching it, that is the *divergence* of the electric field, $\nabla \cdot \mathbf{E}_{\mathbf{r}} = E_{\mathbf{r},x} - E_{\mathbf{r}-\hat{\mathbf{x}},x} + E_{\mathbf{r},y} - E_{\mathbf{r}-\hat{\mathbf{y}},y}$ to have a lattice expression of the *Gauss' law* $\nabla \cdot \mathbf{E}_{\mathbf{r}} = Q_{\mathbf{r}}$ [IM14; Wie13; CW97; Hor81].

Further, the QLMs comprise one realization of compact LGTs, in which the electric lines along the links have a Hilbert space which is finite-dimensional, i. e., each link can saturate and $n_{\mathbf{r},\ell}$ reaches maximum values ($n_{\mathbf{r},\ell} = -S, ..., S$), similarly to angular momentum states [IM14]. In the case of a QLM with $S = 1/2$, each link can be represented by a spin-1/2, and the minimal electric circulation loops called *flippable plaquettes*, which have two states, $|\circlearrowleft\rangle$ and $|\circlearrowright\rangle$ (see the FIG. 1.1). The dynamics of the system is described by the Rokhsar-Kivelson (RK) Hamiltonian [RK88]:

$$H = \sum_{P} -t(|\circlearrowleft\rangle\langle\circlearrowright| + |\circlearrowright\rangle\langle\circlearrowleft|) + V(|\circlearrowleft\rangle\langle\circlearrowleft| + |\circlearrowright\rangle\langle\circlearrowright|), \tag{1.3}$$

inicially proposed in the context of high-temperature superconductors, where the first term produces $|\circlearrowleft\rangle \leftrightarrow |\circlearrowright\rangle$ fluctuations and the second one counts the number of flippable plaquettes, i. e., states $|\circlearrowleft\rangle, |\circlearrowright\rangle$ in the lattice. At $V = t$, the *RK point*, the Hamiltonian becomes a sum of projectors $(|\circlearrowleft\rangle - |\circlearrowright\rangle)(|\circlearrowleft\rangle - |\circlearrowright\rangle)$, a positive definite operator whose lowest eigenvalue corresponds to a zero mode consisting in the superposition of all possible configurations of flippable plaquettes [Fra13].

Although QLMs has finite-dimensional Hilbert spaces at each link, the configuration of ingoing and outgoing links at each vertex is not fixed. We can propose the constraint $\nabla \cdot \mathbf{E_r} = Q_\mathbf{r}$ at each lattice and choose one Hilbert subspace of QLM[IM14]. As discussed in the first paragraph of this section, the case studies selected for this work are $Q_\mathbf{r} = 0$ for every lattice site, and $Q_\mathbf{r} = \pm 2$ per each sublattice [HAMS19].

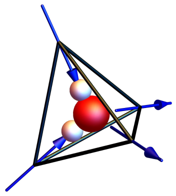

Figure 1.2: *Ices rules*: Representation of the location of protons in water ice.

To understand the *Gauss' law* sector $Q_\mathbf{r} = 0$, we briefly discuss the Bernal-Fowler *ice rules* [MR11b], historically first observed in the internal disposition of water molecules H_2O in ice [BF33] (see FIG. 1.3). There are six different orientations for the two protons H of the water molecule, so the molecule can be mapped as four arrows at the corners of a tetrahedron, where two arrows point inwards, corresponding to the protons, and two outgoing arrows pointing towards the protons of molecules in the neighboring corner-sharing tetrahedra, as depicted in FIG. 1.3 [MTS04; BH20; LMM11].

These systems can be studied using the Q6VM consisting of a square lattice where each site has two ingoing and two outgoing links to fulfill the divergenceless condition, allowing only six possible vertices. The Q6VM was proposed as a 2D ice model by Pauling to calculate the water ice entropy at the zero-temperature limit[Pau35], followed by Slater to study ferroelectric materials [Sla41]. The model was solved exactly by Lieb obtaining the entropy-per-molecule $S = k_B \ln W$[Lie67], where W is the *Lieb's square constant* $W = (4/3)^{3/2}$.

Different rare-earth Ferromagnetic (FM) materials[GM14] have presented a similar behavior [Har+97; Ram+99], whose rare-earth cations form a sublattice of corner-sharing tetrahedra in a Face-Centered Cubic (FCC) lattice

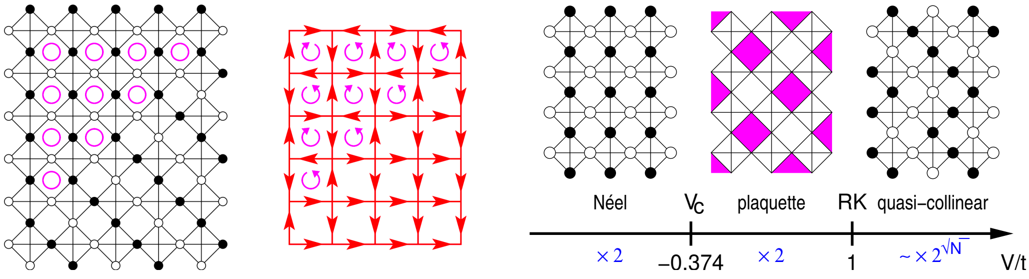

(a) (b) (c)

Figure 1.4: *2D pyrochlore XXZ Heisenberg model as Q6VM*: (a) Mapping of the XXZ Heisenberg model on a checkerboard lattice (a,a) to the Q6VM (a,b) and (b) phase diagram as a function of the parameter $v = V/t$ in Hamiltonian (1.4). [Adapted by permission from the American Physical Society (Shannon *et al.* [SMP04]) Copyright (2004); `https://doi.org/10.1103/PhysRevB.69.220403`].

called *pyrochlore lattice* (see FIG. 1.3a) [LMM11], with an anisotropic exchange that force them to fulfill the ice rules for spin systems: two-in-two-out (see FIG. 1.2). Further, Hermele, Fisher & Balents in [HFB04] showed that a spin-1/2 Heisenberg antiferromagnet in the pyrochlore lattice, with the easy-axis anisotropy that aligns the spins following the ice rule, has a U(1) spin liquid phase whose fractionalized excitations produces an emergent effective Quantum Electrodynamics (QED). Moreover, Castro Neto, Pujol & Fradkin in [CNPF06] used the Q6VM to study electrical properties of water ice by allowing the existence of defects $Q_{\mathbf{r}} = \pm 1$, violations of the ice rules for protons H, finding an effective U(1) gauge description with H-insulator and H-plasma as confined and deconfined phases. Jaubert & Udagawa have recently published a review on spin ices [UJ21] discussing from the very basics to the last developments on the subject such as nonequilibrium properties, experimental explorations for the monopole Coulomb phase, or artificial spin ices.

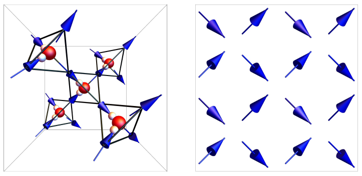

(a) (b)

Figure 1.3: *Q6VM from the water ice*: Pictorical representation of the Quantum 6-Vertex Model (Q6VM) as a 2D model of the water ice in a maximally polarized (ferroelectric) state.

The Q6VM exhibits different phases depending on the value of the parameter $v = V/t$ of the RK Hamiltonian (1.4) tuning the two competing terms: the kinetic term that produces fluctuations with parameter t, and the RK potential V counting the number of flippable paquettes. Thanks to Lieb's solution [Lie67], there is a general agreement in the matter. At $v = 1$, the *RK point*, the Hamiltonian (1.4) becomes a sum of projectors $(|\circlearrowleft\rangle - |\circlearrowright\rangle)(|\circlearrowleft\rangle - |\circlearrowright\rangle)$, a positive definite operator whose ground state is the equal-weight superposition of any zero-energy state, constituting a gappless phase [SMP04]. On the Right Hand Side (RHS) of the RK point (see FIG. 1.1 and 1.4), the region $v > 1$, the Hamiltonian produces a ferromagnetic phase, no flippable plaquettes are found, all the links pointing towards the same di-

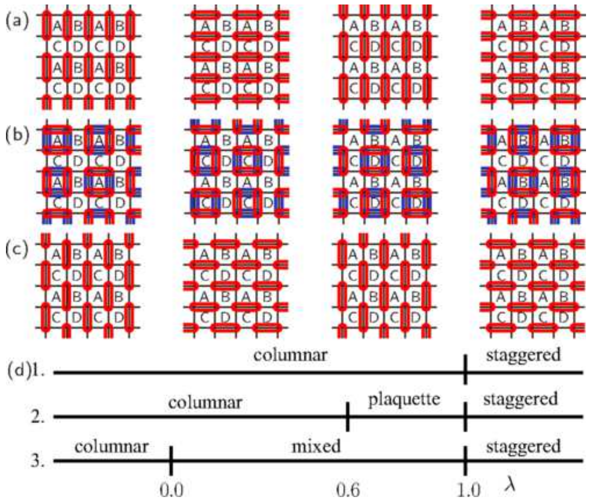

Figure 1.5: *Candidate phase diagram of the Quantum Dimer Model (QDM)*: (a), (b) and (c) show the four inequivalent columnar, plaquette RVB and staggered configurations in the dual sublattices (A,B,C,D). The phase diagrams (d) summarize the different proposals in the literature (read the text for details). [Taken by permission from the American Physical Society (Banerjee *et al.* [Ban+14]) Copyright (2014); `https://doi.org/10.1103/PhysRevB.90.245143`].

rection [MR11a], as shown in FIGs. 1.1, and the system presents a subdimensional deconfinement of the defects violating the ice rules [BT04; SMP04]. On the Left Hand Side (LHS) of RK point, the region $v < 1$, the ground states in the square lattice are broken symmetry phases, in which the charges are confined from the gauge theory point of view [Pol87]. These two phases, separated by a critical point $v_c \sim -0.4$ indicated in FIG. 1.4, are an Antiferromagnetic (AFM) Néel state in the checkerboard lattice for $v < v_c$ that breaks the point group, and a plaquette phase that presents translational symmetry and power-law correlations.

The second case we study, the staggered background $Q_{\mathbf{r}} = \pm 2$ is suited to describe the celebrated QDM, proposed by Rokhsar & Kivelson [RK88], following Pauling's RVB [Pau53] and Anderson's work, advocating that spin-1/2 AFM Hamiltonians not always have an AFM ground state (Néel state), instead, a phase of *resonating* valence-bond pairs of lattice-NN electrons in the spin-singlet state covering the lattice along the links as *hard-core dimers* that *resonate* with the empty links [And73] (see FIG. 1.5). The RK Hamiltonian was originally expressed in terms of dimers as follows:

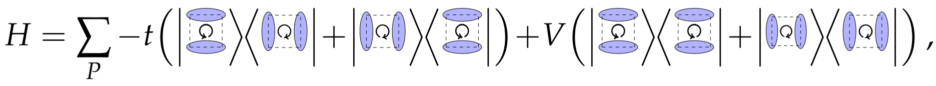

(1.4)

where we have included the flippable plaquettes in order to map the parallel dimers as circulating loops of electric lines in QLM.

In contrast to the Q6VM where we count with Lieb's solution [Lie67], the phase diagram of the QDM is not accurately known in the region $|v| < 1$. Leung *et al.* in [LCR96] proposed a phase diagram with three phases: columnar, plaquette RVB and staggered (see FIG. 1.5). When $v \to -\infty$ the ground state is the gapped *columnar solid* [LCR96; Fra+04] (see FIG. 1.5(a)), with four degenerate configurations of long-range correlated parallel dimers, two horizontal and two vertical depending on the relative position of dimers respect to the sublattices. On the contrary, when $v \to +\infty$ the plaquettes are absent in the gapped *staggered solid*, also fourfold degenerate as shown in FIG. 1.5(c) [LCR96; Fra+04]. At the RK point $v = 1$ the ground state is the RVB state, an equal-weight superposition of all possible dimer coverings of the lattice [Fra13], but the region between columnar and RK point is still a matter of debate. First, Banerjee *et al.* in [Ban+14], and Oakes, *et al.* in [Oak+18] by means of Montecarlo procedures found no phase between the columnar solid and the RK point, as displayed in FIG. 1.5(d)1. Syljuåsen in [Syl06], as well as Leung *et al.* in [LCR96], found the existence of the *plaquette solid*, a staggered configuration of flippable plaquettes of RVB depicted in FIG. 1.5(b), although they dissagree in the value of the critical v of the columnar-to-plaquette transition in FIG. 1.5(d)2. Lastly, Ralko *et al.* propose in [RPM08] a mixed phase continuously interpolated between the columnar solid and the plaquette RVB in the region $0 < v < 1$ (FIG. 1.5(d)3).

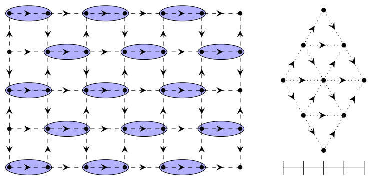

Figure 1.6: *Background configuration for the electric string in QDM*: The sublattice A(B) has vertices $Q_{\mathrm{r}} = \pm 2$, 1-in-3-out (viceversa). The dimer locates in the link flowing inwards sublattice A.

In this context, part i of this work discusses in detail the proposal by Herzog-Arbeitmann, Mantilla & Sodemann [HAMS19]. We address the problem of the phase diagram of the Q6VM and the QDM in a unified framework given by the Abelian QLM in a periodic square lattice $L_x \times L_y$. As already discussed, the Q6VM can be obtained by imposing the condition $Q_{\mathrm{r}} = 0$ at every lattice site, while the QDM by $Q_{\mathrm{r}} = \pm 2$ in a staggered pattern. Additionally, the *winding numbers* $W_{x,y}$ of the system, i.e., the sum of horizontal (vertical) links along one vertical (horizontal) non-contractible loop, work as two additional good quantum numbers to select one topological sector for each system[Fra13; Hoo78]. These sectors are chosen so as the resulting configuration the string is embedded in is a *ground state in the region at the RHS of the RK point*, excluding any flippable plaquette from the background. The construction of the Q6VM selects the maximally polarized sector $W_{x,y} = L_{x,y}$, depicted in FIG. 1.1 for $L_{x,y} = 3$, while the QDM takes the $W_x = L_x$ and $W_y = 0$, resulting in a staggered horizontal configuration of dimers (see FIG. 1.6). A string is then introduced in the system by reversing the orientation of the links along a path γ ending at the defects $Q_{\partial\gamma}$. The flip of the links along γ creates flippable plaquettes at the turning points or *kinks* of the string (FIG. 1.1), where the kinetic term of the RK Hamiltonian in (1.4) produces quantum fluctuations that modify the path γ.

We proceed to calculate the ground states of the electric string to propose a phase diagram for each model in function of $v = V/t$ so that the string can act as a 1D precursor of the phases found in the whole Q6VM and QDM, manifesting by the number of kinks, i.e., flippable plaquettes, the string has.

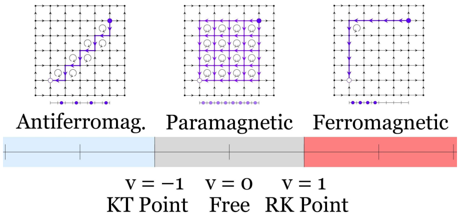

Figure 1.7: *Phase diagram of the electric string in* Q6VM: The FM, gapless paramagnetic and AFM correspond to different paths γ describing the string.

The methodology consists in mapping the string onto a 1D chain occupied by HCB ruled by a bosonic Hamiltonian that embodies the dynamics of the string in terms of HCB hoppings and potential terms. Our results suggest the existence of at least three phases with three critical points: 1) a FM phase minimizing the number of flippable plaquettes, corresponding to the less-kinked path γ of the electric string (RHS of FIG. 1.7), 2) the high-symmetry RK point where any string configuration contributes to the ground state, 3) a gapless paramagnetic phase with ground state described by the path γ that maximizes the number of flippable plaquettes (the point $v = 0$ is a high-symmetry point for the Q6VM), 4) a critical point around $v \sim -1$ suggesting an infinite-order Kosterlitz-Thouless (KT) transition; and 5) a gapped AFM state with ground state corresponding to the maximally kinked path (LHS of FIG. 1.7). We can interpret the phases at the limits $v \to \pm\infty$ with the solids of the 2D models and the liquid-like phase in the region $|v| < 1$ with the plaquette RVB as closely-packed strings because strings can at most intersect yielding a 2-in-2-out or staggered vertex without flippable plaquettes that block further crossings, producing closed resonating strings in direct resemblance of the phase depicted in FIG. 1.5(b). The chapters 2, 3 and 4 discuss extensively the framework of LGTs, its realization in QLMs and the subsectors of Q6VM and QDM on the problem of the phase diagram of the fluctuating electric string.

1.2 BOSONIZATION OF PARTICLE-HOLE EXCITATIONS IN 2D DIRAC FERMIONS

The second framework we address in this work is the problem of describing $\mathbf{Q} = 0$ PHEs in nodal semimetals with graphene as a case study (see FIG. 1.8). The nonperturbative effects of interactions in a 2D Dirac fermion system are captured by a *bosonizaton formalism* proposed in this work, in which the creation of particle-hole pair at momentum $\mathbf{k}$ in the $\mathbf{Q} = 0$ is mapped as the flip of the *pseudospin* $\mathbf{s}_\mathbf{k}$ of the electron, initially oriented towards the Dirac Point (DP) (see FIG. 1.8). The pseudospin $\mathbf{s}_\mathbf{k}$ is reexpressed in terms of HCBs $b_\mathbf{k}$, $b^\dagger_\mathbf{k}$ by means of the Holstein-Primakov (HP) transformations, as well as the associated Hamiltonian which is expanded up to second order in $b_\mathbf{k}$ yielding a quadratic bosonic Hamiltonian with hopping and pairing terms in the reciprocal lattice. The new effective system is a collection of excitons bounded by the effective Coulomb attraction between the electron and the hole. As an application of this framework, we calculate the optical conductivity of graphene, obtaining results in agreement with the experiments and numerical approaches.

Bosonization is a technique to address nonperturbative physics in fermionic systems successfully implemented in 1D. It proceeds in a way that fermionic Hamiltonians involving two-fermion operators (such as the kinetic terms) and 4-fermion operators (interaction terms) can be reexpressed as quadratic in the new bosonic basis so that not only its diagonalization is straightforward but also that it is remarkably successful in capturing the nonperturbative features of 1D systems [Gia03].

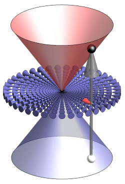

Figure 1.8: *Low-energy band and pseudospin pictures of monolayer graphene.*

The first work in this direction might be Bloch's proposal in [Blo33] on studying excited states of a Fermi gas as *sound waves*, oscillations in the density of the collection of electrons in replacement of the original excited electron and hole DOF. Tomonaga in [Tom50] formalizes Bloch's idea for 1D systems consistently, and Frölich in [Frö53] proposes an extension to 3D Fermi gas in the context of superconductivity. Giamarchi's textbook on physics of 1D quantum system [Gia03] discusses in detail 1D bosonization, Bethe Ansatz, among other methods.

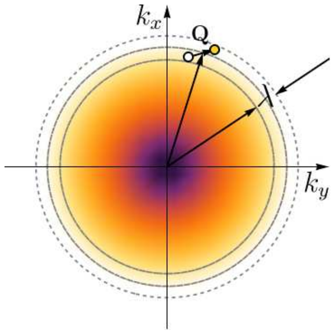

Figure 1.9: *Shell of validity for bosonization in any dimension.* The fermionic DOF outside the shell $k_F - \lambda/2 < |\mathbf{k}| < k_F + \lambda/2$ are integrated out to obtain an effective model where the low-energy excitations are bosonized.

Motivated by the successful description of 1D systems using bosonization, extensions to higher-dimensional systems have been attempted. Luther in [Lut79] extends Tomonaga's bosonization to 3D systems for excitations whose momentum vector **Q** is normal to the Fermi surface. Later, Haldane, in a series of lectures during the International School of Physics "Enrico Fermi" [Hal94] presented how multidimensional fermionic systems can be bosonized by interpreting excitations as deformations of the Fermi surface so as its volume remains intact after interactions are included, in accordance to Luttinger's theorem [Lut60], approach followed by Houghton & Marston in [HM93] which include a calculation of the contribution $T^3 \ln(T)$ to the specific heat of 3D Fermi liquids to do small-angle scatterings, and in later work with Kwong [HKM94] they study the stability of the bosonized Fermi liquid with electron-electron interactions. In the series of articles [CNF94b; CNF94a; CNF95], Castro Neto & Fradkin present a framework to perform bosonization in any number of dimensions within the limit of long wavelengths by bosonizing the low-energy excitations in a shell closely surrounding the Fermi surface (see FIG. 1.9). The previous developments are contained and discussed in detail in the review [HKM00] done by Houghton, Kwong & Marston.

In brief, higher-dimensional bosonization departs from considering the creation of a particle-hole pair $c^{\dagger}_{\mathbf{k}+\mathbf{Q}/2}c_{\mathbf{k}-\mathbf{Q}/2}$ with total momentum $|\mathbf{Q}| \ll k_F$ inside the shell depicted in FIG. 1.9. These are promoted to bosonic operators $b_{\mathbf{k},\mathbf{Q}}$ whose commutators are approximated as a number. The new bosonized Hamiltonian couples bosonic modes with momentum $\mathbf{Q}$ to bosons with either $+\mathbf{Q}$ or $-\mathbf{Q}$, and no other channels are dynamically connected. In other words, a particle hole-pair with momentum $\mathbf{Q} = \mathbf{Q}_1 + \mathbf{Q}_2$ cannot scatter into two particle-hole pairs with momenta $\mathbf{Q}_{1,2}$. Only particle-hole pairs with momentum $\mathbf{Q}$ can scatter into pairs with the same $\mathbf{Q}$ or create pairs with momentum $+\mathbf{Q}$ and $-\mathbf{Q}$. Indeed, the higher-dimensional bosonization approach to PHEs close to the Fermi surface is crucially based on the assumption of separability of the Hilbert space in subspaces labeled by $\mathbf{Q}$, with the hypothesis that it is an asymptotically correct description of such excitations in Landau-Fermi liquids for $|\mathbf{Q}| \ll k_F$.

Further works in higher-dimensional bosonization in different contexts are the description of $(2+1)$-dimensional nonrelativistic fermions using bosonization [Bar+00]; quantum Hall effect [BO00]; bosonization via hydrodynamic variables [Set06] and noncommutative field theory [Pol06]; topological insulators [Cha+13; CRS17]; 2D Fermi liquids in weak magnetic fields [BFR18]; transverse fluctuations called *shear sound* in 2D Fermi liquids [KSV19] where the excitations are tranverse waves instead of longitudinal density fluctuations as shown in FIG. 1.10; and $\mathbf{Q} = 0$ PHEs in two-band systems with Fermi surfaces shrunken to a point such as graphene and topological insulators [MS20].

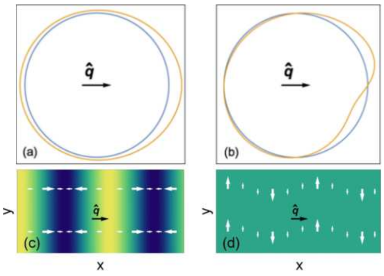

Figure 1.10: *Shear sound in Fermi liquids*. Fermi surface deformation, and density/current fluctuations of zero (a,c) and shear (b,d) sound. [Adapted by permission from the APS (Khoo *et al.* [KSV19]) Copyright (2014); `https://doi.org/10.1103/PhysRevB.99.075434`].

In this context, part ii of this work discusses in detail the proposal done by Mantilla & Sodemann [MS20]. Higher-dimensional bosonization, as stated in the previous works, is not valid for PHEs with momentum $\mathbf{Q} = 0$ since these excitations do not exist in ordinary one-band Fermi liquids (see FIGs. 1.8 and 1.9). Even more, in nodal semimetals, where the Fermi surface shrinks to a point, for instance, Weyl or massless Dirac semimetals, do not admit a description of modes close to the shrunken Fermi surface. We address the problem of developing a systematic bosonization approach to the sector $\mathbf{Q} = 0$ for gapless semimetals. Although our proposal is attempted to be valid in higher dimensions, as a first approach, we focus our discussion only on 2D Dirac fermions, for instance, low-energy modes on the surface of 3D topological insulators or in monolayer graphene, where the latter is our study case. In a few words, we propose a mapping of the interacting PHEs, or excitons, in $\mathbf{Q} = 0$ sector onto a spin-like picture based on the pseudospin operator that comprises the kinetic terms of the fermionic Hamiltonian. The pseudospin is then mapped as HCBs representing the excitons, and yielding a new bosonic quadratic Hamiltonian, whose diagonalization is straightforwards using Bogoliubov-Valatin (BV) transformations [Val58; Bog58].

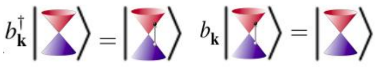

Figure 1.11: *Exciton operators*: The new bosonic operators $b^{(\dagger)}_{\mathbf{k}}$ describe PHEs of 2D Dirac fermions as HCBs in the lattice.

We take borrowed from higher-dimensional bosonization the assumption of separability of the Hilbert space by sectors labeled by $\mathbf{Q}$ and assume that the optical PHEs, i.e., with $\mathbf{Q} = 0$, are decoupled from pairs with finite $\mathbf{Q}$. At low energies, we expect this simplification is valid in phases adiabatically related to free fermions, similarly to how such decoupling allows the description of Fermi liquids which are adiabatically connected to free fermions in the higher dimensional bosonization of Fermi surfaces. Nevertheless, for our formalism, we present a solid and very explicit connection to the conventional Feynman diagrammatic perturbation theory by proving that the solution of our effective bosonic Hamiltonian for optical particle-hole pairs is *exactly equivalent* to the Kadanoff-Baym (KB) Self-Consistent Hartree-Fock (SCHF) resummation [BK61; Bay62] of the particle-hole propagator at $\mathbf{Q} = 0$, associated with the self-consistent Hartree-Fock (HF) approximation to the single particle-particle Green's function (for further details Appendix B discusses this procedure in detail).

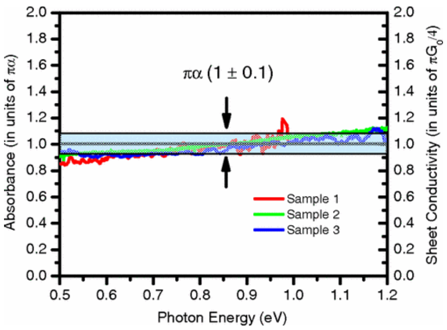

Figure 1.12: *Absorbance and sheet conductivity of graphene*: Absorption spectra for three different samples of graphene over the range of photon energies between 0.5 and 1.2 eV. [Adapted by permission from (a) the American Physical Society (Mak *et al.* [Mak+08]) Copyright (2008); `https://doi.org/10.1103/PhysRevLett.101.196405`].

As an application of our approach we will compute the interaction corrections to the optical conductivity $\sigma(\omega)$ of 2D Dirac fermions with Coulomb interactions, whose strength is parametrized by the effective fine structure constant $\alpha = e^2/\epsilon v$, where v is the velocity of the Dirac fermions and ϵ the dielectric constant of the surrounding medium. This optical conductivity at low energies is determined by fundamental constants of nature and given by $\sigma_0 = e^2/16\hbar$ per Dirac cone [Lud+94; AZS02]. Its zero-frequency limit is not expected to be renormalized by interactions, but Coulomb interactions can produce a slow flow as a function of frequency to such value wirh a nontrivial non-analytic frequency dependence at low energies. The first perturbative approaches done by Mishchenko [Mis08] and Herbut, Juričić & Vafek [HJV08] were in mutual dissagreement. Subsequent studies by Sheehy & Schmalian, [SS09], Abedinpour *et al.* [Abe+11], Sodemann & Fogler [SF12], and Teber & Kotikov [TK14; TK18] among others [Gaz+13; Bar+14a], validated Mishchenko's result. Our approach [MS20] recovers the same result in the perturbative limit, with the advantage that nonperturbative values of α are also accesible, filling this gap in the scarse literature. A Quantum Monte Carlo approach done by Boyda *et al.* on computing $\sigma(\omega)$ concluded that interaction corrections remain relatively small even at $\alpha \sim 2$, with the support of our approach. To conclude, experimental measurements of optical properties in graphene done by Li *et al.* [Li+08], Mak *et al.* [Mak+08] (see FIG. 1.12), and Nair *et al.* [Nai+08] have reported $\sigma(\omega)$ in close agreement with the noninteracting value σ_0, results reproduced by our approach up to $\alpha \sim 5$ with corrections no larger than 4% of σ_0.

1.3 STRUCTURE OF THE DOCUMENT

The document is divided into three parts, the first two, Parts i and ii each subdivided into three chapters comprising the main body, and the last one, Part iii, devoted on exploring new ideas and the conclusions derived from the main body. In the end, a set of short Appendices is added to complement the content:

- Part i QUANTUM LINK MODELS AND FLUCTUATING ELECTRIC STRINGS contains Chapters 2, 3 and 4.
  - Chapter 2 outlines briefly the Abelian formulation of LGTs and QLMs, as well as to establish the notation used in Chapters 3 and 4. The reader familiarized with LGTs can skip this chapter and return in case of need.
  - Chapter 3, based in [HAMS19], studies the phases of an electric string connecting two static sources in the Q6VM, a quantum ice model in the checkerboard lattice, by mapping it into a 1D system of HCBs, mapped further into a XXZ chain.
  - Chapter 4, following [HAMS19], continues the study of the phases of one electric field line but in the QDM, as a 1D precursor of the phases of the whole QDM discussed in the literature.
- Part ii BOSONIZATION OF PARTICLE-HOLE EXCITATIONS IN 2D DIRAC FERMIONS: contains Chapters 5, 6 and 7.
  - Chapter 5 presents summarily the origin of the effective model of 2D Dirac fermions from the tight-binding model of the honeycomb lattice due to sp^2 hybridization of carbon atoms. It also sets the notation used in Chapters 6 and 7. The reader familiarized with the matter can skip this chapter and also return in case of need.
  - Chapter 6, based in [MS20], introduces a bosonization technique to study PHEs in the $\mathbf{Q} = 0$ sector as an extension to the previous techniques for higher-dimensional systems.
  - Chapter 7 discusses the calculation of the optical conductivity of graphene including nonperturbative effects of interations as an application to the bosonization formalism presented in chapter 6 and in [MS20], with a comparison to the results with the literature.

- Part iii New Perspectives and Conclusions: contains Chapters 8 and 9.
    - Chapter 8 discusses current and further developments based in Chapter 6, specifically in describing the weak coupling instability of bilayer graphene derived from electron interactions.
    - Lastly, Chapter 9 outlines the findings in the implementation of HCBs in the contexts of electric strings in 2D LGTs and $\mathbf{Q} = 0$ PHEs in graphene.
- Part iv Appendices: contains further information and details cited through the main parts.
    - App. A has a very brief discussion on Bethe Ansatz and expressions of the ground state energy of the 1D XXZ chain used in Chapter 3.
    - App. B shows the explicit calculation of the KB SCHF approximations of the particle-hole propagator used in Chapter 6.
    - App. C presents a pedagogical calculation of the optical conductivity of Dirac fermions with the method of pseudospin precession, cited in Chapter 7.
    - App. D discusses the procedure to reconfigurate lattice in which we proposed the bosonization in Chapter 6 from a square to a polar lattice, manifestly displaying the rotational symmetry of the thermodynamic limit of interacting electrons in Chapter 7.

The reader interested in the implementation of HCBs in LGTs is invited to focus their reading on Part i. Similarly, the reader interested in the bosonization of 2D Dirac fermions can skip Part i and focus on Part ii and Chapter 8.

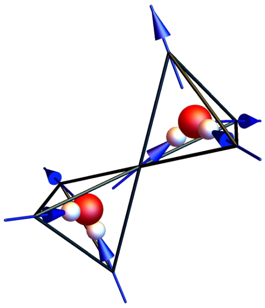

Part I

QUANTUM LINK MODELS AND FLUCTUATING ELECTRIC STRINGS

This part is focused in studying the phases of one electric field string between two static sources as a system to implement hard-core bosons described by the Rokhsar-Kivelson (RK) Hamiltonian in a 2D Abelian Lattice Gauge Theory (LGT). Chapter 2 presents the basic framework of source-free U(1) LGTs in 2D and the Quantum Link Model (QLM) up to the construction of the RK Hamiltonian, solved in the chapters 3 and 4 for the problem of the electric field line in the Quantum 6-Vertex Model (Q6VM) and the Quantum Dimer Model (QDM), respectively, as two subsectors of the U(1) LGT.

2

A BRIEF INTRODUCTION TO LATTICE GAUGE THEORIES

> *Besides language and music, it [mathematics] is one of the primary manifestations of the free creative power of the human mind, and it is the universal organ for world understanding through theoretical construction.*
>
> — Hermann Weyl [Zei11]

The concept of symmetry lies at the very center of physics as a modern science, in its classical but especially in the quantum formulation where the systems are described by complex functions that allow to encompass more directly the sets of transformations, or *groups*, that leave the systems *invariant*[ED79]. The symmetries of a physical system can be discrete or continuous, global or local, spatio-temporal or internal, etc., but one of the most fruitful frameworks correspond to the formulation of theories that are described by *local internal* symmetries, called *gauge theories*.

Although gauge theories were first built in continuous space[JO01], their formulation in a lattice gives several advantages such as the existence of a natural UV-cutoff or their natural implementation in atomic and condensed matter systems characterized by space point groups. Their Hamiltonians are also defined by local terms whose parameters can display many different phases that explain from quark confinement and hadronization in Quantum Chromodynamics (QCD)[KS75; Wil74], spin ice materials[GM14; BHR21], atomic systems[Aid+22; ZCR15] among others.

This chapter is devoted to do discuss the background and notation used to study the problem of a single electric line connecting two static sources in the Quantum 6-Vertex Model (Q6VM) and the Quantum Dimer Model (QDM) in [HAMS19], from the very statement of invariance under local gauge transformations in §2.1, through the formulation of the Abelian Lattice Gauge Theory (LGT) in §2.2, to the introduction of the Quantum Link Model (QLM) and the Rokhsar-Kivelson (RK) Hamiltonian in §2.3, in order to address the problem of a fluctuating electric string in the Q6VM and the QDM as sectors of a QLM in chapters 3 and 4, respectively.

2.1 CONTINUOUS FORMULATION OF U(1) GAUGE THEORIES

The introduction of electromagnetic fields using the Abelian gauge group U(1) is done by imposing the invariance of the equation of motion of a free particle under the local transformation

$$\psi(x) \to V(\chi(x))\psi(x) = e^{ie\chi(x)}\psi(x), \tag{2.1}$$

where $x = (\mathbf{r}, t)$, $V(\chi(x)) \in \mathrm{U}(1)$, and e is the coupling constant that controls the strength of the interaction. The new terms coming from $V(\chi(x))$ are cancelled out when the gauges at x and x' are adequately connected with the introduction of *gauge parallel transporters* $U(x', x) \in \mathrm{U}(1)$[PS95]:

$$\psi(x) \to \psi(x') = U(x', x)\psi(x), \tag{2.2}$$

called as *phase-compensators* since it shifts the phase of $\psi(x)$ when evaluated at the points x and thereafter at x' to keep the gauge invariance. The expression of the gauge transporter $U(x', x)$ is (using relativistic notation $[x^\mu] = (t, \mathbf{r})$ with $[\eta_{\mu\nu}] = \mathrm{diag}(+ - - -)$)[Rot12]:

$$U(x', x) = \mathcal{P} \exp \left[ie \int_C A_\mu(x) dx^\mu \right], \tag{2.3}$$

where $[A_\mu] = (\Phi, -\mathbf{A})$ is the *gauge connections* with components Φ and $\mathbf{A}$ the scalar and vector potentials, respectively, and $\mathcal{P}$ is a path-ordering operator depending on the affine parameter used to map the path $\mathcal{C}$ starting from x and ending at x'. In order to keep the transformation rule in (2.1), the gauge transporter must gauge transform as $U'(x', x) = V(x')U(x', x)V^\dagger(x)$, yielding that the connection has the gauge transformation rule:

$$A_\mu(x) \to A_\mu(x) + \partial_\mu \chi(x), \tag{2.4}$$

(where $[\partial_\mu] = (\partial_t, \nabla)$). As an important definition, the evaluation of the transporter (2.3) along a closed loop defines the *Wilson loop*[CMV14]:

$$L = \mathcal{P} \exp \left[ie \oint_C A_\mu(x) dx^\mu \right], \tag{2.5}$$

which is gauge invariant and encodes the dynamics of the connections as it is briefly presented in §2.1.1. Lastly, the equations of motion are modified by replacing ∂_t and ∇ by the *covariant derivatives*:

$$\partial_\mu \to \partial_\mu - eA_\mu = \begin{cases} \partial_t - e\Phi, \\ \nabla - e\mathbf{A}, \end{cases} \tag{2.6}$$

The gauge transporter is one of the key elements used in the lattice formulation of gauge theories since it contains the transformation rules for finite intervals fixed by the lattice parameters. Similarly, the Wilson loop is fundamental to describe gauge fields in the lattice.

2.1.1 *Gauge field equations*

The gauge connections a.k.a. potentials are dynamical entities whose equations of motion are expressed in terms of the *gauge curvature* $F_{\mu\nu}$, obtained as the commutator of the covariant derivatives $\left[D_\mu, D_\nu\right]\psi(x) = ieF_{\mu\nu}\psi(x)$, where the antisymmetric tensor is given by[Ryd96]

$$F_{\mu\nu} = \partial_\mu A_\nu - \partial_\nu A_\mu. \tag{2.7}$$

Another way to reach the curvature is by evaluating the transporter (2.3) along an infinitesimal closed loop $C = \partial S$ enclosing a surface S, employing the *Stokes' theorem*[CMV14]:

$$\mathcal{P}\exp\left[ie\oint_{\partial S} A_\mu(x)dx^\mu\right] = \exp\left[ie\int_S F_{\mu\nu}(x)d\sigma^{\mu\nu}\right], \tag{2.8}$$

and extracting the change of the wave-function when it is parallel transported along $\mathcal{C}$ as $\psi'(x) - \psi(x) = \frac{ie}{2}F_{\mu\nu}S^{\mu\nu}$, finding that it is proportional to the area $S^{\mu\nu}$ of the surface enclosed by $\mathcal{C}$ contracted with the curvature $F_{\mu\nu}$, i.e., the flux of the component $F_{\mu\nu}$ through the infinitesimal surface $S^{\mu\nu}$.

The components of $F_{\mu\nu}$ are

$$F_{tj} = -\partial_t A_j - \partial_j\Phi = E_j, \quad F_{ij} = \partial_i A_j - \partial_j A_i = \epsilon_{ijk}B_k, \tag{2.9}$$

being $\mathbf{E}$ and $\mathbf{B}$ the *electric* and the *magnetic fields*, respectively, both gauge invariant from the very definition of the Wilson loop (2.5) and explicitely visible in the definition of $F_{\mu\nu}$ in (2.7).

As a consquence of the Jacobi identity applied on the commutators of the covariant derivative, the curvature $F_{\mu\nu}$ fulfills the *Bianchi identities*, that yield the the *homogeneous Maxwell equations* [Ryd96]:

$$\partial_\mu F_{\nu\rho} + \partial_\nu F_{\rho\mu} + \partial_\rho F_{\mu\nu} = 0 \rightarrow \begin{cases} \nabla\cdot\mathbf{B} = 0, \\ \nabla\times\mathbf{E} = -\partial_t\mathbf{B}, \end{cases} \tag{2.10}$$

as geometric constrains in the fields. On the other hand, the Lagrangian containing the kinetic term of the gauge fields and the coupling with the sources, the 4-current $[J_\mu] = (\rho, -\mathbf{J})$, is given by[Ryd96]:

$$\mathcal{L} = -\frac{1}{4}F^{\mu\nu}F_{\mu\nu} - J_\mu A^\mu = \frac{1}{2}\left(\mathbf{E}^2 - \mathbf{B}^2\right) - \rho\Phi + \mathbf{J}\cdot\mathbf{A}, \tag{2.11}$$

and yields the *inhomogeneous Maxwell equations*

$$\partial_\mu F^{\mu\nu} = J^\nu \rightarrow \begin{cases} \nabla\cdot\mathbf{E} = \rho, \\ \nabla\times\mathbf{B} = \mathbf{J} + \partial_t\mathbf{E}, \end{cases} \tag{2.12}$$

where $\rho(x) = \psi^\dagger(x)\psi(x)$ and $\mathbf{J}$ are the matter density and current, respectively. Notice that the the conservation law is automatically fulfilled since $\partial_\mu\partial_\nu F^{\mu\nu} = \partial_\nu J^\nu = 0$ because of $F_{\mu\nu} = -F_{\nu\mu}$.

From the Lagrangian (2.11) it is also possible to obtain the conjugated momentum fields of Φ and $\mathbf{A}$ as[Ryd96]:

$$\pi_V = \frac{\partial\mathcal{L}}{\partial\partial_t\Phi} = 0, \quad \pi_A^k = \frac{\partial\mathcal{L}}{\partial\partial_t A_k} = \left(\partial^k\Phi - \partial^t A^k\right) = E^k. \tag{2.13}$$

We found that $\mathbf{A}$ has the $\boldsymbol{\pi}_A = -\mathbf{E}$ as conjugate momentum (the minus sign comes from the fact that in (2.13) π_A^k is conjugate to $A_k = -A^k$), while Φ

has no conjugate momentum implying that the Euler-Lagrange equation associated to Φ:

$$0 = \nabla \cdot \frac{\partial \mathcal{L}}{\partial \nabla \Phi} - \frac{\partial \mathcal{L}}{\partial \Phi} = \nabla \cdot \mathbf{E} - \rho = 0, \tag{2.14}$$

is, in fact, an equation of constrain that ensures the Gauss law in (2.12) [Kle16], with Φ as the Lagrange multiplier[Wie13]. These facts are going to be crucial when studying gauge fields in a lattice.

Lastly, the Hamiltonian density of the electromagnetic field can be obtained as the time-time component of the *stress-energy tensor* $T_{\mu\nu}$ associated to the Lagrangian (2.11), given by[Ryd96]

$$T_{\mu\nu} = F_{\mu\rho} F_{\nu}^{\ \rho} - \frac{1}{4} \eta_{\mu\nu} F^{\rho\sigma} F_{\rho\sigma}, \tag{2.15}$$

from where we obtained the Hamiltonian density $\mathcal{H} = T_{tt}$ and, in this way:

$$H_{\text{EM}} = \int d^3 x \mathcal{H} = \int d^3 x (\mathbf{E}^2 + \mathbf{B}^2). \tag{2.16}$$

The Hamiltonian can also be obtained as the Legendre transform of the Lagrangian (2.11) with the conjugate momentum field (2.13). The definition (2.16) and the conjugate pair $(\mathbf{A}, -\mathbf{E})$ in (2.13) are the cornerstones of the construction of the lattice formation of gauge theories.

2.1.2 *Gauss' law as generator of the gauge transformations*

When the Hamiltonian of the electromagnetic field in (2.16) is quantized, the canonical fields $\mathbf{A}(\mathbf{r})$ and $\mathbf{E}(\mathbf{r})$ are associated with quantum operators obbeying the commutation relations[Ryd96; PS95]:

$$\left[\hat{A}_i(\mathbf{r}), \hat{A}_j(\mathbf{r}')\right] = \left[\hat{E}_i(\mathbf{r}), \hat{E}_j(\mathbf{r}')\right] = 0, \quad \left[\hat{A}_i(\mathbf{r}), \hat{E}_j(\mathbf{r}')\right] = -i\delta^3(\mathbf{r} - \mathbf{r}')\delta_{ij}, \tag{2.17}$$

along with the corresponding commutation relations for the matter fields (bosons or fermions):

$$\left[\hat{\psi}(\mathbf{r}), \hat{\psi}(\mathbf{r}')\right]_{\pm} = [\hat{\psi}^\dagger(\mathbf{r}), \hat{\psi}^\dagger(\mathbf{r}')]_{\pm} = 0, \quad [\hat{\psi}(\mathbf{r}), \hat{\psi}^\dagger(\mathbf{r}')]_{\pm} = \delta^3(\mathbf{r} - \mathbf{r}'), \tag{2.18}$$

The constraint of the Gauss' law in (2.14) can also be formulated in terms of the operator[IM14; Wie13]

$$\hat{Q}(\mathbf{r}) = \nabla \cdot \hat{\mathbf{E}}(\mathbf{r}) - \hat{\rho}(\mathbf{r}). \tag{2.19}$$

$\hat{Q}(\mathbf{r})$ represents the total charge at the site $\mathbf{r}$, and since it commutes with the quantized Hamiltonian obtained from (2.16):

$$\left[\hat{Q}(\mathbf{r}), \hat{H}\right] = 0, \tag{2.20}$$

it constitutes a good quantum number $q(\mathbf{r})$ that separates the Hilbert space in disconnected sectors $\hat{Q}(\mathbf{r}) \left|q(\mathbf{r})\right\rangle = q(\mathbf{r}) \left|q(\mathbf{r})\right\rangle$ depending on the eigenvalues associated to $\hat{Q}(\mathbf{r})$, which are constants of motion and conserved at each site $\mathbf{r}$. Actually, the sector defined as *physical* corresponds to $\hat{Q}(\mathbf{r})\,|q(\mathbf{r})\rangle = 0$, fulfilling the Gauss' law $\nabla \cdot \hat{\mathbf{E}}(\mathbf{r})\,|q(\mathbf{r})\rangle = 0$. It turns out that the conserved charge of a local gauge symmetry is its generator itself, so we can build the operator[IM14; HAMS19]

$$\hat{\mathcal{U}} = \exp\left(i\int d^3x'\chi(\mathbf{r}')\hat{Q}(\mathbf{r}')\right), \tag{2.21}$$

that acts on any other operator as $\hat{O}(\mathbf{r},\mathbf{r}',...) \to \hat{\mathcal{U}}\hat{O}(\mathbf{r},\mathbf{r}',...)\hat{\mathcal{U}}^\dagger$, and selects the suited gauge transformation at the points $(\mathbf{r},\mathbf{r}',...)$. For instance, the matter fields transform as follows under $\mathcal{U}$:

$$\hat{\psi}(\mathbf{r}) \to \hat{\mathcal{U}}\hat{\psi}(\mathbf{r})\hat{\mathcal{U}}^\dagger = \hat{\mathcal{U}}\hat{\mathcal{U}}^\dagger e^{i\int d^3x'\chi(\mathbf{r}')\delta^{(3)}(\mathbf{r}'-\mathbf{r})}\hat{\psi}(\mathbf{r}) = e^{ie\chi(\mathbf{r})}\hat{\psi}(\mathbf{r}) = V(\mathbf{r})\hat{\psi}(\mathbf{r}),$$

recovering (2.1), and similarly for gauge transporter in (2.3):

$$\hat{U}(\mathbf{r},\mathbf{r}') \to \hat{\mathcal{U}}\hat{U}(\mathbf{r},\mathbf{r}')\hat{\mathcal{U}}^\dagger = e^{ie\chi(\mathbf{r})}\hat{U}(\mathbf{r},\mathbf{r}')e^{-ie\chi(\mathbf{r}')} = V(\mathbf{r})\hat{U}(\mathbf{r},\mathbf{r}')V^\dagger(\mathbf{r}'),$$

The total charge operator $\hat{Q}(\mathbf{r})$ and the gauge transformation $\hat{\mathcal{U}}$ will play an essencial role in the selection of sectors studied in the next sections and chapters.

2.2 U(1) GAUGE THEORIES ON A LATTICE

The discretization of the underlying space yields a lattice of sites $\mathbf{r}$ connected with a finite number of sites by the links $(\mathbf{r},\boldsymbol{\ell})$ where the first component indicates the site where the link starts and the second its direction. For example, in a square lattice the sites are labelled as $\mathbf{r} = (x,y)$, and the links as $(\mathbf{r},\boldsymbol{\ell})$ where $\boldsymbol{\ell} = \{\hat{\mathbf{x}},\hat{\mathbf{y}}\}$ represents the unit vectors of length a (which indeed represents a UV cutoff), so that each site has only two links associated in the positive x- and the y-directions, as shown in FIG. 2.1a.

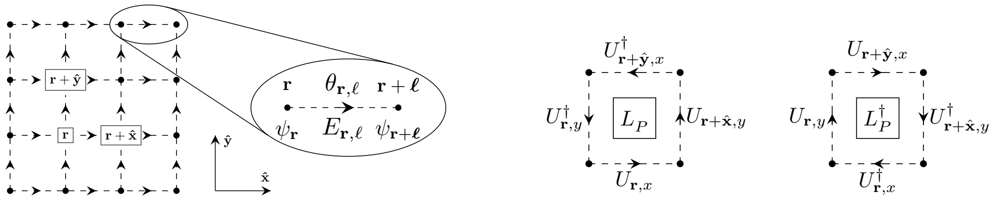
$\mathbf{r}+\hat{\mathbf{y}}$
$\mathbf{r}$
$\mathbf{r}+\hat{\mathbf{x}}$
$\mathbf{r}$
$\theta_{\mathbf{r},\ell}$
$\mathbf{r}+\boldsymbol{\ell}$
$\psi_{\mathbf{r}}$
$E_{\mathbf{r},\ell}$
$\psi_{\mathbf{r}+\boldsymbol{\ell}}$
$\hat{\mathbf{y}}$
$\hat{\mathbf{x}}$
$U^\dagger_{\mathbf{r}+\hat{\mathbf{y}},x}$
$U^\dagger_{\mathbf{r},y}$
L_P
$U_{\mathbf{r}+\hat{\mathbf{x}},y}$
$U_{\mathbf{r},x}$
$U_{\mathbf{r}+\hat{\mathbf{y}},x}$
$U_{\mathbf{r},y}$
$L_P^\dagger$
$U^\dagger_{\mathbf{r}+\hat{\mathbf{x}},y}$
$U^\dagger_{\mathbf{r},x}$

(a) Labelling convention.

(b) Plaquette operators.

Figure 2.1: *2D square lattice labelling rule and plaquette operators.*: The figure shows (a) the labelling rule respect to the site $\mathbf{r}$ and (b) the plaquette operators in the lattice. Notice each site labels the up- and right-Nearest Neighbor (NN) sites,and gauge connections along the links labelled as $(\mathbf{r},\boldsymbol{\ell})$ with $\boldsymbol{\ell} = \{\hat{\mathbf{x}},\hat{\mathbf{y}}\}$. Moreover, L_P increases by a unit the magnetic quantum flux through the cell enclosed by the loop P.

The matter fields $\psi_{\mathbf{r}}$, bosons or fermions, are located on each site $\mathbf{r}$, and their kinetic terms are defined as hoppings to the neighboring sites as

$\psi_{\mathbf{r}}^{\dagger}\psi_{\mathbf{r}+\boldsymbol{\ell}}$. On the other hand, the gauge field $A_{\mathbf{r},\boldsymbol{\ell}}$ is defined along the links playing the role as the connection between the sites when they are gauged locally $\psi_{\mathbf{r}} \to V_{\mathbf{r}}\psi_{\mathbf{r}}$ where $V_{\mathbf{r}} \in \mathrm{U}(1)$, and its conjugate momentum $E_{\mathbf{r},\boldsymbol{\ell}}$, the electric field, is also defined along each link $(\mathbf{r}, \boldsymbol{\ell})$ (FIG. 2.1a).

The finite distance between the different sites enforces that the local gauge transformations have to be compensated not by covariant derivatives, but instead by gauge transporters (2.3) in the lattice:

$$U_{\mathbf{r},\boldsymbol{\ell}} = \exp\left[ie\int_{x'_\ell}^{x'_\ell+a} A_\ell(\mathbf{r})dx'_\ell\right] = \exp\left[i\theta_{\mathbf{r},\boldsymbol{\ell}}\right], \tag{2.22}$$

where the connection is integrated along the link defining a new angular variable, $\theta_{\mathbf{r},\boldsymbol{\ell}} \in [0, 2\pi)$, that replaces $A_{\mathbf{r},\boldsymbol{\ell}}$ and controls the transporter. In this way, $\psi_{\mathbf{r}+\boldsymbol{\ell}}^{\dagger}\psi_{\mathbf{r}}$ is replaced by $\psi_{\mathbf{r}+\boldsymbol{\ell}}^{\dagger}U_{\mathbf{r},\boldsymbol{\ell}}\psi_{\mathbf{r}}$.

2.2.1 *Gauge field Hamiltonian*

The gauge field Hamiltonian is built using the electric fields $E_{\mathbf{r},\boldsymbol{\ell}}$, and the transporters $U_{\mathbf{r},\boldsymbol{\ell}}$ in a shape that is gauge invariant, it is, comprising a lattice analogue of the Wilson loop (2.5) along the smallest non-trivial closed loops P in the lattice, given by[Wie13; IM14]:

$$P = (\mathbf{r}, x) \cup (\mathbf{r}+\hat{\mathbf{x}}, y) \cup (\mathbf{r}+\hat{\mathbf{y}}, x) \cup (\mathbf{r}, y), \tag{2.23a}$$

$$L_P = U_{\mathbf{r},x}U_{\mathbf{r}+\hat{\mathbf{x}},y}U^{\dagger}_{\mathbf{r}+\hat{\mathbf{y}},x}U^{\dagger}_{\mathbf{r},y}. \tag{2.23b}$$

The loop P is called a *plaquette*, and L_P is a *plaquette operator* that creates a magnetic flux through the surface enclosed by P as shown in FIG. 2.1b (note that $L_P^\dagger$ reverses the evaluation along the plaquete). With these elements, the gauge field Hamiltonian can be expressed as[IM14]:

$$H_{\mathrm{EM}} = \frac{e^2}{2a}\sum_{\mathbf{r},\ell} E^2_{\mathbf{r},\ell} + \frac{1}{2e^2a}\sum_P \left(L_P + L_P^\dagger\right) \tag{2.24}$$

that reduces to (2.16) when taking the continuous limit $a \to 0$ with the following rules to renormalize the elements[IM14]:

$$E_{\mathbf{r},\ell} \to \frac{a^2}{e}E_\ell(\mathbf{r}), \quad U_{\mathbf{r},\ell} \to e^{ieaA_\ell(\mathbf{r})} \approx 1 + ieaA_\ell(\mathbf{r}), \tag{2.25a}$$

$$L_P + L_P^\dagger \to e^{iea(\partial_i A_j(\mathbf{r}) - \partial_i A_j(\mathbf{r}))} + \text{h.c.} \approx 2 - e^2a^4F^2_{ij}, \tag{2.25b}$$

with the limits $\sum_{\mathbf{r}}, \sum_P \to \frac{1}{a^2}\int d^2x$ and $\delta_{\mathbf{r}\mathbf{r}'} \to a^2\delta^{(2)}(\mathbf{r}-\mathbf{r}')$.

2.2.2 *Cylindrical algebra from* LGT

The canonical variables $(A_{\mathbf{r},\ell}, E_{\mathrm{r},\ell})$ and the commutation relations in (2.17) are then replaced in the lattice by $(\theta_{\mathbf{r},\ell}, \mathbf{E}_{\mathrm{r},\ell})$ with the commutation relations[IM14; Wie13]:

$$\left[\hat{\theta}_{\mathbf{r},\ell}, \hat{E}_{\mathrm{r}',\ell'}\right] = i\delta_{\mathbf{r}\mathbf{r}'}\delta_{\ell\ell'}, \tag{2.26}$$

which suggest to express $\hat{E}_{\mathrm{r}',\ell'}$ in the *angular basis* as $\hat{E}_{\mathbf{r},\ell}\psi(\mathbf{r}) = -i\frac{\partial}{\partial\theta_{\mathbf{r},\ell}}\psi(\mathbf{r})$. In terms of the transporter, the commutation relations are

$$[\hat{E}_{\mathrm{r},\ell}, \hat{U}_{\mathrm{r}',\ell'}] = +\delta_{\mathbf{r}\mathbf{r}'}\delta_{\ell\ell'}\hat{U}_{\mathrm{r},\ell}, \quad [\hat{E}_{\mathrm{r},\ell}, \hat{U}^{\dagger}_{\mathrm{r}',\ell'}] = -\delta_{\mathbf{r}\mathbf{r}'}\delta_{\ell\ell'}\hat{U}^{\dagger}_{\mathrm{r},\ell}. \tag{2.27}$$

This algebra then defines two reciprocal bases, $|\theta_{\mathbf{r},\ell}\rangle$ and $|n_{\mathbf{r},\ell}\rangle$, each one eigenbasis of conjugate operators:

$$\hat{U}(\theta_{\mathbf{r},\ell})\,|\theta_{\mathbf{r},\ell}\rangle = e^{i\theta_{\mathrm{r},\ell}}\,|\theta_{\mathbf{r},\ell}\rangle\,, \quad \hat{E}_{\mathbf{r},\ell}\,|n_{\mathbf{r},\ell}\rangle = n_{\mathbf{r},\ell}\,|n_{\mathbf{r},\ell}\rangle\,, \tag{2.28}$$

where $n_{\mathbf{r},\ell} \in \mathbb{Z}$ counts the discrete number of electric lines along the link $(\mathbf{r},\ell)$ because $\theta_{\mathbf{r},\ell} \in [0, 2\pi)$ is compact. They are Fourier-conjugated with the rule $\langle\theta_{\mathbf{r},\ell}|n_{\mathbf{r},\ell}\rangle = e^{in_{\mathrm{r},\ell}\theta_{\mathrm{r},\ell}}/\sqrt{2\pi}$. The $|n_{\mathbf{r},\ell}\rangle$ state can then be expressed as[IM14]

$$\begin{aligned} |n_{\mathbf{r},\ell}\rangle &= \int \frac{d\theta_{\mathbf{r},\ell}}{\sqrt{2\pi}} e^{in_{\mathrm{r},\ell}\theta_{\mathrm{r},\ell}}\,|\theta_{\mathbf{r},\ell}\rangle = e^{in_{\mathrm{r},\ell}\hat{\theta}_{\mathrm{r},\ell}} \int \frac{d\theta_{\mathbf{r},\ell}}{\sqrt{2\pi}}\,|\theta_{\mathbf{r},\ell}\rangle \\ &= e^{in_{\mathrm{r},\ell}\hat{\theta}_{\mathrm{r},\ell}} \int \frac{d\theta_{\mathbf{r},\ell}}{\sqrt{2\pi}}\,|\theta_{\mathbf{r},\ell}\rangle = e^{in_{\mathrm{r},\ell}\hat{\theta}_{\mathrm{r},\ell}}\,|n_{\mathbf{r},\ell} = 0\rangle = (\hat{U}_{\mathbf{r},\ell})^{n_{\mathrm{r},\ell}}\,|n_{\mathbf{r},\ell} = 0\rangle\,. \end{aligned} \tag{2.29}$$

where the identity $\mathbf{1} = \int d\theta_{\mathbf{r},\ell}\,|\theta_{\mathbf{r},\ell}\rangle\langle\theta_{\mathbf{r},\ell}|$ was used. Consequently, the state $|n_{\mathbf{r},\ell}\rangle$ can be created by acting $n_{\mathbf{r},\ell}$ times with $\hat{U}_{\mathbf{r},\ell}$ along the link $(\mathbf{r},\ell)$, and then $\hat{U}_{\mathbf{r},\ell}$ (and also $\hat{U}^{\dagger}_{\mathbf{r},\ell}$) acts as a raising (lowering) operator of the electric field line $E_{\mathbf{r},\ell}$ boundlessly, so the Hilbert space is infinite.

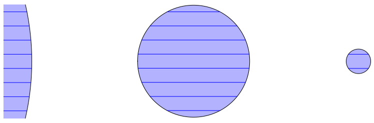
(a) $S = 35/2$. (b) $S = 7/2$. (c) $S = 1/2$.

Figure 2.2: *Cylindrical limit from* QLM

The algebra of $\hat{E}_{\mathrm{r},\ell}, \hat{U}_{\mathrm{r}',\ell'}$ is isomorphic to the cylindrical group[Gil12]:

$$[\hat{L}^{z}_{\mathrm{r},\ell}, \hat{P}^{\pm}_{\mathrm{r},\ell}] = \pm\hat{P}^{\pm}_{\mathrm{r},\ell}, \quad [\hat{P}^{+}_{\mathrm{r},\ell}, \hat{P}^{-}_{\mathrm{r},\ell}] = 0,$$

by corresponding $\{\hat{U}_{\mathbf{r},\ell}, \hat{U}^{\dagger}_{\mathbf{r},\ell}, \hat{E}_{\mathbf{r},\ell}\}$ with $\{\hat{P}^{+}_{\mathrm{r},\ell}, \hat{P}^{-}_{\mathrm{r},\ell}, \hat{L}^{z}_{\mathrm{r},\ell}\}$, where L^z is the rotation about z, and $P^{\pm}$ are the generators of translations along the axis of a cylinder parallel to z in the positive and negative directions. This group constitute the *İnönü-Wigner contraction* of $\mathfrak{so}(3)$, generated by the usual angular momentum algebra[İW53; KW88]:

$$[S^{z}_{\mathrm{r},\ell}, S^{\pm}_{\mathrm{r},\ell}] = \pm S^{\pm}_{\mathrm{r},\ell}, \quad [S^{+}_{\mathrm{r},\ell}, S^{-}_{\mathrm{r},\ell}] = 2S^{z}_{\mathrm{r},\ell}. \tag{2.31}$$

If $S^{\pm}_{\mathrm{r},\ell}$ are expressed as $S^{\pm}_{\mathrm{r},\ell} = U^{(\dagger)}_{\mathrm{r},\ell}/S$ with S the magnitute of the angular momentum, by evaluating large S limit keeping the spacing level ΔS constant, the commutator $[\hat{U}_{\mathrm{r},\ell}, \hat{U}^{\dagger}_{\mathrm{r},\ell}] = 2S^{z}_{\mathrm{r},\ell}/S^2 \to 0$ vanishes and the commutation relations (2.27) of LGT are recovered (see FIG. 2.2).

2.2.3 *Generator of gauge transformations*

In the lattice, the total charge operator $\hat{Q}(\mathbf{r})$ in (2.19) is expressed as follows:

$$\hat{Q}_{\mathbf{r}} = (\hat{E}_{\mathbf{r},x} - \hat{E}_{\mathbf{r}-\hat{\mathbf{x}},x} + \hat{E}_{\mathbf{r},y} - \hat{E}_{\mathbf{r}-\hat{\mathbf{y}},y}) - \hat{\rho}_{\mathbf{r}}, \tag{2.32}$$

where the term in parentheses represents the 2D discrete divergence of the electric field operator $\nabla \cdot \hat{\mathbf{E}}_{\mathbf{r}} = \hat{E}_{\mathbf{r},x} - \hat{E}_{\mathbf{r}-\hat{\mathbf{x}},x} + \hat{E}_{\mathbf{r},y} - \hat{E}_{\mathbf{r}-\hat{\mathbf{y}},y}$ along the links connected to the site $\mathbf{r}$, and $\rho_{\mathbf{r}}$ is the matter densities at the site $\mathbf{r}$. Similarly, the operator $\hat{Q}_{\mathbf{r}}$ commutes with the lattice gauge Hamiltoanian (2.24) providing a good quantum number $q_{\mathbf{r}}$ that separates the Hilbert space in disconnected sectors; the physical sector is also labelled by $q_{\mathbf{r}} = 0$ ensuring the fulfillment of the Gauss' law.

The gauge transformation $\hat{\mathcal{U}}$ of (2.21) in the lattice is

$$\hat{\mathcal{U}} = \exp\left(i\sum_{\mathbf{r}'}\chi_{\mathbf{r}'}\hat{Q}_{\mathbf{r}'}\right), \tag{2.33}$$

and acts suitably on matter and gauge transporter operators

$$\hat{\psi}_{\mathbf{r}} \to \hat{\mathcal{U}}\hat{\psi}_{\mathbf{r}}\hat{\mathcal{U}}^{\dagger} = V_{\mathbf{r}}\hat{\psi}_{\mathbf{r}}, \quad \hat{U}_{\mathbf{r},\ell} \to \hat{\mathcal{U}}\hat{U}(\mathbf{r},\mathbf{r}')\hat{\mathcal{U}}^{\dagger} = V_{\mathbf{r}}\hat{U}_{\mathbf{r},\ell}V^{\dagger}_{\mathbf{r}'}. \tag{2.34}$$

2.3 ABELIAN QUANTUM LINK MODEL

The cylindrical algebra of the gauge potential and the electric field shown in (2.30), in the previous section, invites to invert the İnönü-Wigner contraction $\mathfrak{so}(3) \to \mathfrak{se}(2)$ and consider the links $(\mathbf{r}, \ell)$ as quantum spin-like degrees-of-freedom (DOF) $\mathbf{S}$ where $S = 1/2, 1, 3/2, \ldots$, with a $2S+1$-dimensional Hilbert space, and a set of operators $\mathbf{S}_{\mathrm{r},\ell} = (S^x_{\mathrm{r},\ell}, S^y_{\mathrm{r},\ell}, S^z_{\mathrm{r},\ell})$, in the framework called *Quantum Link Model* (QLM) [Hor81], also called *quantum magnets* [OR90]. Under this perspective, the lattice operators (gauge transporter and electric field) are expressed as follows:

$$\hat{E}_{\mathrm{r},\ell} = \hat{S}^z_{\mathrm{r},\ell}/S, \quad \hat{U}_{\mathrm{r},\ell} = \hat{S}^+_{\mathrm{r},\ell} = \hat{S}^x_{\mathrm{r},\ell} + i\hat{S}^y_{\mathrm{r},\ell}, \quad \hat{U}^{\dagger}_{\mathrm{r},\ell} = \hat{S}^-_{\mathrm{r},\ell} = \hat{S}^x_{\mathrm{r},\ell} - i\hat{S}^y_{\mathrm{r},\ell}, \tag{2.35}$$

where $\hat{S}^{\pm}$ are the rising and lowering operators of the z-component S^z.

Based on the algebra $[S^a_{\mathrm{r},\ell}, S^b_{\mathrm{r}',\ell'}] = i\delta_{\mathrm{rr}'}\delta_{\ell\ell'}S^c_{\mathrm{r},\ell}$ with $a, b, c = x, y, z$, the commutation relations (2.27) are recovered with the addition of the new commutator $[\hat{U}_{\mathrm{r},\ell}, \hat{U}^{\dagger}_{\mathrm{r}',\ell'}] = 2\delta_{\mathbf{rr}'}\delta_{\ell\ell'}\hat{E}_{\mathrm{r},\ell}$, thus fixing the range of states from $-S$ to $+S$ so that $\hat{U}_{\mathrm{r},\ell}$ annihilates a state with $S^z_{\mathrm{r},\ell} = S$, and similarly with $\hat{U}^{\dagger}_{\mathrm{r},\ell}$ and $S^z_{\mathrm{r},\ell} = -S$:

$$U^{\dagger}_{\mathrm{r},\ell}\,|S, S^z = -S\rangle = 0, \quad U_{\mathrm{r},\ell}\,|S, S^z = +S\rangle = 0. \tag{2.36}$$

The LGT-limit corresponds to taking $S \to \infty$ keeping the level spacing to recover the commutativity of $\hat{U}_{\mathrm{r},\ell}$ with $\hat{U}^{\dagger}_{\mathrm{r},\ell}$ and the interpretation of $\hat{U}^{(\dagger)}_{\mathrm{r},\ell}$ as the discrete translators of the state upwards (downwards) the z axis of the cylinder, and indeed increasing (decreasing) the electric line quantum number boundlessly (see FIG. 2.2).

It is important to remark that the local gauge symmetry is warrantied by the covariant action of the operator $\hat{\mathcal{U}}$ in (2.33) on the operators as shown in

(2.34), as well as its commutativity with the Hamiltonian in (2.24). Under the uncontracted algebra $\mathfrak{so}(3)$, the generator $\hat{Q}_{\mathbf{r}}$ is now expressed as

$$\hat{Q}_{\mathbf{r}} = \hat{S}^z_{\mathbf{r},x} - \hat{S}^z_{\mathbf{r}-\hat{\mathbf{x}},x} + \hat{S}^z_{\mathbf{r},y} - \hat{S}^z_{\mathbf{r}-\hat{\mathbf{y}},y}, \tag{2.37}$$

and since the commutation relations of $\hat{E}_{\mathrm{r},\ell}$ with $\hat{U}^{\dagger}_{\mathrm{r},\ell}$ remain intact, the local gauge symmetry holds in the QLM framework and then conforming also a lattice gauge theory.

2.3.1 *QLMs with S = 1/2*

The simplest realization of a QLM consist of choosing $S = 1/2$ spanned by the Pauli matrices $\{\sigma^+_{\mathrm{r},\ell}, \sigma^-_{\mathrm{r},\ell}, \sigma^z_{\mathrm{r},\ell}\}$, in which each spin-like link has only two states, $|+\rangle$ and $|-\rangle$, interpreted as an electric field line directed forward or backwards along the link, respectively (see FIG. 2.3a). The corresponding electric field operators are then expressed as[HAMS19]:

$$\hat{E}_{\mathbf{r},x} = \sigma^z_{\mathbf{r},x}\,, \quad \hat{E}_{\mathbf{r},y} = \sigma^z_{\mathbf{r},y}. \tag{2.38}$$

Similarly, the generator $\hat{Q}_{\mathbf{r}}$ of the gauge transformations (2.32), and the gauge transformation operator $\hat{\mathcal{U}}$ in (2.33) are expressed in terms of the z-Pauli matrix acting on the spins-like links:

$$\nabla \cdot \hat{\mathbf{E}}_{\mathbf{r}} = \sigma^z_{\mathbf{r},x} - \sigma^z_{\mathbf{r}-\hat{\mathbf{x}},x} + \sigma^z_{\mathbf{r},y} - \sigma^z_{\mathbf{r}-\hat{\mathbf{y}},y} \equiv \hat{Q}_{\mathbf{r}}, \tag{2.39}$$

The gauge transporter, on the other hand, is expressed using the raising/lowering operators[HAMS19]:

$$\hat{U}_{\mathbf{r},\ell} = \sigma^+_{\mathbf{r},\ell}\,, \quad \hat{U}^{\dagger}_{\mathbf{r},\ell} = \sigma^-_{\mathbf{r},\ell}\,, \tag{2.40}$$

which transforms suitably under the action of $\mathcal{U}$:

$$\hat{\mathcal{U}}\sigma^{\pm}_{\mathbf{r},\ell}\hat{\mathcal{U}}^{\dagger} = \left(e^{\pm 2i\chi_{\mathbf{r}+\ell}}\right)\sigma^{\pm}_{\mathbf{r},\ell}\left(e^{\mp 2i\chi_{\mathbf{r}}}\right) = e^{\pm 2i(\chi_{\mathbf{r}+\ell}-\chi_{\mathbf{r}})}\sigma^{\pm}_{\mathbf{r},\ell}. \tag{2.41}$$

supporting the idea of understanding the transporters expressed in terms of $\sigma^{\pm}_{\mathbf{r},\ell}$ as charge-hopping or dipole creation operators of the form $c^{\dagger}_{\mathbf{r}+\ell}c_{\mathbf{r}}$, endowing these operators with a notion of directionality (see FIG. 2.3a).

The concatenation of gauge transporters in a line operator $\hat{L}$ in (2.49) are built in QLM framework as

$$\hat{L}_{\pm} = \prod_{(\mathbf{r},\ell)\in\gamma} \hat{U}^{(\dagger)}_{\mathbf{r},\ell} = \prod_{(\mathbf{r},\ell)\in\gamma} \sigma^{\pm}_{\mathbf{r},\ell}, \tag{2.42}$$

where $\hat{L}$ is evaluated along a directed path γ in the lattice starting at the site $\mathbf{r}$ to end at $\mathbf{r}'$. Similarly, the gauge invariance of these operators is warrantied when the path γ closes to obtain a Wilson loop. The expression of this operators along the smallest non-trivial closed loop in (2.23) are

$$\hat{L}_P = \sigma^+_{\mathbf{r},x}\sigma^+_{\mathbf{r}+\hat{\mathbf{x}},y}\sigma^-_{\mathbf{r}+\hat{\mathbf{y}},x}\sigma^-_{\mathbf{r},y}, \quad \hat{L}^{\dagger}_P = \sigma^-_{\mathbf{r},x}\sigma^-_{\mathbf{r}+\hat{\mathbf{x}},y}\sigma^+_{\mathbf{r}+\hat{\mathbf{y}},x}\sigma^+_{\mathbf{r},y}, \tag{2.43}$$

and are represented in FIG. 2.3b.

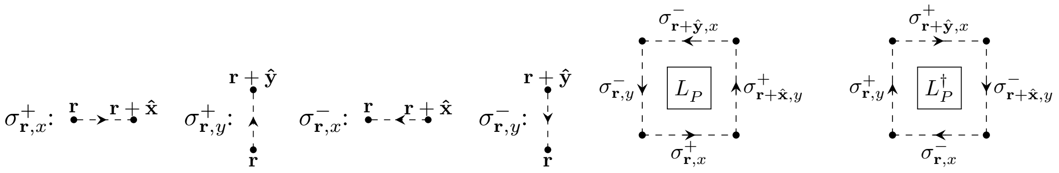
$\sigma^+_{\mathbf{r},x}$
$\mathbf{r}$
$\mathbf{r}+\hat{\mathbf{x}}$
$\sigma^+_{\mathbf{r},y}$
$\mathbf{r}+\hat{\mathbf{y}}$
$\sigma^-_{\mathbf{r},x}$
$\sigma^-_{\mathbf{r},y}$
$\sigma^-_{\mathbf{r}+\hat{\mathbf{y}},x}$
$\sigma^-_{\mathbf{r},y}$
L_P
$\sigma^+_{\mathbf{r}+\hat{\mathbf{x}},y}$
$\sigma^+_{\mathbf{r},x}$
$\sigma^+_{\mathbf{r}+\hat{\mathbf{y}},x}$
$\sigma^+_{\mathbf{r},y}$
$L_P^\dagger$
$\sigma^-_{\mathbf{r}+\hat{\mathbf{x}},y}$
$\sigma^-_{\mathbf{r},x}$

(a) Fundamental link operators. (b) Plaquette operators.

Figure 2.3: *Link and plaquette operators in the $S = 1/2$ QLM*: The gauge transporters as quantum spin operators along the links in QLM allows to associate a notion of directionality in the link depending on the state of the electric line at the link. The associated plaquette operators are therefore conformed by the four links forming the minimal loop with net circulation.

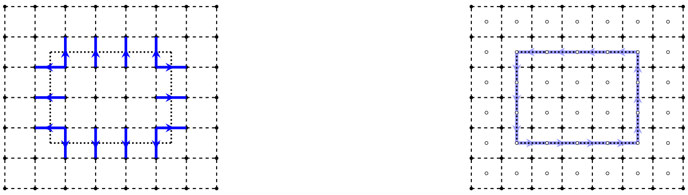

(a) (b)

Figure 2.4: *Dual of the electric field*: The integral Gauss' law in (2.44) that calculate the total electric flux through the boundary ∂S (dotted) of the region S is transformed into an Ampère law of the *dual electric field* $\boldsymbol{\mathcal{E}}$. Note that $\boldsymbol{\mathcal{E}}$ exists on the links of the *dual lattice* (white points).

2.3.2 *'t Hooft operators and winding number sectors*

Due to the fact that $\hat{Q}_{\mathbf{r}}$ in (2.39) is a locally conserved quantity, its integral on a region S is also a conserved quantity of the system corresponsing to the number of oriented electric lines piercing the boundary ∂S, resembling the 2D integral Gauss' law

$$\Phi_E = \int_S \nabla \cdot \mathbf{E} = \sum_{\mathbf{r}\in S} \nabla \cdot \mathbf{E}_{\mathbf{r}} = \sum_{\mathbf{r}\in \partial S} \hat{\mathbf{n}} \cdot \mathbf{E}_{\mathbf{r}} = \oint_{\partial S} (\hat{\mathbf{n}} d\ell) \cdot \mathbf{E}_{\mathbf{r}} \tag{2.44}$$

where $\hat{\mathbf{n}}$ is the normal vector to the region S, and the closed integral is evaluated along the boundary ∂S. The flux integral can be reinterpreted by defining the *dual electric field* $\boldsymbol{\mathcal{E}}_{\mathbf{r},\boldsymbol{\ell}}$[HAMS19]:

$$\boldsymbol{\mathcal{E}}_{\mathbf{r},\boldsymbol{\ell}} = \mathbf{E}_{\mathbf{r},\boldsymbol{\ell}} \times \hat{\mathbf{z}}, \tag{2.45}$$

which resides in the links of the *dual lattice*, allows to reexpress (2.44) as an *Ampère law*, the circulation of $\boldsymbol{\mathcal{E}}$ along the oriented path ∂S as follows (see FIG. 2.4):

$$\Phi_E = \int_S \nabla \cdot \mathbf{E} = \oint_{\partial S} (d\boldsymbol{\ell} \times \hat{\mathbf{z}}) \cdot \mathbf{E}_{\mathbf{r}} = \oint_{\partial S} d\boldsymbol{\ell} \cdot \boldsymbol{\mathcal{E}}, \tag{2.46}$$

so that the circulation of the dual electric field over the contractible closed loop ∂S, equal to the electric flux, is also a constant of motion.

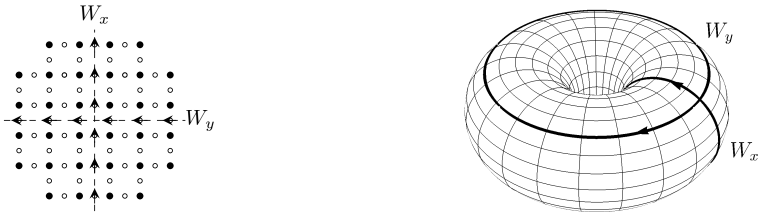

(a) (b)

Figure 2.5: *'t Hooft operators*: In a periodic lattice, the line integral of the dual electric field $\boldsymbol{\mathcal{E}}_{\mathbf{r},\boldsymbol{\ell}}$ in (2.45) along noncontractible loops count the number of times the electric lines *winds* around the orthogonal axes. In a 2D lattice, $\hat{W}_x$ integrates $E_{\mathbf{r},x}$ components along y to yield the winding number around the x axis, and similarly with $\hat{W}_y$[HAMS19], easily seen in the torus $\mathbb{T}^2$ as the two clasees of noncontractible loops.

The line integral in (2.46) is specially useful when spaces with nontrivial topologies are taken into account. In the case of a torus $\mathbb{T}^2 = S^1 \times S^1$ (see FIG. 2.5), there are two classes of non-contractible loops for which the Gauss' law described above is not valid anymore. However, the fact that the Hamiltonian (2.24) is expressed as a sum of local terms, and that it is gauge invariant in the way that $[H_{\text{EM}}, \hat{Q}_{\mathbf{r}}] = 0$, the Hamiltonian will also commute with the operators associated to the line integrals in (2.46) along non-contractible loops[Fra13], known also as *'t Hooft operators*[Hoo78] or *winding operators*.

In the case of the torus $\mathbb{T}^2$ with two classes of non-contractible loops, those ones winding the torus along the x-direction and those ones along the y-direction, there are two 't Hooft operators:

$$\hat{W}_x = +\oint d\ell_y \hat{E}_{\mathbf{r},x} = \sum_{\uparrow} \hat{E}_{\mathbf{r},x}, \quad \hat{W}_y = -\oint d\ell_x \hat{E}_{\mathbf{r},y} = \sum_{\leftarrow} \hat{E}_{\mathbf{r},y}, \tag{2.47}$$

Note that $\hat{W}_x$ sums $\hat{E}_{\mathbf{r},x}$ components in the y-direction, and $\hat{W}_y$ sums $\hat{E}_{\mathbf{r},y}$ components in the negative x-direction, as shown in FIG. 2.5.

The 't Hooft operators commute with the Hamiltonian of the gauge theory since the latter is gauge invariant under the transformation generated by (2.39), and also consists on the sum of local terms. This result implies that $\hat{W}_{x,y}$ label subspaces of the Hilbert space called *winding sectors* that are dinamically disconnected. The invariance under the action of $\hat{W}_{x,y}$ then presents a global symmetry alongside the local gauge symmetry, described by the group $\mathrm{U}(1)_X \otimes \mathrm{U}(1)_Y$ with elements given by:

$$\mathcal{G}(\theta_x, \theta_y) = \exp\left(i\theta_x \hat{W}_x + i\theta_y \hat{W}_y\right). \tag{2.48}$$

The algebra spanned by the 't Hooft operators is based in the commutators of the operators in (2.27). In this way, $\hat{W}_{x,y}$ and any line operator $\hat{L}$ defined as the concatenation of gauge transporters along a path:

$$\hat{L}_{\pm} = \prod_{(\mathbf{r},\boldsymbol{\ell})\in\gamma} \hat{U}^{(\dagger)}_{\mathbf{r},\boldsymbol{\ell}}, \tag{2.49}$$

have the associated commutator:

$$[\hat{W}_\ell, \hat{L}] = [\hat{E}_{\mathbf{r}',\ell'}, \hat{U}^{(\dagger)}_{\mathbf{r}',\ell'}] \prod_{\ell \neq \ell'} \hat{U}^{(\dagger)}_{\mathbf{r},\ell} = \pm \hat{L}. \tag{2.50}$$

where the sign is associated to the orientation of $\hat{L}$. There are two cases depending on the topology of the path followed by L:

1) if γ is a contractible loop, i.e., $\hat{L}$ is a Wilson loop such as L_P in (2.23), it commutes with $\hat{W}_{x,y}$ because they intersect an even number of times that compensate each non-vanishing commutation,

2) if γ is an open path or a noncontractible loop, $\hat{L}^\dagger$ will behave as a raising/lowering operator of $W_{x,y}$, then connecting sectors with different winding numbers.

To finish this section, a good picture to understand these results is based on the transformation law of the transporters $\hat{U}^{(\dagger)}_{\mathbf{r},\ell}$ in (2.49) as charge-hopping or dipole creation operators. The action of $\hat{L}$ along the path of links γ, consisting on raising or lowering the electric quantum numbers at each link, can be understood as the creation or addition of two opposite charges at the endpoints of the path, $\partial\gamma$, connected by the electric line created by $\hat{L}$. In case of $\hat{L}$ operators along noncontractible loops, it is, with a winding number different from zero, they are interpreted as the creation of the charge-anticharge pair and their annihilation after being transported along the noncontractible path, resulting in the change of the winding number.

The two models that are addressed in the next chapters, the Q6VM and the QLM, are two Abelian QLMs in different winding sectors given by[HAMS19]:

$$\hat{W}_x = \sum_{\uparrow} \sigma^z_{\mathbf{r},x}, \quad \hat{W}_y = \sum_{\leftarrow} \sigma^z_{\mathbf{r},y}. \tag{2.51}$$

In the Q6VM the winding numbers are assigned as $W_x = L_x$ and $W_y = L_y$ which fulfill the divergenceless condition $\nabla \cdot \hat{\mathbf{E}}_\mathbf{r} = \hat{Q}_\mathbf{r} = 0$, and in the QDM the winding numbers are $W_x = L_x$ and $W_y = 0$ to fulfill the staggered background $\nabla \cdot \hat{\mathbf{E}}_\mathbf{r} = \hat{Q}_\mathbf{r} = \pm 2$. The selection of these sectors is justified in the next section after the construction of the RK Hamiltonian.

2.3.3 *Construction of the QLM Hamiltonian*

From the fact that QLMs associate spin operators $\hat{S}^\mu_{\mathbf{r},\ell}$ to the gauge fields $\hat{E}_{\mathrm{r},\ell}, \hat{U}_{\mathrm{r},\ell}$ as shown in (2.35), the gauge field Hamiltonian is then expressed as

$$H_{\mathrm{EM}} = \frac{e^2}{2a} \sum_{\mathbf{r},\ell} (\sigma^z_{\mathbf{r},\ell})^2 + \frac{1}{2e^2 a} \sum_P \left(L_P + L_P^\dagger \right), \tag{2.52}$$

where $L_P^\dagger$ is defined as in (2.40). In the realization $S = 1/2$, the electric field terms of the Hamiltonian in (2.24) will reduce to a constant term

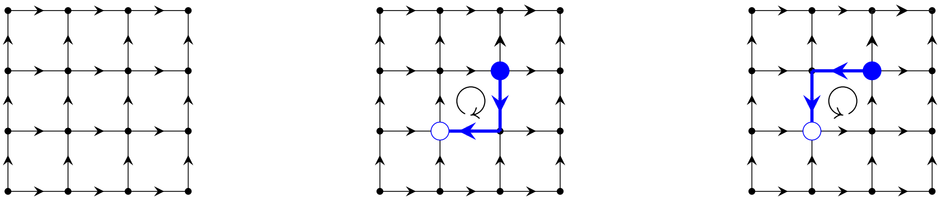

(a) $|0\rangle$ (b) $|\circlearrowright\rangle_P$ (c) $|\circlearrowleft\rangle_P$

Figure 2.6: *Example of an electric field line with a flippable plaquette*: (a) Ground state of a periodic 3×3 square lattice in the maximal winding number sector. (b) Creation of an electric line with defects at the boundaries. (c) Single time step after acting with the Hamiltonian (2.56). Notice the change of the relative orientation of the flippable plaquette

$(\sigma^z_{\mathbf{r},\ell})^2 = \mathbf{1}_{\mathbf{r},\ell}$ which can be ignored. Regarding the magnetic terms, a new term quadratic in $L_P^{(\dagger)}$ is added, the RK term [Wie13; RK88; Fra13]:

$$H_{\text{Pot}} = V \sum_P \left(L_P + L_P^\dagger \right)^2 = V \sum_P \left(L_P^\dagger L_P + L_P L_P^\dagger \right). \tag{2.53}$$

The terms $L_P^{(\dagger)2}$ annihilate any state by fliand can be withdrawn. The remaining number-like operators $L_P^\dagger L_P$ and $L_P L_P^\dagger$ are projectors of the electric field lines along P. For instance[HAMS19]:

$$L_P^\dagger L_P = \left(\frac{1 - \sigma^z_{\mathbf{r},x}}{2} \right) \left(\frac{1 - \sigma^z_{\mathbf{r}+\hat{\mathbf{x}},y}}{2} \right) \left(\frac{1 + \sigma^z_{\mathbf{r}+\hat{\mathbf{y}},x}}{2} \right) \left(\frac{1 + \sigma^z_{\mathbf{r},y}}{2} \right), \tag{2.54}$$

Then, the projectors $L_P^\dagger L_P$ and $L_P L_P^\dagger$ select one configurations of electric field lines circulating along P. The plaquettes that are not annihilated by the projectors $L_P^\dagger L_P$ and $L_P L_P^\dagger$ are called *flippable plaquettes*, existing in two possible states denoted by $|\circlearrowleft\rangle$ and $|\circlearrowright\rangle$[HAMS19].

As an example, the FIG. 2.6 depicts three states in a torus with $L_{x,y} = 3$ sites along x, y in the maximal winding sector $W_{x,y} = L_{x,y} = 3$, as shown in the vacuum state $|0\rangle$ of FIG. 2.6a where all the electric lines point in the same direction, winding the torus along x, y three times. Notice that $|0\rangle$ in the sectors $W_{x,y} = \pm L_{x,y}$ fulfills the Gauss' law (2.39) $\hat{Q}_{\mathbf{r}} |0\rangle = 0$. The FIGs. 2.6b and 2.6c, on the other hand, show one flippable plaquette each, both created after the action onto the vacuum of a Wilson line (2.42) along the blue bold paths, yielding a pair of defects where $\hat{Q}_{\mathbf{r}} = \pm 1$. The state of the electric line is described by the plaquette created when the electric line changes its direction.

In this way, the action of the operators $L_P^{(\dagger)}$ is

$$L_P |\circlearrowright\rangle = |\circlearrowleft\rangle, \quad L_P^\dagger |\circlearrowleft\rangle = |\circlearrowright\rangle, \tag{2.55}$$

so that the magnetic terms in (2.52) induce fluctuations $|\circlearrowleft\rangle \to |\circlearrowright\rangle$ at each plaquette P, and consequently makes the electric string in FIG. 2.6 fluctuate between the two states in FIGs. 2.6b and 2.6c. This fact yields the following expression for the kinetic part of the Hamiltonian:

$$H_{\text{Kin}} = -t\sum_{P}\left(L_P + L_P^{\dagger}\right) = -t\sum_{P}\left(|\circlearrowleft\rangle\langle\circlearrowright| + |\circlearrowright\rangle\langle\circlearrowleft|\right). \tag{2.56}$$

The new potential term in (2.54) counts the number of flippable plaquettes in the system, and can be expressed as projectors as follows[HAMS19; Fra13]:

$$H_{\text{Pot}} = V\sum_{P}\left(L_P^{\dagger}L_P + L_P L_P^{\dagger}\right) = V\sum_{P}\left(|\circlearrowleft\rangle\langle\circlearrowleft| + |\circlearrowright\rangle\langle\circlearrowright|\right). \tag{2.57}$$

Consequently, the Hamiltonian that describes the dynamics of the Abelian QLM is the RK Hamiltonian[HAMS19; RK88; Fra13]:

$$H = \sum_{P} -t(|\circlearrowleft\rangle\langle\circlearrowright| + |\circlearrowright\rangle\langle\circlearrowleft|) + V(|\circlearrowleft\rangle\langle\circlearrowleft| + |\circlearrowright\rangle\langle\circlearrowright|), \tag{2.58}$$

poposed by Rokhsar & Kivelson in [RK88], and extensively used in the study of QDMs as a model for high-temperature supercondutivity. The phase diagram of this system can be described by the unique parameter $v \equiv V/t$ that controls the physics of the system. After a direct inspection, it is noticed that in the limit $v = 1$, also called the RK point, the Hamiltonian is a sum of projectors

$$H = \sum_{P} -t\left(|\circlearrowleft\rangle - |\circlearrowright\rangle\right)\left(|\circlearrowleft\rangle - |\circlearrowright\rangle\right), \tag{2.59}$$

a positive definite operator with zero as minimum eigenvalue, corresponding to a equal-weighted superposition of all the possible configurations of flippable plaquettes in the lattice. This point then separates the phase space in two regions: at the Right Hand Side (RHS) of the RK point any state with flippable plaquettes is penalized with an energy cost V, therefore the gound state is the superposition of all the configurations with no flippable plaquettes (the winding number sectors discussed at the end of the previous sections are grounds states in this regime); and at the Left Hand Side (LHS) of the RK the number of flippable plaquettes is preferred since it implies a lowering in the total energy of the system, and in the limit $v \to -\infty$ the states with the maximal number of flippable plaquettes contributes to the ground state. The section 2.2 contains a brief discussion on the phases of the Q6VM and the QDM.

2.4 CONCLUSIONS

This chapter presents the basic framework needed to address the study cases discussed in chapters 3 and 4. Departing from §2.1 where we briefly discuss an Abelian gauge theory, §2.2 introduces LGTs in a square lattice to later address the the QLM and the RK Hamiltonian in §2.3. The next chapters 3 and 4 discusses in detail the problem of a fluctuating electric string in the sectors corresponding to the Q6VM and the QDM, described both as QLMs with the dynamics given by the RK Hamiltonian (2.58).

3

ELECTRIC STRING IN Q6VM AS A XXZ CHAIN

> *In both cases Nature seems to take advantage of the simple mathematical representations of the symmetry laws. When one pauses to consider the elegance and the beautiful perfection of the mathematical reasoning involved and contrast it with the complex and far-reaching physical consequences, a deep sense of respect for the power of the symmetry laws never fails to develop.*
>
> — Chen-Ning Yang [Yan57]

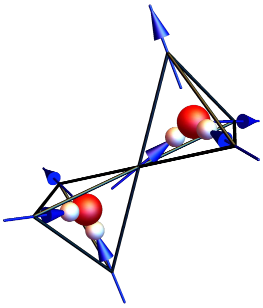

Figure 3.1: *Ices rules*: Pictorical representation of the location of protons in water ice and their displacement vectors.

The crystaline structure of water at standard pressure (10^5 Pa)[PC09] is described by a hexagonal lattice where the oxigen ions O^{2-} conform the vertices, and the protons H^+ the edges. Each vertex can be understood as a tetrahedron containing one water molecule (see FIG. 3.1), where O is located at the center and surrounded by four H, two closer to O (1.72Å) bonded covalently and two farther (2.85Å) resulting from the weakness of the hydrogen bonds of O with H located in Nearest Neighbor (NN) tetrahedra[Isa+99]. This fact is described by the *ice rules*[BF33]: 1) there is one proton along each $O - O$ line, and 2) 2-near-2-far protons per O atom. The ice rules then imply disorder in the location of protons when water molecules form the ice, giving six different options to accomodate the water molecule in each tetrahedron. This was taken into account by Linus Pauling to calculate the finite entropy of water ice at zero temperature resulting from a macroscopically degenerated ground state[Pau35].

Similar entropic behavior at low temperatures have been found in rare-earth Ferromagnetic (FM) materials[GM14] such as $Ho_2Ti_2O_7$[Har+97] or $Dy_2Ti_2O_7$[Ram+99], where the rare-earth cations (Ho and Dy) are arranged in a *pyrochlore lattice* of corner-sharing tetrahedra in a Face-Centered Cubic (FCC) lattice[LMM11] (see FIG. 3.2a). The existence of a strong anisotropic Ising coupling along the diagonals of the cube (111) alignes the spins of the atoms at the corners of the tetrahedra in a 2-in-2-out rule (see FIG. 3.1), resembling the ice rules observed in water. In fact, measurements of low-temperature entropy of $Dy_2Ti_2O_7$ is consistent with the Pauling entropy calculated for water ice[Ram+99].

The disorder of proton position, or spin orientation, in ices can also be understood as a gauge symmetry from the fact that *rotating* the internal

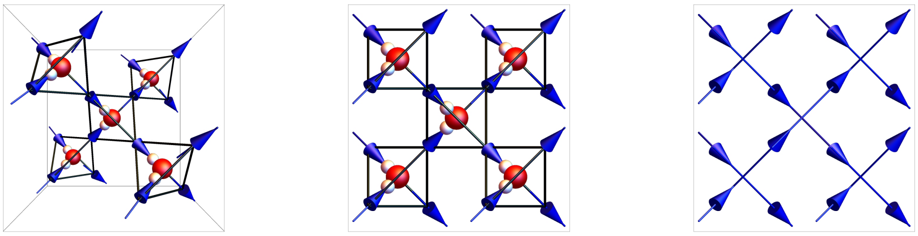

(a) 3D pyrocholore lattic (b) 2D checkerboard (c) Reduction to vertices

Figure 3.2: *Quantum 6-Vertex Model (Q6VM) as a 2D description of water/spin ice*: (a) The orientation of the spins can be mapped one-to-one to the position of protons in water ice in a pyrochlore lattice. (b) The 3D lattice of corner-sharing tetrahedra can be projected onto the plane (100) to obtain a 2D effective model that can be reduced to (c) the Q6VM.

orientation of the tetrahedron does not affect the dynamics of the system. In this way, a Gauss' law emerges from the 2-in-2-out rule in a lattice gauge description where excited states corresponding to 3-in-1-out or viceversa can be understood as *charges* that propagate throughtout the lattice and interact by means of a Coulomb-like potential[CMS08].

The mapping from 2-close-2-far in water ice into 2-in-2-out in rare earth ferromagnets can be seen in FIG. 3.1 where the spins are mapped as displacement vectors of the protons, going inward the tetrahedron for near H to O, and going outwards for far H located in neighboring tetrahedra. A simplified structure of the pyrochlore lattice is depicted in FIG. 3.2a (notice the spin/corner sharing by NN tetrahedra). We can then project this system on the (100) plane as shown in FIG. 3.2b to obtain an effective 2D checkerboard lattice model, and finally it can be mapped to the Q6VM by corresponding a link in a square lattice to each spin (see FIG. 3.2c), used by Pauling to calculate the residual entropy of ice at zero temperature when the six possible vertices (see FIG. 3.3b) have the same energy weights. Complementarily, when the first two vertices in FIG. 3.3b (where the flux does not changes direction) have the lowest energy weight, the ground state will consist on a highly polarized state typical of ferroelectric materials[Sla41].

The present chapter, based in [HAMS19], discusses the behavior of *one electric line* or *string* connecting two defects (vertices violating ice rules) on a 2D periodic lattice $L_x \times L_y$, in the maximally polarized background where the winding numbers (2.51), describing the overall orientation of the links, is maximal ($W_{x,y} = L_{x,y}$) to define a unique ground state. This constraint results in the fulfilment of the ice rules as a Q6VM in the polarized background sector. The electric line is mapped through Hard-core Bosons (HCBs) into a 1D XXZ chain that allows to give a complete description of the phases, resembling a precursor for studying the phases of the whole 2D Q6VM.

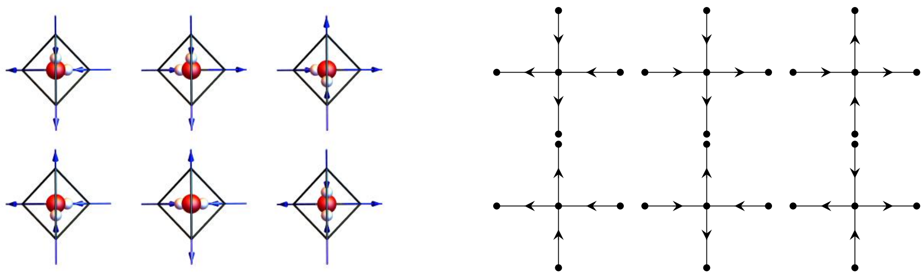

(a) Ice rules for water molecules.

(b) Gauss' law sector $\nabla \cdot \mathbf{E_r} = 0$.

Figure 3.3: *Equivalence between the ice rules and* $\hat{Q}_{\mathbf{r}} = 0$: The structure of the water molecule constrain the configuration of vectors under the 2-in-2-out rule, (b) directly mapped in a square lattice gauge theory where the constrain $\hat{Q}_{\mathbf{r}} = 0$ is fulfilled, resulting in six possible configuration of electric lines used to build the Q6VM.

3.1 REALIZATION OF THE Q6VM IN THE $S = 1/2$ QLM

The Q6VM can be described as a Quantum Link Model (QLM) in a $L_x \times L_y$ square lattice with the superselection rule:

$$\nabla \cdot \mathbf{E_r} = Q_{\mathbf{r}} = 0, \tag{3.1}$$

that is, the Gauss' law is satisfied for the absence of charged matter sources and then restricting electric lines at the nodes or *vertices* of the lattice to one of the six configurations depicted in the FIG. 3.3 and equivalent to the ice rules applied in the checkerboard lattice[RF04]. However, the rule (3.1) is not enough to have a unique ground state in the system as was discussed in the introduction of this chapter. This is solved with the subsidiary conditions that the system is periodic and the winding numbers defined in (2.47) are:

$$W_x = L_x, \quad W_y = L_y, \tag{3.2}$$

i.e., the maximal winding in which all the electric lines point upwards or rightwards. In this state the ground state is unique since it sets that every electric line is in the $+1$ state:

$$\sigma_{\mathbf{r},\ell} = +1, \quad \forall \mathbf{r}, \ell = x, y, \tag{3.3}$$

which is also a zero energy eigenstate, because of the absence of flippable plaquettes depicted in FIG. 2.6, of the Rokhsar-Kivelson (RK) Hamiltonian (2.58):

$$H = \sum_P -t(|\circlearrowleft\rangle\langle\circlearrowright| + |\circlearrowright\rangle\langle\circlearrowleft|) + V(|\circlearrowleft\rangle\langle\circlearrowleft| + |\circlearrowright\rangle\langle\circlearrowright|), \tag{3.4}$$

where the first term is the kinetic magnetic term coming from the U(1) Lattice Gauge Theory (LGT) and the second term is the RK potential counting the number of flippable plaquettes.

The state (3.3) is going to be the background on top of which we define a path γ to create an electric field line using the operator $L_\pm$ in (2.42):

$$\hat{L}_\pm = \prod_{(\mathbf{r},\boldsymbol{\ell})\in\gamma} \hat{U}^{\gamma}_{\mathbf{r},\boldsymbol{\ell}} = \prod_{(\mathbf{r},\boldsymbol{\ell})\in\gamma} \sigma^{\pm}_{\mathbf{r},\boldsymbol{\ell}}, \tag{3.5}$$

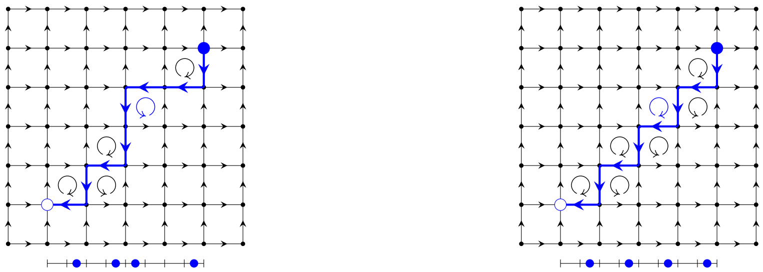

(a) State with five flippable plaquettes.

(b) State with seven flippable plaquettes.

Figure 3.4: *Two dynamically-connected states of an electric string and mapping to a 1D system*: (a) The state at $t = 0$ has five flippable plaquettes with a potential energy energy of $5V$. Below there is the equivalent configuration in the HCB chain. (b) The state at $t = 1$ has seven flippable plaquettes with potential energy energy $7V$. This is also a maximally kinked state corresponding to a Charge Density Wave (CDW) in the HCB picture[HAMS19].

containing at the boundary $\partial\gamma$ two static defects where $Q_{\partial\gamma} = \pm 2$. The electric line is the dynamical system that evolves under the Hamiltonian (3.4) acting on each ones of the flippable plaquettes created at the vertices where the path γ changes its direction, as it is shown in the FIG. 3.4 where we can see how the electric line changes after one time step.

3.2 MAPPING THE ELECTRIC STRING TO THE XXZ CHAIN

We can map the electric field line onto a conventional 1D system by *unfolding* the string into a chain of $L \equiv \ell_x + \ell_y$ sites labeled by i, containing HCBs defined by the following commutation relations

$$[b_i, b_j] = [b_i^\dagger, b_j^\dagger] = 0, \quad i \neq j \tag{3.6a}$$

$$\{b_i, b_i^\dagger\} = 1\,, \tag{3.6b}$$

in such a way that every vertical segment is mapped into a occupied site and every horizontal into an empty site. Since the string does not change its length, there is a global $\mathrm{U}(1)$ symmetry associated to the conservation of L, and indeed, of the total number of particles give by

$$N_b = \sum_i b_i^\dagger b_i = \ell_y, \tag{3.7}$$

that suggests the definition of the filling fraction

$$\nu = \frac{N_b}{L} = \frac{1}{1 + \ell_x/\ell_y}. \tag{3.8}$$

The Hamiltonian (3.4) is mapped into a 1D HCB system as

$$H_{6v} = \sum_{i=1}^{L} -t(b_i^\dagger b_{i+1} + h.c.) + V(n_i - n_{i+1})^2. \tag{3.9}$$

The first term corresponds to the kinetic magnetic term describing the plaquette flipping, where the horizontal and vertical segments comprising the corner are interchanged, corresponding to the hopping of a boson onto the NN sites. The second term, describing the RK potential that counts the total number of corners, i.e., of flippable plaquettes, implies the change of direction of the electric string. This change of direction is mapped as the difference of occupation number in the bosonic picture $\Delta n_i = n_i - n_{i+1}$, thus each flippable plaquette corresponds to the existence of an occupied site next to an empty site.

Although the bosonic Hamiltonian (3.9) is exactly solvable by means of the Bethe Ansatz, it can be further transformed into a physical system well studied in the literature: the XXZ spin chain. The 1D HCB Hamiltonian (3.9) can be mapped one-to-one onto spin 1/2 degrees of freedom:

$$n_i = s_i^z + \frac{1}{2}, \quad b_i^\dagger = s_i^+, \quad b_i = s_i^-, \tag{3.10}$$

where $s_i^\pm = (s_i^x \pm i s_i^y)/2$, and $s_i^{x,y,z}$ fulfill the spin commutation relations:

$$\left[s_i^\mu, s_i^\nu\right] = 2i\epsilon^{\mu\nu\rho} s_i^\rho. \tag{3.11}$$

The new Hamiltonian in terms of spin operators is

$$H_{6v} = -J \sum_{i=1}^{L} \left(s_i^x s_{i+1}^x + s_i^y s_{i+1}^y + v s_i^z s_{i+1}^z - \frac{v}{4} \right) \tag{3.12}$$

where $J = 2t$ is the exchange energy, and $v = V/t$ the $z-$axis anisotropy. This is a generalization of the XY Hamiltonian obtained in [Orl92] to non-zero values of v. This is the well-known XXZ spin chain which is an exactly solvable model [YY66b; YY66c; YY66d].

3.3 PHASES OF THE ELECTRIC STRING FROM THE XXZ CHAIN

At zero magnetization, i.e., half filling, there are three phases and three critical points for XXZ model (see Appendix A):

1. $1 < v$: a gapped FM phase with ground state in the sector $|M| \neq 1$ given by:

$$|0_{\uparrow\downarrow}\rangle = \bigotimes_{i=1}^{L_0} |\uparrow_i\rangle \prod_{i=L_0+1}^{L} |\downarrow_i\rangle, \quad |0_{\uparrow\downarrow}\rangle = \bigotimes_{i=1}^{L_0} |\uparrow_i\rangle \prod_{i=L_0+1}^{L} |\uparrow_i\rangle, \tag{3.13}$$

   where L_0 is the position of the domain wall.

2. $v = 1$: RK point, a gapless isotropic FM with $\mathrm{SU}(2)$ symmetry in the spin picture. At this point, the two terms of the RK Hamiltonian (3.4) consists on a sum of projectors that produce the ground state maximally degenerate where all the states have zero energy. where domain walls appear because the magnetization is conserved.

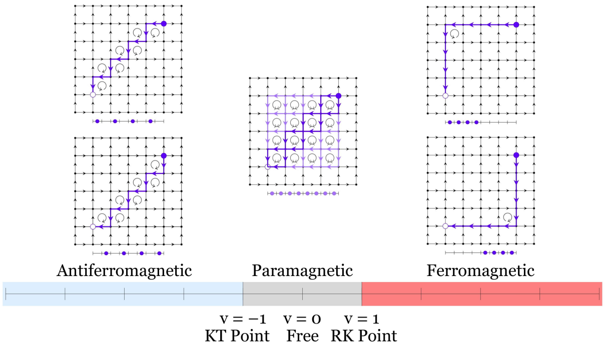

Figure 3.5: *Exact phase diagram of the electric string from the XXZ chain at $M = 0$*: The exact mapping of the electric string to the XXZ chain yields the whole phase diagram of the string, comprising a gapped AFM phase, a gapless XY-like phase and a gapped FM phase. The string is a 1D precursor of the whole 2D Q6VM without the prescription of the winding numbers (3.2). Adapted from [HAMS19].

3. $-1 < v < 1$: a gapless XY-like paramagnetic phase with power-law correlations. At $v = 0$ the system is describable by free fermions using the Jordan-Wigner (JW) transformations.
4. $v = -1$: Kosterlitz-Thouless (KT) point, a gapless isotropic Antiferromagnetic (AFM) phase showing an infinite-order phase transition.
5. $-1 < v$: a gapped AFM phase with two degenerate ground states:

$$|0_{\uparrow\downarrow}\rangle = \bigotimes_{i=\text{odd}}^{L} |\uparrow_i\downarrow_{i+1}\rangle\,, \quad |0_{\downarrow\uparrow}\rangle = \bigotimes_{i=\text{odd}}^{L} |\downarrow_i\uparrow_{i+1}\rangle\,. \tag{3.14}$$

The FIG. 3.5 shows a pictorical representation of the phase diagram indicating the three critical points.

According to Yang & Yang article series [YY66a; YY66b; YY66c; YY66d], the energy density of the ground state of the XXZ chain can be expressed as

$$\begin{aligned} E(v, M) &= f(v, M)L + O(L^{-1}), \\ M &= \frac{2}{L}\sum_i s_i^z = \frac{\ell_y - \ell_x}{L} \end{aligned} \tag{3.15}$$

where M is the conserved magnetization and $f(v, M)$ is the free energy density. In [YY66c] there is a rigorous and self-contained calculation of $f(v, M)$ for the different phases using the Bethe Ansatz (some expressions are shown in Appendix A). We have applied some results to describe the phase diagram of the electric string.

3.3.1 $v > 1$: *FM insulator*

Let us begin from the Right Hand Side (RHS) of the RK point. For the sector $|M| = 1$, the ground state $E = 0$ is the trivial fully polarized state (3.13) with

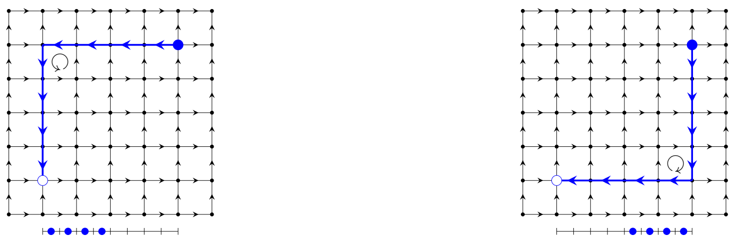
(a) (b)

Figure 3.6: *Electric string in Q6VM in the FM phase* $1 < v$: In the region $1 < v$, the string assumes a configuration that minimizes the number of flippable plaquettes, those are one of the two paths, (a) and (b), along the bounding rectangle whose opposite vertices are the defects $Q = \pm 2$. and the corresponding bosonic picture is a phase separation[HAMS19].

$L_0 = L$, that is, no domain walls. On the other hand, when $|M| < 1$, the system develops in its ground state one domain wall located at $L_0 \in \{1, L\}$ in a way that the magnetization is conserved. This domain wall is manifested as a phase separation in the bosonic picture, which indeed corresponds to the electric string approaching to the rectangular boundary whose corners are the defects $Q \pm 2$ as displayed in FIG. 3.6 (notice the representation of the boson phase separation below each square lattice).

We can use a semiclassical continuum description to model the domain wall when its width is largerthan the lattice parameter, i.e., $v \to 1$. Using the remaining symmetry $\mathrm{U}(1)$ hold by the z-axis anisotropy, we can describe the spin in the xz plane in terms of θ, the parameter of $\mathrm{U}(1)$, as follows:

$$s_i^z \to \cos\theta(x), \quad s_i^x \to \sin\theta(x). \tag{3.16}$$

This parametrization allows us to express the total energy, in units where the lattice spacing is one, as

$$E = \int_0^L dx \left(\frac{\rho}{2} \left(\frac{d\theta}{dx} \right)^2 - \lambda \cos^2\theta \right), \tag{3.17}$$

where $\rho = J$ and $\lambda = J(v-1)$. Then the problem becomes variational and consists on finding the function $\theta(x)$ such that $E(\theta(x))$ is stationary (a minimum in this case). Using the Euler-Lagrange equations[Arn89], we can find the solution in terms of the Jacobi amplitudes for finite L, that in the limit $L \to 0$ yields that

$$s^z(x) = \tanh \frac{x - x_0}{w}, \tag{3.18}$$

where w is the width of the domain wall:

$$w = \frac{1}{\sqrt{2(v-1)}} \tag{3.19}$$

and its position x_0 fixes the magnetization as

$$\frac{x_0}{L} = \frac{1-M}{2}. \tag{3.20}$$

The solution indeed has the asymptotes $\theta(x) = 0, \pi$ consistent with the phase separation in the bosonic picture except in the region $|x - x_0| \lesssim w$, the domain wall, that contributes to the system energy as $\mathcal{O}(L^0)$, up to leading order, given by

$$E \approx 2\sqrt{2}J\sqrt{v-1}. \tag{3.21}$$

This results can be interpreted as a subdimensional deconfinement of the defects to the RHS of the RK point, in the staggered phase[SMP04; BT04], because the displacement of the defects along the horizontal and vertical directions, that is, following the direction of the polarized background (see FIG. 3.6), there is no energy cost. On the other hand, and in contrast to fracton models such as [Cha05; Haa11; Yos13; VHF15; Pre17], the diagonal displacement of the defects implies crossing polarized lines in the background and the creation of a new domain wall with cost of $2\sqrt{2}J\sqrt{v-1}$.

3.3.2 $v = 1$: *RK point*

At the RK point we have $\mathrm{U}(1) \to \mathrm{SU}(2)$, the isotropic FM Heisenberg chain with symmetry $\mathrm{SU}(2)$ is restored from the XXZ one. The new ground state has energy $E = 0$ and is given by (3.13), a tensor product of spins alingned in the same directon, but without domain wall, i.e., the spins can smoothly cant in any direction without energy cost so that they keep aligned. In terms of the electric string, this result means that, in the ground state, we will have $E = 0$ energy cost for any displacement of the defects $Q = \pm 2$, implying a form of *perfect charge deconfinement* in contrast to the usual deconfiment where the string tension vanishes for large charge separations in the thermodynamical limit.

This results can also me understood in terms of the original RK Hamiltonian (3.4), which comprises a sum of projectors at the RK point and all the zero-energy states are ground states of the system[Fra13]. The background configuration we have considered by setting the winding numbers $W_{x,y} = L_{x,y}$ also belongs to the set of ground states, so there is no energy cost when we displace the charges and energy dependence on the distance, implying that the electric string as exactly zero tension.

3.3.3 $-1 < v < 1$: *Gapless phase*

At the Left Hand Side (LHS) of the RK point and the RHS of the KT transition, ($|v| < 1$), we have a gapless phase with power-law correlations where the magnetic kinetic term of the RK Hamiltonian (3.4) dominates, implying the occurrence of strong resonances between the plaquette states $|\circlearrowleft\rangle \leftrightarrow |\circlearrowright\rangle$. This region can be understood by examining the system at the critical point $v = 0$, where the bosonic Hamiltonian (3.9) has no interaction and the system can be described as free fermions after having mapped it into a 1D

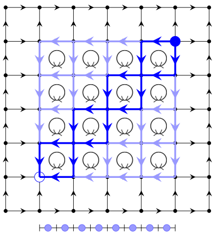

Figure 3.7: *Electric string in Q6VM in the gapless phase* $-1 < v < 1$: The region $|v| < 1$ is dominated by the magnetic kinetic term of the Hamiltonian (3.4) with strong quantum fluctuations around the maximally kinked path along the diagonal of the bounding rectangle.

fermion chain using the JW transformations. The energy of the ground state is then

$$f(0,M) = -\frac{J}{\pi}\cos\frac{\pi}{2}M, \tag{3.22}$$

whose minimum corresponds to $f(0, M = 0) = 0$. The zero-magnetization state corresponds in the electric string picture to the maximally kinked paths along the diagonal of the bounding rectangle (see FIG. 3.7).

Before crossing the KT point into the AFM phase, it is important to note that in te gapless phase, the strong plaquette resonances, corresponding to boson hoppins in the bosonic picture, can be interpreted as a 1D precursor of the full 2D zero-winding phase of resonating plaquettes. However, because the electric strings interact strongly under the Hamiltonian (3.4), the gapless phase found for a single string can correspond to the plaquette crystalline phase found numerically by [SMP04; Ban+14].

3.3.4 $v \leq -1$: *KT transition and AFM insulator*

Further in the LHS sector of the RK point, aat $v = -1$, the system undergoes a form of the KT transition and the free energy is smooth to all orders [YY66c]. We found another SU(2) symmetry in this point by rotating the spins on alternating sites to flip the sign of the XY terms (see Appendix A). In consequence, $H_{v=1} = -H_{v=-1}$, and the ground state at $v = -1$, corresponding to a spin singlet (3.14), is the highest excited state at $v = 1$ with grouns state given by the fully polarized spin configuration expressed in (3.13).

After overpassing the KT point, when $v < -1$ the gap reopens and the system becomes AFM for the rest of the parameter space. This state corresponds to the CDW in the bosonic picture, and in the string picture to the maximally kinked path approaching the diagonal of the bounding rectangle (see FIG. 3.8) with its quantum fluctuations freezing out for larger $|v|$. This state is similar to the preferred path of the electric string in FIG. 3.7 with the big difference in the relevance of quantum fluctuations since the phase is gapless at $v = 0$.

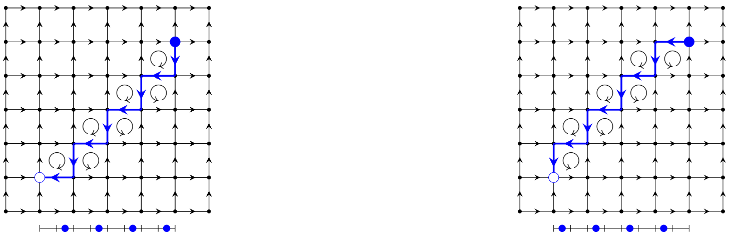

(a) (b)

Figure 3.8: *Electric string in* Q6VM *in the* AFM *phase* $v < -1$: When $v < -1$, the energy is minimized by maximizing the number of flippable plaquettes. Thus, the system displays a ground state describeg by the maximally kinked string with supressed quantum fluctuatins (in contrast to FIG. 3.7), approaching the diagonal of the bounding rectangle whose opposite vertices are the defects $Q = \pm 2$. and the corresponding bosonic picture is a CDW[HAMS19].

3.4 NUMERICAL APPROACH: DRUDE WEIGHT AND SYSTEM SIZE EFFECTS

Althought the electric string in the Q6VM has been exactly mapped to the XXZ chain, we complement the analytical results obtained in the previous sections with explicit numerical solutions using exact diagonalization for a periodic system with sizes $L = 3, ..., 8$. Since the linear momentum is conserved in the sytem, this constitutes a good quantum number and allow block-diagonalization. Additionally, we add a sligth modification in the kinetic part of the Hamiltonian (3.9), where the hopping term that connects the last site L with the first one is multiplied by a phase ϕ as follows:

$$H_{6v,closed} = H_{6v,open} + e^{i\phi} t b_1^\dagger b_L + h.c. \tag{3.23}$$

This phase shift does not imply a breaking of the translational invariance since ϕ can be splitted throughout the whole chain by changing the gauge via a unitary transformation

$$b_j^\dagger \to e^{i\frac{i\phi}{L}} b_j^\dagger, \tag{3.24}$$

leading to a complex hopping coefficient $te^{i\phi/L}$. Then, we numerically diagonalize the Hamiltonian (3.23) for different values of ϕ, we extract the lowest eigenvalue E_0 as a function of ϕ. FIG. 3.9 shows the dependence of the two lowest energy eigenvalues on v with $\phi = 0$ after having block-diagonalized the Hamiltonian in the eight momentum sectors. We can see a sharp discontinuity in the first derivative of the eigenenergies respect to v at the RK point, $v = 1$, indicating the expected emergence of the zero-energy manifold from the Hamiltonian (3.4). A different case is observed at the KT point, where the transition is slightly visible by the change of concavity of the eigenenergies around $v = -1$. The expected gap openings for the limits $v \to \pm\infty$ is satisfactorily shown, consistent with insulating-conducting-insulating transitions obtained from the analytical results of the previous sections.

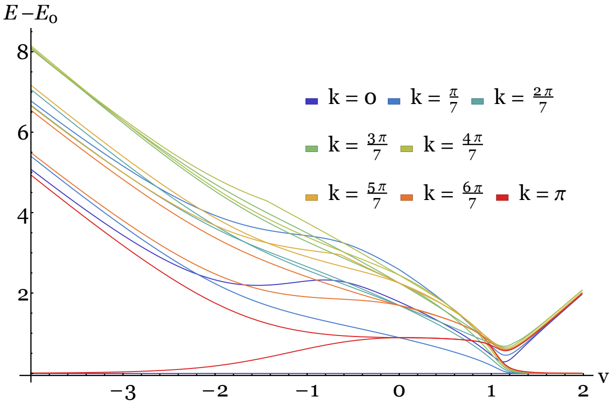

Figure 3.9: *Two lowest energy levels vs. v in Q6VM*: Lowest energies levels for a ring with $L = 7$ and $\phi = 0$. When $v \to -\infty$ the $k = 0$ and π CDW states become degenerate, and a gap opening for domain walls as lowest energy excitations. The gaps close at $v = 0$ in agreement to free fermion description. There is a sharp discontinuity at $v = 1$ corresponding to the RK point, followed by the gap opening of the phase-separated states with all the k sectors becoming degenerate as $v \to \infty$[HAMS19].

The phase transitions can also be found if we calculate the *Drude weight*[Koh64]:

$$\mathcal{D} \equiv L\frac{d^2 E_0}{d\phi^2}, \tag{3.25}$$

interpreted as the stiffness of the system respect to the twisting of the boundary conditions, represented by the phase ϕ. The Drude weight is a good parameter to characterize how much conducting or insulating a phase is, in a way that vanishing values of $\mathcal{D}$ for certain parameters (for instance, $v \to \infty$) imply an insulating phase, and viceversa. In FIG. 3.10 we can see the Drude weight $\mathcal{D}$ calculated numerically from the Hamiltonian (3.23) as a function of v, with an inset in the top right showing the second derivative of $\mathcal{D}$ respect to v as a parameter since abrupt changes in the concavity of $\mathcal{D}(v)$ indicate phase transitions.

As expected, FIG. 3.10 displays results in good agreement with the analytical results obtained from the XXZ chain: an insulating phase for $v > 1$, a condunting phase in the region $|v| < 1$ and an insulating phase for $v < -1$. The sharpness of the transitions depends on the system size, being difficult to notice for $L = 3$ and improved as L gets larger (notice the transition at the RK point where a sharp drop of $\mathcal{D}$ can be found for $L = 8$). On the other hand, the infinite-order transition at the KT point $v = -1$ shows a slower convergence for larger system sizes, so the conducting-to-insulating transition at the LHS of the RK points is more difficult to notice. Also the drop of $\mathcal{D}$ with $v \to -\infty$ is slower, suggesting that the system is able to conduct for v lower than -1.

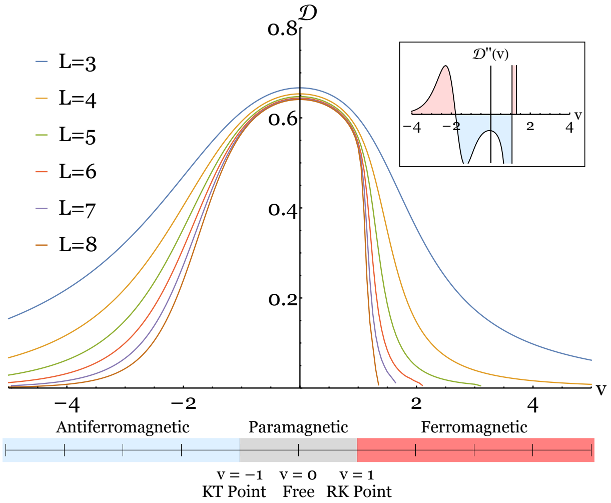

Figure 3.10: *Phase diagram at $M = 0$ and Drude weight in the* Q6VM: Drude weight for systems of size $L = 3, \dots, 8$ using exact diagonalization. At the RK the transition is evident due to $\mathcal{D} \to 0$ at $v = 1$. For the infinite order KT transition the convergence is slower at $v = -1$ and the transition is less evident. The inset shows $\frac{d^2\mathcal{D}}{d^2v}$ where sign changes roughlt indicate the phase transitions.

3.5 SUMMARY AND DISCUSSION

We have studied the phase diagram of one fluctuating electric string in the Q6VM described by the RK Hamiltonian (3.4) as the Wilson path connecting two defects $Q = \pm 2$ on a background corresponding to the fully polarized system set by the maximal winding numbers $W_{x,y} = L_{x,y}$ and fulfill the ice rules $Q_{\mathbf{r}} = 0$ (except for the defects). The background is actually a ground state of the Hamiltonian (3.4) at the RHS of the RK point, where (3.4). We have describe the electric string connecting the defects $Q = \pm 2$ by exactly mapping it onto a 1D system of HCBs, that we mapped further onto the spin-1/2 XXZ chain, an exactly solvable system whose ground state has beed studied in detail.

The phases of the electric string are summarized in the FIGs. 3.5 and 3.10, and more slightly in FIG. 3.8 by the gap opening between the two lowest energy levels. The phase diagram consists on a gapped AFM phase at the LHS ($v < -1$) of the KT point ($v = -1$), a gapless XY system in the region $|v| < 1$, and a gapped Ising FM at the RHS of the RK point ($v > 1$). The phases of the 1D electric string are natural 1D precursors to the full 2D phases, seen in numerical studies of the Q6VM [SMP04; Ban+13].

4

ELECTRIC LINE IN THE QDM AS A HARD-CORE BOSON TWO-LEG LADDER

> *The ability to reduce everything to simple fundamental laws does not imply the ability to start from those laws and reconstruct the universe.*
>
> — P. W. Anderson. [And72]

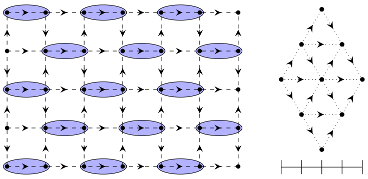

Figure 4.1: *Background configuration for the electric string in Quantum Dimer Model (QDM)*: The sublattice A(B) has vertices $Q_{\mathbf{r}} = \pm 2$, 1-in-3-out (viceversa). The dimer locates in the link flowing inwards sublattice A.

The previous chapter has discussed the problem of a fluctuating electric string in the Quantum 6-Vertex Model (Q6VM) based on the formalism of Lattice Gauge Theories (LGTs) we briefly review in chapter 2. The Q6VM was obtained as an Abelian Quantum Link Model (QLM) fulfilling the ice rules $Q_{\mathbf{r}} = 0$ with the subsidiary condition of the maximal winding numbers. The second study case we proposed in the introduction and chapter 2 was the QLM described by a staggered charge background $Q_{\mathbf{r}} = \pm 2$ where one sublattice violates the ice rules with three links goung inwards and one goung outwards, and viceversa for the other sublattice as shown in FIG. 4.1. This configuration allows us to address the problem of the electric string in the context of the QDM.

QDMs were proposed by Rokhsar & Kivelson in [RK88] based on the ideas of Pauling [Pau53] and Anderson [And73] in the search of a ground state for a spin-1/2 Antiferromagnetic (AFM) Hamiltonian made up of spin-singlet pairs of Nearest Neighbor (NN) electrons in the lattice, represented by the Einstein-Podolsky-Rosen (EPR) state [Fra13]:

$$|(ij)\rangle = \frac{1}{\sqrt{2}}\left(|\uparrow_i\downarrow_j\rangle - |\uparrow_j\downarrow_i\rangle\right). \tag{4.1}$$

This statement can be realized by proposing a lattice model with *hard-core dimers* along the links representing the electron pairs in the EPR and the empty links as electron paris with no correlation.

The dynamics of this system is dictated by the Rokhsar-Kivelson (RK) Hamiltonian [RK88]:

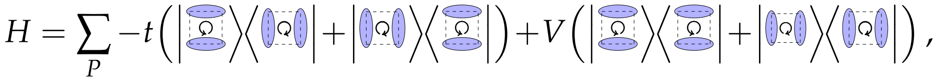

(4.2)

where each flippable plaquette is mapped as two parallel dimers, and the relative orientation of the dimer pair corresponds to the states $|\circlearrowleft\rangle$ and

$|\circlearrowright\rangle$ of the flippable plaquettes (see FIG. 4.2). In this way, the Hamiltonian makes each parallel dimer pair *resonate* between its horizontal and vertical configurations, while the RK potential penalizes each plaquette with an energy cost V.

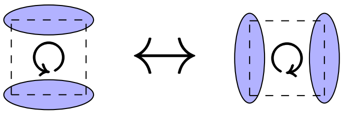

Figure 4.2: *The dimer resonance process in the QLM*: The kinetic term of the RK Hamiltonian in (4.2) makes the parallel dimers switch between the horizontal and vertical configurations, mapped from the $|\circlearrowleft\rangle$ and $|\circlearrowright\rangle$ in QLMs.

As already discussed in the introduction, at the RK point, $v = V/t = 1$, we find that the ground state is described by the Resonant Valence Bond (RVB) state, the equal-weight superposition of all closely-packed dimer configurations in the square lattice [Fra13]. Similarly, by direct inspection on the RK Hamiltonian we can expect that the phase in the limit $v \to \infty$, at the Right Hand Side (RHS) of the RK point, contains no flippable plaquettes so as its energy is minimal as shown in FIG. 4.1, called *staggered phase*; and the phase in the limit $v \to -\infty$, at the Left Hand Side (LHS) of $v = 1$, maximizes the number of flippable plaquettes, yielding a long-range configuration of parallel dimers known as *columnar phase*. Both constitute two classes of *valence-bond crystalline phases* [Fra13]. In the introduction we have also briefly reviewed some of the different proposals in describing the phases in the region $|v| \lessapprox 1$ between the two crystalline phases where there are proposals going from the transition of the columnar to the staggered phase at the RK point without any phase in between [Ban+14; Oak+18], to the existence of intermediating phases in the region $|v| \lessapprox 1$: one suggestes that a *plaquette solid*, a staggered configuration of flippable plaquettes of RVB, exists at the LHS of the RK point, starting from some critical value v_c up to $v = 1$ [Syl06; LCR96]; and the other brings the idea of a mixed phase continuously interpolated between the two crystalline phases in the region $0 < v < 1$[RPM08]. It is recommended to examine FIG. 1.5 to get a better understanding in the controversy involving the phase diagram of the QDM.

In this chapter we study in detail the phases of the fluctuating electric string in a very similar fashion as presented in chapter 3 but in the charge staggered background $Q_{\mathbf{r}} = \pm 2$ and with the subsidiary conditions in the winding numbers to obtain the configuration displayed in FIG. 4.1.

4.1 REALIZATION OF THE QDM IN THE $S = 1/2$ QLM

Following the same methodology proposed for the Q6VM in chapter 3, the QDM can be realized as a QLM in a $L_x \times L_y$ square lattice with the superselection rule:

$$\nabla \cdot \mathbf{E}_{\mathbf{r}} = Q_{\mathbf{r}} = 2(-1)^{x+y}, \tag{4.3}$$

instead of satisfying the Gauss' law (and the ice rules in terms of the Q6VM), the lattice is filled with positive and negatives charges at the sites of the

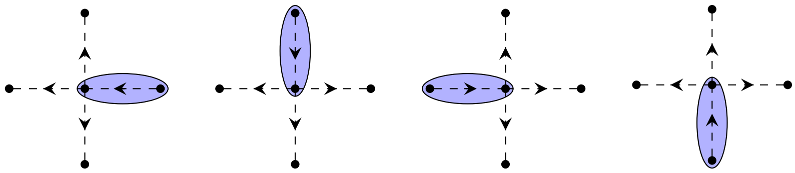

Figure 4.3: *Vertices consistent with* $Q_\mathbf{r} = 2(-1)^{x+y}$: The staggered configuration of charges in the 2D square lattice yields four possible vertices with one electric line going in the opposite direction respect to the other three, so that the dimer is assigned to that link in order to map the QLM onto the QDM.

sublattices, called A when $Q_\mathbf{r} = +2$ and B when $Q_\mathbf{r} = -2$. The A sublattice thus contains vertices with three outgoing electric lines and one ingoing line, and the contrary for the B sublattice. So, we asign the existence of a dimer to the link that is distinguishable from the other three and flows from the sublattice B to the sublattice A (see FIG. 4.3). In this way, the condition (4.3) waranties that every site in the lattice will be touched by only one dimer, dimer overlapping is forbidden and the allowed configurations of the electric lines are in one-to-one correspondance to a closely packed configuration of dimers covering the lattice.

The condition (4.3) is also supplemented defined by the winding numbers (2.51):

$$W_x = 0, \quad W_y = L_y, \tag{4.4}$$

i.e., the vertical lines get the maximal winding with all the electric lines point upwards, while the horizontal lines add up to zero from a staggered configuration, as shown in FIG. 4.1. In this sector the ground state is unique since it sets that every electric line is described as follows:

$$\sigma_{\mathbf{r},x} = (-1)^x, \quad \sigma_{\mathbf{r},y} = +1, \quad \forall \mathbf{r}, \ell = x, y. \tag{4.5}$$

The absence of flippable plaquettes in the staggered vacuum makes it an exact zero-energy eigenstate of the the RK Hamiltonian (4.2) at the RHS of the RK point. The RK Hamiltonian rules the dynamics of an electric string added when we modify the background staggered charge configuration by acting with a path operator $L_\pm$ defined in (2.42):

$$\hat{L}_\pm = \prod_{(\mathbf{r},\boldsymbol{\ell})\in\gamma} \hat{U}^\gamma_{\mathbf{r},\boldsymbol{\ell}} = \prod_{(\mathbf{r},\boldsymbol{\ell})\in\gamma} \sigma^\pm_{\mathbf{r},\boldsymbol{\ell}}, \tag{4.6}$$

that, in contrast to the case studied in the previous chapter, has to satisfy special conditions to be a valid path, as discussed in the next section.

4.2 CONSTRUCTION OF AN ELECTRIC STRING IN THE QDM

The path is set to begin from and end in the sublattice A, where the background charges are $Q_\mathbf{r} = +2$. It is possible to begin the paths from the sublattice B but the last portions of the electric string will remain static

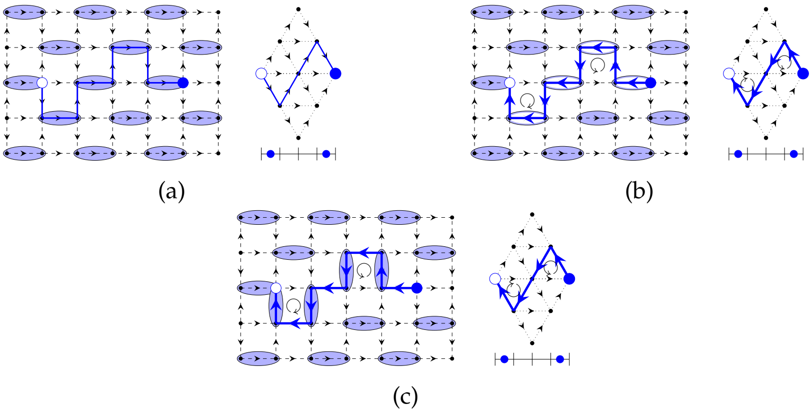
(a)
(b)
(c)

Figure 4.4: *Construction of an electric string on the staggered vacuum of* QDM: (a) A path is traced following a sequence of dimer occupied and empty links between two sites in the sublattice A. (b) the electric lines in the links along the path are revered to create the string, and the dimers are *dragged* to the left. (c) a new dimer configuration is obtained with parallel dimers[HAMS19].

under the action of the Hamiltonian (4.2) because of the absence of flippable plaquettes at the ends of the string. Then, we select a site of the sublattice A where we place a defect $Q_{\mathbf{r}f} = +4$, and draw a directed path that goes always against the flow of the background electric lines given by (4.5) (have into account that going with the flow does not create an electric string distinguishable from the background). Such paths will pass through a sequence of links alternating the presence or absence of a dimer, so that a path including two consecutive empty links (without dimer) will be considered invalid. The path ends at the sublattice A with the creation of a defect $Q_{\mathbf{r}0} = 0$ (see FIG. 4.4a).

When the path is complete, we reverse the direction of the electric lines of every link crossed, so that $Q_{\mathbf{r}f} = +4$ is the source of the string and $Q_{\mathbf{r}0} = 0$ the sink. The reassignation of the electric lines changes the orientation of the electric lines given by (4.5) and consequently of the dimers by shifting the empty and occupied sites, as depicted in FIG. 4.4b. This can also be seen as the dimers crossed by the string are *dragged* towards the sink defect $Q_{\mathbf{r}0} = 0$, leaving the site of the source $Q_{\mathbf{r}f} = +4$ untouched by any dimer and the site of $Q_{\mathbf{r}0}$ with two dimers overlapping. The reassignation of dimers in the new positions will give us a configuration containing *dimer plaquettes*, each one with an energy cost of V under the action of the potential term of the RK Hamiltonian (4.2) (see FIG. 4.4c). These elements also fluctuate between the horizontal and vertical configurations, corresponding to the fluctuations $|\circlearrowleft\rangle \leftrightarrow |\circlearrowright\rangle$ produced by the kinetic term.

4.3 MAPPING THE ELECTRIC STRING IN QDM TO A TWO-LEG LADDER

4.3.1 *QLM in a triangular lattice*

The electric string built in the previous section and depicted in the FIG. 4.5 with the new dimer configuration can be mapped into a QLM in a triangular lattice where the ice rules are satisfied and the three directions defined at each site are polarized (see the triangular lattice in FIG. 4.4a where the background links have not being modified). This mapping consists on shrinking the dimers of the background configuration to points that form a triangular lattice. The rules assigned in (4.3) and (4.5) transform into new ice rules for a triangular lattice $Q_{\triangle} = 0$ and the maximal winding number used for the Q6VM in chapter 3.

In addition to the flippable plaquettes found in the Q6VM associated to corners or kinks in the path, in the triangular lattice a horizontal path produces two flippable plaquettes above and below the path, as shown in FIG. 4.5b. The existence of horizontal path is an intermediate state between the two kinked configurations observed in the Q6VM and shown in FIG. 3.4, because each cell of the square lattice is divided into two triangular cells. This fact implies that the length of the electric string is not conserved under the action of the RK Hamiltonian (4.2), and the mapping to a 1D chain will not be straightforward as in the Q6VM.

4.3.2 *From the triangular lattice to the two-leg ladder*

The existence of these two different kinds of paths requires to implement a mapping onto a 1D chain with two classes of sites, even and odd, which can also be seen as an asymmetric two-leg ladder, and a Hard-core Boson (HCB) placed in an even or odd site does not have the same dynamics under the action of (4.2). As shown in FIGs. 4.4c or 4.5, the chain is obtained by projecting the triangular lattice onto the horizontal axis, creating the 1D lattice. The two classes of sites in the horizontal chain are projected as ticks that indicate the sites of the triangular lattice (similar to the Q6VM) and are called *odd sites*, while the triangular links are represented as short segments (new sites in between of the 1D chain found for the Q6VM) and are called *even sites* (see FIGs. 4.4c or 4.5 for clarification).

The placement of HCBs in the 1D chain will be more complex than in the Q6VM where the vertical segments of the string correspond to a HCB in a certan site and for a horizontal segments the site is left empty. In this case, the rules are the following (observe FIG. 4.5 as the instructions are given):

- an upward segment of the string (observe the arrow) corresponds to a HCB occuping an odd site (short segments).
- a downward segment of the string corresponds to an empty site.

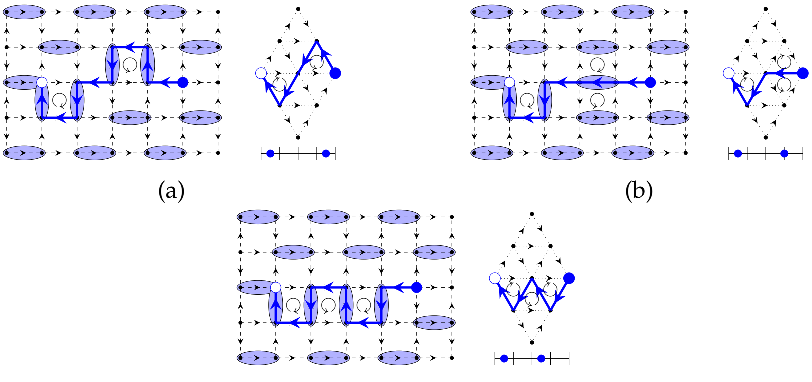
(a)
(b)
(c)

Figure 4.5: *Successive states of an open string under the action of the* RK *Hamiltonian* (4.2): (a) Inicial state of the string with two flippable plaquettes. (b) First state after the action of (4.2) in the right plaquette. Notice the horizontal path in the triangular lattice and the intermediate hopping to an even site in the 1D chain. (c) Second step after the action of (4.2) in the same plaquette (right top). The horizontal line is now kinked downwards and the boson has hopped to an odd site[HAMS19].

- a horizontal segment in the triangular lattice corresponds to a HCB placed in an even site (ticks) (FIG. 4.5b).

The positions of the defects in the dimer lattice are assigned as $(0, 0)$ for $Q_{\mathbf{r}0} = 0$ and $(2\ell_x, \ell_y)$ for $Q_{\mathbf{r}0} = +4$, where we count each horizontal link as 1/2 (in FIG. 4.5 $Q_{\mathbf{r}f}$ is located at $(4, 0)$ where $\ell_x = 2$ and $\ell_y = 0$). Then, the number of sites in the 1D chain is $L = 4\ell_x - 1$ and the total number of bosons is $\ell_x - \ell_y$ (in FIG. 4.5 we have $L = 7$ and $N = 2$).

4.3.3 *Construction of the 1D bosonic Hamiltonian*

The kinetic term of the RK Hamiltonian in (4.2) is easily mapped into simple single-particle hopping terms:

$$H_{hop} = -\sum_i t b_i^\dagger b_{i+1} + h.c., \tag{4.7}$$

where each hopping is associated to a change in the configuration of the electric string, that is, the flip of a plaquette (in the dimer configuration changing the orientation of the parallel dimers, and in the triangular as the flipping between horizontal and kinked segments (see FIG. 4.5). However, in contrary to the Q6VM, the mapping to the 1D chain of HCBs is not one-to-one in the QDM. We are required to project out configurations that are possible in the bosonic picture. The following items include terms to the bosonic Hamiltonian by examining minuciously each one of the conditions we need to have a fair mapping of the electric string onto the 1D chain:

- two bosons cannot occupy NN sites with one site being even (tick) and the other site being odd (segment), and similarly two bosons cannot be in consecutive even sites because they do not have associated dimer configuration (see FIG. 4.5b representing bosons at even sites in the closest configuration). Then we add the term

$$H_{con} = U\sum_{i} n_i n_{i+1} + U\sum_{i\,even} n_i n_{i+2}, \quad U \to \infty, \tag{4.8}$$

where $U \to \infty$ projects out the aforementioned bosonic configurations.

- every flippable plaquette in the triangular lattice given by a kinked segment of the string is mapped as a boson occuping an odd site for the upward segment of the string and an odd empty site for the downward segment (see FIG. 4.5), so the change of occupation for the odd sites is penalized by an energy of V, similar to the mapping for the Q6VM in (3.9):

$$H_{pot,1} = V\sum_{i\,odd} (n_i - n_{i+2})^2. \tag{4.9}$$

- every horizontal segment of the string has two adjacent flippable plaquettes (see FIG. 4.5b) so is penalized by $2V$. This term can be included as a chemical potential counting only bosons in even sites:

$$H_{pot,2} = 2V\sum_{i\,even} n_i. \tag{4.10}$$

- there is one less flippable plaquette when a horizontal segment of the string meets with a downward segment. In the bosonic picture it corresponds to a configuration where two bosons occupied sites separated by three units, so we have to subtract one penalization of V for such configurations:

$$H_{pot,3} = -V\sum_{i} n_i n_{i+3}. \tag{4.11}$$

The resulting bosonic Hamiltonian that maps the electric string in the QDM onto the 1D chain is

$$H_{dimer} = H_{hop} + H_{pot,1} + H_{pot,2} + H_{pot,3} + H_{con}. \tag{4.12}$$

It is a generalization of the bosonic Hamiltonian (4.2) for the Q6VM and imply a series of consequences that difficult the analytical resolution of the problem. For instance, when $V = 0$, (4.12) cannot be mapped as free fermions anymore due to the constraint (4.8) that warranties the representability of bosonic configurations in the dimer picture.

Regarding the symmetries of the two-ladder chain, the Hamiltonian is particle-hole invariant, which can be seen as the invariance under reflexions about the horizontal axis intersecting $Q_{\mathbf{r}0} = 0$, the charge at the origin, similarly to the invariance under reflexions about the diagonal intersecting the origin in the Q6VM. Moreover, for periodic chains, the system is translationally invariant under translations by two sites given by:

$$[H, T] = 0, \quad T b_i^{\dagger} T^{-1} = b_{i+2}^{\dagger}. \tag{4.13}$$

This symmetry will be useful to diagonalize the Hamiltonian by blocks labelled by momentum.

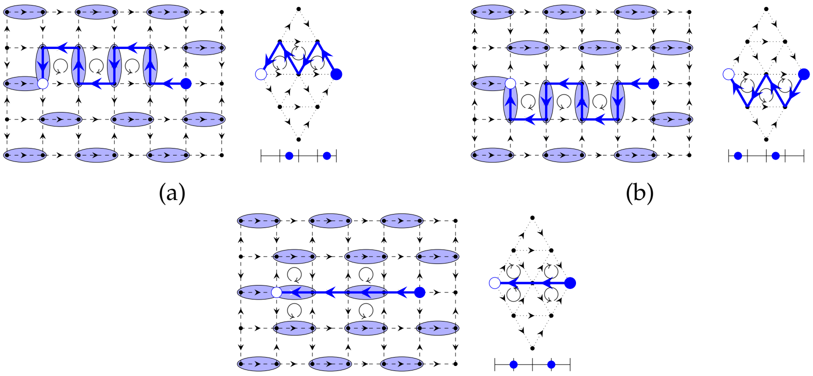
(a) (b) (c)

Figure 4.6: *Electric string in QDM in the CDW phase* $V < t$: Odd and even CDW states. Figures (a) and (c) show CDW on odd sites and are related under the particle-hole-like symmetry, while (b) shows the CDW on even sites[HAMS19].

4.4 PHASES OF THE ELECTRIC STRING FROM THE BOSONIC TWO-LEG LADDER

The lack of an analytical solution of the bosonic Hamiltonian (4.12) forces us to take an perturbative approach in the regions at the LHS and RHS of the RK point. A further numerical analysis done in the last section of the chapter will give us a further insight in the properties of the system. Additionally, we will restrict the analysis to the *quarter filling* sector, that is, when the defects are only horizontally displaced from each other by $\ell_x = L$ and $\ell_y = 0$ in the triangular lattice as has been shown in FIGs. 4.4 and 4.5 for $L = 2$. This sector offers the largest Hilbert space, so we expect it can be a good precursor to the behavior of the whole 2D QDM. Lastly, we will consider a periodic chain with length $\ell = 4L$ and $N = \ell_x - \ell_y = L$ bosons to use the conservation of total many-body momentum.

4.4.1 *LHS of the RK point: Charge Density Wave (CDW) states*

In the region at the LHS of the RK point, for large negative V the dominant terms in the bosonic Hamiltonian (4.12) are the potentials counting the flippable plaquettes, and the kinetic term can be introduced as a small perturbation on the classical ground states shown in FIG. (4.8). These are mapped as CDW states in the bosonic picture where the occupation number fluctuates slightly. Due to the two-leg ladder, we have two CDW states in the 1D chain that spontaneously break the translational symmetry dictated by (4.13) that in the limit $V \to -\infty$ are given by

$$|odd\rangle = \prod_{i=0}^{L-1} b^{\dagger}_{4i+1} |0\rangle\,, \quad |even\rangle = \prod_{i=1}^{L} b^{\dagger}_{4i-2} |0\rangle\,, \tag{4.14}$$

and the additional copies by translating the states by two units. The state $|odd\rangle$ for the odd sites analogous to the CDW states in Q6VM (expressed in

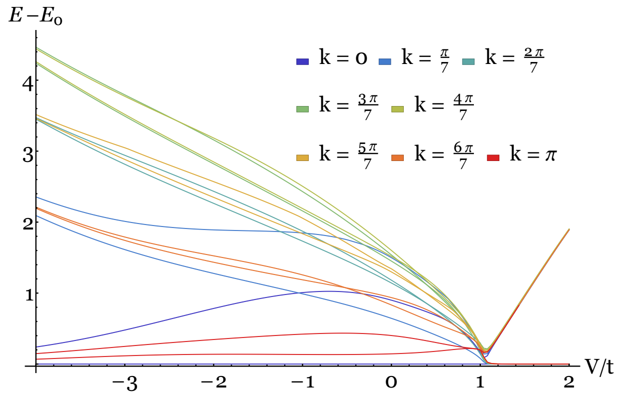

Figure 4.7: *Two lowest energy levels vs. V/t in* QDM: Lowest energy states obtain with exact diagonalization for a ring with $L = 7$ and $\phi = 0$. The region $V \to -\infty$ shows quasi-degenerate $k = 0$ and π CDW states with a gap opening for te lowest energy excitations. There is no gap closing at $V = 0$ because of the constraint H_{con} in (4.8). The expected sharp discontinuity at the RK point $V = t$ is obtained, followed by approximate degenerate energy states at all k sectors forming the phase-separated states in (4.16)[HAMS19]. It is illustrative to compare with FIG. 3.9.

the XXZ picture in (3.14)) corresponding to the maximally kinked path in the triangular lattice (see FIGs. 4.8a and 4.8b). The other state, $|even\rangle$, an *even* CDW where the bosons are located at the even sites, does not have an analogy in the Q6VM. This one corresonds to the maximally straight path (see FIG. 4.6c)

Since the states (4.14) belong to two different symmetry sectors, the ground state will be determined by the fluctuations produced by the kinetic term as follows from perturbation theory at fourth order in t:

$$\frac{E_{odd}}{L} = 2V - \frac{2t^2}{|V|} + \frac{t^4}{|V|^3} + O(t^6), \quad \frac{E_{even}}{L} = 2V - \frac{2t^2}{|V|} + 0 + O(t^6). \qquad (4.15)$$

The zeroth order is given by the energy penalty due to the flippable plaquettes. The first and all odd orders vanish because of the global gauge invariance that flip the sign of t. Since up to second order the two CDW states still have the same energy, we are required to go up to forth order, where the even CDW turns out to be the true ground state. We can understand this results from the fact that H_{con} in (4.8) forbids the bosons in the even sites to hopp closer in contrast to bosons in the odd sites that can delocalize without any infinite energy penalty of $U \to \infty$, as shown in the energy spectrum at $L = 7$ in FIG. 4.7 obtained with exact diagonalization, where the two lowest energy levels are plotted vs. V/t. Notie the four degenerate ground states in momentum sectors $k = 0$ and π, along with the lowest energy excitations above them.

For the region where $V \sim t$, the bosons spread throughout the chain in both lattices, meaning stronger fluctuations of the string in the dimer and triangular lattice pictures, to lower their energy. we can expect a transition

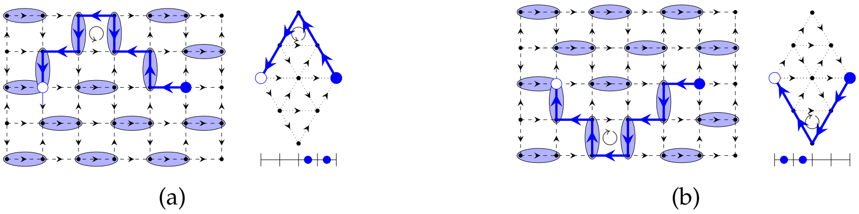

Figure 4.8: *Electric string in* QDM *in the* FM *phase* $t < V$: The string assumes a configuration that minimizes the number of flippable plaquettes, those are the paths, (a) and (b), along the bounding parallelogram with opposite vertices at the defects in the triangular lattice, and the corresponding bosonic picture as a phase separation[HAMS19].

at $V = -t$ similar to the Kosterlitz-Thouless (KT) point in the Q6VM because of the increasing relevance of the kinetic term. On the contrary, the picture of free fermions at $V = 0$ is impossible in the QDM because of the constraint (4.8) making the system strongly interacting in the whole V/t axis.

4.4.2 *RHS of the RK point: phase-separated states*

As expected from the Hamiltonian (4.2), we find a phase transition at the RK point, where the zero-energy manifold emerges because of the sum of projectors that we obtain when $V = t$ as can be seen in FIG. 4.7, where it is noticeable the discontinuity of the first derivative of the low energy spectrum for all the momentum sectors (in a system of size $L = 7$).

The region at the RHS of the RK point is more similar that one observed in the Q6VM in chapter 3. In the bosonic picture there is a NN attraction produced by the term $H_{pot,1}$ in (4.9) that cluster the bosons in a phase-separated state. Have into account that this clustering is only possible in the odd sublattice because of the constraint H_{con} in (4.8). In the triangular lattice, this manifests as the string approaching the bounding parallelogram as shown in FIG. 4.8 as the Ferromagnetic (FM) phase of the electric string in the Q6VM approaching the bounding rectangle (see FIG. 3.6). To finish the analysis of open strings, the energy density is concentrated at the domain wall, where the boson occupation number changes, with an energy penalty of V as $V \to \infty$, in complete agreement with the FM phase in Q6VM and similar implications such as the vanishing string tension when the defects move along the links of the lattice due to the polarized background in the square lattice for the Q6VM and the triangular lattice for the QDM.

For a periodic string we have two domain walls associated to the flippable plaquettes at the reconnection of the string (one flippable plaquette is possible only for open chains). In the limit $V \to t$ we would obtain a quasi-degenerate manifold due to the delocalization of the domain walls that can propagate throughout the ring. At quarter filling, the $2L$ quasi-degenerate states are given by the Bloch waves

$$|k\rangle = \frac{1}{\sqrt{2L}} \sum_{n=0}^{2L-1} e^{-ikn} \prod_{i=1}^{L} b^{\dagger}_{2i+1+2n} |0\rangle \ , \tag{4.16}$$

where $k \in {}^{2\pi n}/_{2L}$ and $n \in \mathbb{Z}$. The energy of these domain walls is approximately given by

$$E = 2V - \frac{2t^2}{V} + \dots, \tag{4.17}$$

at second order in t/V, and the penalty of $2V$ is due to the existence of the two flippable plaquettes. In this case we also have the case where the energy is concentrated at the domain walls, leaving the strings tensionless and yielding the sub-dimensional deconfinement as well as no additional flippable plaquettes are created because of their high energetic cost.

where the energy between the bosons is zero, and all the energy of the phase is concentrated at the domain wall. This results corresponds to the low-dimenstional deconfinement we have found in Q6VM where we are free to move the defects along the axes

4.5 NUMERICAL APPROACH: DRUDE WEIGHT AND SYSTEM SIZE EFFECTS

The limit cases $V \to \pm\infty$ lead to classical insulating CDW and phase-separated states at the LHS and RHS of the RK point, respectively. However, based on the results obtained for the Q6VM in chapter 3 and the stronger quantum fluctuations due to the kinetic term of the Hamiltonians (4.2) and (4.12) in the region $|V| < t$, we can expect that metallic Luttinger-liquid-like states could appear between the two limit cases. This hypothesis can be tested using the Drude weight introduced in chapter 3. Following a similar procedure, we diagonalized numerically the Hamiltonian (4.2) using the physical states of the string instead of the bosonic picture to avoid the implementation of a larger Hilbert space with the constraints H_{con} in (4.8). The system consists in a ring of size $L = 2, ..., 7$ with the modification of the boundary twist introduced in (3.23):

$$H_{dimer,closed} = H_{dimer,open} + e^{i\phi} t b^{\dagger}_1 b_L + h.c. \tag{4.18}$$

The results presented in FIG. 4.7 are for $\phi = 0$. The rest of the values were taken into account to calculate the Drude weight $\mathcal{D}$ defined in (3.25):

$$\mathcal{D} \equiv L \frac{d^2 E_0}{d\phi^2}, \tag{4.19}$$

plotted in FIG. 4.9 vs. $v = V/t$ for the different momentum sectors.

The main features, displayed in FIG. 4.9, resemble the results obtained for the Q6VM (see FIG. 3.10). The conducting phase in the region $V \sim t$ is

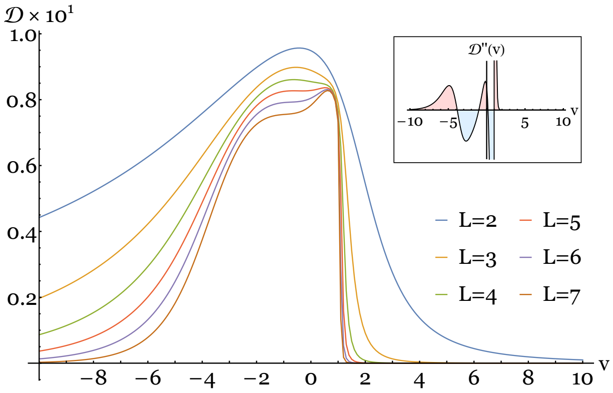

Figure 4.9: *Two lowest energy levels vs. v for each k momentum sector*: Drude weight of H_{dimer} is computed for systems $L = 2, \dots, 7$ via exact diagonalization for the ground state in the $k = 0$ momentum sector. The RK point appears sharply at $v = 1$ and there is evidence for an intermediate conducting phase. Unlike the Q6VM, there is much more structure in the putative critical region; as shown in the inset, the second derivative of the Drude weight for $L = 7$ changes sign three times[HAMS19].

clearly visible, as well as the two insulating phases as the limit cases when $V \to \pm\infty$. The RK point is shown clearly as a sharp drop in $\mathcal{D}$ for system sizes larger than $L = 3$. There seems to be another phase transition at the LHS of the RK point that is less visible, requiring larger system sizes to realize the behavior in the thermodynamic limit.

As expected from the additional terms in the bosonic Hamiltonian (4.12) to represent fairly the electric string, but still interestingly, the Drude weight $\mathcal{D}$ in the conducting phase manifests a more complex behavior than its Q6VM counterpart. The concavity $\frac{d^2\mathcal{D}}{d^2v}$ plotted in the inset in the top left corner of FIG. 4.9 changes not two, but four times, corresponding to the small pick of $\mathcal{D}$ in the region $0 < v < 1$ and suggesting the presence of more than one conducting phase between the classical ground states at $V \to \pm\infty$. The verification of this hypothesis requires to scale to much larger system sizes available using other numerical methods such as Density Matrix Renormalization Group (DMRG) studies.

4.6 SUMMARY AND DISCUSSION

We have studied the problem of a single fluctuating quantum electric field lines connecting two isolated charge monomers in the QDM and Q6VM. By constructing these isolated strings on top of trivial inert vacua that appear as ground states to the right of the RK point, we have been able to map the problems exactly onto conventional one-dimensional systems with local Hamiltonians.

In the case of the QDM, the electric field line maps exactly onto a one-dimensional lattice of HCBs with two sites per unit cell (or equivalently a two-leg spin-1/2 ladder). We have not been able to solve this problem analytically but have been able to understand perturbatively the phases that occur far away from the RK point. These two phases correspond to a CDW state (analogous to the Ising AFM in the Q6VM case) and a phase separated state (analogous to the phase separated Ising FM in the Q6VM case). These two states are the natural precursors to the columnar and the staggered phases of the full two-dimensional QDM. Subdimensional deconfinement appears in the phase separated state, corresponding to the deconfinement in the staggered dimer phase [BT04]. By numerically computing the Drude weight, we have found evidence for a liquid state intervening between the two crystals that exist away from the RK point. We interpret this liquid, delocalized phase as the one-dimensional precursor of the plaquette valence bond solid in the full two-dimensional problem.

The resemblance of the quasi-one-dimensional single electric field line problems that we have studied and the full two-dimensional problems indicates that the behavior of the latter might be understood by thinking of them as a closely packed array of electric field lines which by themselves are undergoing non-trivial phase transitions. More specifically, as we described in §4.1, the decoupling of the Hilbert space into winding sectors can be interpreted as a conservation law for the the total number of electric field lines. The zero winding sector where the global ground state of the full Hilbert space resides at the left of the RK point contains a large number of such electric field lines. These lines can be viewed as bosonic strings with hard-core interactions so that the electric field lines do not overlap. This perspective provides a natural understanding of why the crystalline phases of the one-dimensional electric field line survive in the fully two-dimensional multistring case. However, these strong interactions are presumably responsible for the freezing out of the quantum fluctuations of the Luttinger liquid type phase that we have encountered, transforming it into the resonant plaquette crystal state that is seen in numerical studies of the full two-dimensional problem of the six-vertex model. We hope that in the future, more systematic numerical studies of our current setting and of its generalizations to the few strings problems might offer an alternative window the behavior of the less well understood aspects of the presumed resonant plaquette phase of the QDM.

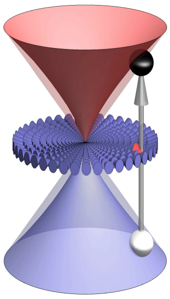

Part II

BOSONIZATION OF PARTICLE-HOLE EXCITATIONS IN 2D DIRAC FERMIONS

This part is devoted to the problem of bosonization of particle-hole excitations of interacting electrons in graphene. Chapter 5 is a brief review of the electronic properties of graphene emerging from its honeycomb lattice, keystone in producing the Dirac cones. Chapter 6 presents a bosonization technique to address non-perturbatively the electron interactions for the $\mathbf{Q} = 0$ particle-hole excitations. Lastly, Chapter 7 applies the techinique introduced in the previous chapter to the non-perturbative calculation of the optical conductivity of graphene.

5

GRAPHENE IN A NUTSHELL

> *We are probably digging too deep within established areas, leaving plenty of unexplored stuff under the surface, just one poke away. When one dares to try, rewards are not guaranteed, but at least it is an adventure.*
>
> — Sir Andre K. Geim [Gei11]

The discovery and control of several substances has implied in history turning points in the development of humanity, which include the furnace of different metals, the knowledge on chemical elements and the design of new materials. In that way, graphene is among the new materials discovered in the last decades that open the study of fundamental physics as well as promising technological applications. Although graphene was already virtually employed since the invention of the graphite pencil in the 16th century[Pet92], its properties theoretically predicted in 1947[Wal47] and progressively approached during the 20th century[Boe+62], it was until 2004 when a single layer of graphite was isolated and caracterized[Nov+04; Nov+05].

This chapter is a brief review in the lattice and band structure of monolayer graphene as our study case for the second part of this work consisting in an extension of the higher-dimensional frameworks of bosonization [HKM00]. §5.1 presents a discussion about the hybridizations of carbon orbitals and the honeycomb lattice as a result of the sp^2 hybridization present in graphene. Then, the tight-binding in a honeycomb lattice used to describe graphene is built in §5.2. Lastly, §5.3 introduces the effective 2D Dirac fermion Hamiltonian that is used in the next chapters 6 and 7. The reader is free to skip §5.1 and §5.2 and do a quick reading of §5.3 to know the notation used in the next chapters and come back to the previous sections for clarification if needed.

5.1 ORIGIN OF THE HEXAGONAL STRUCTURE

Carbon (C), as the basis of the organic chemistry, presents a high versatility when bonding with other atoms. It is due to the electron content of C with four valence electrons, having then four electrons occupying the eight states available in the orbitals $2s2p$[Goe11]. Although the electronic configuration of C in its ground state, $1s^2 2s^2 2p^2$, presents a doubly-occupied $2s$ orbital and only $2p$ orbitals singly-occupied leaving the last one empty, when the atom forms bonds with other atoms, one of the electrons of the doubly-occupied $2s$ is promoted to the last empty $2p$ by the cost of 4.2 eV such that there are now four singly-occupied orbitals in the outer shell whose electrons form

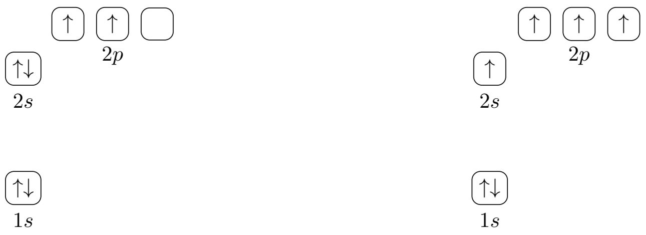

Figure 5.1: *Carbon electronic configuration*: The ground state of C atoms $1s^2 2s^2 2p^2$ with two valence electrons, and the excited state $1s^2 2s^1 2p^3$ with four valence electrons involved in chemical bonding[Goe11].

part of the molecular orbitals (see FIG. 5.1). The energy paid to promote the electron from $2s$ orbital to $2p$ is obtained from the exothermic process of chemical bonding, in which the atoms energy decreases when the wave functions overlap[Kat12].

5.1.1 *Hybrid orbitals in C*

The energy gained when chemical bonding happens is maximized if the wave functions are aligned between the atom cores and take maximal values there. This is done by the superposition of orbitals in the outer shell or the *hybridization* of the $2s$ and $2p$ orbitals, whose orientation is dictated by the spherical harmonics Y_l^m with $l = 0$ and $l = 1$, that can be assignated to states as follows:

$$\begin{aligned} |s\rangle &= Y_0^0(\theta,\phi) = \sqrt{\tfrac{1}{4\pi}}, & |x\rangle &= Y_1^x(\theta,\phi) = \sqrt{\tfrac{3}{4\pi}} s_\theta c_\phi, \\ |z\rangle &= Y_1^0(\theta,\phi) = \sqrt{\tfrac{3}{4\pi}} c_\theta, & |y\rangle &= Y_1^y(\theta,\phi) = \sqrt{\tfrac{3}{4\pi}} s_\theta s_\phi. \end{aligned} \tag{5.1}$$

where $Y_1^{x(y)} = (Y_1^{+1} \pm Y_1^{+1})/\sqrt{2}$, and the radial part is factored out since it contributes equally as a first approximation[Kat12]. Then, the states can be combined as

$$|n\rangle = \sum_{i=s,x,y,z} c_{ni} |i\rangle \,, \tag{5.2}$$

where $n = 1, ..., 4$ are the *hybrid orbitals*, new orthogonal states that are orientated to maximize the overlapping. This procedure can be extended to d orbitals using $Y_{2,m}(\theta,\phi)$ harmonics in the third block of periodic table to understand covalend and cordinated bonds in transition metals and heavier non-metals.

In C atoms, there are three types of hybridization depending on the number of $2p$ orbitals involved in the maximization of overlapping to form σ bonds (invariant under rotations about the interatomic axis) or π bonds ($\mathbb{Z}_2$-symmetric with a node along the interatomic axis) :

- *sp*: involves only $2s2p_z$ orbitals to form two collinear orbitals along the z axis:

$$|1\rangle = \tfrac{1}{\sqrt{2}}(|s\rangle + |z\rangle), \quad |2\rangle = \tfrac{1}{\sqrt{2}}(|s\rangle - |z\rangle), \tag{5.3}$$

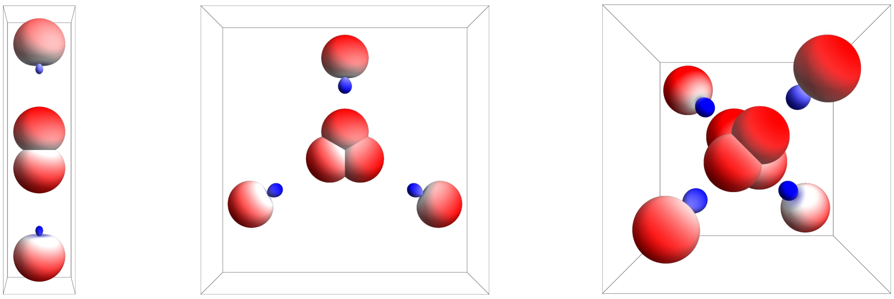

(a) sp (b) sp^2 (c) sp^3

Figure 5.2: *Hybrid atomic orbitals*: The maximization of overlapping of atomic wave functions decrases the total energy of the molecule, and then the orbitals mix among them to reach the new eigenstates given by the three possible hybridizations of C electrons depending on the surroinding atoms C is going to bond[Kat12].

with two $2p_{x,y}$ remaining intact and orthogonal to the sp axis. It is useful to understand triple bonds (e.g. acetylene $HC \equiv CH$), comprising a σ bond involving the sp in between and two π bonds involving the $2p_{x,y}$.

- sp^2: involves $2s2p_x2p_y$ orbitals to form:

$$\begin{aligned} |1\rangle &= \tfrac{1}{\sqrt{3}}(|s\rangle + \sqrt{2}\,|x\rangle), \\ |2\rangle &= \tfrac{1}{\sqrt{6}}(\sqrt{2}\,|s\rangle - |x\rangle + \sqrt{3}\,|y\rangle), \\ |3\rangle &= \tfrac{1}{\sqrt{6}}(\sqrt{2}\,|s\rangle - |x\rangle - \sqrt{3}\,|y\rangle), \end{aligned} \tag{5.4}$$

  forming three triangular coplanar orbitals on the xy plane, with $2p_z$ intact. It is useful to understand double bonds (e.g. ethylene $H_2C = CH_2$), comprising a σ bond involving one sp^2 orbital and one π bond involving $2p_z$.

- sp^3: involves the four orbitals to form:

$$\begin{aligned} |1\rangle &= \tfrac{1}{2}(|s\rangle + |x\rangle + |y\rangle + |z\rangle), \quad & |2\rangle &= \tfrac{1}{2}(|s\rangle + |x\rangle - |y\rangle - |z\rangle), \\ |3\rangle &= \tfrac{1}{2}(|s\rangle - |x\rangle + |y\rangle - |z\rangle), \quad & |4\rangle &= \tfrac{1}{2}(|s\rangle - |x\rangle - |y\rangle + |z\rangle), \end{aligned} \tag{5.5}$$

  displaying four orbitals distributin at the corners of a tetrahedron centered in the nucleus of the atom. The sp^3 can form only σ bonds (e.g. methane CH_4 or ethane $H_3C - CH_3$).

The diamond structure is described using sp^3 because of the tetrahedral symmetry on the way each C in the lattice binds with its neighbors (see FIG. 5.2c), and linear acetylenic carbon consists on a polymetric chain of doubles bonds where every C is in sp hybridization[Xue+04] (FIG. 5.2a). Other allotropes of C such as graphite, carbon nanotubes or fullerenes are based in graphene, where C is in sp^2. The trigonal structure of the sp^2 planar orbitals (FIG. 5.2b) are the key of garphene's hexagonal structure, while the remaining p_z orbital, perpendicular to the plane, are actively involved in the electronic properties of graphene and its derived allotropes.

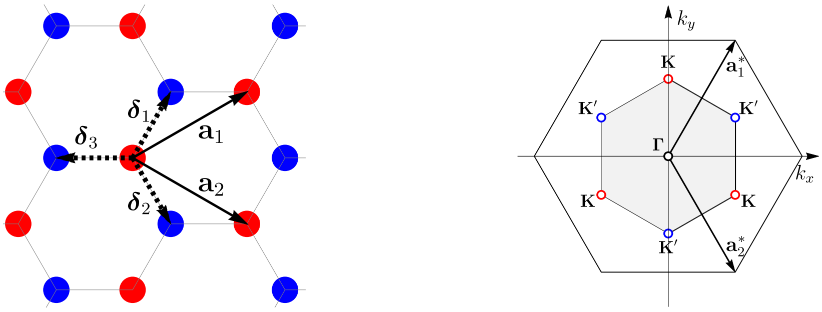

(a) (b)

Figure 5.3: *Direct and reciprocal lattice of the honeycomb*: (a) $\mathbf{a}_{1,2}$ are the basis vectors of the triangular Bravais lattice, and $\delta_{1,2,3}$ the NN vectors with $|\delta| = 1.42$Å. (b) Reciprocal lattice with basis vectors $\mathbf{a}^*_{1,2}$ and first Brillouin zone (shaded) centerer at $\mathbf{\Gamma}$. The Dirac points are located at the corners $\mathbf{K}$ and $\mathbf{K}'$.

5.1.2 *Honeycomb lattice*

The honeycomb lattice consists on a triangular Bravais lattice with basis vectors given by[Kat12]:

$$\mathbf{a}_1 = \frac{a}{2}(3, \sqrt{3}), \quad \mathbf{a}_2 = \frac{a}{2}(3, -\sqrt{3}), \tag{5.6}$$

where a is the lattice parameter with a length around 1.42 Å the CC bond length associated to a double bond with the π electrons delocalized through the lattice. At each triangular unit cell there are two kinds of C atoms depending on how they bond with their Nearest Neighbor (NN), one belonging to the sublattice A (red dots in FIG. 5.3a) that bonds with three C in sublattice B with vectors given by

$$\delta_1 = \frac{a}{2}(1, \sqrt{3}), \quad \delta_2 = \frac{a}{2}(1, -\sqrt{3}), \quad \delta_3 = a(-1, 0), \tag{5.7}$$

and similarly with C atoms belonging to sublattice B (blue dots in FIG. 5.3a).
The associated reciprocal lattice obtained with the condition $\mathbf{a}_i \cdot \mathbf{a}_j^* = 2\pi\delta_{ij}$ can be expressed as:

$$\mathbf{a}_1^* = \frac{2\pi}{3a}(1, \sqrt{3}), \quad \mathbf{a}_2^* = \frac{2\pi}{3a}(1, -\sqrt{3}), \tag{5.8}$$

also generating a diatomic triangular lattice with a hexagonal Brillouin zone. Two kinds on symmetry points in the Brillouin zone are depicted in FIG. 5.3b, where the important ones to describe low-energy levels are given by the wave vectors:

$$\mathbf{K} = \frac{2\pi}{3a}\left(1, \frac{1}{\sqrt{3}}\right), \quad \mathbf{K}' = \frac{2\pi}{3a}\left(1, -\frac{1}{\sqrt{3}}\right), \tag{5.9}$$

These are the characteristic *Dirac points Dirac Point* (DP), where the low-energy excitations with the characteristic conical dispersion relation of graphene are found, as is briefly described in the next sections.

5.2 TIGHT-BINDING APPROACH

The wave function of an electron in the π orbitals with wave vector $\mathbf{k}$ in graphene is expanded in two components referring to which sublattice the electron is, as follows[Goe11]

$$\psi_{\mathbf{k}}(\mathbf{r}) = a_{\mathbf{k}}\psi_{\mathbf{k}}^{(A)}(\mathbf{r}) + b_{\mathbf{k}}\psi_{\mathbf{k}}^{(B)}(\mathbf{r}), \tag{5.10}$$

whose expansion in Bloch waves is given by

$$\psi_{\mathbf{k}}^{(N)}(\mathbf{r}) = \sum_{\mathbf{R}_l} e^{i\mathbf{k}\cdot\mathbf{R}_l}\phi^{(N)}(\mathbf{r}+\delta_j-\mathbf{R}_l), \quad N = A, B, \tag{5.11}$$

where $\phi^{(N)}(\mathbf{r})$ are the wave function of the $2p_z$ orbital located at the lattice sites $\mathbf{R}_l - \delta_j$. The wave functions $\phi^{(N)}(\mathbf{r})$ are solution of the *atomic Hamiltonian*

$$\hat{H}_0\phi^{(N)}(\mathbf{r}) = \left(\frac{\mathbf{k}^2}{2m} + U(\mathbf{r})\right)\phi^{(N)}(\mathbf{r}) = \epsilon^N\phi^{(N)}(\mathbf{r}), \tag{5.12}$$

where $U(\mathbf{r})$ is the internal potential of each atom before bonding.

The Hamiltonian of the crystal can be expressed asgoerbig2011electronic

$$\hat{H}\psi_{\mathbf{k}}^{\lambda}(\mathbf{r}) = \left(\hat{H}_0 + V\right)\psi_{\mathbf{k}}^{\lambda}(\mathbf{r}) = \epsilon_{\mathbf{k}}^{\lambda}\psi_{\mathbf{k}}^{\lambda}(\mathbf{r}) \tag{5.13}$$

where V is the potential acting in one electron produced by the other atoms, and $\epsilon_{\mathbf{k}}^{\lambda}$ with $\psi_{\mathbf{k}}^{\lambda}(\mathbf{r})$ are the dispersion relation and the wave function of the electrons in the band λ (two for the case of a bipartite lattice as in graphene). Using the Ansatz in (5.10), the Schrödinger equation in (5.13) can then be expressed as the quadratic form[Goe11]:

$$\begin{pmatrix} a_{\mathbf{k}}^* & b_{\mathbf{k}}^* \end{pmatrix} \mathcal{H}_{\mathbf{k}} \begin{pmatrix} a_{\mathbf{k}} \\ b_{\mathbf{k}} \end{pmatrix} = \begin{pmatrix} a_{\mathbf{k}}^* & b_{\mathbf{k}}^* \end{pmatrix} \mathcal{S}_{\mathbf{k}} \begin{pmatrix} a_{\mathbf{k}} \\ b_{\mathbf{k}} \end{pmatrix} \tag{5.14}$$

where $\mathcal{H}_{\mathbf{k}}$ and $\mathcal{S}_{\mathbf{k}}$ are the matrix elements of the Hamiltonian and the wave overlapping:

$$\mathcal{O}_{\mathbf{k}} = \begin{pmatrix} \psi_{\mathbf{k}}^{(A)}(\mathbf{r})\hat{O}\psi_{\mathbf{k}}^{(A)}(\mathbf{r}) & \psi_{\mathbf{k}}^{(A)}(\mathbf{r})\hat{O}\psi_{\mathbf{k}}^{(B)}(\mathbf{r}) \\ \psi_{\mathbf{k}}^{(B)}(\mathbf{r})\hat{O}\psi_{\mathbf{k}}^{(A)}(\mathbf{r}) & \psi_{\mathbf{k}}^{(B)}(\mathbf{r})\hat{O}\psi_{\mathbf{k}}^{(B)}(\mathbf{r}) \end{pmatrix}. \tag{5.15}$$

In this way, the solution of the problem will lie on the *secular equation*

$$\left|\mathcal{H}_{\mathbf{k}}^{MN} - \epsilon_{\mathbf{k}}^{\lambda}\mathcal{S}_{\mathbf{k}}^{MN}\right| = 0, \tag{5.16}$$

where $M, N = A, B$ are the sublattice indices.

5.2.1 *Hopping and overlapping matrices in* NN *approximation*

One realization of the secular equation is done by defining the *overlapping density* $s_{\mathbf{k}}^{MN}$ and the *hopping matrix* $t_{\mathbf{k}}^{MN}$ as follows:

$$o_{\mathbf{k}}^{MN} = \sum_{\mathbf{R}_l} e^{i\mathbf{k}\cdot\mathbf{R}_l} \int d^2 r \phi^{(M)*}(\mathbf{r}) \hat{O} \phi^{(N)}(\mathbf{r} + \delta_{MN} - \mathbf{R}_l), \tag{5.17}$$

where $\delta_{MN} = \delta_M - \delta_N$ and the integral is done througout the whole system. The operator $\hat{O} = \mathbf{1}$ for the overlapping density and $\hat{O} = V$ for the hopping matrix. Have into account that the matrix elements of $o_{\mathbf{k}}^{MN}$ refer to the overlap of the wave function of an atom in sublattice M with another one in sublattice N. As an addional comment, $s_{\mathbf{k}}^{MN}$ is called overlapping density because $s_{\mathbf{k}}^{MN} = \mathcal{S}_{\mathbf{k}}^{MN}/\mathcal{N}$, where $\mathcal{N}$ is the total number of unit cells in the system.

The next step consist of calculating $o_{\mathbf{k}}^{MN}$ only for the NN atoms of an arbitrary atom in the sublattice A, that is, one atom connected to the first three atoms of the other sublattice, $B_{1,2,3}$, and neglecting any hopping or overlapping involving longer distances in the lattice (such as terms involving atoms in the same sublattice). Since A and B_3 are connected by δ_3 with only one non-zero component, it can be used to define the real parameters

$$o = \int d^2 r \phi^{(A)*}(\mathbf{r}) \hat{O} \phi^{(B)}(\mathbf{r} + \delta_3), \tag{5.18}$$

where $o = s, t$ when $\hat{O} = \mathbf{1}, V$, respectively. The hopping and overlapping with the other two atoms $B_{1,2}$ will contribute with phase factors associated to the change in the direction of the Bloch waves when translating from B_3 to B_1 or B_2, which can be expressed with the phase factor

$$\gamma_{\mathbf{k}} = 1 + e^{i\mathbf{k}\cdot\mathbf{a}_1} + e^{i\mathbf{k}\cdot\mathbf{a}_2}, \tag{5.19}$$

and yielding the off-diagonal contributions $t_{\mathbf{k}}^{AB} = t\gamma_{\mathbf{k}}$ and $s_{\mathbf{k}}^{AB} = s\gamma_{\mathbf{k}}$. It is important to remember that $t_{\mathbf{k}}^{AA} = t_{\mathbf{k}}^{BB} = 0$, but $s_{\mathbf{k}}^{AA} = t_{\mathbf{k}}^{BB} = 1$ from the normalization of atomic wave functions $\phi^{(N)}(\mathbf{r})$, giving at the end the matrices

$$t_{\mathbf{k}} = \begin{pmatrix} 0 & t\gamma_{\mathbf{k}}^* \\ t\gamma_{\mathbf{k}} & 0 \end{pmatrix}, \quad s_{\mathbf{k}} = \begin{pmatrix} 1 & s\gamma_{\mathbf{k}}^* \\ s\gamma_{\mathbf{k}} & 1 \end{pmatrix}. \tag{5.20}$$

5.2.2 *Dispersion relation for π electrons*

When having into account the crystal Hamiltonian in (5.13) separated into atomic and interatomic parts, together with the definition of the hopping and overlapping matrices that allow to express (5.13) as

$$\mathcal{H}_{\mathbf{k}}^{MN}/\mathcal{N} = \epsilon^{(M)} s_{\mathbf{k}}^{MN} + t_{\mathbf{k}}^{MN}, \tag{5.21}$$

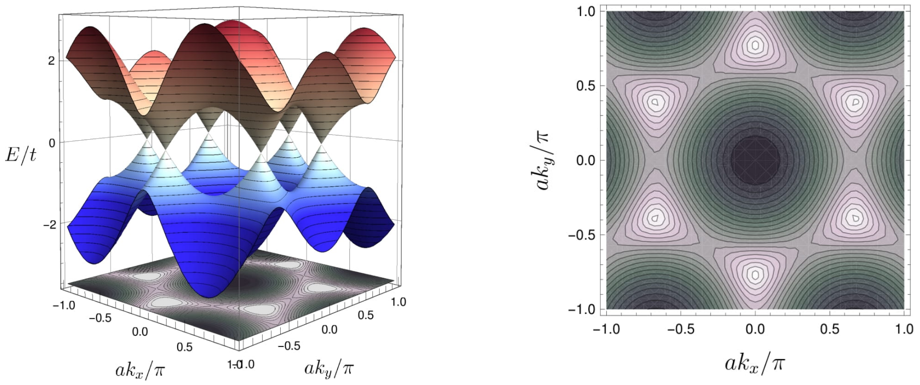

(a) (b)

Figure 5.4: *Band structure of graphene*: (a) Valence band (VB) (blue) and Conduction band (CB) (red) obtained from the tight-binding Hamiltonian as $\epsilon_{\mathbf{k}}^{\pm}$ in (5.24). (b) Contour plot of the VB in the first Brillouin zone. $\mathbf{\Gamma}$, $\mathbf{K}$ and $\mathbf{K}'$ points are clearly visible.

the secular equation in (5.16) can then be expressed as

$$\left| t_{\mathbf{k}}^{MN} - \left(\epsilon_{\mathbf{k}}^{\lambda} - \epsilon^{(M)} \right) s_{\mathbf{k}}^{MN} \right| = 0. \tag{5.22}$$

The internal atomic energy $\epsilon^{(M)}$ can be interpreted as an *on-site* potential, but since $\epsilon^{(A)} = \epsilon^{(B)}$, this term contributes as a constant term to the energy that can be withdrawn without physical consequences, yielding the equation

$$\left| t_{\mathbf{k}}^{MN} - \epsilon_{\mathbf{k}}^{\lambda} s_{\mathbf{k}}^{MN} \right| = \begin{vmatrix} -\epsilon_{\mathbf{k}}^{\lambda} & \left(t - \epsilon_{\mathbf{k}}^{\lambda} s\right) \gamma_{\mathbf{k}}^{*} \\ \left(t - \epsilon_{\mathbf{k}}^{\lambda} s\right) \gamma_{\mathbf{k}} & -\epsilon_{\mathbf{k}}^{\lambda} \end{vmatrix} = 0, \tag{5.23}$$

where $\gamma_{\mathbf{k}}$ is given in (5.19).

The solutions of (5.23) are

$$\epsilon_{\mathbf{k}}^{\pm} = \frac{t}{s \pm \left|\gamma_{\mathbf{k}}\right|^{-1}} \approx \pm t \left|\gamma_{\mathbf{k}}\right| - st\gamma_{\mathbf{k}}^{*}\gamma_{\mathbf{k}} + \mathcal{O}(s^2), \tag{5.24}$$

where $t = -2.97$ eV[Goe11; Kat12], and the overlap is assumed small, that is $s \ll 1$. At zeroth-order in s, it is found that the band structure of the honeycomb lattice fulfills the *particle-hole symmetry* $\epsilon_{\mathbf{k}}^{\lambda} = -\epsilon_{\mathbf{k}}^{\bar{\lambda}}$, i.e., the CB and VB are completely symmetric (up to contributions of the overlapping as shown in the RHS of (5.24)).

The FIG. 5.4 displays the bands of the bonding π and antibonding π^* electrons, also known as the VB and CB, respectively. Due to the fact that each C contributes with three sp^2 electrons forming the honeycomb lattice and one non-hybridized p_z that delocalizes on the plane at the *charge-neutrality point* (one electron per C), the VB π will be occupied up to the touching points, also called DPs, making the Fermi surface to shrink to a point. The reason for such a name roots in expanding the solution of (5.24) around $\mathbf{K}$ and $\mathbf{K}'$, yielding the effective dispersion relation depending on $\mathbf{q} = \mathbf{k} - \mathbf{K}$ as

$$\epsilon_{\mathbf{q}}^{\pm} \approx \pm v \left|\mathbf{q}\right| + \mathcal{O}\left[\left({}^{q}/_{K}\right)^2 \right], \tag{5.25}$$

where v is the Fermi velocity[VKG10]:

$$v = \frac{3|t|a}{2}, \tag{5.26}$$

with a numerical value of $v \approx 10^6 \mathrm{m}/\mathrm{s}$ [Kat12; CN+09].

5.3 EFFECTIVE 2D DIRAC FERMION HAMILTONIAN

The previous Hamiltonian allows to implement a continuum model in which the hopping matrices are given parameters that have already integrated out the interatomic potentials giving a finite Fermi velocity v, and the orbitals are expressed in the Fock space by means of the fermionic creation and annihilation operators, $\hat{\psi}^\dagger_\sigma(\mathbf{r})$ and $\hat{\psi}_\sigma(\mathbf{r})$ respectively, where $\sigma = \{\uparrow, \downarrow\}$ is the *pseudospin* index indicating the sublattice in which the operator acts, i.e., pseudospin $\uparrow$ and $\downarrow$ correspond to sublattices A and B, respectively[Kat12].

Therefore, $\hat{\psi}^\dagger_\sigma(\mathbf{r})$ creates an electron at position $\mathbf{r}$ and pseudospin σ:

$$\hat{\psi}^\dagger_\sigma(\mathbf{r}) \left|0\right\rangle_{\mathbf{r}} = \left|\sigma\right\rangle_{\mathbf{k}}, \tag{5.27}$$

so the operators can be arranged in a 2-component spinor:

$$[\hat{\psi}_\sigma(\mathbf{r})] = \begin{pmatrix} \hat{\psi}_\uparrow(\mathbf{r}) \\ \hat{\psi}_\downarrow(\mathbf{r}) \end{pmatrix}. \tag{5.28}$$

In this basis, the Hamiltonian near the DP at $\mathbf{K}$ can be expressed as the Dirac Hamiltonian in 2D[Wal47; VKG10]:

$$H_{\text{kin}} = -iv\xi \int d^2r \hat{\psi}^\dagger_\sigma(\mathbf{r}) \left(\nabla \cdot \boldsymbol{\sigma}_{\sigma\sigma'}\right) \hat{\psi}_{\sigma'}(\mathbf{r}), \tag{5.29}$$

where $\boldsymbol{\sigma} = (\sigma^x \, \sigma^y)$ are the x and y components of the Pauli matrices:

$$\sigma^x = \begin{pmatrix} 0 & 1 \\ 1 & 0 \end{pmatrix}, \quad \sigma^y = \begin{pmatrix} 0 & -i \\ i & 0 \end{pmatrix}, \quad \sigma^z = \begin{pmatrix} 1 & 0 \\ 0 & -1 \end{pmatrix}. \tag{5.30}$$

The Dirac Hamiltonian for the electrons at $\mathbf{K}'$ is simply $H^{\text{T}}_{\text{kin}}$, the transpose on the pseudospin indices. The specification about in which *valley*, $\mathbf{K}$ or $\mathbf{K}'$, the electron is is done by the *isospin* index ξ[Goe11], i.e., isospin $\xi = \{+, -\}$ correspond to valleys $\mathbf{K}$ and $\mathbf{K}'$. The physical spin of the electrons therefore constitutes a third index that should be taken into account to deal with magnetic fields or spin-orbit coupling (pseudospin-spin coupling)[Kat12]. However, for the present discussion the Hamiltonian is diagonal in both the physical spin of the electrons and the isospin (known as *spin-valley degeneracy*[Goe11]), then they are traced out yielding a factor of 4 in the physical observables such as the optical conductivity in chapter 7.

In the reciprocal basis, the Hamiltonian is diagonal in the momentum index and can be expressed as[MS20]:

$$H_{\text{kin}} = v\xi \sum_{\mathbf{k},\sigma,\sigma'} \hat{\psi}^\dagger_{\mathbf{k},\sigma} \left(\mathbf{k} \cdot \boldsymbol{\sigma}_{\sigma\sigma'}\right) \hat{\psi}_{\mathbf{k},\sigma'}, \tag{5.31}$$

still requiring to be diagonalized in the pseudospin basis to obtain the band basis $s = \{+, -\}$. The local kinetic term of (5.39) is ($e^{\pm i\phi} = \hat{k}_x \pm i\hat{k}_y$):

$$\begin{aligned}\hat{\psi}^{\dagger}_{\mathbf{k}\sigma}\left(\mathbf{k}\cdot\boldsymbol{\sigma}_{\sigma\sigma'}\right)\hat{\psi}_{\mathbf{k}\sigma'} &= \begin{pmatrix}\hat{\psi}^{\dagger}_{\mathbf{k}\uparrow} & \hat{\psi}^{\dagger}_{\mathbf{k}\downarrow}\end{pmatrix}\begin{pmatrix}0 & ke^{-i\phi}\\ ke^{+i\phi} & 0\end{pmatrix}\begin{pmatrix}\hat{\psi}_{\mathbf{k}\uparrow}\\ \hat{\psi}_{\mathbf{k}\downarrow}\end{pmatrix}\\ &= k(e^{-i\phi}\hat{\psi}^{\dagger}_{\mathbf{k}\uparrow}\hat{\psi}_{\mathbf{k}\downarrow} + e^{+i\phi}\hat{\psi}^{\dagger}_{\mathbf{k}\downarrow}\hat{\psi}_{\mathbf{k}\uparrow}),\end{aligned} \tag{5.32}$$

which is diagonalized by the transformation

$$\begin{pmatrix}\hat{\psi}_{\mathbf{k}\uparrow}\\ \hat{\psi}_{\mathbf{k}\downarrow}\end{pmatrix} = \frac{1}{\sqrt{2}}\begin{pmatrix}e^{-i\phi/2} & e^{-i\phi/2}\\ e^{+i\phi/2} & -e^{+i\phi/2}\end{pmatrix}\begin{pmatrix}\hat{\psi}_{\mathbf{k}+}\\ \hat{\psi}_{\mathbf{k}-}\end{pmatrix}, \tag{5.33}$$

yielding the diagonal 2D Dirac Hamiltonian in the band basis,

$$H_{\text{kin}} = v\xi \sum_{\mathbf{k},s,s'} \hat{\psi}^{\dagger}_{\mathbf{k},s}\left(\mathbf{k}\cdot\sigma^{z}_{\sigma\sigma'}\right)\hat{\psi}_{\mathbf{k},s'}, \tag{5.34}$$

with σ^z the third z-Pauli matrix. The physical system then consists on four flavors of Dirac fermions ($2_{\text{spin}} \otimes 2_{\xi}$) propagating on a 2D plane with constant phase speed v and a charge degree of freedom determined by the band index: $s = +$ corresponds to *electrons* and $s = -$ to *holes* with dispersion relations given by $\epsilon^{s}_{\mathbf{k}} = sv\,|\mathbf{k}|$.

5.4 ELECTRON-ELECTRON INTERACTIONS

The introduction of interactions to the system can be done by adding density-density interaction terms mediated by the Coulomb potential[Nag99]:

$$\begin{aligned}H_{\text{pot}} &= \frac{1}{2A}\sum_{\mathbf{q}\neq 0} V_{\mathbf{q}}\left[\hat{\rho}_{\mathbf{q}}\hat{\rho}_{-\mathbf{q}} - N\right]\\ &= \frac{1}{2A}\sum_{\mathbf{q}\neq 0}\sum_{\mathbf{k}\mathbf{k}'}\sum_{\sigma\sigma'} V_{\mathbf{q}}\hat{\psi}^{\dagger}_{\mathbf{k}'+\mathbf{q},\sigma'}\hat{\psi}^{\dagger}_{\mathbf{k}-\mathbf{q},\sigma}\hat{\psi}_{\mathbf{k},\sigma}\hat{\psi}_{\mathbf{k}',\sigma'},\end{aligned} \tag{5.35}$$

where N is the number of electrons contained in the area A (the contribution of N to the Hamiltonian is a constant term that can be ignored),

$$\hat{\rho}_{\mathbf{q}} = \int d^2r\, e^{-i\mathbf{q}\cdot\mathbf{r}}\hat{\rho}(\mathbf{r}) = \sum_{\mathbf{k}\mathbf{k}'}\sum_{\sigma\sigma'} V_{\mathbf{q}}\hat{\psi}^{\dagger}_{\mathbf{k},\sigma}\hat{\psi}_{\mathbf{k}+\mathbf{q},\sigma'} \tag{5.36}$$

is the Fourier transform of the electronic density $\hat{\rho}(\mathbf{r}) = \sum_{\sigma}\hat{\psi}^{\dagger}_{\sigma}(\mathbf{r})\hat{\psi}_{\sigma}(\mathbf{r})$, and $V_{\mathbf{q}}$ is the Fourier transform of the Coulomb potential[Mis08; MS20]:

$$V_{\mathbf{q}} = \frac{2\pi e^2}{\kappa}\frac{e^{-|\mathbf{q}|/\mathcal{K}}}{|\mathbf{q}|}, \tag{5.37}$$

expressed in the position basis as

$$V(\mathbf{r}) = \frac{e^2}{\kappa}\frac{1}{\sqrt{r^2 + (2\pi/\mathcal{K})^2}}, \tag{5.38}$$

where $\mathcal{K}$ is the UV cutoff of the system. The exponential damping in (5.37) avoids the need of introducing sharp cutoffs that uncomplete the Hilbert space, spoililng the consistency of the approach[Mis08]. In consequence, the total Hamiltonian of the system is given by

$$\begin{aligned} H = v &\sum_{\mathbf{k},\sigma,\sigma'} \hat{\psi}^{\dagger}_{\mathbf{k},\sigma} \left(\mathbf{k}\cdot\boldsymbol{\sigma}_{\sigma\sigma'}\right) \hat{\psi}_{\mathbf{k},\sigma'} \\ &+ \frac{1}{2A} \sum_{\mathbf{q}\neq 0} \sum_{\mathbf{k}\mathbf{k}'} \sum_{\sigma\sigma'} \hat{\psi}^{\dagger}_{\mathbf{k}'+\mathbf{q},\sigma'} \hat{\psi}^{\dagger}_{\mathbf{k}-\mathbf{q},\sigma} \hat{\psi}_{\mathbf{k},\sigma} \hat{\psi}_{\mathbf{k}',\sigma'}, \end{aligned} \tag{5.39}$$

The major effect of the introduction of interactions in the system of 2D massless Dirac fermions is the renormalization of the coupling $\alpha = e^2/\kappa v$ where v, the Fermi velocity, substitutes the speed of light c, suggesting to call it *graphene structure constant*. First order perturbative approaches propose that α runs with the energy as [GGV94; Mis08]:

$$\tilde{\alpha}(\omega) = \frac{\alpha}{1+\frac{\alpha}{4}\ln\left(\frac{E_{\mathrm{UV}}}{\omega}\right)}, \tag{5.40}$$

where $E_{\mathrm{UV}} = \mathcal{K}v$ is the kinetic energy evaluated at the UV cutoff. The running of α is actually due to the renormalization of the Fermi velocity[GGV94; Mis08]:

$$\frac{v(\omega)}{v} = 1 + \frac{\alpha}{4}\ln\left(\frac{\mathcal{K}v}{\omega}\right), \tag{5.41}$$

thus showing a logarithmic divergence when $k \to 0$, important to study particle-hole excitations (PHEs) in graphene and response functions such as the optical conductivity. Cyclotron mass measurements in suspended monolayer graphene have corroborated the logarithmic corrections to the Fermi velocity due to electron-electron interactions[Eli+11; Kot+12].

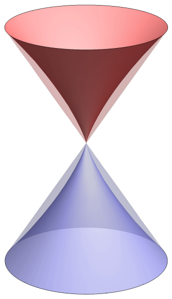

Figure 5.5: *Log-shaped Dirac cone*: Dirac cones after including self-energy corrections producing the log dependent Fermi velocity in (7.3) [GGV94]. Outer surface represent Dirac cones without corrections [Eli+11; Kot+12].

Further interaction effects are treated with different approaches such as Density Matrix Renormalization Group (DMRG) [Gol+16; PMR19; HL16], GW[Tre+08], Quantum Monte Carlo[Ben+18; Zha+21; MDF15], Self-Consistent Hartree-Fock (SCHF) (summarized in Appendix B), among many others. The next chapter addresses the problem of interacting 2D Dirac fermions with a new bosonization technique suited for gapless optical PHEs, and the Chapter 7 employs this technique to address the optical conductivity of interacting Dirac fermions.

6

BOSONIZATION OF THE Q = 0 CONTINUUM OF DIRAC FERMIONS

> *Science is a field which grows continuously with ever expanding frontiers. Further, it is truly international in scope. Any particular advance has been preceded by the contributions of those from many lands who have set firm foundations for further developments.*
>
> — John Bardeen [Bar72]

Among the main problems in condensed matter physics, the properties of strongly interacting systems constitutes one of the most difficult to be adressed. However, one-dimensional systems have been successfully studied in the non-perturbative regime using bosonization [Gia03], which relies on describing the low-energy physics of the system at the Fermi points as bosons representing oscillations about the equilibrium [Hal05]. On the contrary, the extensions of the formalism to higher dimensions is still an open problem [Lut79; Hal05; HM93; HKM00].

One of these methods [CNF94b; Hal05; HKM00] consists by assigning a boson to each PHE of the system, which are interpreted as fluctuations of the Fermi surface inside an energy shell λ as depicted in FIG. 6.1b. One excitation is then described by the creation of an out of the Fermi surface with the operator $c^{\dagger}_{\mathbf{k}+\mathbf{Q}/2}$, and the annihilation of a state inside the Fermi surface with the operator $c_{\mathbf{k}-\mathbf{Q}/2}$, interpreted also as the creation of a hole. Therefore, the PHE characterized by the wave vectors $\mathbf{k}$ and $\mathbf{Q}$ is described as the composite operator

$$b^{\dagger}_{\mathbf{k},\mathbf{Q}} = c^{\dagger}_{\mathbf{k}+\mathbf{Q}/2} c_{\mathbf{k}-\mathbf{Q}/2}. \tag{6.1}$$

The bosonization approach described in [CNF94b; Hal05; HM93; Lut79] can be obtained by promoting the above operators to a conventional set

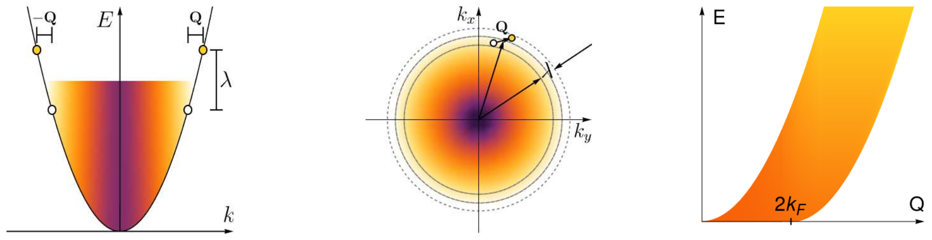

(a) (b) (c)

Figure 6.1: *particle-hole excitations (PHEs) in an usual Fermi liquid*: (a) A usual Fermi liquid with one band will present (b) an extended Fermi surface where the PHEs are produced with finite $\mathbf{Q}$[CNF94b]. (c) Particle-hole continuum showing no PHEs with $\mathbf{Q} = 0$.

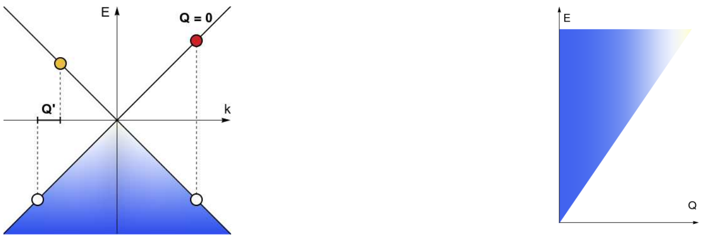

(a) (b)

Figure 6.2: *PHEs in a non-doped nodal semimetal*: (a) Both PHEs with $\mathbf{Q} = 0$ and $\mathbf{Q} \neq 0$ exist in the system, as shown in (b) by the particle-hole continuum with a pleny of states available in the subspace $\mathbf{Q} = 0$. [MS20].

of bosonic operators $b^{\dagger}_{\mathbf{k},\mathbf{Q}}$ whose commutator can be approximated as a number. The wave vector $|\mathbf{Q}| \ll k_F$ then describes a small displacement of the electron and the hole respect to the Fermi surface described by the Fermi momentum k_F. The bosonized Hamiltonian can be obtained by keeping the bosonic bilinear terms that couple only bosonic modes modes with $\mathbf{Q}$ and $-\mathbf{Q}$, i.e., bosons with momentum $\mathbf{Q}$ scatter only into other bosons with momentum $\mathbf{Q}$, or creates a pair with momenta $+\mathbf{Q}$ and $-\mathbf{Q}$. The idea is that even after this simplification the resulting model still captures the correct behavior of the interacting Fermi liquid for asymptotically small energies and wavevectors. This idea is central to the success of this higher dimensional bosonization.

The previous approach works well for systems with a finite Fermi momentum and then an extended Fermi boundary. The formalism present in this work is then natural extension of the previous procedure to the case when there is more than one band with gapless excitations near $\mathbf{Q} = 0$, as it is the case of Weyl or massless Dirac semimetals where the Fermi boundary has indeed shrunken to a point (see FIG. 6.2). Additionaly, two-band system host a set of non-trivial gapless optical $\mathbf{Q} = 0$ PHEs not accesible with known higher-dimensional bosonization procedures. One extension to this problem is proposed in [MS20], based on the separability of the Hilbert space so that $\mathbf{Q} = 0$ can be approximately separated from the sectors with $\mathbf{Q} \neq 0$ keeping the resuls of [CNF94b] of coupling $\mathbf{Q}$ and $-\mathbf{Q}$ sectors but in this case $\mathbf{Q} = 0$. The validity of the proposed bosonization approach in the separability of the Hilbert space is firmly supported in being consistent to the conventional Feynman diagrammatic perturbation theory. This approach is presented in the Appendix B, where the solution of the effective bosonic Hamiltonian for the optical particle-hole pairs is *exactly equivalent* to the Kadanoff-Baym (KB) Self-Consistent Hartree-Fock (SCHF) [BK61; Bay62] of the particle-hole propagator at $\mathbf{Q} = 0$.

This chapter discusses the bosonization technique presented in [MS20] in the context of PHEs of a undoped 2D system of massless Dirac fermions desbribed by the Hamiltonian in (5.39) introduced in the chapter 5.

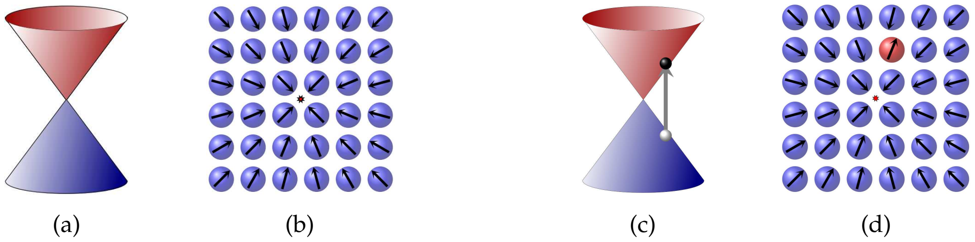
(a) (b) (c) (d)

Figure 6.3: *Creation of an electron-hole pair in* $\mathbf{Q} = 0$ *sector as the flipping of a pseudospin on a vortex configuration*: The grond state consists in (a) the Valence band (VB) completely filled up to the Dirac Point (DP) and the Conduction band (CB) empty, corresponding to (b) the pseudospin vortex pointing towards the DP. One PHE (c) leaves a hole in the VB while the corresponding electron occupies the CB at the same wave vector **k**, corresponding to (d) one pseudospin flip at site **k**.

6.1 EFFECTIVE HAMILTONIAN AND HILBERT SPACE

The microscopic Hamiltonian used to describe the system of 2D Dirac fermions is the effective Hamiltonian proposed in (5.39) ($\hbar = 1$):

$$\begin{aligned} H = {} & v \sum_{\mathbf{k},\sigma,\sigma'} \psi^\dagger_{\mathbf{k},\sigma} \left(\mathbf{k} \cdot \boldsymbol{\sigma}_{\sigma\sigma'}\right) \psi_{\mathbf{k},\sigma'} \\ & + \frac{1}{2A} \sum_{\mathbf{k}\mathbf{k}'} \sum_{\sigma\sigma'} V_{\mathbf{q}} \psi^\dagger_{\mathbf{k}'+\mathbf{q},\sigma'} \psi^\dagger_{\mathbf{k}-\mathbf{q},\sigma} \psi_{\mathbf{k},\sigma} \psi_{\mathbf{k}',\sigma'}, \end{aligned} \tag{6.2}$$

where A is the system area, and $V_{\mathbf{q}}$ is the Fourier transform of the interaction potential of (5.37):

$$V_{\mathbf{q}} = \frac{2\pi e^2}{\kappa} \frac{e^{-|\mathbf{q}|/\mathcal{K}}}{|\mathbf{q}|}, \tag{6.3}$$

The dispersion relation of the noninteracting system is depicted in FIG. 6.3a, where the upper (red) cone is the CB and the lower (blue) cone the VB. To simplify the description, the fermions are assumed moving in a 2D Torus $\mathbb{T}^2$ (see FIG. 2.5b) to quantize the momentum in a square lattice in the reciprocal space. At each site of the reciprocal lattice there exist four states: empty $|0\rangle_{\mathbf{k}}$, singly occupied $|\uparrow\rangle_{\mathbf{k}}, |\downarrow\rangle_{\mathbf{k}}$ and doubly occupied $|\uparrow\downarrow\rangle_{\mathbf{k}}$, and together they span the many-body Hilbert space as the tensor product of all the sites of the lattice:

$$\mathcal{H} = \bigotimes_{\mathbf{k}} \left(|0\rangle_{\mathbf{k}} \oplus |\uparrow\rangle_{\mathbf{k}} \oplus |\downarrow\rangle_{\mathbf{k}} \oplus |\uparrow\downarrow\rangle_{\mathbf{k}}\right). \tag{6.4}$$

The kinetic term in (6.2) produces no fluctuations between the occupancy of the momentum sites, and favors a ground state with singly occupied states with the pseudospin $\mathbf{s}_{\mathbf{k}} = \sum_{\sigma\sigma'} \psi^\dagger_{\mathbf{k}\sigma} \sigma_{\sigma\sigma'} \psi_{\mathbf{k}\sigma'}$ forming a vortex pointing towards the origin, i. e., the DP (see FIG. 6.3b). One excitation at a site **k** (FIG. 6.3c) can be seen as the flip of the pseudospin $|\downarrow\rangle_{\mathbf{k}} \to |\uparrow\rangle_{\mathbf{k}}$, shown in FIG. 6.3d as the red arrow pointing outwards.

The interactions are a form of pair hopping terms that have a finite amplitude to induce transitions into states with doubly occupied sites and empty sites. Crucially, the subspace of the Hilbert space with singly occupied sites is equivalent to the space of particle-hole pairs with zero total momentum, $\mathbf{Q} = 0$, while those states with doubly occupied and empty sites contain PHEs of finite momentum $\mathbf{Q}$.

6.2 EFFECTIVE HEISENBERG HAMILTONIAN

In this section we discuss in detail the projection of the Hamiltonian onto the singly-occupied Hilbert space $\mathcal{H}_{\text{sing}}$ as part of the bosonization formalism. Inspired by the decoupling of particle hole excitations with different $\mathbf{Q}$ in higher dimensional bosonization approaches, the Hamiltonian in (6.2) is projected onto the Hilbert space of singly occupied sites in the momentum lattice, depicted in FIG. 6.3b. This Hilbert space contains a spin-1/2 at each momentum site:

$$\mathcal{H}_{\text{sing}} = \bigotimes_{\mathbf{k}} \left(|\uparrow\rangle_{\mathbf{k}} \oplus |\downarrow\rangle_{\mathbf{k}} \right), \tag{6.5}$$

corresponding to $\mathbf{Q} = 0$ excitations only. We will denote the projector onto this subspace by $\mathcal{P}$. Our mathematical task is therefore to project the full interacting Hamiltonian from (6.2) onto the subspace $\mathcal{H}_{\text{sing}}$, which we will describe next.

To accomplish the projection we first need to eliminate the off-diagonal matrix elements that scatter electrons onto different momenta $\mathbf{Q}$ that would lead to doubly occupied or empty states in momentum. This leads us then to constraining the momentum transfer of the interaction term in (6.2) to a momentum site swapping

$$\psi^\dagger_{\mathbf{k}'+\mathbf{q}\sigma}\psi^\dagger_{\mathbf{k}-\mathbf{q}\sigma'}\psi_{\mathbf{k}\sigma'}\psi_{\mathbf{k}'\sigma} \to \psi^\dagger_{\mathbf{k}\sigma}\psi^\dagger_{\mathbf{k}'\sigma'}\psi_{\mathbf{k}\sigma'}\psi_{\mathbf{k}'\sigma}, \tag{6.6}$$

in order to stay inside $\mathcal{H}_{\text{sing}}$.

On the other hand, the fermion kinetic term can be expressed in terms of the pseudospin operator:

$$\mathbf{s}_{\mathbf{k}} = \sum_{\sigma\sigma'} \psi^\dagger_{\mathbf{k}\sigma}\boldsymbol{\sigma}_{\sigma\sigma'}\psi_{\mathbf{k}\sigma'}, \tag{6.7}$$

and similarly, the fermion bilinears in (6.6) can also be expressed by inverting the definition of the pseudospin operator (6.7), as follows:

$$\psi^\dagger_{\mathbf{k}\sigma}\psi_{\mathbf{k}\sigma'} = \frac{1}{2}\sum_{\mu=0}^{3} \sigma^{\mu}_{\sigma\sigma'} s^{\mu}_{\mathbf{k}}. \tag{6.8}$$

with $\sigma^0_{\sigma\sigma'} = \delta_{\sigma\sigma'}$ the identity matrix, and

$$s^0_{\mathbf{k}} = \sum_{\sigma\sigma'} \psi^\dagger_{\mathbf{k}\sigma}\delta_{\sigma\sigma'}\psi_{\mathbf{k}\sigma'} = n_{\mathbf{k}} = 1, \tag{6.9}$$

the particle number operator at site $\mathbf{k}$, constrained to be one in $\mathcal{H}_{\text{sing}}$. The interaction term can then be rearranged to match momentum labels and replaced them with spin operators yielding

$$\begin{aligned}\sum_{\sigma\sigma'}\psi^\dagger_{\mathbf{k}\sigma}\psi_{\mathbf{k}\sigma'}\psi^\dagger_{\mathbf{k}'\sigma'}\psi_{\mathbf{k}'\sigma} &= \frac{1}{4}\sum_{\mu\nu\sigma\sigma'}\sigma^\mu_{\sigma\sigma'}s^\mu_{\mathbf{k}}\sigma^\nu_{\sigma'\sigma}s^\nu_{\mathbf{k}'}\\ =\frac{1}{4}\sum_{\mu\nu}\text{tr}\,(\sigma^\mu\sigma^\nu)s^\mu_{\mathbf{k}}s^\nu_{\mathbf{k}'} &= \frac{1}{2}\sum_{\mu\nu}\delta^{\mu\nu}s^\mu_{\mathbf{k}}s^\nu_{\mathbf{k}'} = \frac{1+\mathbf{s}_{\mathbf{k}}\cdot\mathbf{s}_{\mathbf{k}'}}{2},\end{aligned}$$

where $\text{tr}\,(\sigma^\mu\sigma^\nu) = 2\delta^{\mu\nu}$. The identity in the last result corresponds to the occupation number at the sites $\mathbf{k}$ and $\mathbf{k}'$ and gives a constant term, while the second one describes a long-range Heisenberg exchange term between isospin operators.

Gathering the different terms previously described, we arrive at the form of the Hamiltonian from (6.2) projected onto the subspace of singly occupied sites in momentum space, which has the form of a Heisenberg model:

$$\mathcal{P}H\mathcal{P} = \sum_{\mathbf{k}} v\mathbf{k}\cdot\mathbf{s}_{\mathbf{k}} - \sum_{\mathbf{k}\neq\mathbf{k}'}\frac{V_{\mathbf{k}-\mathbf{k}'}}{4A}\mathbf{s}_{\mathbf{k}}\cdot\mathbf{s}_{\mathbf{k}'}. \tag{6.10}$$

where the first term is a Zeeman vortex field with the effective magnetic field $v\mathbf{k}$, thus making all the pseudospins points towards the DP in the ground state, and the second term is a long-range exchange coupling mediated by the effective coupling $J_{\mathbf{q}} = V_{\mathbf{q}}/4A$.

6.3 QUADRATIC BOSONIC HAMILTONIAN

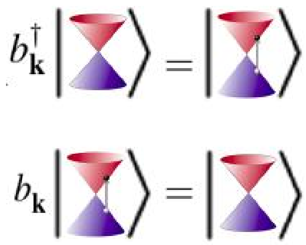

Figure 6.4: *Exciton creation and annihilation operators*: The new bosonic operators $b^{(\dagger)}_{\mathbf{k}}$ describe PHEs of 2D Dirac fermions as bosons in the 2D lattice.

Although this Hamiltonian is not exactly solvable, the fluctuations around the non-interacting state can be described by a Holstein-Primakov (HP) expansion in spin-wave approximation [Aue12]. To do so, we choose a spin basis that diagonalizes the kinetic energy at each momentum site, given by

$$\mathbf{s}_{\mathbf{k}} = -s^z_{\mathbf{k}}\hat{\mathbf{k}} + s^x_{\mathbf{k}}\hat{\mathbf{z}} + s^y_{\mathbf{k}}\hat{\boldsymbol{\phi}}, \tag{6.11}$$

which diagonalizes the kinetic term. On this basis, the Hamiltonian can be expanded in a bosonic representation (see FIG. 6.4) by means of the HP transformations:

$$\begin{aligned} s^z_{\mathbf{k}} &= 2\left(S - b^\dagger_{\mathbf{k}}b_{\mathbf{k}}\right) = 1 - 2b^\dagger_{\mathbf{k}}b_{\mathbf{k}},\\ s^x_{\mathbf{k}} &\approx \sqrt{2S}\left(b_{\mathbf{k}} + b^\dagger_{\mathbf{k}}\right) = b_{\mathbf{k}} + b^\dagger_{\mathbf{k}},\\ is^y_{\mathbf{k}} &\approx \sqrt{2S}\left(b_{\mathbf{k}} - b^\dagger_{\mathbf{k}}\right) = b_{\mathbf{k}} - b^\dagger_{\mathbf{k}}.\end{aligned} \tag{6.12}$$

The term corresponding to the exchange coupling in Eq. (6.10) can be transformed into pairing and hopping terms of bosons up to bilinears:

$$\begin{aligned} \mathbf{s}_{\mathbf{k}} \cdot \mathbf{s}_{\mathbf{k}'} \approx &\left(1 - 2b^{\dagger}_{\mathbf{k}} b_{\mathbf{k}} + 2b^{\dagger}_{\mathbf{k}'} b_{\mathbf{k}'}\right) \cos\phi_{\mathbf{k}\mathbf{k}'} \\ &+ \left(b^{\dagger}_{\mathbf{k}} b_{\mathbf{k}'} + b_{\mathbf{k}} b^{\dagger}_{\mathbf{k}'}\right) \left(1 + \cos\phi_{\mathbf{k}\mathbf{k}'}\right) \\ &+ \left(b^{\dagger}_{\mathbf{k}} b^{\dagger}_{\mathbf{k}'} + b_{\mathbf{k}} b_{\mathbf{k}'}\right) \left(1 - \cos\phi_{\mathbf{k}\mathbf{k}'}\right). \end{aligned} \tag{6.13}$$

The resulting bosonic Hamiltonian after the HP transformations is:

$$\begin{aligned} H_{HP} = &\sum_{\mathbf{k}} 2v|\mathbf{k}| b^{\dagger}_{\mathbf{k}} b_{\mathbf{k}} + \sum_{\mathbf{k}\neq\mathbf{k}'} \frac{V_{\mathbf{k}-\mathbf{k}'}}{A} b^{\dagger}_{\mathbf{k}} b_{\mathbf{k}} \cos\phi_{\mathbf{k}\mathbf{k}'} \\ &- \sum_{\mathbf{k}\neq\mathbf{k}'} \frac{V_{\mathbf{k}-\mathbf{k}'}}{4A} \left(1 + \cos\phi_{\mathbf{k}\mathbf{k}'}\right) \left(b^{\dagger}_{\mathbf{k}} b_{\mathbf{k}'} + b_{\mathbf{k}} b^{\dagger}_{\mathbf{k}'}\right) \\ &- \sum_{\mathbf{k}\neq\mathbf{k}'} \frac{V_{\mathbf{k}-\mathbf{k}'}}{4A} \left(1 - \cos\phi_{\mathbf{k}\mathbf{k}'}\right) \left(b^{\dagger}_{\mathbf{k}} b^{\dagger}_{\mathbf{k}'} + b_{\mathbf{k}} b_{\mathbf{k}'}\right). \end{aligned} \tag{6.14}$$

The first line contains the kinetic and self-energy terms. The second line can be viewed as boson hopping terms in the momentum lattice. The third line can be viewed as pairing terms which change the number of bosons.

It is convenient to re-express the Hamiltonian in a Bogoliubov-Valatin (BV) basis given by

$$B^{\dagger}_{\mathbf{k}} = \begin{pmatrix} b^{\dagger}_{\mathbf{k}} & b_{\mathbf{k}} \end{pmatrix}, \tag{6.15}$$

the Hamiltonian can be expressed as

$$H_{HP} = \sum_{\mathbf{k},\mathbf{k}'} B^{\dagger}_{\mathbf{k}} H_{\mathbf{k}\mathbf{k}'} B_{\mathbf{k}'}. \tag{6.16}$$

The matrix elements $H_{\mathbf{k}\mathbf{k}'}$ are given by

$$H_{\mathbf{k}\mathbf{k}'} = \delta_{\mathbf{k}\mathbf{k}'} \begin{pmatrix} 2E_{\mathbf{k}} & 0 \\ 0 & -2E_{\mathbf{k}} \end{pmatrix} - T_{\mathbf{k}\mathbf{k}'}, \tag{6.17}$$

where $E_{\mathbf{k}} = v|\mathbf{k}| + \Sigma_{\mathbf{k}}$ is the bare kinetic energy dressed by the Hartree-Fock (HF) self-energy given by:

$$\Sigma_{\mathbf{k}} = \frac{1}{2A} \sum_{\mathbf{p}} V_{\mathbf{k}-\mathbf{p}} \cos\phi_{\mathbf{k}\mathbf{p}}, \tag{6.18}$$

and $T_{\mathbf{k}\mathbf{k}'}$ is the matrix describing hoppings and pairings:

$$T_{\mathbf{k}\mathbf{k}'} = \frac{V_{\mathbf{k}-\mathbf{k}'}}{4A} \begin{pmatrix} 1 + \cos\phi_{\mathbf{k}\mathbf{k}'} & 1 - \cos\phi_{\mathbf{k}\mathbf{k}'} \\ 1 - \cos\phi_{\mathbf{k}\mathbf{k}'} & 1 + \cos\phi_{\mathbf{k}\mathbf{k}'} \end{pmatrix}. \tag{6.19}$$

The system can therefore be understood as a collection of excitons, composite bosons created as the bound state of an electron and a hole by the Coulomb attraction between them. The matrix in (6.19) then describes the hopping and pairing interactions between the electrons.

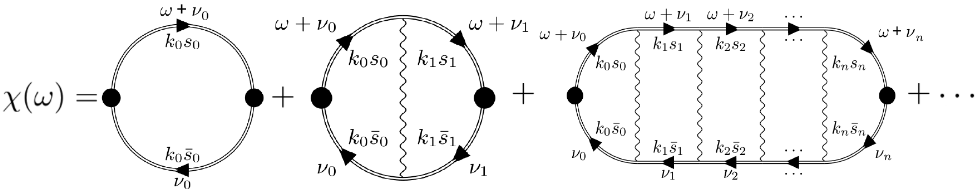

Figure 6.5: *Particle-hole operator by* KB SCHF *resummation*: The propagator of a coherent particle-hole pair with interactions is described by a Bathe-Salpeter ladder that connects one by one the particle and hole dressed propagators (including the correspoding HF self-energies. $\chi(\omega)$ is equivalent to the propagator of the modes obtained from the bosonized Hamiltonian (6.16).

6.4 CONNECTION TO DIAGRAMATIC PERTURBATION THEORY

This section discusses the connection between the bosonization framework developed in the previous sections and the traditional Feynman diagrammatic methods of many-body theory. We will demonstrate here that the solution of the bilinear bosonized Hamiltonian in (6.16) is equivalent to the calculation of the electron-hole propagator by means of the KB resummation of the Feynman diagrams resulted from the SCHF approximation of the single-particle Green function that incorporates the self-energy corrections. The boson creation operator $b^\dagger_{\mathbf{k}}$ introduced by the HP transformation in (6.12) correspods to the creation of a $\mathbf{Q} = 0$ interband particle-hole $b^\dagger_{\mathbf{k}} = \psi^\dagger_{\mathbf{k}+}\psi_{\mathbf{k}-}$, where the subindex $s = +, -$ denotes respectively the CB and VB according to the pseudospin-band transformation presented in (5.33). In other words, we will argue that the propagator of the modes obtained from the bosonized Hamiltonian in (6.16) is equivalent to the particle-hole propagator within the KB SCHF resummation.

The coherent propagation of an electron in the CB and the corresponding hole in the VB is given by:

$$\chi^{s_1s_2}_{\mathbf{k}_1\mathbf{k}_2}(t) = -iT\left\langle \psi^\dagger_{\mathbf{k}_1s_1}(t)\psi_{\mathbf{k}_1\bar{s}_1}(t)\psi^\dagger_{\mathbf{k}_2\bar{s}_2}(0)\psi_{\mathbf{k}_2s_2}(0)\right\rangle. \tag{6.20}$$

The Appendix B presents an explicit calculation where all the terms of the KB SCHF resummation are taken into account by means of a Bethe-Salpeter ladder series, in which all the internal one-particle Green functions

$$G^{s_1s_2}_{\mathbf{k}}(\omega) = \mathbf{k}s_1 \bullet\!\!\longrightarrow\!\!\bullet\, \mathbf{k}s_2 = \frac{\delta_{s_1s_2}}{\omega - s_1(E_{\mathbf{k}} - i\eta)}. \tag{6.21}$$

have been dressed with the HF self-energies as dictated by SCHF[BK61; Bay62], and $i\eta$ is the standard infinitesimal imaginary frequency that regularizes the time-ordered propagator[GV05]. These are the propagators that we use to construct the *sides* of the Bethe-Salpeter ladder, as shown in FIG. 6.5.

The zeroth order of the Bethe-Salpeter ladder is the dressed non-interacting diagram shown from left to right in FIG. 6.5, whose mathematical expression is:

$$\chi^{(0)s_0s_1}_{\mathbf{k}_0\mathbf{k}_1}(\omega) = -\delta_{\mathbf{k}_0\mathbf{k}_1}\delta_{s_0s_1}\left(\frac{\delta_{s_0,1} - \delta_{s_0,-1}}{\omega - 2s_0(E_{\mathbf{k}_0} - i\eta)}\right). \tag{6.22}$$

The next term is the first order ladder in the series, where the interaction matrix (6.19) has been introduced as band-conserving and changing processes; its mathematical expression is (B.13) in the Appendix B. The n-th term is the multiplication from the left and the right of the interaction matrix in (6.19); its expression is (B.13).

From the fact that, after having integrated over internal intermediate frequencies v_i (see FIG. 6.5 where v_i describe the frequencies of the hole propagators), the intermediate Green functions are all constrained to satisfy $s = s'$, meaning that the intermediate pairs always have one electron in the CB and the other in the VB. The series shown in FIG. 6.5 can be expressed as a matrix geometric series involving $\chi^{(0)}{}^{s_0 s_1}_{\mathbf{k}_0\mathbf{k}_1}$ in (6.22) and $T^{s_0 s_1}_{\mathbf{k}_0\mathbf{k}_1}$ in (6.19):

$$\chi(\omega) = \chi^0(\omega) + \chi^0(\omega)T\left(\chi^0(\omega) + \chi^0(\omega)T\chi^0(\omega) + \cdots\right),$$

whose solution has the form:

$$\chi^{-1}_{\mathbf{k}_0\mathbf{k}_f}(\omega) = -(\omega - i\eta)\tau^z\delta_{\mathbf{k}_0\mathbf{k}_f} - H_{\mathbf{k}_0\mathbf{k}_f}, \tag{6.23}$$

where $H_{\mathbf{k}_0\mathbf{k}_f}$ is given in (6.17) and τ^z is the diagonal Pauli matrix within the $2x2$ BV indices introduced in (6.15). The structure of this correlator is equal to the propagator of the HP bosons of the Hamiltonian (6.17). The above leads us therefore to conclude that the exciton propagator calculated using the Bethe-Salpeter ladder, in FIG. 6.5, has an identical effective Hamiltonian to the one obtained from the HP bosonic Hamiltonian in (6.17), demonstrating that the bosonized Hamiltonian is equivalent to self-consistent KB resummation of the particle-hole propagator.

6.5 PARAMETRIZATION OF THE RECIPROCAL SPACE

Although the fermion system was assumed with finite size so that the reciprocal space can be described by a discrete lattice, it is desirable to re-express the problem in a lattice that makes rotational symmetry manifest to exploit this symmetry of the thermodynamic limit. Consequently, it is convenient to perfom a reparametrization of the reciprocal lattice so that it holds the symmetries the system already exhibits in the kinetic and potential terms of (6.2) and (6.16).

6.5.1 *Coordinate transformation*

The Appendix D discusses the lattice parametrization in more detai, but we review the key points of the re-parametrization here. The reciprocal space can be reparametrize by a new coordinate $\mathbf{z}(\mathbf{k})$ that labels the sites in the quadratic form of the boson Hamiltonian in the new lattice:

$$H_{HP} = \sum_{\mathbf{z},\mathbf{z}'} B^\dagger_{\mathbf{z}} H_{\mathbf{z}\mathbf{z}'} B_{\mathbf{z}'}, \tag{6.24}$$

the coordinate transformation must preserve the underlying microscopic normalization of the states. This is satisfied if the boson operators and the Hamiltonian in the new lattice are rescaled as follows:

$$B_{\mathbf{z}} = J(\mathbf{z}) B_{\mathbf{k}}, \quad H_{\mathbf{z}\mathbf{z}'} = J(\mathbf{z}) J(\mathbf{z}') H_{\mathbf{k}\mathbf{k}'}, \tag{6.25}$$

where $J(\mathbf{z}'(\mathbf{k}))$ is the Jacobian of the transformation $\mathbf{z}(\mathbf{k})$:

$$J(\mathbf{z}) = \sqrt{D(\mathbf{z}) \left(\frac{\Delta z_1 \Delta z_2}{\Delta k_1 \Delta k_2} \right)}, \tag{6.26}$$

$\Delta k_i = 2\pi / L_i$ is the spacing in the square lattice (FIG. 6.6a), and Δz_i are the spacings in the new coordinate system (see Appendix D for details).

6.5.2 *Polar parametrization*

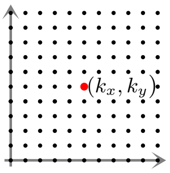

(a) Cartesian lattice

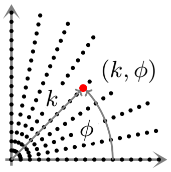

(b) Polar lattice

Figure 6.6: *Coordinate systems in the reciprocal space*: (a) Squared lattice in which the bosonization technique was initially proposed, and (b) polar lattice (k_m, ϕ_n) that displays the rotational symmetri of interacting 2D Dirac fermions in graphene.

The rotational invariance in the thermodynamic limit can be captured with the following polar parametrization $\mathbf{z} = (k, \phi)$ shown in FIG. 6.6b:

$$k_m = \frac{\mathcal{K}}{\sqrt{2}} \tan^2(m\Delta\theta), \quad \phi_n = n\Delta\phi, \tag{6.27}$$

where (k_m, ϕ_n) are the polar coordinates of a given site in the polar momentum lattice depicted in FIG. 6.6b, $\mathcal{K}$ is the Ultraviolet (UV) momentum scale, $\Delta\theta = (\pi/2)/(M+1)$, $\Delta\phi = 2\pi/(2L+1)$, and $n = 0, ..., 2L$, $m = 1, ..., M$. The radial discretization in (6.27) has been chosen to have a faster numerical convergence at low energies than a uniform radial coordinate $k_m = m\Delta\theta\mathcal{K}$ because (6.27) is denser at small k and more dilute at large k. Nevertheless, we have verified explicitly by chaging the function in (6.27) that our results described below are independent of the specific choice of the radial discretization once the grids become sufficiently dense, as it is shown in the next sections of this chapter. Notice also that the parametrization 6.27 does not implement a hard cutoff but the largest momentum apporaches infinity as $M \to \infty$. The UV cutoff is implemented by the Coulomb potential (6.3) following [Mis08].

6.5.3 *Angular momentum channels*

The polar lattice allows to exploit the rotational invariance by allowing to block-diagonalize the Hamiltonian by angular momentum channels ℓ. By applying the transformation from Eq. (6.25) to the boson Hamiltonian from

Eq. (6.24) and further using the angular Fourier transform in (D.17), the Hamiltonian in (6.24) is transformed into:

$$B_m^{\ell} = \sum_{\ell=-L}^{L} e^{i\ell\phi_n} B_{mn}, \tag{6.28a}$$

$$H_{HP} = \sum_{m\ell} B_m^{\ell\dagger} H_{mm'}^{\ell} B_{m'}^{\ell}, \tag{6.28b}$$

made up of $2L+1$ independent Hamiltonians of 1D bosonic systems spanning the remaining radial coordinate. Therefore the problem reduces to a set of bosons moving in an effective one dimensional space for each angular momentum channel which in general needs to be solved numerically.

6.6 DISCUSSION AND SUMMARY

A formalism to address non-perturbative effects in the sector $\mathbf{Q} = 0$ of PHEs of 2D Dirac fermions has been introduced. It is constructed by projecting the Hamiltonian (6.2) into the Hilbert subspace of singly-occupied states in the momentum lattice, resulting in an effective spin-1/2 Heisenberg model describing the dynamics of the pseudospins $\mathbf{s_k} = \sum_{\sigma\sigma'} \psi^{\dagger}_{\mathbf{k}\sigma} \sigma_{\sigma\sigma'} \psi_{\mathbf{k}\sigma'}$, one located at each site of the momentum lattice. This model is then mapped into a system of Hard-core Bosons (HCBs) by means of the HP transformations that replaces each pseudospin operator $\mathbf{s_k}$ by a boson at the same site $\mathbf{k}$. When the pseudospin points towards the DP, there is no boson at $\mathbf{k}$, and when the pseudospin points away from the DP we have one boson at $\mathbf{k}$.

To support the validity of this approach, we showed that the KB resummation of the particle-hole propagator associated with the SCHF approximation to the single particle Green function of the fermionic Hamiltonian (6.2), is equivalent to the propagator of the bosonic modes obtained from the bosonized Hamiltonian (6.16). We expect that this formalism captures the low-energy properties of the semi-metallic phase that evolves adiabatically from the free fermions upon increasing the strength of electron-electron interactions.

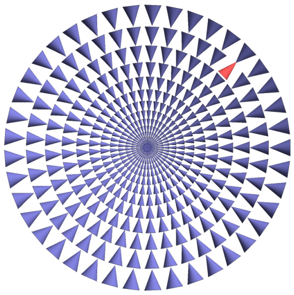

Figure 6.7: *Zeeman vortex in the polar lattice*: The reparametrization of the square to the polar lattice allows to incorporate the symmetries in the thermodynamic limit. The PHE is displayed as the red arrow flipped respect to the ground state represented as the Zeeman vortex around the DP.

In the next chapter, the bosonization technique presented here will be applied to the calculation of the optical conductivity of 2D interacting Dirac fermions. We will indeed find that the method is able to not only reproduce the previous results in the literature obtained perturbatively, but also captures non-perturbative effects that opens the possibility to address strongly-interacting systems from this picture of excitonic bosonized Hamiltonians in higher dimensions.

7

NON-PERTURBATIVE CORRECTIONS TO THE OPTICAL CONDUCTIVITY OF 2D DIRAC FERMIONS

> *The scientist's inquiry into the causes of things is providing an ever more extensive understanding of nature. In consequence, science is more important than ever for industrial technology.*
>
> — Kenneth G. Wilson [Wil96]

One of the most remarkable physical properties of 2D Dirac fermions studied in the previous chapter about graphene is the value of their *optical conductivity*, in terms of fundamental constants of nature[Mis08; Kat12]:

$$\sigma_0 = 4 \times \frac{e^2}{16\hbar}, \tag{7.1}$$

where the factor 4 is due to the *spin-valley* degeneracy (see §5.3). This result is described in the Appendix C using the *pseudospin precession formalism*. This prediction has been corroborated in experiments measuring the transmitivity, proportional to the optical conductivity[Kat12], finding values very close to the non-interacting fermions [Li+08; Mak+08; Nai+08].

Interactions can be accounted for perturbatively using the two Feynman diagrams shown in FIG. 7.2 describing the first-order self-energy and vertex corrections to the particle-hole propagator using several methods such as Kubo formula, polarization operator, kinetic theory[Mis08] among others, yielding the relative correction $\tilde{\sigma}(\omega)$ of the optical conductivity

$$\tilde{\sigma}(\omega) = \frac{\sigma(\omega) - \sigma_0}{\sigma_0} = \frac{C\alpha}{1 + \frac{\alpha}{4}\ln\left(\frac{\mathcal{K}v}{\omega}\right)}, \tag{7.2}$$

as a consequence of the renormalization of the Fermi velocity in (5.41) [GGV94]:

$$\frac{v(\omega)}{v} = 1 + \frac{\alpha}{4}\ln\left(\frac{\mathcal{K}v}{\omega}\right). \tag{7.3}$$

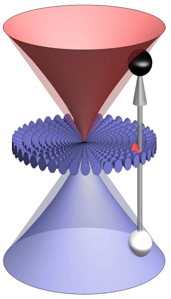

Figure 7.1: *PHE in the Dirac cone*: Creation of a PHE (exciton) as the flip of the pseudospin at site **k** (in-plane red arrow), bosonized as a Hard-core Boson (HCB) using the formalism of chapter 6.

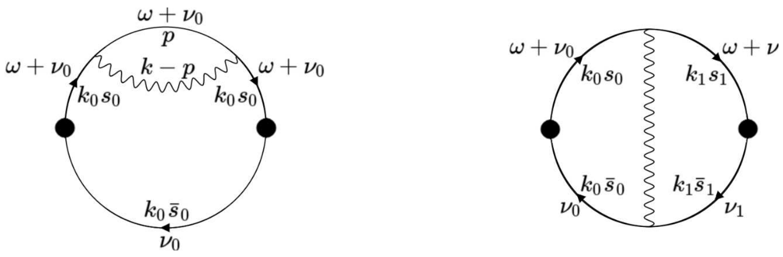

(a) Self-energy.

(b) Vertex.

Figure 7.2: *Self-energy and vertex corrections to the conductivity* $\sigma(\omega)$: First order diagrams involved in the perturvative calculation of the optical conductivity $\sigma(\omega)$ and the polarization $\Pi(\omega, q)$. Adapted from [Mis08].

It is worth noting that there was considerable disagreement in the earlier literature regarding the value of the constant C in (7.2). One of the calculations performed by Herbut *et al.* in [HJV08] obtained that:

$$C = \frac{25 - 6\pi}{12} \approx 0.51. \tag{7.4}$$

However another calculation performed by Mishchenko in [Mis08] obtained instead the following value:

$$C = \frac{19 - 6\pi}{12} \approx 0.01. \tag{7.5}$$

Mishchenko in [Mis08] argued that different methods (polarizability, Kubo formula, kinetic equation) can differ unless the Ultraviolet (UV) cutoff is implemented appropriately. We have indeed followed the spirit of this important point emphasized in [Mis08] when we introduced the Coulomb potential was introduced in (5.37). Further studies [SS09; Abe+11; SF12; Gaz+13; Bar+14b; TK14; TK18] have supported that the conclusions of value of C reached in [Mis08] are correct, and that contrary results are ultimately mistaken. On the other hand, non-perturbative approaches have been scarse. One approach using Quantum Monte Carlo [Boy+16] to calculate the optical conductivity suggests that interection corrections are still small for even couplings as large as $\alpha \sim 2$.

Our bosonization technique introduced in Chapter 6 and [MS20] recovers the result of [Mis08; SS09; Abe+11; SF12; Gaz+13; Bar+14b; TK14; TK18] for weak interactions $\alpha \ll 1$ from non-pertutbative results that extend to finite α that are also in agreement with the Quantum Monte Carlo approaches [Boy+16] and the experimental observations [Li+08; Mak+08; Nai+08]. Additionaly, this chapter discusses the treatment of the optical conductivity in the framework of bosonization as well as the numerical aspects, such as the Infrared (IR) regularization of the potential, in order to get the corrections $\tilde{\sigma}(\omega)$.

7.1 OPTICAL CONDUCTIVITY

The bosonization formalism presented in Chapter 6 will be applied to the calculation corrections of the optical conductivity $\sigma(\omega)$ of Dirac fermions interacting via Coulomb forces. The optical conductivity will be calculated from the current-current correlator using the Kubo approach[GV05]:

$$\chi_{\mu\nu}(t) = i\Theta(t)A\left\langle\left[j_\mu(t), j_\nu(0)\right]\right\rangle. \tag{7.6}$$

The current operator can be expressed as the pseudospin operator times the Fermi velocity:

$$\mathbf{j} = \frac{v}{A}\sum_{\mathbf{k}}\psi^\dagger_{\mathbf{k}\sigma_1}\boldsymbol{\sigma}_{\sigma_1\sigma_2}\psi_{\mathbf{k}\sigma_2} = \frac{v}{A}\sum_{\mathbf{k}}\hat{\mathbf{s}}_{\mathbf{k}}. \tag{7.7}$$

The above expression is exact and we would like to emphasize that this opeators carries a total momentum $\mathbf{Q} = 0$, and therefore it is an operator that can be represented within the Hilbert subspace $\mathcal{H}_{\text{sing}}$ in (6.5). The current operator is then expressed in the axes system introduced in (6.11):

$$\mathbf{j} = \frac{v}{A}\sum_{\mathbf{k}}\left(-s^z_{\mathbf{k}}\hat{\mathbf{k}} + s^x_{\mathbf{k}}\hat{\mathbf{z}} + s^y_{\mathbf{k}}\hat{\boldsymbol{\phi}}\right). \tag{7.8}$$

7.1.1 *Bosonized current operator and susceptibility*

After applying the Holstein-Primakov (HP) expansion for the pseudospin operators presented in (6.12), the current can be expanded in powers of bosonic operators, beng the leading order linear in $b^\dagger_{\mathbf{k}}$:

$$\mathbf{j} \approx v\sum_{\mathbf{k}} s^y_{\mathbf{k}}\hat{\boldsymbol{\phi}} = v\sum_{\mathbf{k}} i(b^\dagger_{\mathbf{k}} - b_{\mathbf{k}})\hat{\boldsymbol{\phi}} = v\sum_{\mathbf{k}} iB^\dagger_{\mathbf{k}}\mathbf{I}\hat{\boldsymbol{\phi}}, \tag{7.9}$$

with the vector $\mathbf{I} = \text{diag}(\mathbb{I}) = (1, -1)^{\mathrm{T}}$ the diagonal of the Bogoliubov-Valatin (BV) commutator matrix (D.4), needed in order to represent the current operator as a superposition of the BV boson $B^\dagger_{\mathbf{k}}$.

The real part of the optical conductivity can be ontained from the imaginary part of the susceptibility

$$\chi_{\mu\nu}(t) = i\Theta(t)A\left\langle\left[j_\mu(t), j_\nu(0)\right]\right\rangle, \tag{7.10}$$

where $\mu, \nu = x, y$. Due to the large symmetry of the problem, it is sufficient to compute only the x-component of the current density without loss of generality:

$$j_x = v\sum_{\mathbf{k}} i\mathbf{I}^{\mathrm{T}}B_{\mathbf{k}}\sin\phi_{\mathbf{k}}. \tag{7.11}$$

The j_x is then reexpressed in terms of the new polar lattice in (6.27):

$$j_x = i\frac{v\mathcal{K}\sqrt{\Delta\theta\Delta\phi}}{2\pi\sqrt{A}}\sum_{mn} S_m B_{mn}\sin\phi_n, \tag{7.12}$$

where $n \in \{-L, \cdots, +L\}$, and $m \in \{1, \cdots, 2M\}$, spanning the BV operator

$$[B_m^{\ell\dagger}] = \begin{pmatrix} b_{0n}^\dagger & \cdots & b_{Mn}^\dagger & b_{0n} & \cdots & b_{Mn'} \end{pmatrix} \tag{7.13}$$

and the Jacobian of the transformation has been combined with the vector **I** as follows

$$[S_m] = \begin{pmatrix} t_0 & \cdots & t_M & -t_0 & \cdots & -t_M \end{pmatrix}. \tag{7.14}$$

with $t_m = \sqrt[3]{\tan(\theta_m)}\sec(\theta_m)$. Next, the current $j_{x\phi}$ is reexpressed in terms of the angular momentum channels after applying the angular Fourier transform (D.17) to the bosons. Because the current transforms as a vector under rotations, the calculation of the conductivity only requires solving the boson bilinear Hamiltonian (6.28) for the angular momentum channels $\ell = \pm 1$. This can also be seen in (7.11) where the $\sin\phi_{\mathbf{k}}$ factor selects the channels $\ell = \pm 1$. Then, the current operator is finally expressed as

$$j_x = i\frac{v\mathcal{K}\sqrt{\Delta\theta}}{2\sqrt{2\pi A}}\sum_m S_m(B_m^1 - B_m^{-1}). \tag{7.15}$$

The corresponding susceptibility is given by

$$\begin{aligned} \chi_{xx}(t) = {} & i\Theta(t)\frac{v^2\mathcal{K}^2\Delta\theta}{8\pi}\times \\ & \times\sum_{mm'}\left(S_m\left\langle\left[B_m^1(t), B_{m'}^{1\dagger}(0)\right]\right\rangle S_{m'} + S_m\left\langle\left[B_m^{-1}(t), B_{m'}^{-1\dagger}(0)\right]\right\rangle S_{m'}\right). \end{aligned} \tag{7.16}$$

but from the fact that the system has inversion symmetry it follows that $\ell = 1$ and $\ell = -1$ yield the same contributions, and therefore the expression of the susceptibility in terms of the BV bosons is

$$\chi_{xx}(t) = i\Theta(t)\frac{v^2\mathcal{K}^2\Delta\theta}{8\pi}\sum_{mm'} S_m\left\langle\left[B_m^1(t), B_m^{1\dagger}(0)\right]\right\rangle S_{m'}. \tag{7.17}$$

7.1.2 *Susceptibility in terms of the eigenstates*

To proceed we diagonalize the Hamiltonian (**??**) for the $\ell = 1$ angular momentum channel via a BV transformation, expressed as follows:

$$B_m^1 = \sum_n R_{mn} D_n, \tag{7.18a}$$

$$H_{mm'}^1 = \sum_{nn'} R_{mn}\Omega_{nn'}R_{n'm'}^*, \tag{7.18b}$$

where $\Omega_{nn'} = \operatorname{diag}\begin{pmatrix}\omega_0 & \cdots\omega_M & -\omega_0 & \cdots -\omega_M\end{pmatrix}$ is the diagonal matrix of the eigenvalues of the $\ell = 1$ block of the HP Hamiltonian in (6.28) [Hem80].

Replacing such transformations in Eq. (7.17) and dropping the subindices we get

$$\chi(t) = i\Theta(t)\frac{v^2\mathcal{K}^2\Delta\theta}{8\pi}\sum_{mn} e^{-i\Omega_{nn}t} S_m R_{mn} \left\langle \left[D^1_n \,, D^{1\dagger}_{n'} \right] \right\rangle R^*_{n'm'} S_{m'}. \tag{7.19}$$

which, because of $\left\langle \left[D^1_n \,, D^{1\dagger}_{n'} \right] \right\rangle = \mathbb{I}_{nn'}$ ($\mathbb{I}$ is the BV commutator matrix in (D.4)), yields

$$\chi(t) = i\Theta(t)\frac{v^2\mathcal{K}^2\Delta\theta}{8\pi}\sum_{mn} e^{-i\Omega_{nn}t} S_m R_{mn} \mathbb{I}_{nn'} R^*_{n'm'} S_{m'}. \tag{7.20}$$

Then, we take the Fourier transform of $\chi(t)$ to get the frequency-dependent susceptibility

$$\chi(\omega) = \frac{v^2\mathcal{K}^2\Delta\theta}{8\pi}\sum_{mn} \frac{S_m R_{mn} \mathbb{I}_{nn'} R^*_{n'm'} S_{m'}}{\omega - \Omega_{nn} + i\eta} \tag{7.21}$$

Finally, we take the imaginary part of Eq. (7.21) to get the optical conductivity depending on frequency as the following Lehmann-type representation[GV05]:

$$\begin{aligned} \sigma(\omega) &= -\frac{e^2}{\omega}\mathrm{Im}[\chi(\omega)] \\ &= \frac{v^2\mathcal{K}^2\Delta\theta}{4}\sum_m \left| \sum_n R^*_{mn} S_n \right|^2 \frac{\delta(\omega - \omega_m)}{\omega_m}. \end{aligned} \tag{7.22}$$

7.1.3 *Regularization of the Lehman representation*

In the Lehmann representation, or *exact eigenstates representation*[GV05], $\mathrm{Im}[\chi(\omega)]$ consists of a train of Dirac delta functions in the frequency axis, each one corresponding to one of the eigenvalues of the Hamiltonian so that only at those energies there is a contribution to the susceptibility. In the thermodynamic limit where the spectrum becomes dense these delta functions merge and in the thermodynamic limit will yield a continuous function. However, in system with a discrete number of levels, the discreteness of the Dirac deltas remains and require to be regularize for numerical purposes. Here we do a simple regularization by replacing each Dirac delta by rectangular distributions with width $\Delta\omega_m = \omega_m - \omega_{m-1}$ and height $1/\Delta\omega_m$, between two adjacent energy levels ω_m and ω_{m-1} assuming the ordering $\omega_m > \omega_{m-1}$. In this way, the conductivity is replaced by the following approximate form:

$$\sigma(\omega_m) = \frac{v^2\mathcal{K}^2\Delta\theta}{4}\frac{|\sum_n R^*_{mn} S_n|^2}{\omega_m(\omega_m - \omega_{m-1})}. \tag{7.23}$$

7.2 NUMERICAL APPROACH: IR REGULARIZATION AND SYSTEM SIZE EFFECTS

To perform numerical calculations, it is convenient to use a Coulomb interaction that has an explicit short distance or UV, and long distance or IR, regularization of the form:

$$V_{\mathbf{q}} = \frac{2\pi e^2}{\kappa}\left(\frac{e^{-|\mathbf{q}|/\mathcal{K}} - e^{-|\mathbf{q}|/\mathcal{K}_{\mathrm{IR}}}}{|\mathbf{q}|}\right), \tag{7.24}$$

where $\mathcal{K}$ is the large momentum cutoff and $\mathcal{K}_{\mathrm{IR}}$ is the small momentum cutoff. Physically $\mathcal{K}$ is of the order of the inverse lattice spacing and $\mathcal{K}_{\mathrm{IR}}$ can be literally viewed as controlled by the inverse distance to a metallic plane where image charges are produced. Throughout the numerical analysis, the UV cutoff $\mathcal{K}$ is set to be the unit of momentum, and $v\mathcal{K}$ the unit of frequency.

The focus of the work is on results that are universal and independent of these limits. To do so, only the information that numerically remains invariant under the change of the IR cutoff has been extracted. We describe the details of this procedure in the next subsections. The study of the effects that explicitly depend on the IR cutoff might be physically meaningful in the sense that they might allow to model the modifications produced by a nearby screening gate, however they are not the focus of our current work.

7.2.1 *Discretization size dependence*

The calculation of the corrections to optical conductivity $\tilde{\sigma}(\omega)$ consists in solving the 1D bosonic BV Hamiltonian (6.28) in the angular momentum channel $\ell = 1$. This is done using exact diagonalization of the $2M \times 2M$ matrix generated with the radial coordinate

$$k_m = \frac{\mathcal{K}}{\sqrt{2}}\tan^2(\theta_m) = \frac{\mathcal{K}}{\sqrt{2}}\tan^2\left(\frac{\pi/2}{M+1}\right), \tag{7.25}$$

where M is the number of cuts done along the radial coordinate, chosen in the range from $M = 10^2$ to 10^4. As an illustrative example, FIG. 7.3 displays the behavior of the conductivity as a function of M for $\alpha = 1$.

The evident size effects on $\tilde{\sigma}(\omega)$ reinforces the need of taking the thermodynamic limit $M \to \infty$. This extrapolation is done using the dataset $10^3 \leq M \leq 10^4$, by fitting a linear function that depends on $1/M$:

$$\tilde{\sigma}(\omega, M) = \tilde{\sigma}(\omega) + \frac{\Delta\tilde{\sigma}(\omega)}{M}. \tag{7.26}$$

The robustness of the extrapolation was ensured by using a second dataset, $6 \times 10^3 \leq M \leq 10^4$, to verify that $\tilde{\sigma}(\omega)$ extracted from the linear fitting for both extrapolations lie on top of each other with the essentially the same values.

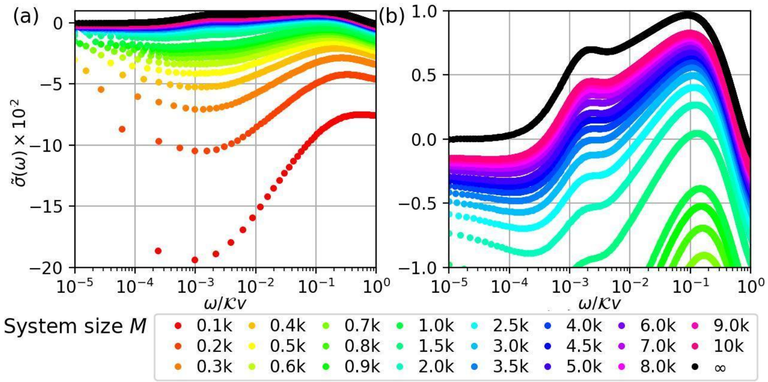

Figure 7.3: *System size effects on* $\tilde{\sigma}(\omega)$: Optical conductivity $\tilde{\sigma}(\omega)$ vs. system size or discretization of the k axis with $\mathcal{K}_{\text{IR}}/\mathcal{K} = 10^{-4}$ and $\alpha = 1$[MS20].

7.2.2 *Dependence on the* IR *cutoff*

After having taken the thermodynamic limit $M \to \infty$, it is important to analyze the effects of the IR cutoff for different values of $\mathcal{K}_{\text{IR}}$ in the range from $0.5\mathcal{K}$ to $10^{-4}\mathcal{K}$. The FIG. 7.4 displays the corrections $\tilde{\sigma}(\omega)$ for $\alpha = 0.02$, 0.2, and 2. From the lowest frequencies to the highest, it can be seen a quick rise of $\tilde{\sigma}(\omega)$, from the non-interacting value, that finishes in a bump located around $\omega \sim v\mathcal{K}_{\text{IR}}$, followed by, depending on the value of the IR/UV ratio, a region where $\tilde{\sigma}(\omega)$ seems to be independent of $\mathcal{K}_{\text{IR}}$, to decrease above $\omega > 0.1v\mathcal{K}$ and reach the non-interacting result around $\omega \sim v\mathcal{K}$. Therefore, the quick rise and the bump are effects of the mechanism producing the IR cutoff (e.g., the screening produced by conductors in the surroundings of the graphene layer).

We see in FIG. 7.4 that different system with different IR cutoffs have the same universal conductivity above certain frequency. Below this frequency the different curves corresponding to different IR cutoffs *escape* this universal curve. Our focus is on determining this universal curve describing the behavior of the ideal unscreened Coulomb interaction. In conclusion, the

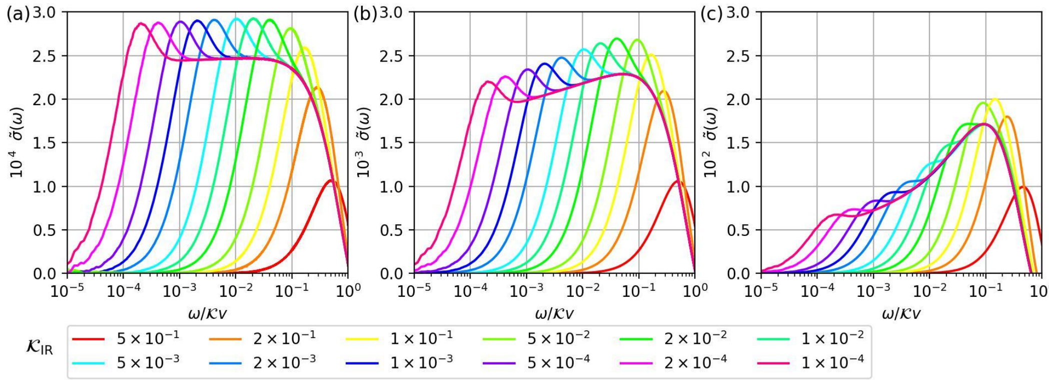

Figure 7.4: IR *cutoff effects on* $\tilde{\sigma}(\omega)$ *in the thermodynamic limit*: The left panel corresponds to $\alpha = 0.02$, the middle to $\alpha = 0.2$, and the right to $\alpha = 2$. The lower inset shows the color convention for different choices of IR cutoff[MS20].

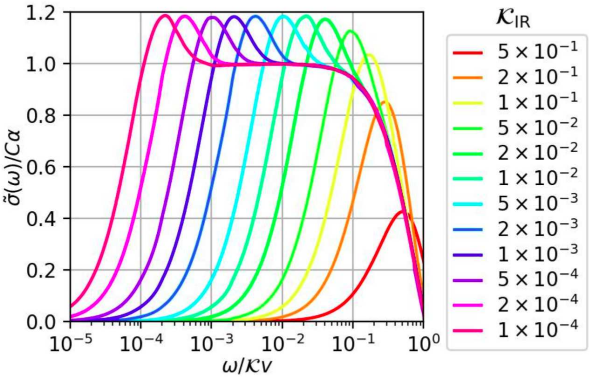

Figure 7.5: *Perturbative effects of the* IR *cutoff on* $\sigma(\omega)/C\alpha$: Perturbative corrections to first order of α for several values of the IR cutoff. The plateau at intermediate frequencies reproduces the result of [Mis08]. The full detailed frequency dependence of the conductivity coincides with the bosonization approach at weak coupling (compare e.g. with panel (a) of FIG. 7.4)[MS20].

existence of an overall overlap extending for many orders of magnitude of ω ensures the capture of the effects produced by the unscreened potential, that is, (7.24) when $\mathcal{K}_{\mathrm{IR}} \to 0$.

7.2.3 *Comparison of numerical results with corrections from first order perturbation theory*

The features described in the previous section, i.e., the rise of $\tilde{\sigma}(\omega)$ from zero, the bump located around $v\mathcal{K}_{\mathrm{IR}}$ and the IR independent region in intermediate frequencies, can be obtained from perturbation theory by calculating $\tilde{\sigma}(\omega)$ including only the Feynman diagrams in FIG. 7.2 and using the IR screened Coulomb potential (7.24). Both contributions are based in the self-energy $\Sigma_{\mathbf{k}}$. Its expression for a potential given by (7.24) is

$$\Sigma_{\mathbf{k}}^{\mathcal{K}} = \frac{\alpha v k}{4}\left[I_0\left(\frac{k}{2\mathcal{K}}\right)K_0\left(\frac{k}{2\mathcal{K}}\right) + I_1\left(\frac{k}{2\mathcal{K}}\right)K_1\left(\frac{k}{2\mathcal{K}}\right)\right], \tag{7.27}$$

where I_m and K_m are the modified Bessel functions of first and second kind. In this way, the dispersion relation corresponding to (7.24) is $E_{\mathbf{k}} = v|\mathbf{k}| + \Sigma_{\mathbf{k}}^{\mathcal{K}} - \Sigma_{\mathbf{k}}^{\mathcal{K}_{\mathrm{IR}}}$, with the phase and group velocities given by

$$v_\phi(\mathbf{k}) = \frac{E_{\mathbf{k}}}{k}, \quad v_g(\mathbf{k}) = \frac{dE_{\mathbf{k}}}{dk}. \tag{7.28}$$

The self-energy contribution $\sigma_\Sigma(\omega)$, depicted in FIG. 7.2a, is given by

$$\begin{aligned}\frac{\sigma_\Sigma - \sigma_0}{\sigma_0} &= \frac{v^2}{v_\phi(\mathbf{k})v_g(\mathbf{k})} - 1 \\ &\approx \frac{1}{2}\left[I_0\left(\frac{k}{2\mathcal{K}_{\mathrm{IR}}}\right)K_0\left(\frac{k}{2\mathcal{K}_{\mathrm{IR}}}\right) + I_0\left(\frac{k}{2\mathcal{K}}\right)K_0\left(\frac{k}{2\mathcal{K}}\right)\right],\end{aligned} \tag{7.29}$$

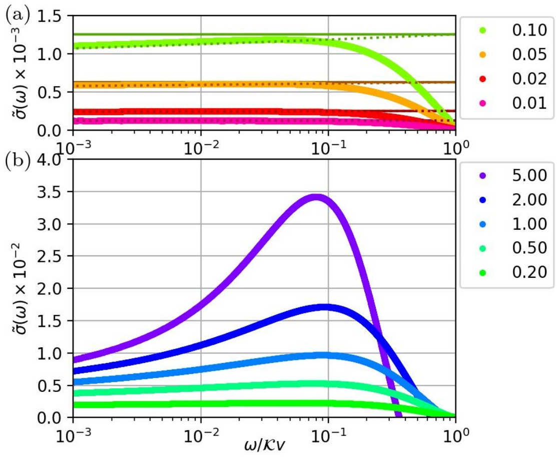

Figure 7.6: *Corrections to the optical conductivity for different couplings* α *with* $M \to \infty$ *and* $\mathcal{K}_{\mathrm{IR}}/\mathcal{K} = 10^{-4}$: (a) Conductivity at weak couplng. Thick: Numerical data. Dotted: RG correction $\tilde{\sigma}(\omega)$. Solid: perturbative correction from Ref. [Mis08]. (b) Conductivity at strong coupling[MS20].

where the expression before expanding is the full correction with the dressed propagators. The vertex contribution $\sigma_V(\omega)$, depicted in FIG. 7.2b, is given by

$$\frac{\sigma_V}{\sigma_0} = \frac{\sigma_\Sigma}{\sigma_0} \int \frac{d^2p}{(2\pi)^2} V_{\mathbf{k}-\mathbf{p}} \frac{k\cos\theta_{\mathbf{k}-\mathbf{p}}(p + q\cos\theta_{\mathbf{k}-\mathbf{p}})}{k^2 - p^2}. \tag{7.30}$$

The total perturbative optical conductivity $\sigma = \sigma_\Sigma + \sigma_V$ is depicted in FIG. 7.5 as $\sigma(\omega)/C\alpha$ with $C = (19 - 6\pi)/12$ so that only the IR cutoff is the relevant parameter. It is therefore found that all the features, including the bump near the IR cutoff, that were obtained in the perturbative approach are indeed correctly reproduced by the bosonization technique with the advantage of extending such results to the non-perturbative regime.

7.2.4 *Optical conductivity for several coupling constants*

FIG. 7.6 shows the corrections to the optical conductivity $\tilde{\sigma}(\omega)$ in the thermodynamic limit $M \to \infty$ and with the smallest IR screening $\mathcal{K}_{\mathrm{IR}} = 10^{-4}\mathcal{K}$ in two different panels: the upper panel (a) shows $\tilde{\sigma}(\omega)$ for perturbative values of α that can have a quick convergence in perturbative expansions, and the lower panel (b) shows $\tilde{\sigma}(\omega)$ for bad or non-perturbative values of α.

According to [Mis08] and the correction to the optical conductivity (7.2) in the perturbative regime, the leading order correction to the optical conductivity is linear in α and independent of ω:

$$\tilde{\sigma} \approx C\alpha + \mathcal{O}(\alpha^2), \tag{7.31}$$

with $C = (19 - 6\pi)/12$. This correction is shown by thin solid horizontal lines in Fig. 7.6a, alongside the numerical results obtained from the diagonalization of the bosonized Hamiltonian (6.28) in the channel $\ell = 1$. There is a visible agreement of both perturbative and numerical results up to a weak logarithmic running of $\tilde{\sigma}$ which actually corresponds to the logarithmic running of the coupling constant (and indded of the Fermi velocity) at small frequencies, expected from the perturbative Renormalization Group (RG) analysis:

$$\tilde{\sigma}(\omega) = \frac{C\alpha}{1 + \frac{\alpha}{4} \ln\left(\frac{\mathcal{K}v}{\omega}\right)} \approx C\alpha \left(1 + \frac{\alpha}{4} \ln\left(\frac{\omega}{\mathcal{K}v}\right)\right). \tag{7.32}$$

The RG running of the optical conductivity can be tested by fitting the logarithmic model:

$$\tilde{\sigma}_{\text{lin}}(\omega) = \tilde{\sigma}_0 + \tilde{\sigma}_1 \ln\left(\frac{\omega}{\mathcal{K}v}\right). \tag{7.33}$$

The coefficients obtained are listed in TAB. 7.1 and the resulting curves are plotted in FIG. 7.7, showing a reasonable agreement for the smallest values of α that decreases as α becomes larger. Thus, the bosonization technique demonstrates to be in good agreement with the RG results up to second order in α, as shown by the dotted lines in FIG. 7.6a. Finally, as expected, non-perturbative values of α show strong deviations from the RG pertubative calculations, noticiable in FIG. 7.6.

α	$C\alpha \times 10^{-4}$	$C\alpha^2/4 \times 0^{-7}$	$\tilde{\sigma}_0 \times 10^{-4}$	$\tilde{\sigma}_1 \times 10^{-7}$
0.01	1.254	3.134	1.255	2.552
0.02	2.507	12.53	2.515	10.42
0.05	6.269	78.36	6.341	67.11
0.10	12.54	313.4	12.80	251.6

Table 7.1: *Detail of the RG running of $\tilde{\sigma}(\omega)$ for small α*: Coefficients of linear regression for $\tilde{\sigma}(\omega)$ in the interval $\omega/\mathcal{K}v \in [10^{-3}, 10^{-2}]$[MS20].

Although the bosonized Hamiltonian (6.28) has been solved for couplings up to $\alpha = 5$, the relative corrections to the optical conductivity are not larger than 4%, indicating the considerable resilience of $\sigma(\omega)$ for 2D Dirac fermions before effects of electron-electron interactions. This result, on the other hand, is in agreement with the current experiments that are consistent to non-interacting Dirac fermions up to 10% of the measurement[Li+08; Mak+08; Nai+08]. Further corrections such as Random Phase Approximation (RPA) that have into account the screening of the Coulomb potential might even weaken the effects of interactions because of the reduction of the effective value of α[SF12; MS20].

7.3 DISCUSSION AND SUMMARY

We have applied the bosonization formalism introduced in Chapter 6 to compute the Coulomb interaction corrections to the optical conductivity

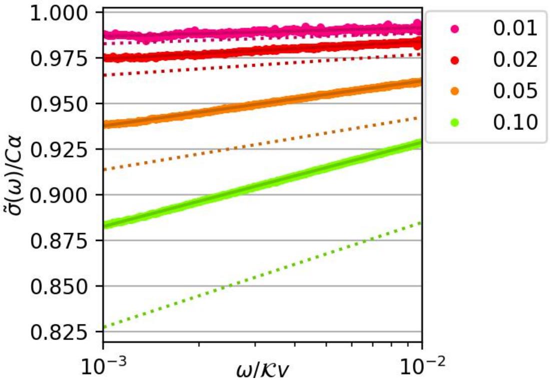

Figure 7.7: *Detail of the* RG *running of* $\tilde{\sigma}(\omega)$ *for small* α: Numerical calculation of the conductivity (color lines) and the the expected value from the leading order perturbative RG (dotted lines). The logarithmic running of the coupling constant leads to a visible linear logarithmic drift of the conductivity at weak coupling[MS20].

of Dirac fermions and found that it recovers the results of perturbative renormalization group at weak coupling [Mis08] and extended them to strong coupling. Remarkably, we have found that the Coulomb interaction corrections remain very weak ($\sim$ 4%) up to values of the effective fine structure constant $\alpha \sim 5$, in agreement with experiments in graphene that have measured a value of the optical conductivity that is consistent with the free electron theory [Li+08; Mak+08; Nai+08]. Although our discussion has been restricted to 2D Dirac fermions, our approach can be naturally generalized to other multi-band semi-metals and higher dimensions, such as Weyl semimetals [AMV18] and novel nodal fermions [Bra+16], providing an interesting tool to capture non-perturbative effects of interactions on the correlation functions of $\mathbf{Q} = 0$ operators of these phases.

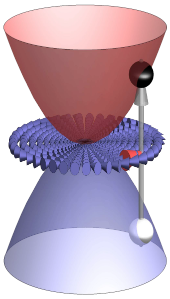

Part III

WEAK COUPLING INSTABILITY, NEW PERSPECTIVES & CONCLUSIONS

This part is devoted to discussed current unpublised ideas and further research projects that can be derived from the parts i and ii. The chapter 8 in particular addresses the weak coupling instability of bilayer graphene when interactions are included using the bosonization formalism introduced in chapter 6. Lastly, chapter 9 outlines the main findings of this work and presents some projects that can be developed from the effective models we have proposed based in hard-core bosons, such as the electric strings in lattice gauge theories, and particle-hole excitations in nodal semimetals.

8

WEAK COUPLING INSTABILITY IN BILAYER GRAPHENE FROM A BOSONIZATION PICTURE

> *... the state of a really big system does not at all have to have the symmetry of the laws which govern it; in fact, it usually has less symmetry.*
>
> — Philip W. Anderson [And72]

As discussed in chapter 5, carbon-based materials present different allotropes with unique electronic features of interest in condensed matter and material sciences. If we stay in the allotropes associated with C atoms in the sp^2 hybridization, the superposition of two graphene layers in the AB, also called Bernal stacking, configuration yields a new band structure with new properties with respect to monolayer graphene[Kat12]. The most important one is the existence of a parabolic dispersion relation at the band-touching points $\mathbf{K}$ and $\mathbf{K}'$ that modifies the density of states, and consequently, all the low-energy physics that was observed in monolayer such as the featureless optical conductivity associated to gapless Dirac fermions [MAF07; CTV12]; alongside, there are two new gapped bands irrelevant for such a regime. Furthermore, adding a small twist of one layer with respect to the other [BM11] yields materials that can exhibit superconducting as well as insulating phases depending on the electron density, and the temperature [Cao+18; Cho+19]. Thus, despite its structural simplicity, bilayer graphene is on its own, a material that displays a fertile framework with recent research interest.

On the other hand, the bosonization technique we have discussed in part ii is able to describe the interaction effects in Dirac fermions described by a linear dispersion relation. Moreover, this formalism can be applied to different nodal semimetals alongside monolayer graphene such as Weyl semimetals or edge modes observed in topological insulators, both described by linear dispersion relations close to the band-touching points. However, we can relax the linear-dispersion condition, searching for a generalization of the bosonization formalism to also include, for instance, parabolic dispersion relations such as the band structure observed in bilayer graphene. In this chapter, we will study a second application of our technique in calculating the weak coupling instability due to electron interactions in Bernal-stacked bilayer graphene. First, §8.1 briefly introduces the band structure of AB bilayer graphene. §8.2 discusses the extension of the formalism presented in chapter 6 to study $\mathbf{Q} = 0$ particle-hole excitations (PHEs) excitations two or more graphene layers. Then, §8.3 presents the two potentials, Gaussian and Coulomb, we use to introduce electron-electron interactions in bilayer graphene and study the corresponding instabilities produced by each one.

Afterward, we propose in §8.4 a small discussion on the physical picture to understand the weak coupling instability in bilayer graphene inspired in superconductivity. §8.5 describes in detail the numerical procedures and results by doing exact diagonalization to the bosonic Hamiltonian, finding that the instability can be described resembling the Cooper instability. Lastly, §8.6 outlines some conclusions and discusses further studies to understand the weak instability in the bosonization picture.

8.1 BAND STRUCTURE OF BERNAL-STACKED BILAYER GRAPHENE

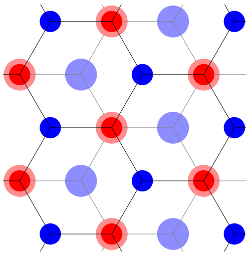

Figure 8.1: *Lattice of bilayer graphene*: The red and blue dots represent the top layer joined by gray links; the light red and blue wider dots joint by black links represent the bottom layer.

Monolayer graphene is one of the different possible allotropes of carbon experimentally accesible by exfoliation of graphite layers. The addition of a second layer changes the electronic properties of the material at low energies. For instance, the linear dispersion relation observed in graphene, resembling relativistic massless particles describeb by the Dirac cones, is replaced by two paraboloids touching at the vertices (gapless) and the curvature of the band is interpreted as the effective mass M_e of the new quasiparticles following a Galilean dispersion relation $\epsilon_{\mathbf{p}} = \mathbf{p}^2/2M_e$. This situation appears when we have *Bernal stacking* (also called AB) of two graphene layers: atoms of sublattice A (red dots in FIG. 8.1) lie above a sublattice A atom of the layer below, while atoms of sublattice B (blue dots in FIG. 8.1) lie directly above the center of the hexagonal cells in the bottom layer.

The band structure of bilayer graphene in Bernal stacking is displayed in FIG. 8.2, where the four bands originate from the four-atom primitive cell of the lattice in FIG. 8.1. In a system at the *charge neutrality point*, two bands are gapped and are not involved in the low-energy physics, while the remaining two have an effective paraboloid shape close the Dirac Point (DP) instead of the conical one found in monolayer graphene. The following Hamiltonian describes a system of 2D electrons with a parabolic dispersion relation:

$$H_{\text{kin}} = \sum_{\mathbf{k},\sigma,\sigma'} \epsilon_{\mathbf{k}} \hat{\psi}^{\dagger}_{\mathbf{k},\sigma} \begin{pmatrix} 0 & e^{-2i\phi} \\ e^{+2i\phi} & 0 \end{pmatrix} \hat{\psi}_{\mathbf{k},\sigma'}, \tag{8.1}$$

where $\epsilon_{\mathbf{k}} = k^2/2M_e$, $k = |\mathbf{k}| = \sqrt{k_x^2 + k_y^2}$, $\phi = \arctan(k_y/k_x)$ is the polar angle between the momentum vector and the x axis in the reciprocal lattice, and $M_e = d^2\epsilon_{\mathbf{k}}/dk^2$, the curvature of the parabolic band. corresponds to an

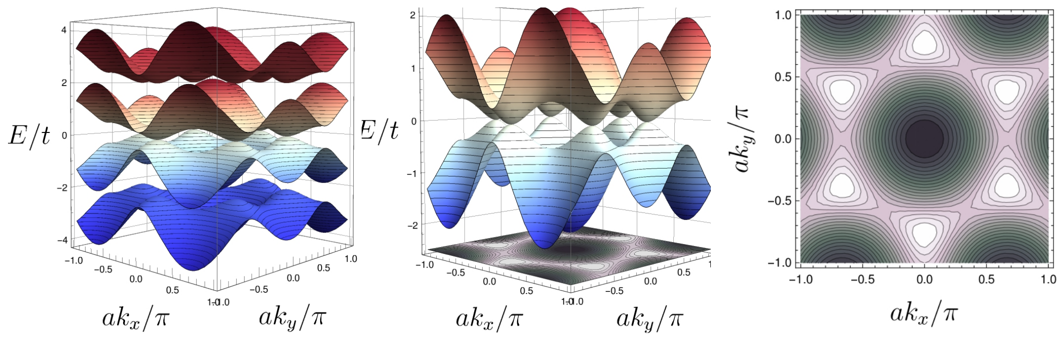

(a) (b) (c)

Figure 8.2: *Band structure of bilayer graphene*: (a) Valence band (VB) (blue) and Conduction band (CB) (red) obtained from the tight-binding Hamiltonian as $\epsilon^{\pm}_{\mathbf{k}} = \pm k^2/2M_e$ in (8.1). (b) Contour plot of the VB in the first Brillouin zone.

effective electron mass of $\approx 5 \times 10^{-2} m_e$, where $m_e \approx 9 \times 10^{-31}$ kg for the free electron [Zyl+20]. This Hamiltonian can be expressed as

$$H = E_{UV} \sum_{\mathbf{k}\sigma\sigma'} \left(\frac{|\mathbf{k}|}{\mathcal{K}}\right)^2 \psi^{\dagger}_{\mathbf{k}\sigma} \left(\hat{\mathbf{k}}_2 \cdot \boldsymbol{\sigma}_{\sigma\sigma'}\right) \psi_{\mathbf{k}\sigma'}, \tag{8.2}$$

where $\boldsymbol{\sigma} = (\sigma^x, \sigma^y)$ are the Pauli matrices (5.30), and $\hat{\mathbf{k}}_2 = (\cos(2\phi), \sin(2\phi))$ is the unit vector of the Zeeman vortex depicted in FIG. 8.3d, $\mathcal{K}$ is the Ultraviolet (UV) momentum cutoff, and $E_{\text{UV}} = \mathcal{K}^2/2M_e$ is the energy UV cutoff, defined as the kinetic term evaluated at $\mathcal{K}$. The following section generalizes this Hamiltonian when m is larger than 2, and monolayer as well as bilayer graphene can be described as two special cases.

8.2 GENERALIZATION OF THE EFFECTIVE HAMILTONIAN OF GRAPHENE

The low-energy modes found in graphene where two or more layers are superposed in Bernal stacking (as shown in FIG. 8.1) can be modelled by the Hamiltonian given by [Kat12]:

$$\begin{aligned} H = {} & E_{UV} \sum_{\mathbf{k}\sigma\sigma'} \left(\frac{|\mathbf{k}|}{\mathcal{K}}\right)^m \psi^{\dagger}_{\mathbf{k}\sigma} \left(\hat{\mathbf{k}}_m \cdot \boldsymbol{\sigma}_{\sigma\sigma'}\right) \psi_{\mathbf{k}\sigma'} \\ & + \frac{1}{2A} \sum_{\mathbf{k}\mathbf{k}'} \sum_{\sigma\sigma'} V_{\mathbf{q}} \psi^{\dagger}_{\mathbf{k}'+\mathbf{q}\sigma} \psi^{\dagger}_{\mathbf{k}-\mathbf{q}\sigma'} \psi_{\mathbf{k}\sigma'} \psi_{\mathbf{k}'\sigma}, \end{aligned} \tag{8.3}$$

where $\mathcal{K}$ is the unit of momentum, E_{UV} the kinetic term evaluated at $\mathcal{K}$, A is the system area, m is the number of layers in Bernal stacking, $V_{\mathbf{q}}$ is the Fourier-transformed interaction potential that are written below, and

$$\hat{\mathbf{k}}_m = (\cos(m\phi), \sin(m\phi)) \tag{8.4}$$

is the unit vector of the pseudospin. This Hamiltonian is a generalization of the cases for monolayer graphene in (6.2), and bilayer graphene in (8.2).

(a) Monolayer low-energy bands

(b) Bilayer low-energy bands

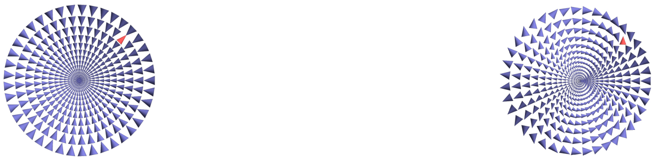

(c) Monolayer pseudospin vortex

(d) Bilayer pseudospin vortex

Figure 8.3: *Monolayer and bilayer graphene in the pseudospin picture*: Depiction of the band structure and vector field $-\hat{\mathbf{k}}_m = -(c_{m\phi}, s_{m\phi})$ representing the ground state for (a,c) $m = 1$ and (b,d) $m = 2$. The production of an exciton at $\mathbf{k}$ $(|\downarrow\rangle_{\mathbf{k}} \to |\uparrow\rangle_{\mathbf{k}})$ is represented by the red arrow.

8.2.1 *Density of states in monolayer and bilayer graphene*

The expression of E_{UV} depends on the number of graphene layers: for $m = 1$ we have $E_{\text{UV}} = v\mathcal{K}$ where v is the Fermi velocity of electrons in the Dirac cones shown in FIG. 8.3a; and for $m = 2$, the case in which we focus in this chapter,

$$E_{\text{UV}} = \frac{\mathcal{K}^2}{2M_e}, \tag{8.5}$$

where M_e is proportional to the curvature of the Dirac *paraboloids* depicted in FIG. 8.3b(a), and describes a fermion of mass M_e with Galilean dispersion relation $\epsilon_{\mathbf{k}} = |\mathbf{k}|^2/2M_e$, in contrast to the relativistic dispersion relation of Dirac fermions $\epsilon_{\mathbf{k}} = v|\mathbf{k}|$. We can also comment here the density of states per spin per valley given by

$$D(\epsilon) = \frac{\mathcal{K}^2}{2\pi m} \sqrt[m]{\frac{\epsilon^{2-m}}{E_{\text{UV}}^2}}. \tag{8.6}$$

For monolayer graphene we obtain that

$$D(\epsilon) = \frac{\epsilon}{2\pi v^2}, \tag{8.7}$$

and for bilayer graphene we get

$$D(\epsilon) = \frac{M_e}{2\pi}. \tag{8.8}$$

The main difference between the monolayer and bilayer cases is the vanishing density of states at $\epsilon = 0$ in monolayer graphene, corresponding to the DP, whilst for bilayer graphene the density of states is constant and independent of ϵ. This difference plays a crucial role for the results reported in this chapter.

Following the procedure proposed in [MS20] and chapter 6, we place the fermions on a 2D torus so that the momentum space is described by a square lattice, and on each one of the lattice sites $\mathbf{k}$ can be empty $|0\rangle_{\mathbf{k}}$, singly-occupied $|\uparrow\rangle_{\mathbf{k}}$, $|\downarrow\rangle_{\mathbf{k}}$ or doubly-occupied $|\uparrow\downarrow\rangle_{\mathbf{k}}$.

8.2.2 *Projection onto $Q = 0$ sector and effective Heisenberg pseudospin Hamiltonian*

The states are then projected onto the Hilbert subspace of the sector $\mathbf{Q} = 0$, so that the remaining subspace is described by a spin lattice with two states $|\uparrow\rangle_{\mathbf{k}}$, $|\downarrow\rangle_{\mathbf{k}}$ per site $\mathbf{k}$, and the projected Hamiltonian takes once again the form of the one describing a spin-1/2 Heisenberg system as in (6.10):

$$\mathcal{PHP} = E_{UV} \sum_{\mathbf{k}} \left(\frac{|\mathbf{k}|}{\mathcal{K}} \right)^m \hat{\mathbf{k}}_m \cdot \mathbf{s}_{\mathbf{k}} - \sum_{\mathbf{k} \neq \mathbf{k}'} \frac{V_{\mathbf{k}-\mathbf{k}'}}{4A} \mathbf{s}_{\mathbf{k}} \cdot \mathbf{s}_{\mathbf{k}'}, \tag{8.9}$$

where $\mathbf{s}_{\mathbf{k}}$ is the *pseudospin operator*:

$$\mathbf{s}_{\mathbf{k}} = \sum_{\sigma\sigma'} \psi^{\dagger}_{\mathbf{k}\sigma} \boldsymbol{\sigma}_{\sigma\sigma'} \psi_{\mathbf{k}\sigma'}. \tag{8.10}$$

Similarly to the case of monolayer graphene studied in chapter 6, the second term in (8.9) is a long-range pseudospin exchangethe kinetic term. However, the first one is mapped onto an m-fold Zeeman vortex

$$\mathbf{B}^m_{\mathbf{k}} = E_{UV} \left(\frac{|\mathbf{k}|}{\mathcal{K}} \right)^m \hat{\mathbf{k}}_m, \tag{8.11}$$

depicted in FIGs. 8.3c and 8.3d for $m = 1$ and $m = 2$, respectively, and then $\mathbf{B}^m_{\mathbf{k}}$ describes the effective Zeeman vortex in monolayer graphene as the special case when $m = 1$.

8.2.3 *Zeeman vortex coordinates and HCB operators*

The new Zeeman vortex $\mathbf{B}^m_{\mathbf{k}}$ fixes the orientation of the pseudospin in the ground state for the noninteracting case $V_{\mathbf{q}} = 0$, which can be described using the following unit vectors that describe the twisting of the noninteracting ground state observed in FIG. 8.3d:

$$\begin{aligned} \hat{\mathbf{k}}_m &= c_{m\phi} \hat{\mathbf{x}} + s_{m\phi} \hat{\mathbf{y}}, \\ \hat{\boldsymbol{\phi}}_m &= c_{m\phi} \hat{\mathbf{y}} - s_{m\phi} \hat{\mathbf{x}}. \end{aligned} \tag{8.12}$$

The pseudospin operators are then expressed in the following basis:

$$\mathbf{s}_{\mathbf{k}} = -s^3_{\mathbf{k}} \hat{\mathbf{k}}_m + s^1_{\mathbf{k}} \hat{\mathbf{z}} + s^2_{\mathbf{k}} \hat{\boldsymbol{\phi}}_m, \tag{8.13}$$

that simplifies the kinetic term by *unfolding* the twisting of $\hat{\mathbf{k}}_m$, so that $\hat{\mathbf{k}}_m \cdot \mathbf{s}_\mathbf{k} = -s^3_\mathbf{k}$ in the new basis (8.13). Moreover, the pseudospin exchange term in (8.10) is expanded as

$$\mathbf{s}_\mathbf{k} \cdot \mathbf{s}_{\mathbf{k}'} = (s^3_\mathbf{k} s^3_{\mathbf{k}'} + s^2_\mathbf{k} s^2_{\mathbf{k}'}) c_{m\phi\mathbf{k}\mathbf{k}'} + (s^2_\mathbf{k} s^3_{\mathbf{k}'} - s^3_\mathbf{k} s^2_{\mathbf{k}'}) s_{m\phi\mathbf{k}\mathbf{k}'} + s^1_\mathbf{k} s^1_{\mathbf{k}'}. \tag{8.14}$$

In the m-folded coordinates (8.13), the Hamiltonian (8.9) is then expanded in Hard-core Boson (HCB) operators by means of the Holstein-Primakov (HP) transformations:

$$\begin{aligned} s^3_\mathbf{k} &= 2\left(S - b^\dagger_\mathbf{k} b_\mathbf{k}\right) = 1 - 2b^\dagger_\mathbf{k} b_\mathbf{k}, \\ s^1_\mathbf{k} &\approx \sqrt{2S}\left(b_\mathbf{k} + b^\dagger_\mathbf{k}\right) = b_\mathbf{k} + b^\dagger_\mathbf{k}, \\ is^2_\mathbf{k} &\approx \sqrt{2S}\left(b_\mathbf{k} - b^\dagger_\mathbf{k}\right) = b_\mathbf{k} - b^\dagger_\mathbf{k}. \end{aligned} \tag{8.15}$$

and then giving the physical picture of $s^3_\mathbf{k}$ as a measure of the occupation number of HCBs at $\mathbf{k}$:

$$|\uparrow\rangle_\mathbf{k} \to |0\rangle_\mathbf{k}, \quad |\downarrow\rangle_\mathbf{k} \to |1\rangle_\mathbf{k}. \tag{8.16}$$

The pseudospin exchange is therefore expanded up to bosonic bilinears:

$$\begin{aligned} \mathbf{s}_\mathbf{k} \cdot \mathbf{s}_{\mathbf{k}'} \approx &\ (1 - 2b^\dagger_\mathbf{k} b_\mathbf{k} - 2b^\dagger_{\mathbf{k}'} b_{\mathbf{k}'}) \\ &+ (b^\dagger_\mathbf{k} b_{\mathbf{k}'} + b_\mathbf{k} b^\dagger_{\mathbf{k}'})(1 + c_{m\phi\mathbf{k}\mathbf{k}'}) \\ &+ (b^\dagger_\mathbf{k} b^\dagger_{\mathbf{k}'} + b_\mathbf{k} b_{\mathbf{k}'})(1 - c_{m\phi\mathbf{k}\mathbf{k}'}) \\ &+ i(b^\dagger_\mathbf{k} - b^\dagger_{\mathbf{k}'} - b_\mathbf{k} + b_{\mathbf{k}'}) s_{m\phi\mathbf{k}\mathbf{k}'}, \end{aligned} \tag{8.17}$$

where the terms of the last row cancel each other when summing on $\mathbf{k}$ indices.

The resulting Hamiltonian is

$$\begin{aligned} H_{HB} = &\sum_\mathbf{k} 2E_{UV}\left(\frac{|\mathbf{k}|}{\mathcal{K}}\right)^m b^\dagger_\mathbf{k} b_\mathbf{k} + \sum_{\mathbf{k}\neq\mathbf{k}'} \frac{V_{\mathbf{k}-\mathbf{k}'}}{A} c_{m\phi\mathbf{k}\mathbf{k}'} b^\dagger_\mathbf{k} b_\mathbf{k} \\ &- \sum_{\mathbf{k}\neq\mathbf{k}'} \frac{V_{\mathbf{k}-\mathbf{k}'}}{4A} (1 + \cos(m\phi_{\mathbf{k}\mathbf{k}'}))(b^\dagger_\mathbf{k} b_{\mathbf{k}'} + b_{\mathbf{k}'} b^\dagger_\mathbf{k}) \\ &- \sum_{\mathbf{k}\neq\mathbf{k}'} \frac{V_{\mathbf{k}-\mathbf{k}'}}{4A} (1 - \cos(m\phi_{\mathbf{k}\mathbf{k}'}))(b^\dagger_\mathbf{k} b^\dagger_{\mathbf{k}'} + b_{\mathbf{k}'} b_\mathbf{k}), \end{aligned} \tag{8.18}$$

where the first row is the bosonic kinetic term with self-energy corrections, and the second and third rows are bosonic hopping and pairing terms on the momentum lattice, respectively. This Hamiltonian is a generalization of (6.14) for multiple graphene layers as can be observed in the argument of the hopping and pairing terms in addition to the expected modification of the kinetic term of HCBs, where the number of layers m is incorporated in the phase of the angle bwtween $\mathbf{k}$ and $\mathbf{k}'$. Of course, the monolayer case is recovered by taking $m = 1$.

8.2.4 *Bogoliubov-Valatin basis*

In complete analogy to chapter 6, it is convenient to express the quadratic bosonic Hamiltonian in (8.18) in the Bogoliubov-Valatin (BV) basis

$$B^\dagger_{\mathbf{k}} = (b_{\mathbf{k}}\ b^\dagger_{\mathbf{k}}) \tag{8.19}$$

that fulfills the bosonic commutation relations

$$\left[B_{\mathbf{k}}, B^\dagger_{\mathbf{k}'}\right] = \mathbb{1}\delta_{\mathbf{k}\mathbf{k}'}, \tag{8.20}$$

where $\mathbb{1} = \mathrm{diag}(+1, -1)$. Consequently, in this basis the Hamiltonian can be expressed as shown in chapter 6:

$$\begin{aligned} H_{HB} &= \sum_{\mathbf{k}\mathbf{k}'} B^\dagger_{\mathbf{k}} H_{\mathbf{k}\mathbf{k}'} B_{\mathbf{k}'}, \\ H_{\mathbf{k}\mathbf{k}'} &= 2\delta_{\mathbf{k}\mathbf{k}'} \begin{pmatrix} E^m_{\mathbf{k}} & 0 \\ 0 & E^m_{\mathbf{k}} \end{pmatrix} - T^m_{\mathbf{k}\mathbf{k}'}, \end{aligned} \tag{8.21}$$

where $E^m_{\mathbf{k}} = E_{UV}(|\mathbf{k}|/\mathcal{K})^m + \Sigma^m_{\mathbf{k}}$, with the Hartree-Fock self-energy $\Sigma^m_{\mathbf{k}} = \sum_{\mathbf{k}'} V_{\mathbf{k}-\mathbf{k}'} \cos(m\phi_{\mathbf{k}\mathbf{k}'})/2A$ already included, and $T^m_{\mathbf{k}\mathbf{k}'}$ is

$$T^m_{\mathbf{k}\mathbf{k}'} = \frac{V_{\mathbf{k}\mathbf{k}'}}{4A} \begin{pmatrix} 1 + \cos(m\phi_{\mathbf{k}\mathbf{k}'}) & 1 - \cos(m\phi_{\mathbf{k}\mathbf{k}'}) \\ 1 - \cos(m\phi_{\mathbf{k}\mathbf{k}'}) & 1 + \cos(m\phi_{\mathbf{k}\mathbf{k}'}) \end{pmatrix}. \tag{8.22}$$

The method followed The method was shown to be equivalent to the self-consistent Kadanoff-Baym particle-hole propagator in [MS20]. Similar aspects such as the re-expression of the momentum space as a polar lattice to resort the azimuthal symmetry and the factorization in independent angular momentum channels ℓ are similar to [MS20] with minor differences detaily described in Appendix D. The final expresssion of the Hamiltonian in polar coordinates is

$$H_{HB} = \sum_{\ell n n'} B^{\ell\dagger}_n H^\ell_{nn'} B^\ell_{n'}, \tag{8.23}$$

where the n index labels the radial slices k_n given explicitly below, and ℓ labels the block-diagonal sectors corresponding to the angular momentum channels of the system.

8.3 INTERACTION POTENTIALS

We propose two potentials with different long and short-range behaviors to explore the system:

- a Gaussian potential:

$$V_{\mathbf{r}} = V_0 e^{-r^2/2a^2}, \tag{8.24}$$

where $r = |\mathrm{r}| = \sqrt{x^2 + y^2}$, V_0 the is intensity of the Gaussian potential and a is the width or *spreading* of the potential in the real space. Its corresponding 2D Fourier transform is

$$V_{\mathbf{q}} = 2\pi a^2 V_0 e^{-a^2 q^2/2}, \tag{8.25}$$

that can be reexpressed as

$$V_{\mathbf{q}} = \frac{E_{UV}}{\mathcal{K}^2}\left(g e^{-(aq)^2/2}\right), \tag{8.26}$$

where $q = |\mathbf{q}| = \sqrt{q_x^2 + q_y^2}$, and $g = 2\pi(a\mathcal{K})^2 V_0/E_{\mathrm{UV}}$ is the coupling constant defined as the intensity of the Gaussian potential respect to the UV energy scale E_{UV}. The potential is further modified as follows,

$$V_{\mathbf{q}} = \frac{E_{UV}}{\mathcal{K}^2}\left[g\left(1 + \frac{b^2 q^2}{2}\right) e^{-\frac{a^2 q^2}{2}}\right], \tag{8.27}$$

to explore the interplay of two different length scales a and b. A depiction of the potential is in FIG. 8.4a for $1 < r < \infty$.

- a Coulomb-like potential:

$$V_{\mathbf{r}} = \frac{e^2}{\kappa}\left(\frac{1}{\sqrt{r^2 + a^2}} - \frac{1}{\sqrt{r^2 + b^2}}\right), \tag{8.28}$$

where $r = |\mathbf{r}|$, e is the elementary electric charge, κ is the substrate dielectric constant, and a and b are length scales used to regularize the potential defined in (7.24), playing the role of UV and Infrared (IR) cutoffs, respectively. Its corresponding 2D Fourier transform is

$$V_{\mathbf{q}} = \frac{2\pi e^2}{\kappa}\frac{e^{-aq} - e^{-bq}}{q}, \tag{8.29}$$

that can be reexpressed as

$$V_{\mathbf{q}} = \frac{E_{\mathrm{UV}}}{\mathcal{K}^2}\left(g\frac{e^{-aq} - e^{-bq}}{q/\mathcal{K}}\right), \tag{8.30}$$

where $q = |\mathbf{q}|$, and $g = 2\pi e^2\mathcal{K}/\kappa E_{\mathrm{UV}}$ is the coupling constant, also defined as the ratio between the intensity of the potential and the UV energy scale E_{UV}. The potential is depicted in FIG. 8.4b for different values of r in the interval $(0, 1)$.

Both potentials can be compared by defining the *effective coupling*:

$$g_{\mathrm{eff}} = N(\epsilon = 0)\lim_{|\mathbf{q}|\to 0} V_{\mathbf{q}} \tag{8.31}$$

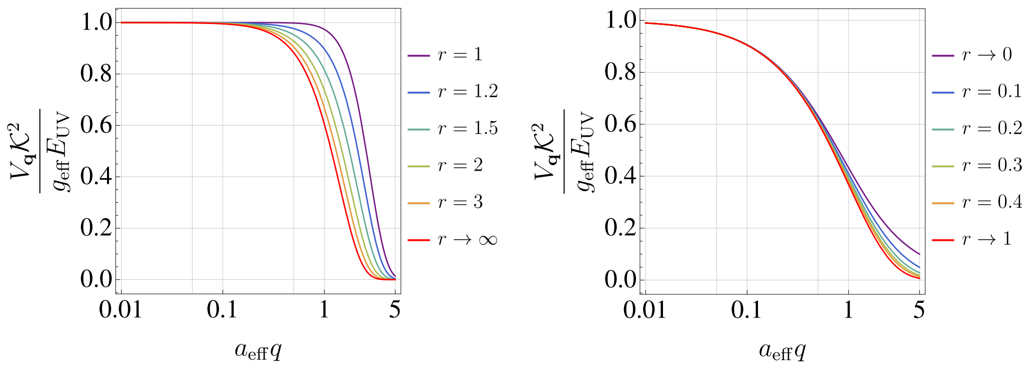

(a) Gaussian potential (b) Coulomb potential

Figure 8.4: *Electron-electron interaction potentials*: Depiction of (a) the Gaussian=like potential (8.26), and (b) the Coulomb-like potential (8.30) for different values of the length-scale ratio $r = a/b$. Notice that the potentials are mostly concentrated in the region $|\mathbf{k}| \lesssim a_{\text{eff}}$, approximately resembling the potential (8.36) used to calculate the Bardeen-Cooper-Schrieffer (BCS) gap (8.37).

where $N(\epsilon)$ is the density of states of the free system defined in (8.6), and the *effective spreading*:

$$a_{\text{eff}} = \sqrt[n]{\frac{-1}{n!} \lim_{|\mathbf{q}|\to 0} \left(\frac{1}{V_{\mathbf{q}}} \frac{\partial^n V_{\mathbf{q}}}{\partial |\mathbf{q}|^n} \right)}, \tag{8.32}$$

given as the coefficient of the next-to-leading order expansion in $|\mathbf{q}|$ ($n = 2$ for the Gaussian potential and $n = 1$ for the Coulomb potential). In this way, by defining the length-scale ratio $r = a/b$, the Gaussian potential is described by

$$g_{\text{eff}} = \frac{g}{4\pi}, \quad a_{\text{eff}} = a\sqrt{1 + \frac{1}{r^2}}, \tag{8.33}$$

while the Coulomb potential is described by the parameters

$$g_{\text{eff}} = \frac{g(b-a)}{4\pi\mathcal{K}}, \quad a_{\text{eff}} = \frac{a+b}{2}. \tag{8.34}$$

Notice that the Gaussian potential (8.26) is recovered from (8.27) when $r \to \infty$. Lastly, FIG. 8.4 displays the Gaussian and Coulomb potentials normalized as $V_{\mathbf{q}}\mathcal{K}^2/g_{\text{eff}}E_{\text{UV}}$ vs. $a_{\text{eff}}q$ for different values of $r = a/b$, according to the definition of the parameters g_{eff} and a_{eff} in (8.31) and (8.32), respectively.

8.4 BCS INSTABILITY IN PSEUDOSPIN PICTURE

Electron-electron interactions are usually repulsive do to the nature of the Coulomb potentials with an increase of the energy of the system when electrons are closer due to the sign of electric charge. However, when effective attractive interactions emerge in the system, for instance, the phonon-mediated interaction in BCS model, the system is driven out of the fixed point associated to Landau Fermi liquids towards a new ground state adiabatically disconnected described by the BCS ansatz[Sch18]:

$$|\psi_{\mathrm{BCS}}\rangle = \prod_{\mathbf{k}} \left(u_{\mathbf{k}} + v_{\mathbf{k}} \psi^{\dagger}_{\mathbf{k}\uparrow} \psi^{\dagger}_{\bar{\mathbf{k}}\downarrow} \right) |0\rangle \,, \tag{8.35}$$

where $\psi^{\dagger}_{\mathbf{k}\sigma}$ creates an electron with momentum $\mathbf{k}$ and spin σ, and $\bar{\mathbf{k}} = -\mathbf{k}$. One of the results is the opening of a gap $\Delta_{\mathbf{k}}$ that penalizes the creation of Cooper pairs $b^{\dagger}_{\mathbf{k}} = c^{\dagger}_{\mathbf{k}\uparrow} c^{\dagger}_{\bar{\mathbf{k}}\downarrow}$. The solution of the gap equation in BCS theory for a potential given by

$$V_{\mathbf{k}\mathbf{k}'} = \begin{cases} -V_0 & \text{for } |\epsilon_k|, |\epsilon_{k'}| < \omega_D, \\ 0 & \text{otherwise,} \end{cases} \tag{8.36}$$

with the Debye frequency ω_D acting as a cutoff for the phononic-mediated interaction, is given by[Sch18]

$$\Delta_0 = \omega_D \frac{1}{\sinh\left(\frac{1}{V_0 D(\epsilon_F)}\right)} \approx 2\omega_D \exp\left(-\frac{1}{V_0 D(\epsilon_F)} \right), \tag{8.37}$$

where the second term is obatined after assuming the *weak coupling limit* $V_0 D(\epsilon_F) \ll 1$. Under our notation in (8.31), $V_0 D(\epsilon_F) \to g_{\mathrm{eff}}$.

Although in bilayer graphene at the charge neutrality point, that is, when the chemical potential is $\mu = 0$ and the Fermi surface is at the DP, we do not have an actual extended Fermi surface, we have a constant finite density of states for parabolic dispersion relations, $D(\epsilon) = M_e/2\pi$. Additionally, there exists an attractive potential between electrons with momentum $\mathbf{k}$ in the CB and holes with momentum $\bar{\mathbf{k}}$ in the VB, both created by the operator $\psi^{\dagger}_{\mathbf{k}s}$ where $s = +1/-1$ for CB/VB, respectively. The effective spreadings a_{eff} we have defined in the previous section can work as the range of non-vanishing interactions, and the effective couplings g_{eff} determine the intensity of the interaction, such as ω_D and V_0 respectively. Under the previous assumptions, we can expect to find an excitonic instability in bilayer graphene that can resemble BCS theory with the consequence of a gap opening that penalizes the creation of excitons $b^{\dagger}_{\mathbf{k}} = \psi^{\dagger}_{\mathbf{k}+} \psi^{\dagger}_{\bar{\mathbf{k}}-}$.

In the bosonization picture, we have obtain a quadratic bosonic Hamiltonian in terms of excitonic operators $b^{\dagger}_{\mathbf{k}}$ that is straightforwardly diagonalized using the BV transformations. We can expect that te excitonic instability appears in this picture as an unstable mode, a couple of conjugated imaginary eigenvalues that suggest the system is finding a new ground state different from that one we have assumed in terms of Landau Dirac liquid with the Zeeman vortex in FIG. 8.3d. To test this hypothesis, we proceed to use exact diagonalization in the Hamiltonian (8.23) with a systematic variation of the parameters of the system, such as the effective spreadings and couplings, or by selecting the angular momentum channels ℓ, as it is discussed in detail in the next section.

8.5 NUMERICAL PROCEDURE

We solve the $2N \times 2N$ bosonic Hamiltonian H_{HB} in (8.23) using exact diagonalization in a systematic exploration of the parameter space:

- Angular momentum ℓ = 0, 1, 2, 3, 4, 5.
- Radial slices N = 100, 200, 300, 400, 500.

The effective spreadings a_{eff} and couplings g_{eff} are explored differently for each potential indicated in each section, and the UV cutoff is set to the unit of momentum and energy, i.e., $\mathcal{K} = 1$ and $E_{\text{UV}} = 1$.

Regarding the spacing of the lattice for the radial component of the momentum $k_n = k(\theta_n, \Delta\theta)$, App. D has an extended discussion on different radial parametrizations. We concluded to use a tangent parametrization given by

$$k_n = \frac{\mathcal{K}}{2} \tan^4(n\Delta\theta), \tag{8.38}$$

and spacing $\Delta\theta = \pi/(2(N+1))$. Consequently, the Hamiltonian is evaluated in the parameter space given by $\{\ell,\ g_{\text{eff}},\ a_{\text{eff}},\ r,\ N\}$ (remember that $r = a/b$, the ratio of the two length scales defined in the potentials in §8.3). Later, after evaluating the potential for the five radial slices, we take the infinite size limit $N \to \infty$ to be sure that the results are independent of the particular discretization chosen during the numerical procedures.

8.5.1 *Numerical BCS instability*

By diagonalizing the bosonic Hamiltonian H_{HB} (8.23) with the two potentials (8.26) and (8.30), we have foun that the system displays the unstable mode only in the angular momentum channels $\ell = 0$ and $\ell = 2$. The mode is characterized by two imaginary eigenvalues $\{\zeta^\ell, \zeta^{\ell *}\}$ of the Hamiltonian (8.23) and two mutually conjugated eigenstates $(\mathbf{A}^\ell, -i\mathbf{A}^{\ell *})$ and $(\mathbf{A}^{\ell *}, +i\mathbf{A}^\ell)$ with $\mathbf{A}^\ell$ as an N-complex vector that parametrize the eigenstates. The rest of the $2N-2$ eigenvalues are real and come by pairs $\{\omega_n^\ell, \omega_n^\ell\}$ with their corresponding $N-1$ pairs of real eigenstates.

8.5.2 *Functional form of the instability*

The first Ansatz we use to describe the unstable mode found by exact diagonalization is:

$$\zeta^\ell(g_{\text{eff}}, a_{\text{eff}}, r) = C^\ell(a_{\text{eff}}, r) e^{-\frac{4\pi G^\ell(a_{\text{eff}}, r)}{g_{\text{eff}}}}, \tag{8.39}$$

where we have assumed the separability of the dependence on a_{eff} and g_{eff} in the coefficients $C^\ell(a_{\text{eff}}, r)$ and $G^\ell(a_{\text{eff}}, r)$. The fittings to the Ansatz are shown in FIGs. 8.5 and 8.6 for the Gaussian and the Coulomb potentials,

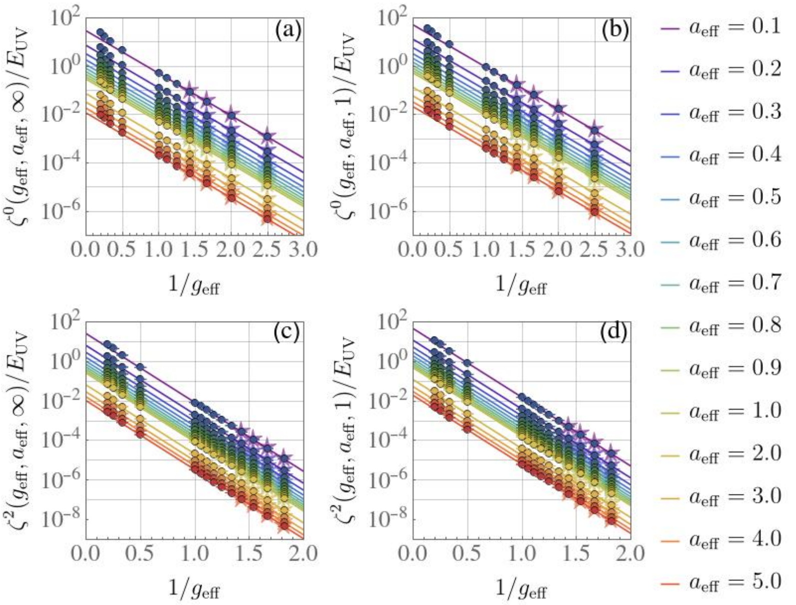

Figure 8.5: *Unstable mode in bilayer graphene with Gaussian-like potential*: Modulus of the imaginary eigenvalues $\{\zeta^\ell, \zeta^{\ell *}\}$ for $\ell = 0, 2$ obtained by exact diagonalization of the bosonic quadratic Hamiltonian (8.18) with electron-electron interactions described by the Gaussian-like potential (8.26). The potential parameters are $r = a/b$, $g_{\rm eff} = g_{\mathcal{K}}/4\pi$, and $a_{\rm eff} = a\sqrt{1 + 1/r^2}$. The fitting is done using the starred dots and the Ansatz (8.39).

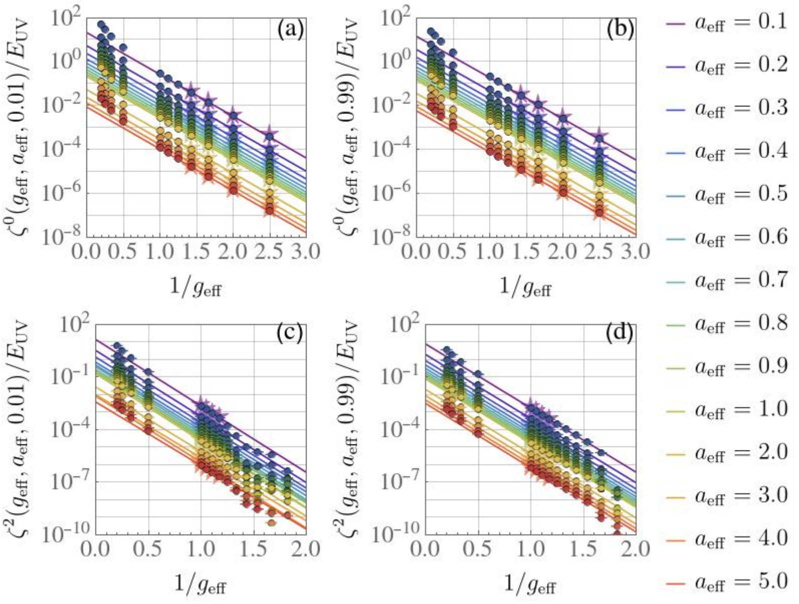

Figure 8.6: *Unstable mode in bilayer graphene with Coulomb-like potential*: Modulus of the imaginary eigenvalues $\{\zeta^\ell, \zeta^{\ell *}\}$ for $\ell = 0, 2$ obtained by exact diagonalization of the bosonic quadratic Hamiltonian (8.18) with electron-electron interactions described by the Coulomb-like potential (8.30). The potential parameters are $r = a/b$, $g_{\rm eff} = g(b-a)/(4\pi\mathcal{K})$, and $a_{\rm eff} = (a+b)/2$. The fitting is done using the starred dots and the Ansatz (8.39).

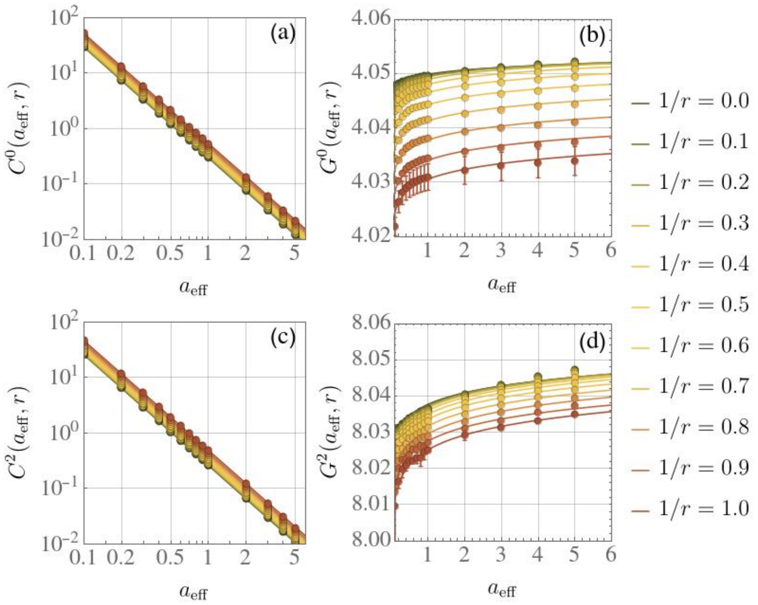

Figure 8.7: *Coefficients $C^\ell(a_{\text{eff}}, r)$ and $G^\ell(a_{\text{eff}}, r)$ for Gaussian potential*: Numerical results after fitting the dataset in FIG. 8.5 to the Ansatz (8.39). $C^\ell(a_{\text{eff}}, r)$ is described by a power law of a_{eff}, while $G^\ell(a_{\text{eff}}, r)$ has a weak dependence on a_{eff} that can be neglected. The fittings are done to the power laws 8.40.

respectively, where the starred dots are the datapoints we chose to fit in the weak coupling limit.

The numerical values of the coefficients $C^\ell(a_{\text{eff}}, r)$ and $G^\ell(a_{\text{eff}}, r)$ are displayed in FIGs. 8.7 and 8.8 for the Gaussian and Coulomb potentials. It is easy to note that $C^\ell(a_{\text{eff}}, r)$ presents a strong dependence on a_{eff} that can be modelled by a power law, in contrast to $G^\ell(a_{\text{eff}}, r)$ whose variations in function of a_{eff} affect only the second decimal place. We assume that both coefficients are power laws:

$$C^\ell(a_{\text{eff}}, r) = \left(\frac{A^\ell(r)}{a_{\text{eff}}}\right)^{\mathsf{a}^\ell(r)}, \quad G^\ell(a_{\text{eff}}, r) = \left(\frac{G^\ell(r)}{a_{\text{eff}}}\right)^{\mathsf{g}^\ell(r)}, \tag{8.40}$$

used to fit the results in FIGs. 8.7 and 8.8.

The coefficients $A^\ell(r)$ and $G^\ell(r)$, and the exponents $\mathsf{a}^\ell(r)$ and $\mathsf{g}^\ell(r)$ are displayed in FIGs. 8.9, where we can noticed that $\mathsf{a}^\ell(r) \approx 2$ and $\mathsf{g}^\ell(r) \approx 0$ up to the second decimal place in a good approximation. This results allow us to assume the following expression to describe the unstable mode found numerically:

$$\zeta^\ell(g_{\text{eff}}, a_{\text{eff}}, r) = \left(\frac{A^\ell(r)}{a_{\text{eff}}}\right)^2 e^{-\frac{4\pi G^\ell(r)}{g_{\text{eff}}}}, \tag{8.41}$$

and the values of the coefficients $A^\ell(r)$ and $G^\ell(r)$ are well described by the FIGs. 8.9b,d, for the Gaussian potential, and 8.9f,h for the Coulomb potential.

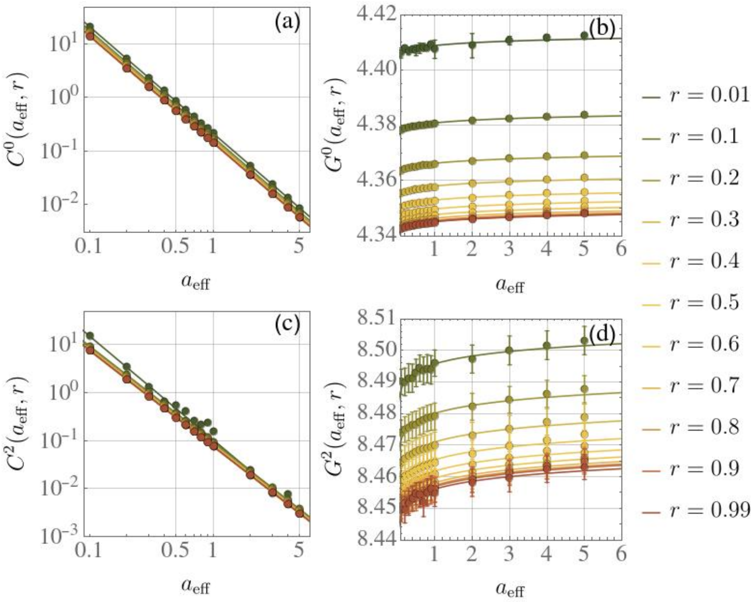

Figure 8.8: *Coefficients* $C^\ell(a_{\text{eff}}, r)$ *and* $G^\ell(a_{\text{eff}}, r)$ *for Coulomb potential*: Numerical results after fitting the dataset in FIG. 8.6 to the Ansatz (8.39). The Coulomb potential has similar results to the Gaussian potential shown in FIG. 8.7, where $C^\ell(a_{\text{eff}}, r)$ is a power law of a_{eff}, and $G^\ell(a_{\text{eff}}, r)$ can be assumed independent of a_{eff}. The fittings are done to the power laws 8.40.

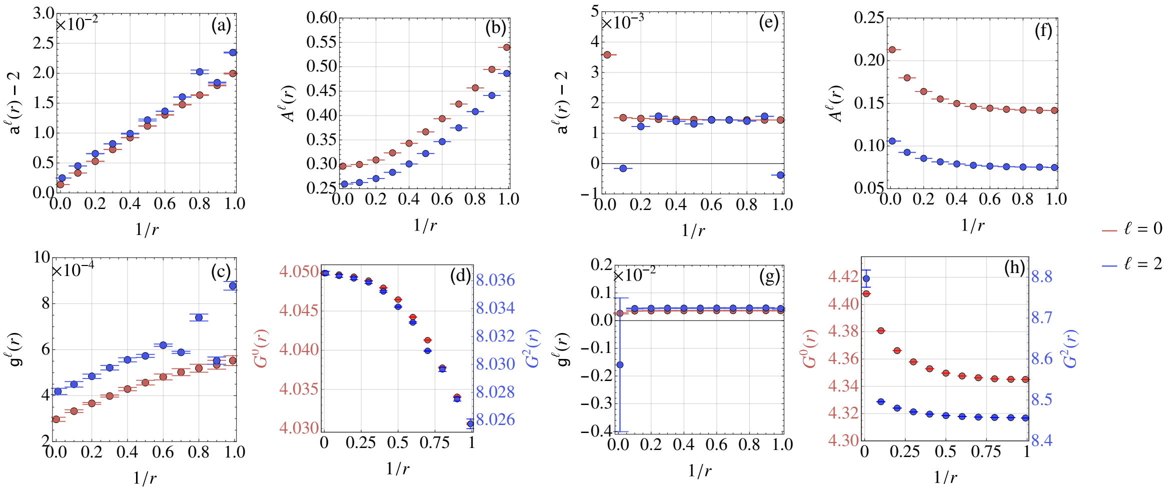

Figure 8.9: *Power-law parameters for Gaussian and Coulomb potentials*: Coefficients $A^\ell(r)$ and $G^\ell(r)$, and exponents $\mathrm{a}^\ell(r)$ and $\mathrm{g}^\ell(r)$ for (a,b,c,d) the Gaussian, and for (e,f,g,h) the Coulomb potential, resulting from fitting the dataset in FIG. 8.7 to the Ansatz (8.40). The power laws yield $\mathrm{a}^\ell(r) \approx 2$ and $\mathrm{g}^\ell(r) \approx 0$, supporting that $G^\ell(a_{\text{eff}}, r) = G^\ell(r)$ can be assumed independent of a_{eff}. The coefficients $A^\ell(r)$ and $G^\ell(r)$ are used in the resulting Ansatz (8.41) to describe the unstable mode.

8.5.3 *Comparison to the instability from BCS theory*

The expression (8.41) we have found to describe the unstable mode found using exact diagonalization to the bosonic quadratic Hamiltonian (8.18) resembles the expression (8.37) obtained in the BCS model of superconductivity. If we do a direct comparison, we identify the Debye frequency ω_D with $\left(A^{\ell}(r)/a_{\text{eff}}\right)^2$, and the coupling of the potential $g_{\text{eff}} = V_0 D(\epsilon_F)$ with $g_{\text{eff}}/4\pi G^{\ell}(r)$.

These results can be understood by doing a short analysis in the shape of the Gaussian and Coulomb potentials we have used to describe electron-electron interactions. FIG. 8.4 shows the normalized potentials $V_{\mathbf{q}}\mathcal{K}^2/g_{\mathcal{K}}E_{\text{UV}}$ vs. $a_{\text{eff}}k$, as expressed in (8.26) and (8.30), for different values of the length-scale ratio $r = a/b$. We can notice that, in addition to the isotropy, the potentials are mostly concentrated for momentum scales $|\mathbf{k}| \lesssim a_{\text{eff}}$ similarly to the potential (8.36) where $V_{\mathbf{k}\mathbf{k}'} \neq 0$ in a shell centered at the Fermi momentum k_F with width given by the Debye frequency ω_D. In the case of graphene at the charge neutrality point, where the Fermi surface has shrunk to a point $k_F = 0$, the potentials can be approximated by $g_{\mathcal{K}}E_{\text{UV}}/\mathcal{K}^2$ in a disk of radius $E_{\text{UV}}/(a_{\text{eff}}\mathcal{K})^2$ around the DP, so that the coefficients $A^{\ell}(r)$ and $G^{\ell}(r)$ can be understood as geometrical factors associated to the finite slope of the potential around $k \sim 1/a_{\text{eff}}$. We leave the calculation of these coefficients for future advances that will be reported in the literature.

8.6 CONCLUSIONS

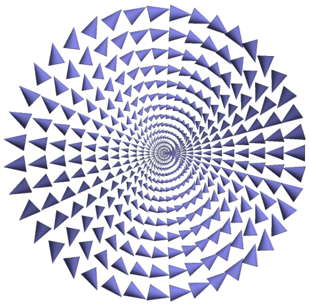

Figure 8.10: *Zeeman vortex in bilayer graphene*: Similarly to monolayer graphene, the kinetic term can be expressed as a Zeeman term involving the pseudospin $\mathbf{s}_{\mathbf{k}}$ coupled to a 2-folded Zeeman vortex.

This chapter discusses the weak coupling instability in bilayer graphene under the bosonization picture discussed in chapters 6 and 7. The generalization of the bosonization formalism to address bilayer (and multiple-layer) graphene relies in the modification of the Zeeman vortex used to express the ground state of the free system described by the Hamiltonian (8.3) with $V_{\mathbf{q}} = 0$, and depicted in FIG. 8.10. This results in a the modification in the kinetic term $2E_{UV}(|\mathbf{k}|/\mathcal{K}) \to 2E_{UV}(|\mathbf{k}|/\mathcal{K})^m$, and in the angular factors in the hopping and pairing terms $\phi_{\mathbf{k}\mathbf{k}'} \to m\phi_{\mathbf{k}\mathbf{k}'}$ of the bosonic quadratic Hamiltonian (8.18), where m is the number of layers of the system.

From the fact that bilayer graphene exhibits a finite density of states at the DP, we can expect an instability resulting from the effective attractive potential between CB electrons and VB holes to form excitons, in a similar fashion to the phononic attractive potential between spin-up and spin-down electrons to form Cooper pairs in BCS theory. The instability manifests as two mutually-conjugated imaginary eigenvalues

$\{\zeta^\ell, \zeta^{\ell*}\}$ in the angular momentum channels $\ell = 0$ and $\ell = 2$. By doing a systematic exploration of the parameter space and calculating the infinite-size limits, we obtained the unstable modes depicted in FIGs. 8.5 and 8.6 for the Gaussian (8.26) and Coulomb potentials (8.30) we chose to address the problem. We have found an Ansatz that describes the unstable mode that resembles the gap equation (8.37) of BCS theory. This result could be understood as the formation of an excitonic condensate at the ground state of the system that results in a gap opening at the DP for the $\ell = 0$ and $\ell = 2$ channels.

Further steps focus on describing the new ground state in the original fermionic operators, yielding the new band structure resulting from the weak coupling instability. The method consists of inverting the procedure followed to obtain the bosonic Hamiltonian so that the instabilities contribute with additional terms in the original fermionic Hamiltonian. Furthermore, two instabilities in $\ell = 0$ and $\ell = 2$ suggest the existence of two competing phases describing the new ground state: a gapped phase associated with the instability in $\ell = 0$ and a nematic phase associated with $\ell = 2$ that breaks the rotational invariance of the model. The successful description of these phases in the bosonization formalism will not only yield a new picture of interaction instabilities in bilayer graphene but also shows the path we should follow to extend the current formalism to describe gapped fermions, at the moment excluded when we express the fermionic Hamiltonian in terms of on-plane pseudospin operators $\mathbf{s}_\mathbf{k} = s^x_\mathbf{k}\hat{\mathbf{x}} + s^y_\mathbf{k}\hat{\mathbf{y}}$. Consequently, we expect that the $s^z_\mathbf{k}$, i. e., the off-plane component, also contributes to the pseudospin configuration of the ground state. The results obtained in describing the new ground state and the extension of bosonization to gapped fermions are planned to be published in the literature in the forthcoming months.

9

CONCLUSIONS

> *I think that modern physics has definitely decided in favor of Plato. In fact the smallest units of matter are not physical objects in the ordinary sense; they are forms, ideas which can be expressed unambiguously only in mathematical language.*
>
> — Werner Heisenberg [Von68]

Quantum many-body systems exhibit physical properties that can involve many relevant degrees-of-freedom (DOF) coming from low-energy excitations. Direct computation of these problems usually implies a huge computational cost that also might not offer a satisfactory physical picture of the mechanisms occurring in the system. These problems can sometimes be circumvented by mapping the system into a simpler one under certain assumptions whose solution is more straightforward, and in some cases yield clearer insight on the physics involved beyond the resolution of a mathematical problem. The present work has used a mapping onto Hardcore Bosons (HCBs) in two different physical problems: a fluctuating electric string in the context of Lattice Gauge Theories (LGTs) discussed in part i, and the extension of bosonization techniques to $\mathbf{Q} = 0$ excitations with graphene as study case, discussed in part ii and chapter 8.

Part i deals with LGTs in a 2D square lattice, in the realization as Abelian Quantum Link Models (QLMs). We have studied the phases of a fluctuating electric line described as a Wilson line along a path γ where two charges $Q_{\partial\gamma}$ lie at its boundary $\partial\gamma$. The motivation to address this problem comes from the description of the phase diagram of the Quantum 6-Vertex Model (Q6VM) and the Quantum Dimer Model (QDM), obtained as two special cases achieved by selecting one of the different sectors determined by the distribution of charges $Q_{\mathbf{r}}$ at each site of the lattice: $Q_{\mathbf{r}} = 0$ for the Q6VM to fulfill the ice rules, and $Q_{\mathbf{r}} = \pm 2$ for the QDM. Both models are ruled by the Rokhsar-Kivelson (RK) Hamiltonian:

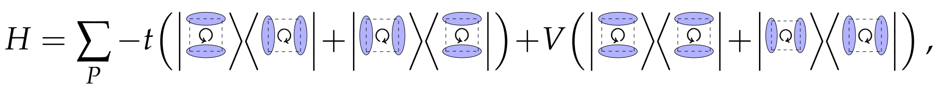
(9.1)

with parameter $v = V/t$, tuning the energy cost of creating a flippable plaquette vs. the quantum fluctuations $|\circlearrowright\rangle \leftrightarrow |\circlearrowleft\rangle$ produced by the kinetic terms, with the RK point as the phase where potential and inetic terms are equal in magnitude, and the ground state is described by the celebrated Nearest Neighbor (NN) Resonant Valence Bond (RVB) state. Roughly, the two models exhibit three phases along the v-axis: a gapped Ferromagnetic (FM) phase at the Right Hand Side (RHS) of the RK point where the number of flippable is minimized as $v \to \infty$, and two phases at the Left Hand Side (LHS)

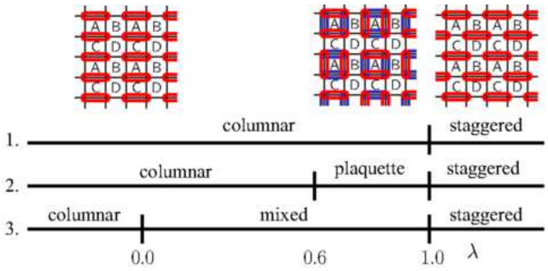

Figure 9.1: *Possible phase diagrams of the* QDM: The proposed phases for the QDM are the columnar, the plaquette RVB, and the staggered phase. The phase diagrams (1,2,3) summarize the different proposals in the literature. [Adapted by permission from the American Physical Society (Banerjee *et al.* [Ban+14]) Copyright (2014); `https://doi.org/10.1103/PhysRevB.90.245143`].

of the RK point: a plaquette RVB phase where each plaquette fluctuates between the two possible states $|\circlearrowright\rangle \leftrightarrow |\circlearrowleft\rangle$ in a checkerboard pattern in the square lattice, and a gapped Antiferromagnetic (AFM) phase where the number of flippable plaquettes is maximized to lower the energy of the ground state energy as $v \to -\infty$. The phase diagram of the Q6VM is well understood [SMP04], but there are different proposals for the QDM regarding the intervening phase between the FM and the AFM phases [Ban+14; Oak+18; Syl06; LCR96; RPM08].

We address this problem in [HAMS19] by studying the phase diagram of one electric field line in the two sectors defined by $Q_{\mathbf{r}}$ that selects between the Q6VM and the QDM, within a sector of winding numbers so that the electric field line is embedded in a background with no flippable plaquettes, that is, in a ground state at the RHS of the RK that remains frozen under the action of the RK Hamiltonian. FIG. 9.2a displays one configuration of the electric string in the Q6VM with the corresponding mapping onto a HCB 1D chain that is further mapped onto the XXZ spin-1/2 chain. Similarly, FIG. 9.2b shows one configuration of the electric string in the QDM, with two mappings onto a triangular lattice fulfilling the ice rules and further onto a HCB two-leg ladder chain.

The advantage of having mapped the electric string onto the XXZ chain for the Q6VM lies in the fact that the system is exactly solvable [YY66a; YY66b;

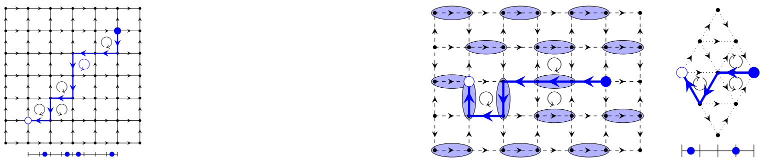

(a) Fluctuating string in the Q6VM.

(b) Fluctuating string in the QDM.

Figure 9.2: *Fluctuating electric string in the* QLM: Two configurations of the electric string embedded in the charge background that generates (a) the Q6VM and (b) the QDM in the corresponding winding number sectors that sets the background with no flippable plaquettes. Below we see the respective mappings onto HCBs in a 1D chain, with a mapping onto a triangular lattice for the QDM [HAMS19].

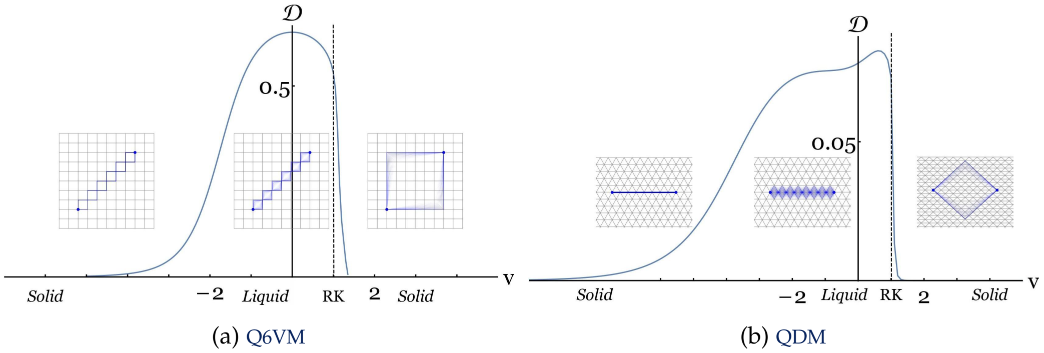

(a) Q6VM (b) QDM

Figure 9.3: *Phase diagram and Drude weight of the electric string*: Insets depict the ground state of the electric field lines in the different regimes for (a) the Q6VM and (b) the QDM. (a) The string in the Q6VM presents a fluid state intervening between two solids as precursors to the columnar and staggered phases, while the liquid phase is a precursor to the resonant plaquette phase in two dimensions. (b) The phase diagram of the string in the QDM resembles the Q6VM. However, we rely only in exact diagonalization for small system sizes in the QDM [HAMS19].

YY66c; YY66d] and its phase diagram is known. We can then obtain the phase diagram in FIG. 9.2a where we have included the Drude weight $\mathcal{D}$ as a function of v as a parameter describing the conductivity of each phase which was estimated from direct exact diagonalization of small system sizes. The limits $v \to \pm\infty$ exhibit two solid phases corresponding to the columnar phase for $v \to -\infty$ and the staggered phase for $v \to \infty$ in accordance with the phase diagram of the whole 2D Q6VM. There is a third phase intervening between the two solids with a large $\mathcal{D}$ corresponding to a gapless paramagnetic phase in the XXZ phase in the regime $|v| < 1$. This phase is a gapless Luttinger liquid which can be interpreted as a precursor to the RVB plaquette phase by interpreting it as a closely packed ensemble of fluctuating strings in the square lattice. On the contrary, we do not have a direct mapping to a well-known model for the QDM, so we addressed the problem using exact diagonalization for system sizes up to $L = 8$ lattice sites in the 1D chain. We have also calculated the Drude weight as a parameter to test the conductivity of the phase, obtaining a diagram that closely resembles the phases of the Q6VM, as shown in FIG. 9.2b.

Further projects derived from the part i of this work can address the problem of multiple strings in the square lattice (the triangular lattice can also be included because of the one-to-one mapping from the QDM). We can propose two electric strings in the lattice whose maximal rectangles overlap, each described by a 1D HCB chain. We then include inter-chain interactions that describe the close interaction of the strings such that the ice rules $Q_{\mathbf{r}} = 0$ are hold. This is automatically fulfilled with the implementaion of HCBs in the chain, where the presence of two strings in the same link is forbidden. Interesting cases can be studied in the maximal overlapping of the bounding rectangles, specially in the AFM phase since the strings will maximize the number of flippable plaquettes and consequently assume the kinked configuration. The presence of a second string might modify the paths in the AFM so that we can expect a combined configuration that maximizes the number of flippable plaquettes, selecting paths of parallel ladders spaced by two cells in a sort of effective attractive interaction between strings. On the contrary, the FM phase minimizes the number of flippable plaquettes, so it might produce effective repulsive interactions between strings that force them to assumed the paths along the bounding rectangles. As a last comment, recent implementation of LGTs in cold atom systems [Aid+22] opens the posibility of implementing the problem of the fluctuating electric string in a square lattice using devices based on ultracold atoms in optical lattices [Wie13] by setting the vertices $Q_{\mathbf{r}}$ in the suited sectors and access the Q6VM or the QDM. This posibility is mostly attractive for the QDM since it has not been exactly solved in the approach discussed in chapter 4, with special interest in the region $|v| < 1$ we there exists the posibility to find more than one phase as the Drude weight $\mathcal{D}$ suggests in FIG. 9.3b with the small bump just at the LHS of the RK point.

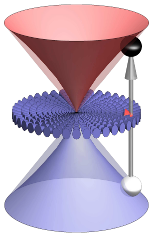

Figure 9.4: *Bosonization of particle-hole excitations (PHEs) of gapless fermions*: By restricting the Hilbert space to $\mathbf{Q} = 0$, a PHE at momentum $\mathbf{k}$ can be mapped as the flip of the pseudospin $\mathbf{s}_{\mathbf{k}}$ and ultimately as a HCB. The expansion up to quadratic terms then yields the bosonic Hamiltonian (9.3). (a) Monolayer and (b) bilayer graphene are described by $m = 1$ and $m = 2$, respectively.

Part ii presents a second framework where mappings using HCBs belong part to the formulation of an extension to higher-dimensional formalisms [Lut79; Hal94; HM93; HKM94; CNF94b; CNF94a; HKM00], where the PHEs close to the Fermi surface are treated as bosons $b^{\dagger}_{\mathbf{k},\mathbf{Q}} = c^{\dagger}_{\mathbf{k}+\mathbf{Q}/2}c_{\mathbf{k}-\mathbf{Q}/2}$, yielding a bosonic quadratic Hamiltonian departing from a fermionic Hamiltonian involving bilinears in the kinetic term and quartic terms in the interactions, thus this formalism then studies PHEs with finite $\mathbf{Q}$ that extends from a finite Fermi surface. Consequently, materials such as nodal semimetals where the Fermi surface is shrunk to a point, as well as the existence of PHEs with $\mathbf{Q} = 0$ due to the existence of two bands, requires an extension of the implementation of previous bosonization techniques.

We have proposed in chapter 6 the extension to bosonization in nodal semimetals [MS20] described by the Hamiltonian (6.2):

$$\begin{aligned} H = E_{UV} \sum_{\mathbf{k}\sigma\sigma'} \left(\frac{|\mathbf{k}|}{\mathcal{K}}\right)^m \psi^{\dagger}_{\mathbf{k}\sigma} \left(\hat{\mathbf{k}}_m \cdot \boldsymbol{\sigma}_{\sigma\sigma'}\right) \psi_{\mathbf{k}\sigma'} \\ + \frac{1}{2A} \sum_{\mathbf{k}\mathbf{k}'} \sum_{\sigma\sigma'} V_{\mathbf{q}} \psi^{\dagger}_{\mathbf{k}'+\mathbf{q}\sigma} \psi^{\dagger}_{\mathbf{k}-\mathbf{q}\sigma'} \psi_{\mathbf{k}\sigma'} \psi_{\mathbf{k}'\sigma'}, \end{aligned} \tag{9.2}$$

where $\mathcal{K}$ is the unit of momentum, E_{UV} the kinetic term evaluated at $\mathcal{K}$, A is the system area, m is the number of layers in Bernal stacking, $V_{\mathbf{q}}$ is the

Fourier-transformed interaction potential. The projection of the Hamiltonian onto the Hilbert subspace of $\mathbf{Q} = 0$ PHEs allows to reexpress the model in terms of the pseudospin $\mathbf{s}_{\mathbf{k}} = \sum_{\sigma,\sigma'} \psi^{\dagger}_{\mathbf{k},\sigma} \sigma_{\sigma\sigma'} \psi_{\mathbf{k},\sigma'}$ involved in the kinetic term. Lastly, the pseudospins are expanded via the Holstein-Primakov (HP) transformation, obtaining at the end a bosonic bilinear Hamiltonian that can be solved by exact diagonalization. This procedure is exactly equivalent to the Kadanoff-Baym (KB) Self-Consistent Hartree-Fock (SCHF) resummation of the $\mathbf{Q} = 0$ particle-hole propagator as discussed in App. B. The resulting Hamiltonian is

$$\begin{aligned} H_{HB} = &\sum_{\mathbf{k}} 2E_{UV} \left(\frac{|\mathbf{k}|}{\mathcal{K}}\right)^m b^{\dagger}_{\mathbf{k}} b_{\mathbf{k}} + \sum_{\mathbf{k}\neq\mathbf{k}'} \frac{V_{\mathbf{k}-\mathbf{k}'}}{A} c_{m\phi_{\mathbf{k}\mathbf{k}'}} b^{\dagger}_{\mathbf{k}} b_{\mathbf{k}} \\ &- \sum_{\mathbf{k}\neq\mathbf{k}'} \frac{V_{\mathbf{k}-\mathbf{k}'}}{4A} (1 + \cos(m\phi_{\mathbf{k}\mathbf{k}'}))(b^{\dagger}_{\mathbf{k}} b_{\mathbf{k}'} + b_{\mathbf{k}'} b^{\dagger}_{\mathbf{k}}) \\ &- \sum_{\mathbf{k}\neq\mathbf{k}'} \frac{V_{\mathbf{k}-\mathbf{k}'}}{4A} (1 - \cos(m\phi_{\mathbf{k}\mathbf{k}'}))(b^{\dagger}_{\mathbf{k}} b^{\dagger}_{\mathbf{k}'} + b_{\mathbf{k}'} b_{\mathbf{k}}), \end{aligned} \tag{9.3}$$

where $\phi_{\mathbf{k}\mathbf{k}'}$ is the angle between momentum vectors $\mathbf{k}$ and $\mathbf{k}'$.

In chapters 7 and 8 we have presented two implementations of the bosonization procedure to address physical properties of graphene. Chapter 7 discussed how to calculate the optical conductivity of one graphene layer with electrons interactiong via a Coulomb potential [MS20]. Since bosonization allows to access the nonperturbative strong interacting regimes, our results not only reproduce the analytical [Mis08] and numerical results [SS09; Abe+11; SF12; Gaz+13; Bar+14b; TK14; TK18] found in the literature for perturbative couplings $\alpha < 1$, but also extends to the strong coupling region $\alpha \sim 1$ where we found still small corrections to the optical conductivity that do not overpass 4% of the non-interacting value, in agreement with Quantum Monte Carlo simulations [Boy+16].

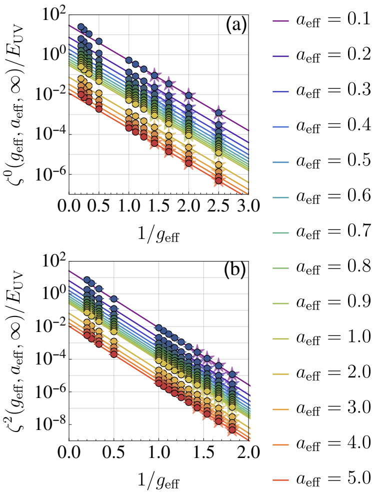

Figure 9.5: *Weak coupling instability in bilayer graphene due to Gaussian electron-electron interaction.*: By restricting the Hilbert space to $\mathbf{Q} = 0$, a PHE at momentum $\mathbf{k}$ can be mapped as the flip of the pseudospin $\mathbf{s}_{\mathbf{k}}$ and ultimately as a HCB.

Chapter 8, presented a study on the weak coupling instability found in bilayer graphene when electron-electron interactions are included, in this case, a Gaussian-like potential (8.26) and a Ultraviolet (UV)/Infrared (IR)-regularized Coulomb potential (8.30). After diagonalizing the quadratic Hamiltonian (9.3) with $m = 2$, we found an unstable mode as a pair of mutually conjugated imaginary eigenvalues ζ^{ℓ}, plotted in FIG. 9.5 for the Gaussian potential. The instabilities were found in the $\ell = 0$ and $\ell = 2$ angular momentum channels so that we could associate them with two competing phases: a gapped phase ζ^0 rotationally symmetric, and a nematic phase ζ^2 that spontaneously breaks the rotational symmetry. The numerical Ansatz we use to describe the instabilities is given by

$$\zeta^{\ell}(g_{\text{eff}}, a_{\text{eff}}, r) = \left(\frac{A^{\ell}(r)}{a_{\text{eff}}}\right)^2 e^{-\frac{4\pi G^{\ell}(r)}{g_{\text{eff}}}}, \tag{9.4}$$

where $A^{\ell}(r)$ and $G^{\ell}(r)$ are length and coupling scales depending on the parameters of the potential. The functional form of the instability can be interpreted as a Bardeen-Cooper-Schrieffer (BCS)-like model where the particle-hole interactions creates a boson $b^{\dagger}_{\mathbf{k}} = \psi^{\dagger}_{\mathbf{k}+}\psi^{\dagger}_{\bar{\mathbf{k}}-}$, composed by two fermions with the same momentum vector $\mathbf{k}$ but opposite pseudospin $s = \pm$. Current efforts are focused on describing the new ground state of the system, yielding the approach we can follow to extend bosonization to gapped systems.

The bosonization formalism is not only valid to describe electron interactions in graphene, but also 2D Dirac fermions as low-energy modes on the boundary of 3D topological insulators. Moreover, the procedure is valid for higher-dimensional systems such as 3D Weyl semimetals [AMV18] where the *gaplessness* is topologically protected and the Fermi surface at the charge neutrality is also shrunk to a point. The main goal in forthcoming works are devoted to extend the bosonization procedure my relaxing the assumptions we have done to obtain the bosonic Hamiltonian (9.3): gapless fermions, $\mathbf{Q} = 0$ PHEs, partcle-hole symmetric band structure, two-band models and charge neutrality. Two examples of procedures we can follow to achieve the generalization can be discussed for gapped and doped systems. In the one hand, bosonization for gapped fermions can involve contributions of the $s^z_{\mathbf{k}}$ component of the pseudospin to the non-interacting ground state, as it is expected to be observed for bilayer graphene. On the other hand, doped systems imply the existence of two types of PHEs: intraband and interband excitations. Intraband PHEs only occured in the partially-filled band as excitations close to the finite Fermi surface, describable with bosonization discussed in the review It is possible to generalize the formalism to $\mathbf{Q} \neq 0$ PHEs, enabling the formalism to address new physical systems such as excitonic condensation in different materials such as $1T - \text{TiSe}_2$ [Mon+09] and WTe_2 [Sun+22; Jia+22].

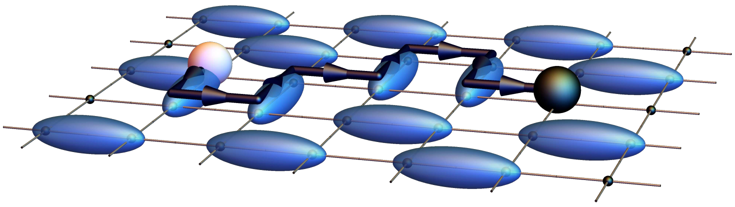

Part IV

APPENDICES

Appendix A contains a brief overview of Bethe Ansatz and the Yang-Yang ground state energies of the XXZ chain. App. B discusses the Kadanoff-Baym (KB) self-consistent Hartree-Fock (SCHF) approximation as a consistency proof of bosonization of Dirac fermions. App. C shows a short calculation of the optical conductivity of Dirac fermions using pseudospin precession formalism. Lastly, App. D discusses the momentum lattice reparametrization to resemble symmetries of the system in continuum limit.

A

YANG & YANG'S EXPRESSIONS OF GROUND STATE ENERGY OF XXZ CHAIN USING BETHE ANSATZ

The article series [YY66a; YY66b; YY66c; YY66d] treats in detail and rigurously the problem on finding explicit expressions the ground state of the Hamiltonian

$$H = -\frac{1}{2}\sum_{i=1}^{N}\left[\sigma_i^x\sigma_{i+1}^x + \sigma_i^y\sigma_{i+1}^y + \Delta\sigma_i^z\sigma_{i+1}^z\right], \tag{A.1}$$

where $\sigma_i^{x,y,z}$ are the Pauli matrices, normalized as $\left(\sigma_i^{x,y,z}\right)^2 = 1$, acting as operators on a spin-1/2 at the site $i = 1, ..., N$, and Δ is a parameter controlling the anisotropy of the chain.

The magnetization per site y is defined as the eigenvalue of the operator[YY66a]

$$Y = \frac{1}{N}\sum_i \sigma_i^z, \tag{A.2}$$

and states the problem of calculating the function

$$f(\Delta, y) = \lim_{N\to\infty}\frac{E_0}{Nz}, \tag{A.3}$$

where E_0 is the lowest eigenvalue of (A.1) for a fixed magnetization y, and z is the number of NN at each site, begin $z = 2$ for the 1D periodic chain.

A.1 BETHE ANSATZ

The solution proposed in [YY66b; YY66c] follows from the *Bethe Ansatz*, a expansion in plane waves of all the permutation of m down-spins respect to a reference state in which all the sites are in up-spin states[Fra+17]. The eigenstates of the Hamiltonian (A.1) are then proposed to be of te form

$$|\psi\rangle = \sum_P A_P e^{i\sum_j p_{P_j} x_j}, \tag{A.4}$$

where P are all the possible permutations of m sites where the down-spins are located, the *quasi-momenta* p_j are in the intervals

$$\begin{array}{rcl} -\pi < p_j < \pi & \text{for} & \Delta \leq 1, \\ -(\pi-\mu) < p_j < \pi-\mu & \text{for} & -1 \leq \Delta < 1, \end{array} \tag{A.5}$$

where $\Delta = -\cos\mu$ with $0 \leq \mu < \pi$, and complementarily $\Delta = -\cosh\lambda$ with $\lambda > 0$ when $\Delta \leq 1$. In order to have (A.4) as a solution of (A.1) and satisfy the eigenvalue equation $H\left|\psi\right\rangle = E\left|\psi\right\rangle$, the energy E should be

$$E = -\frac{N\Delta}{2} + \sum_{j=1}^{m} 2\left(\Delta - \cos p_j\right), \tag{A.6}$$

and using (A.6), the amplitudes must fulfill the conditions

$$\frac{A_P}{A_{P'}} = e^{i\Theta(p,q)} = -\frac{2\Delta e^{ip} - 1 - e^{i(p+q)}}{2\Delta e^{iq} - 1 - e^{i(p+q)}}, \tag{A.7}$$

where P and P' differ only in the interchange of the quasi-momenta p and q, and $\Theta(p,q)$ is the *scattering phase*. This is satisfied for the solutions if the *Bethe equations*:

$$Np_j = 2\pi I_j - \sum_{l\neq j}^{m} \Theta(p_j, p_l). \tag{A.8}$$

In the continuum limit when N and $m \to \infty$ with m/N finite, (A.8) can be expressed as

$$p = 2\pi f - \int \Theta(p,q)\rho(q)dq \tag{A.9}$$

where $f = I/N$ and $df/dp = \rho(p)$ is the number of states in the interval p and $p + dp$. The magnetization is then reexpressed as

$$\frac{1}{2}(1-y) = \frac{m}{N} = \int_{-Q}^{Q} \rho(p)dp, \tag{A.10}$$

and alongside (A.6), the energy density is now

$$f(\Delta, f) = -\frac{\Delta}{4} + \frac{\Delta}{2}(1-y) - \int_{-Q}^{Q} \rho(p)\cos p dp \rho(p)dp. \tag{A.11}$$

From (A.10), by fixing the magnetization y, we can obtain the limits $-Q$ and Q of the integral, which are then used in (A.11) to determine the energy density[YY66b; YY66c].

A.2 EXPLICIT FORMULAS FOR $f(\Delta, 0)$

The reference [YY66c] presents a piece-wise function $f(v,y)$ spanning the three phases displayed by the XXZ chain[Fra+17; Bon87]:

1. $1 < \Delta$: a gapped FM phase with maximal magnetization at the ground state given by $|0\rangle = \bigotimes_{i=1}^{N} |\uparrow_i\rangle$. The expression of $f(v,0)$ is given by

$$f(\Delta, 0) = -\frac{\Delta}{4}, \tag{A.12}$$

2. $\Delta = 1$: a gapless isotropic FM with symmetry SU(2), and *magnons* as excitations as well as *strings* or *complexes*, bound states of clustered flipped spins.

3. $-1 < \Delta < 1$ a gapless paramagnetic phase. At $\Delta = 0$ the system becomes a XX model, non-interacting, and describable by free fermions using the JW transformations. The expression of $f(v, 0)$ is given by

   $$f(\Delta, 0) = \frac{\cos\mu}{4} - \frac{\sin\mu}{\mu}\int_{-\infty}^{\infty} \frac{\mu \sin\mu dx}{2\cos(\pi x)(\cosh(2\mu x) - \cos\mu)}, \quad \text{(A.13)}$$

   where $\Delta = -\cos\mu$ with $0 \leq \mu < \pi$,

4. $\Delta = -1$: a gapless isotropic AFM phase with *spinons* as spin-1/2 excitations. The expression of $f(v, 0)$ is given by

   $$f(\Delta, 0) = \frac{1}{4} - \ln 2, \quad \text{(A.14)}$$

5. $\Delta < -1$: a gapped AFM phase with two degenerate ground states $|0_{\uparrow\downarrow}\rangle = \bigotimes_{i=\text{odd}}^{N} |\uparrow_i \downarrow_{i+1}\rangle$ and $|0_{\downarrow\uparrow}\rangle = \bigotimes_{i=\text{odd}}^{N} |\downarrow_i \uparrow_{i+1}\rangle$, and excitations described as *domain walls* where the two states $|0_{\uparrow\downarrow}\rangle$ and $|0_{\downarrow\uparrow}\rangle$ appear in the chain with two consecutive alinged spins. The expression of $f(v, 0)$ is given by

   $$f(\Delta, 0) = \frac{\cosh\lambda}{4} - \frac{\sinh\lambda}{\lambda}\left(\frac{\lambda}{2} + 2\lambda \sum_{n=1}^{\infty} \frac{1}{1 + e^{2\lambda n}}\right), \quad \text{(A.15)}$$

   where $\Delta = -\cosh\lambda$ with $\lambda > 0$.

B

KADANOFF-BAYM (KB) SELF-CONSISTENT HARTREE-FOCK (SCHF) APPROXIMATION

The bosonization technique presented in chapter 6 consisted on transforming the Hamiltonian of 2D Dirac fermions in (5.39) and (6.2)

$$\begin{aligned} H = v &\sum_{\mathbf{k},\sigma,\sigma'} \psi^{\dagger}_{\mathbf{k},\sigma} \left(\mathbf{k}\cdot\boldsymbol{\sigma}_{\sigma\sigma'}\right) \psi_{\mathbf{k},\sigma'} \\ &+ \frac{1}{2A} \sum_{\mathbf{k}\mathbf{k}'} \sum_{\sigma\sigma'} V_{\mathbf{q}} \psi^{\dagger}_{\mathbf{k}'+\mathbf{q},\sigma'} \psi^{\dagger}_{\mathbf{k}-\mathbf{q},\sigma} \psi_{\mathbf{k},\sigma} \psi_{\mathbf{k}',\sigma'}, \end{aligned} \tag{B.1}$$

deduced from the molecular structure of graphene in chapter 5, into a new quadratic bosonic Hamiltonian that describe the physics of excitons in the $\mathbf{Q} = 0$ sector. Such a Hamiltonian in (6.16) is given by

$$H_{HP} = \sum_{\mathbf{k},\mathbf{k}'} B^{\dagger}_{\mathbf{k}} H_{\mathbf{k}\mathbf{k}'} B_{\mathbf{k}'}, \tag{B.2}$$

in the Bogoliubov basis in (6.15):

$$B^{\dagger}_{\mathbf{k}} = \begin{pmatrix} b^{\dagger}_{\mathbf{k}} & b_{\mathbf{k}} \end{pmatrix}. \tag{B.3}$$

The matrix elements of (B.2) are given by

$$H_{\mathbf{k}\mathbf{k}'} = \delta_{\mathbf{k}\mathbf{k}'} \begin{pmatrix} 2E_{\mathbf{k}} & 0 \\ 0 & -2E_{\mathbf{k}} \end{pmatrix} - T_{\mathbf{k}\mathbf{k}'}, \tag{B.4}$$

with $E_{\mathbf{k}} = v|\mathbf{k}| + \Sigma_{\mathbf{k}}$ the dressed kinetic energy, $\Sigma_{\mathbf{k}}$ the Hartree-Fock self-energy and $T_{\mathbf{k}\mathbf{k}'}$ the interaction matrix in the band basis:

$$T_{\mathbf{k}\mathbf{k}'} = \frac{V_{\mathbf{k}_0-\mathbf{k}_f}}{4A} \begin{pmatrix} 1+\cos\phi_{\mathbf{k}\mathbf{k}'} & 1-\cos\phi_{\mathbf{k}\mathbf{k}'} \\ 1-\cos\phi_{\mathbf{k}\mathbf{k}'} & 1+\cos\phi_{\mathbf{k}\mathbf{k}'} \end{pmatrix}. \tag{B.5}$$

This appendix is then devoted to present the calculation of the particle-hole propagator incluing all the terms of the KB SCHF resummation using a Bethe-Salpeter ladder (see FIG. B.2) and show that is exactly equivalent to the propagator of the modes described by the Hamiltonian (B.2).

B.1 DETAILS OF CONNECTION TO PERTURBATION THEORY

B.1.1 *Bare and dressed fermion propagators*

The propagator of the Dirac fermions without interactions described by the Hamiltonian (5.34) in the band basis is given by:

$$G^{(0)}_{ss'}(\omega,\mathbf{k}) = \mathbf{k}s \bullet\!\!\longrightarrow\!\!\bullet\; \mathbf{k}s' = \frac{\delta_{ss'}}{\omega - s(v|\mathbf{k}| - i\eta)}. \tag{B.6}$$

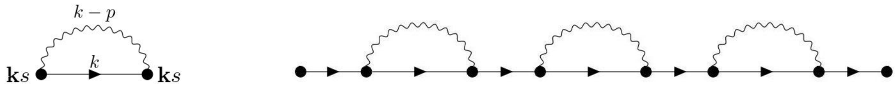

(a) One-loop self-energy.

(b) Successive self-energy insertions in the propagator of a free fermion.

Figure B.1: *Dressed propagator as a Dyson series*: The interactions modify the propagator of the 2D Dirac fermions resulting in a modification of the dispersion relation found in (5.34).

The corresponding Hartree-Fock self-energy of the fermions is:

$$\Sigma_{\mathbf{k}} =$$

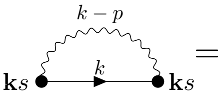

$$= \frac{1}{2A}\sum_{\mathbf{p}} V_{\mathbf{k}-\mathbf{p}} \cos\phi_{\mathbf{kp}}. \tag{B.7}$$

Then, the self-energy corrections to the bare propagator can be arranged in a Dyson series, as shown in FIG. B.1b, to get the dressed fermionic propagator:

$$G_{ss'}(\omega, \mathbf{k}) \quad =$$

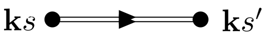

$$= \frac{\delta_{ss'}}{\omega - s(E_{\mathbf{k}} - i\eta)}, \tag{B.8}$$

where $E_{\mathbf{k}} = v|\mathbf{k}| + \Sigma_{\mathbf{k}}$. Equivalently, the dressed propagator in matrix notation in the band basis can be expressed as:

$$G^{-1}(\omega, \mathbf{k}) = \begin{pmatrix} \omega - E_{\mathbf{k}} + i\eta & 0 \\ 0 & \omega + E_{\mathbf{k}} - i\eta \end{pmatrix}. \tag{B.9}$$

B.1.2 *Bethe-Salpeter ladder*

The particle-hole propagator (6.20), given by

$$\chi^{s_1 s_2}_{\mathbf{k}_1 \mathbf{k}_2}(t) = -iT\left\langle \psi^{\dagger}_{\mathbf{k}_1 s_1}(t)\psi_{\mathbf{k}_1 \bar{s}_1}(t)\psi^{\dagger}_{\mathbf{k}_2 \bar{s}_2}(0)\psi_{\mathbf{k}_2 s_2}(0)\right\rangle, \tag{B.10}$$

can be explicitely calculated using the Kadanoff-Baym (KB) conserving approximation that results from the Self-Consistent Hartree-Fock (SCHF) approximation to the single particle Green function, consisting in the sum of the infinite series of the Bethe-Salpeter ladder (see FIG. B.2) for the particle-hole propagator, with internal Hartree-Fock (HF)-dressed Green functions such as (B.9).

The zeroth order (no interaction lines piercing the particle or hole propagators) of the series, shown in FIG. B.2a, is given by

$$\begin{aligned} \chi^{(0)ss'}_{\mathbf{k}}(\omega) &= -\int \frac{d\nu}{2\pi i} G_{\mathbf{k}s}(\omega + \nu) G_{\mathbf{k}s'}(\nu) \\ &= -\int \frac{d\nu}{2\pi i} \frac{1}{(\omega + \nu) + s'(E_{\mathbf{k}} - i\eta)} \frac{1}{\nu + s(E_{\mathbf{k}} - i\eta)} \\ &= -\delta_{s',\bar{s}} \left(\frac{\delta_{s,+} - \delta_{s,-}}{\omega - (s - s')(E_{\mathbf{k}} - i\eta)} \right), \end{aligned} \tag{B.11}$$

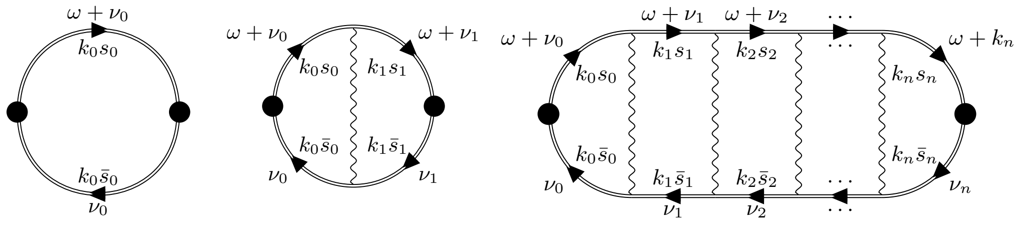

(a) (b) (c)

Figure B.2: *Bethe-Salpeter ladder of the self-consistent Hartree-Fock approximation*: Diagrams associated to the zeroth (a), first (b) and n-order (c) corrections of the Bethe-Salpeter ladder[MS20].

with the corresponding matrix expression in the band basis:

$$\chi^{(0)}_{\mathbf{k}_0}(\omega) = \begin{pmatrix} \frac{-1}{\omega+(2E_{\mathbf{k}_0}-i\eta)} & 0 \\ 0 & \frac{1}{\omega-(2E_{\mathbf{k}_0}-i\eta)} \end{pmatrix}. \tag{B.12}$$

The next terms of the series involves interaction lines connecting the particle and hole propagators, which can be included using the interaction matrix from Eq. (B.5). The diagram involved at first order in the Bethe-Salpeter ladder is shown in the Fig. B.2b, and is given by (summation on any repeated index is assumed):

$$\chi^{(1)s_0 s_f}_{\mathbf{k}_0\mathbf{k}_f}(\omega) = \chi^{(0)s_0 s_f}_{\mathbf{k}_0\mathbf{k}_f}(\omega) + \chi^{(0)s_0}_{\mathbf{k}_0}(\omega)\, T^{s_0 s_f}_{\mathbf{k}_0\mathbf{k}_f}\, \chi^{(0)s_f}_{\mathbf{k}_f}(\omega). \tag{B.13}$$

where $\chi^{(0)s_0}_{\mathbf{k}_0}$ is a short-hand of $\chi^{(1)s_0 s_f}_{\mathbf{k}_0\mathbf{k}_f}$ that has into account that it is non-zero when $\mathbf{k}_0 = \mathbf{k}_f$ and $s_0 s_f$. Similarly the n-th term of the series, shown in Fig. B.2c, is given by

$$\begin{aligned} \chi^{(n)s_0 s_f}_{\mathbf{k}_0\mathbf{k}_f}(\omega) &= \chi^{(0)s_0 s_f}_{\mathbf{k}_0\mathbf{k}_f}(\omega) + \chi^{(0)s_0}_{\mathbf{k}_0}(\omega)\, T^{s_0 s_f}_{\mathbf{k}_0\mathbf{k}_1}\, \chi^{(0)s_f}_{\mathbf{k}_f}(\omega) \\ &+ \chi^{(0)s_0}_{\mathbf{k}_0}(\omega)\, T^{s_0 s_1}_{\mathbf{k}_0\mathbf{k}_1}\, \chi^{(0)s_1}_{\mathbf{k}_1} \cdots \chi^{(0)s_{n-1}}_{\mathbf{k}_{n-1}}\, T^{s_{n-1}s_f}_{\mathbf{k}_{n-1}\mathbf{k}_f}\, \chi^{(0)s_f}_{\mathbf{k}_n}(\omega). \end{aligned} \tag{B.14}$$

B.1.3 *Particle-hole propagator and comparison to HP boson propagator*

The full summation can therefore be expressed as a geometric series:

$$\begin{aligned} \chi(\omega) &= \chi^0(\omega) + \chi^0(\omega) T \chi^0(\omega) + \chi^0(\omega) T \chi^0(\omega) T \chi^0(\omega) + \cdots \\ &= \chi^0(\omega) + \chi^0(\omega) T \left(\chi^0(\omega) + \chi^0(\omega) T \chi^0(\omega) + \cdots \right), \end{aligned} \tag{B.15}$$

which correspond to a Dyson-like equation for the dressed particle-hole propagator $\chi(\omega)$:

$$\chi^{s_0 s_f}_{\mathbf{k}_0\mathbf{k}_f}(\omega) = \chi^{(0)s_0 s_f}_{\mathbf{k}_0\mathbf{k}_f}(\omega) + \chi^{(0)s_0}_{\mathbf{k}_0}(\omega)\, T^{s_0 s_1}_{\mathbf{k}_0\mathbf{k}_1}\, \chi^{s_1 s_f}_{\mathbf{k}_1\mathbf{k}_f}(\omega), \tag{B.16}$$

whose solution is given by:

$$\left(\chi^{-1}\right)^{s_0 s_f}_{\mathbf{k}_0\mathbf{k}_f}(\omega) = \delta^{s_0 s_f}_{\mathbf{k}_0\mathbf{k}_f} \left(\chi^{(0)-1}\right)^{s_0}_{\mathbf{k}_0}(\omega) + T^{s_0 s_f}_{\mathbf{k}_0\mathbf{k}_f}. \tag{B.17}$$

Replacing the results from Eq. (B.12) and (B.5), the explicit expression of the particle-hole propagator is:

$$\begin{aligned}\chi^{-1}_{\mathbf{k}_0\mathbf{k}_f}(\omega) = &-\begin{pmatrix}\omega + 2E_{\mathbf{k}_0} - i\eta & 0 \\ 0 & \omega - 2E_{\mathbf{k}_0} - i\eta\end{pmatrix} \\ &- \frac{V_{\mathbf{k}_0-\mathbf{k}_f}}{4A}\begin{pmatrix}1+\cos\phi_{0f} & 1-\cos\phi_{0f} \\ 1-\cos\phi_{0f} & 1+\cos\phi_{0f}\end{pmatrix}.\end{aligned} \tag{B.18}$$

or, by using the definition of the HP Hamiltonian in (6.16) of the main text we get the final expression of the exciton propagator, given by

$$\chi^{-1}_{\mathbf{k}_0\mathbf{k}_f}(\omega) = -(\omega - i\eta)\tau^z\delta_{\mathbf{k}_0\mathbf{k}_f} - H_{\mathbf{k}_0\mathbf{k}_f}, \tag{B.19}$$

where τ^z is the z-Pauli matrix.

The structure of this correlator is identical to the propagator of the HP bosons of the Hamiltonian (6.16). From the above, we can assert that the full resummation of the KB conserving approximation associated with SCHF is equivalent to solving the HP bilinear boson problem.

C

OPTICAL CONDUCTIVITY FROM PSEUDOSPIN PRECESSION

This chapter is devoted to present the *pseudospin precession formalism*[Kat12], consisting on taking the picture of the pseudospin (and indeed the sublattice ocupation) as a vector precessing about the direction of the oscillatory electric field of an electromagnetic wave, in a similar fashion to the Larmor precession of a magnetic dipole about a magnetic field. The optical conductivity for $T = 0$ given by

$$\sigma_0 = \frac{e^2}{4\hbar}, \tag{C.1}$$

is the keystone of the research presented in chapter 7.

C.1 MINIMAL COUPLING AND BAND (ELECTRON-HOLE) BASIS

The interacion of Dirac fermions with the electromagnetic field is described by the Dirac Hamiltonian with the minimal coupling to the vector potential **A**

$$\hat{H} = \hbar v \sigma \cdot (\mathbf{p} - e\mathbf{A}) = \hbar v \sigma \cdot \left(\mathbf{p} + \frac{ie}{2\omega}\mathbf{E}\right) \tag{C.2}$$

described by a monochromatic plane wave whose wave vector is normal to the xy plane, so **A** and therefore **E** lie on the plane

$$\begin{aligned} \mathbf{A}(t) &= \mathbf{A}_0 \exp(-i\omega t) \\ \mathbf{E}(t) &= -\frac{\partial}{\partial t}\mathbf{A}(t) = i\omega\mathbf{A}_0 \end{aligned} \tag{C.3}$$

The Dirac Hamiltonian in the momentum basis with minimal coupling to the electromagnetic field can be expressed as

$$\hat{H} = \sum_{\mathbf{p}} \psi^\dagger_{\mathbf{p}} \left(v\sigma \cdot \mathbf{p} - ie\mathbf{E} \cdot \boldsymbol{\nabla}_{\mathbf{p}}\right) \psi_{\mathbf{p}} \tag{C.4}$$

where $\psi^\dagger_{\mathbf{p}} = (\psi^\dagger_{\mathbf{p}\uparrow}, \psi^\dagger_{\mathbf{p}\downarrow})$ are the electron creation operators in sublattices A or B in the pseudospin basis. With the transformation

$$\begin{pmatrix} \psi_{\mathbf{k}A} \\ \psi_{\mathbf{k}B} \end{pmatrix} = \frac{1}{\sqrt{2}} \begin{pmatrix} 1 & 1 \\ e^{i\phi_{\mathbf{k}}} & -e^{i\phi_{\mathbf{k}}} \end{pmatrix} \begin{pmatrix} \xi_{\mathbf{k}1} \\ \xi_{\mathbf{k}2} \end{pmatrix} \tag{C.5}$$

the free Dirac Hamiltonian is diagonalized by the hole and electron operators $(\xi_{\mathbf{k}1}, \xi_{\mathbf{k}2})$

$$\hat{H}_0 = \sum_{\mathbf{k}} \hbar v k \left(\xi^\dagger_{\mathbf{k}2}\xi_{\mathbf{k}2} - \xi^\dagger_{\mathbf{k}1}\xi_{\mathbf{k}1}\right) \tag{C.6}$$

C.2 EQUATIONS OF MOTION OF CHARGE AND PSEUDOSPIN DENSITIES

The time evolution of the density matrix is given by

$$i\hbar\frac{\partial\hat{\rho}_{\mathbf{k}}}{\partial t} = \left[\hat{H},\hat{\rho}_{\mathbf{k}}\right] = \hbar v\mathbf{k}\left[\hat{\sigma},\hat{\rho}_{\mathbf{k}}\right] - e(\mathbf{E}\cdot\nabla_{\mathbf{k}})\hat{\rho}_{\mathbf{k}}. \tag{C.7}$$

The density matrix can be expressed as $\hat{\rho}_{\mathbf{k}} = n_{\mathbf{k}}\hat{1} + m_{\mathbf{k}}\hat{\sigma}$, where $n_{\mathbf{k}}$ and $m_{\mathbf{k}}$ are the charge and pseudospin densities.

$$\begin{aligned}\frac{\partial n_{\mathbf{k}}}{\partial t} &= -\frac{e}{\hbar}(\mathbf{E}\cdot\nabla_{\mathbf{k}})n_{\mathbf{k}}\\ \frac{\partial \mathbf{m}_{\mathbf{k}}}{\partial t} &= -\frac{e}{\hbar}(\mathbf{E}\cdot\nabla_{\mathbf{k}})\mathbf{m}_{\mathbf{k}} + 2v(\mathbf{k}\times\mathbf{m}_{\mathbf{k}})\end{aligned} \tag{C.8}$$

Since the average current is given by $\mathbf{j} = \mathrm{Tr}(\hat{j}\hat{\rho}_{\mathbf{k}}) = 2ev\sum_{\mathbf{k}}\mathbf{m}_k$, only the pseudospin equation is required.

The equation is solved with the pseudospin $\mathbf{m}_{\mathbf{k}}(t) = \mathbf{m}^0_{\mathbf{k}} + \delta\mathbf{m}_{\mathbf{k}}e^{-i\omega t}$ where the second contribution is proportional to the oscillating electric field, $\delta\mathbf{m}_{\mathbf{k}} \sim \mathbf{E}_0$, so it lies on the xy plane. The equation of motion of $\mathbf{m}_{\mathbf{k}}$ gets the new form

$$\frac{\partial \delta\mathbf{m}_{\mathbf{k}}}{\partial t} = -\frac{e}{\hbar}(\mathbf{E}\cdot\nabla_{\mathbf{k}})\mathbf{m}_{\mathbf{k}} + 2v(\mathbf{k}\times\delta\mathbf{m}_{\mathbf{k}}) \tag{C.9}$$

The z-component of $\delta\mathbf{m}_{\mathbf{k}}$ only precess about $\mathbf{k}$ and can be replaced in the equations of motion of x and y components.

C.3 OPTICAL CONDUCTIVITY FROM FERMI-DIRAC DISTRIBUTIONS AT FINITE TEMPERATURE

By choosing $\mathbf{E}_0$ along the x direction, $j_x = \sigma(\omega)E$, where $\sigma(\omega)$ is the optical conductivity of the Dirac fermions

$$\sigma(\omega,T) = -\frac{8ie^2v^3}{\hbar\omega}\sum_{\mathbf{k}}\frac{k_y}{\omega^2-4v^2k^2}\left(k_y\frac{\partial m^{x(0)}_{\mathbf{k}}}{\partial k_x} - k_x\frac{\partial m^{x(0)}_{\mathbf{k}}}{\partial k_y}\right) \tag{C.10}$$

The static contribution to the pseudospin $\hat{\mathbf{m}}_{\mathbf{k}}$ is obtained from the thermal equilibrium of the hole-electron operators $\langle\xi^{\dagger}_{\mathbf{k}A(B)}\xi_{\mathbf{k}A(B)}\rangle = f_{\mathbf{k}1(2)}$ given by Fermi-Dirac distributions with energies $\mp\hbar vk$. So that,

$$\mathbf{m}^{(0)}_{\mathbf{k}} = \frac{\mathbf{k}}{2k}(f_{\mathbf{k}1} - f_{\mathbf{k}2}) \tag{C.11}$$

Consequently, the optical conductivity is given by

$$\sigma(\omega,T) = -\frac{2ie^2v^3}{\hbar\omega}\sum_{\mathbf{k}}\frac{k(f_{\mathbf{k}1}-f_{\mathbf{k}2})}{(\omega+i\delta)^2-4v^2k^2} \tag{C.12}$$

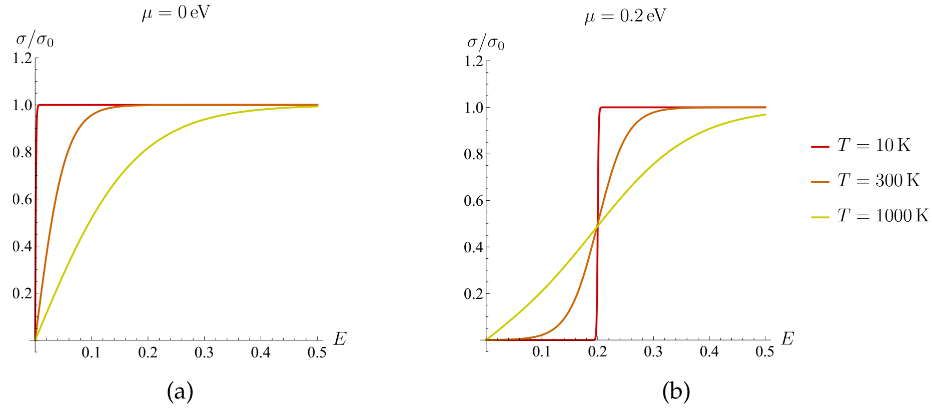

Figure C.1: *Optical conductivity vs. energy for graphene at finite temperature with noninteracting electrons*: The optical conductivity for noninteracting Dirac fermions is given by the constant $\sigma_0 = e^2/4\hbar$ times a Heviside function that *turns on* the response for energies above the chemical potential, i. e., (a) the Dirac point energy when $\mu = 0$, and (b) a finite chemical potential $\mu > 0$. Finite temperature populates states above the chemical potential, modifying the shape of the optical conductivity in accordance to the Fermi-Dirac distribution $f(E)$.

$$\begin{aligned}\mathrm{Re}\sigma(\omega, T) &= \frac{\pi e^2 v^2}{2\hbar\omega}\sum_{\mathbf{k}}(f_{\mathbf{k}1} - f_{\mathbf{k}2})\delta(\omega - 2vk) \\ &= \frac{e^2}{16\hbar}\left\{f\left(-\frac{\hbar\omega}{2}\right) - f\left(+\frac{\hbar\omega}{2}\right)\right\}\end{aligned} \tag{C.13}$$

The universal conductivity of graphene with the four-fold degeneracy of valley/spin electrons at $T = 0\,\mathrm{K}$ is

$$\mathrm{Re}\sigma(\omega, 0) = \begin{cases} 0, & \omega < 2|\mu| \\ \frac{e^2}{4\hbar}, & \omega > 2|\mu| \end{cases} \tag{C.14}$$

D

MOMENTUM SPACE REPARAMETRIZATION

The block diagonalization of quadratic Hamiltonians such as the Bogoliubov Hamiltonian in (6.16) not only easen the implementation of exact diagonalization, but also offers a richer description of the physical systems involved. Especially, systems with rotational symmetry in the reciprocal space are block-diagonalizable by means of angular momentum channels. This requires to take the system in the Cartesian lattice of departure (see FIG. D.1a) and evaluate the continuum limit to rediscretize it into a polar lattice (see FIG. D.1b) where the angular momentum channels can be extracted. The whole procedure must preserve the volume of the phase space and the commutation relations of the operators. This chapter is devoted to the procedure of lattice reparametrization used in the research presented in chapter 7.

D.1 GENERAL COORDINATE TRANSFORMATIONS ON THE CONTINUUM LIMIT

First, the quadratic Hamiltonian in the Bogoliubov basis (6.16):

$$H_{HB} = \sum_{\mathbf{k}\mathbf{k}'} B^{\dagger}_{\mathbf{k}} H_{\mathbf{k}\mathbf{k}'} B_{\mathbf{k}'}, \tag{D.1}$$

originally expressed in the square lattice (see FIG. D.1a) is reexpressed in the continuum limit by defining new rescaled Hamiltonian and boson operators as follows (see FIG. D.1b):

$$B(\mathbf{k}) \equiv \lim_{\Delta k \to 0} \frac{B_{\mathbf{k}}}{\sqrt{\Delta k_x \Delta k_y}}, \tag{D.2a}$$

$$H(\mathbf{k}, \mathbf{k}') \equiv \lim_{\Delta k \to 0} \frac{H_{\mathbf{k}\mathbf{k}'}}{\Delta k_x \Delta k_y}, \tag{D.2b}$$

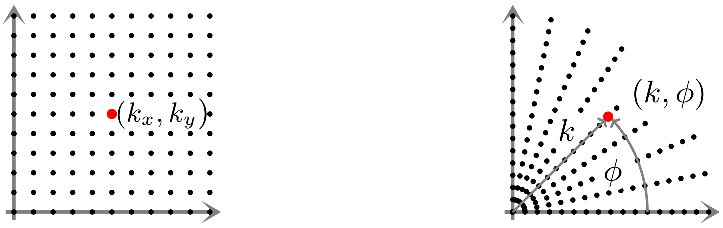

(a) (b)

Figure D.1: *Coordinate systems in the reciprocal space*: (a) Original squared lattice, (b) polar lattice (k_m, ϕ_n).

where $\Delta k_{x,y} = 2\pi/\sqrt{A}$, A is the area of the system that is assumed squared. The discrete lattice of momenta with square symmetry is depicted in D.1a. The above re-definitions allow to obtain the following continuum commutation relations for the Bogoliubov boson operators:

$$\left[B(\mathbf{k}), B^{\dagger}(\mathbf{k}')\right] = \lim_{\Delta k \to 0} \mathbb{I}\frac{\delta_{\mathbf{k}\mathbf{k}'}}{(\Delta k)^2} = \mathbb{I}\delta^2(\mathbf{k}-\mathbf{k}'), \tag{D.3}$$

where

$$\mathbb{I} = \begin{pmatrix} 1 & 0 \\ 0 & -1 \end{pmatrix}. \tag{D.4}$$

With these rescalings, the sums over momenta can be securely substituted by continuum integrals, obtaining the continuum version of the boson Hamiltonian H_{HP} from Eq. (D.1):

$$\begin{aligned} \mathcal{H}_{HP} &= \lim_{\Delta k \to 0} \int \frac{d^2k}{(\Delta k)^2} \frac{d^2k'}{(\Delta k)^2} B^{\dagger}_{\mathbf{k}} H_{\mathbf{k}\mathbf{k}'} B_{\mathbf{k}'} \\ &= \lim_{\Delta k \to 0} (\Delta k)^4 \int \frac{d^2k}{(\Delta k)^2} \frac{d^2k'}{(\Delta k)^2} B^{\dagger}_{\sigma}(\mathbf{k}) H(\mathbf{k},\mathbf{k}') B_{\sigma}(\mathbf{k}') \\ &= \int d^2k d^2k' \hat{B}^{\dagger}(\mathbf{k}) H(\mathbf{k},\mathbf{k}') \hat{B}\ (\mathbf{k}'). \end{aligned} \tag{D.5}$$

From this continuum Hamiltonian we can perfom a change of coordinates $\mathbf{k}(\mathbf{z})$ with Jacobian $D(\mathbf{z}) = |\frac{\partial \mathbf{k}}{\partial \mathbf{z}}|$ with the following redefinitions:

$$B(\mathbf{z}) = \sqrt{D(\mathbf{z})} B(\mathbf{k}(\mathbf{z})), \tag{D.6a}$$

$$H(\mathbf{z},\mathbf{z}') = \sqrt{D(\mathbf{z})D(\mathbf{z}')} H(\mathbf{k}(\mathbf{z}),\mathbf{k}(\mathbf{z}')), \tag{D.6b}$$

whose purpose is to mantain the same form of the commutation relations and the Hamiltonian as follows:

$$\left[B(\mathbf{z}), B^{\dagger}(\mathbf{z}')\right] = \mathbb{I}\delta^2(\mathbf{z}-\mathbf{z}'), \tag{D.7a}$$

$$\mathcal{H}_{HP} = \int d^2z d^2z' \hat{B}^{\dagger}(\mathbf{z}) H(\mathbf{z},\mathbf{z}') \hat{B}\ (\mathbf{z}'). \tag{D.7b}$$

Lastly, the new coordinate system is rediscretized into a new lattice (see FIG. D.2c). Thus, the boson and Hamiltonian operators must be rescaled accordingly:

$$B_{\mathbf{z}} \leftarrow \sqrt{\Delta z_1 \Delta z_2} B(\mathbf{z}), \tag{D.8a}$$

$$H_{\mathbf{z},\mathbf{z}'} \leftarrow \Delta z_1 \Delta z_2\, H(\mathbf{z},\mathbf{z}'), \tag{D.8b}$$

that yield the new discrete commutation relations

$$\left[B_{\mathbf{z}}, B^{\dagger}_{\mathbf{z}'}\right] = \mathbb{I}\delta_{\mathbf{z}\mathbf{z}'} \leftarrow \mathbb{I}\Delta k_1 \Delta k_2 \delta^2(\mathbf{z}-\mathbf{z}') \tag{D.9}$$

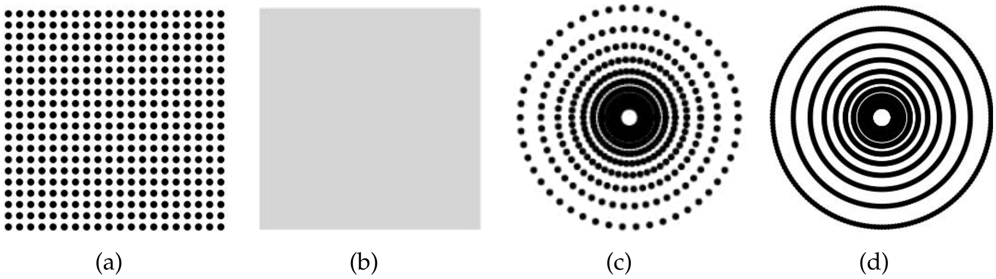

Figure D.2: *Reconfiguration of the momentum lattice*: (a) Original squared lattice, (b) continuum limit, (c) polar lattice (k_m, ϕ_n), and (d) $2L+1$ 1D lattices (k_n) labelled by the angular momentum number ℓ.

and Hamiltonian in the new lattice:

$$H_{HP} = \sum_{\mathbf{z},\mathbf{z}'} B^\dagger_{\mathbf{z}} H_{\mathbf{z}\mathbf{z}'} B_{\mathbf{z}'}. \tag{D.10}$$

Therefore, in summary, the relation between operators and the Hamiltonian matrix in the new lattice defined by the discretization of the coordinates $\mathbf{z}(\mathbf{k})$, with the original operators and Hamiltonian of the square lattice is:

$$B_{\mathbf{z}} = \sqrt{D(\mathbf{z})\frac{\Delta z_1 \Delta z_2}{\Delta k_x \Delta k_y}} B_{\mathbf{k}} \tag{D.11a}$$

$$H_{\mathbf{z}\mathbf{z}'} = \sqrt{D(\mathbf{z})D(\mathbf{z}')}\frac{\Delta z_1 \Delta z_2}{\Delta k_x \Delta k_y} H_{\mathbf{k}\mathbf{k}'} \tag{D.11b}$$

The idea is that the Hamiltonian H_{HP} in Eq. (D.10) will produce the same physical results as the one in the square lattice in Eq. (6.16) of the main text in the thermodynamic limit.

D.2 POLAR RE-DISCRETIZATION

The new coordinate system is $\mathbf{z} = (k, \phi)$, where k is the radius of the momentum vector and ϕ its polar angle (see FIGs. D.1b and D.2c). We parametrize the radial coordinate as a function $k(\theta)$ with the corresponding Jacobian:

$$D(\theta) = k\frac{dk}{d\theta}, \tag{D.12a}$$

where $\mathcal{K}$ is the UV momentum scale, so $\theta \in [0, \pi/2)$ is an affine parameter that labels the radial slices that is chosen to be uniformly discretized, similar to ϕ:

$$\theta_m = m\Delta\theta, \quad m \in \{1, \cdots, M\}, \tag{D.13a}$$

$$\phi_n = n\Delta\phi, \quad n \in \{0, \cdots, 2L\}, \tag{D.13b}$$

where

$$\Delta\theta = \frac{\pi/2}{M+1}, \tag{D.14a}$$

$$\Delta\phi = \frac{2\pi}{2L+1}. \tag{D.14b}$$

After replacing (D.21) and (D.12) into (D.11), the new expressions for $B_{\mathbf{k}}$ and $H_{\mathbf{k}\mathbf{k}'}$ in the polar lattice are:

$$B^n_m = \frac{\mathcal{K}}{2\pi}\sqrt{A\Delta\theta\Delta\phi}\, t_m B^\dagger_{\mathbf{k}_{mn}}, \tag{D.15a}$$

$$H^{nn'}_{mm'} = \frac{\mathcal{K}^2}{(2\pi)^2} A\Delta\theta\Delta\phi\, t_m t_{m'} H_{\mathbf{k}_{mn}\mathbf{k}_{m'n'}}, \tag{D.15b}$$

where $t(\theta_m) = \sqrt{\tan(\theta_m)}\sec(\theta_m)$ and $\mathbf{k}_{mn} = \mathbf{k}(\theta_m, \phi_n)$. Finally, the whole Hamiltonian is

$$H_{HP} = \sum_{mn}\sum_{m'n'} B^{n\dagger}_m H^{nn'}_{mm} B^{n'}_{m'} \,. \tag{D.16}$$

D.3 ANGULAR MOMENTUM CHANNELS

Because the Hamiltonian matrix $H_{\mathbf{k}\mathbf{k}'}$ that enters into the Hamiltonian H_{HP} in (D.1) only depends on the difference between the polar angles $\phi - \phi'$, the angular momentum ℓ of the bosons is a conserved quantitiy and constitute a good quantum number that block-diagonalizes the Hamiltonian (D.16). Consequently, the polar angles for the fields B^n_m and the matrix $H^{nn'}_{mm'}$ are Fourier transformed respect to ϕ (see FIG. D.2d):

$$B^n_m = \frac{1}{\sqrt{2L+1}} \sum_{\ell=-L}^{L} e^{-i\ell\phi_n} B^\ell_{m}, \tag{D.17a}$$

$$H^{nn'}_{mm'} = \sum_{\ell=-L}^{L} e^{-i\ell(\phi_n - \phi_{n'})} H^\ell_{mm'}, \tag{D.17b}$$

such that the total Bogoliubov Hamiltonian decomposes into a direct sum of $2L+1$ 1D Hamiltonians for different angular mommentum channels:

$$H_{HP} = \sum_{mm'\ell} B^{\ell\dagger}_m H^\ell_{mm'} B^\ell_{m'}. \tag{D.18}$$

The problem of calculating the optical conductivity of 2D interacting Dirac fermions is addressed in Chapter 7 using the block-diagonal Hamiltonian in (D.18).

D.4 SELECTION OF THE RADIAL PARAMETRIZATION

We have tried two different discretizations along the radial coordinate:

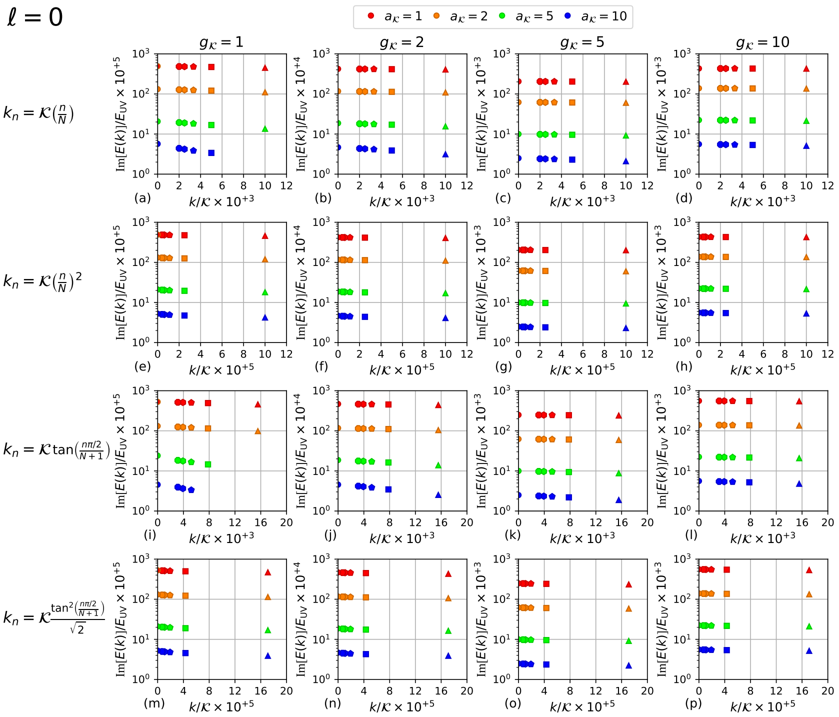

Figure D.3: *First sample of numerical results using different radial parametrizations*. Unstable mode found in bilayer graphene using the Gaussian potential (8.26) in the angular momentum channel $\ell = 0$.

- Discretization by powers of n ($R \in \mathbb{N}$):

$$k_n = \mathcal{K}(n\Delta\theta), \tag{D.19}$$

with Jacobian given by

$$D_n = \mathcal{K}^2 R\Delta k (n\Delta\theta)^{2R-1}, \tag{D.20}$$

and spacing $\Delta\theta = 1/N$.

- Discretization by tangent of n ($R \in \mathbb{N}$):

$$k_n = \frac{\mathcal{K}}{\sqrt{R}} \tan^R(n\Delta\theta), \tag{D.21}$$

with Jacobian given by

$$D_n = K^2 \Delta\theta \sec^2(n\Delta\theta) \tan^{2R-1}(n\Delta\theta), \tag{D.22}$$

and spacing $\Delta\theta = \pi/(2(N+1))$.

FIGs. D.3 and D.4 show a sample of unstable modes derived from the weak coupling instability in bilayer graphene discussed in chapter 8 using exact diagonalization with five different number of radial slices: $N = 100$, 200, 300, 400 and 500. We have used the Gaussian potential (8.26) with $b = 0$ for different couplings and spreadings, where a smaller spreading $a_{\mathcal{K}}$ or

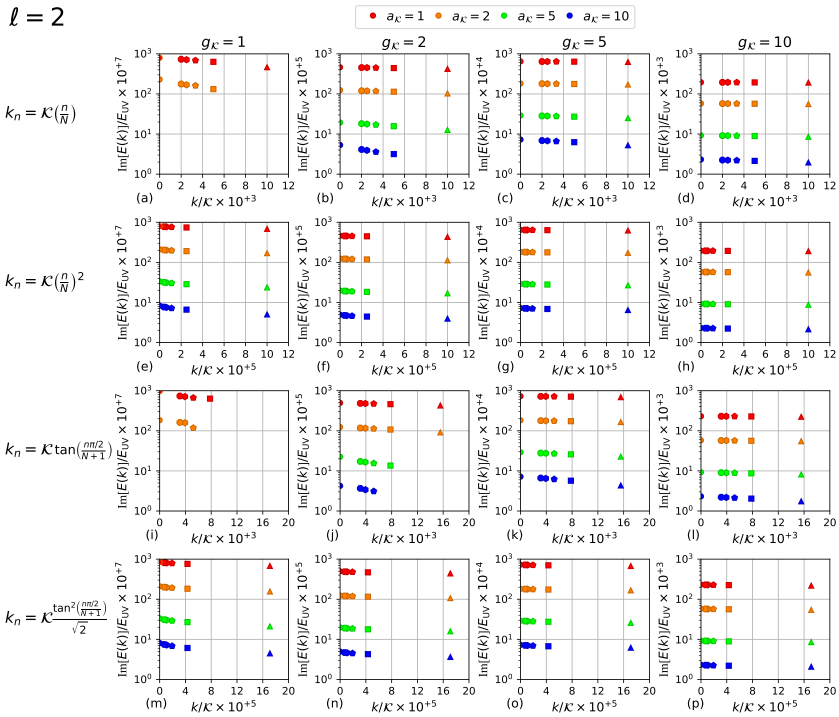

Figure D.4: *Second sample of numerical results using different radial parametrizations*. Unstable mode found in bilayer graphene using the Gaussian potential (8.26) in the angular momentum channel $\ell = 2$.

a larger coupling $g_{\mathcal{K}}$ implies a stronger interaction. The y axis represents the magnitude of the unstable mode, that is, the modulus of the associated imaginary eigenvalue, while the x axis represents the smallest radial slice, $n = 1$, using each parametrization.

We have found two unstable modes in the angular momentum channels $\ell = 0$ and $\ell = 2$, shown in FIG. D.3 and FIG. D.4, respectively. We can see that the tangent parametrization with $R = 2$ is the best one in capturing the unstable modes using the smallest number of radial slices, especially in FIG. D.4 where the power and tangent parametrizations were not able to yield the majority of instabilities for $g_{\mathcal{K}} = 1$ and making impossible to calculate the infinite-size limits $N \to \infty$, plotted as the dots at $k/\mathcal{K} = 0$.

This short analysis made us to use the tangent parametrization of the radial coordinate with $R = 2$ for the problem of the optical conductivity discussed in chapter 7 and $R = 4$ for the search of the weak coupling instability in chapter 8. The different powers R in each problem is the minimum R that yields well-behaved infinite-size limits in each problem.

BIBLIOGRAPHY

[Abe+11] Saeed H Abedinpour, Giovanni Vignale, A Principi, Marco Polini, Wang-Kong Tse, and AH MacDonald. "Drude weight, plasmon dispersion, and ac conductivity in doped graphene sheets." In: *Physical Review B* 84.4 (2011), p. 045429.

[AGD12] Alekseĭ Alekseevich Abrikosov, Lev Petrovich Gorkov, and Igor Ekhielevich Dzyaloshinski. *Methods of quantum field theory in statistical physics*. Courier Corporation, 2012.

[Aid+22] Monika Aidelsburger, Luca Barbiero, Alejandro Bermudez, Titas Chanda, Alexandre Dauphin, Daniel González-Cuadra, Przemysław R Grzybowski, Simon Hands, Fred Jendrzejewski, Johannes Jünemann, et al. "Cold atoms meet lattice gauge theory." In: *Philosophical Transactions of the Royal Society A* 380.2216 (2022), p. 20210064.

[And72] Philip W Anderson. "More is different: broken symmetry and the nature of the hierarchical structure of science." In: *Science* 177.4047 (1972), pp. 393–396.

[And73] Philip W Anderson. "Resonating valence bonds: A new kind of insulator?" In: *Materials Research Bulletin* 8.2 (1973), pp. 153–160.

[AZS02] Tsuneya Ando, Yisong Zheng, and Hidekatsu Suzuura. "Dynamical conductivity and zero-mode anomaly in honeycomb lattices." In: *Journal of the Physical Society of Japan* 71.5 (2002), pp. 1318–1324.

[AMV18] NP Armitage, EJ Mele, and Ashvin Vishwanath. "Weyl and Dirac semimetals in three-dimensional solids." In: *Reviews of Modern Physics* 90.1 (2018), p. 015001.

[Arn89] Vladimir Arnold. "Mathematical methods of classical mechanics Springer-Verlag." In: *New York* (1989).

[Aue12] Assa Auerbach. *Interacting electrons and quantum magnetism*. Springer Science & Business Media, 2012.

[BHR21] Debasish Banerjee, Emilie Huffman, and Lukas Rammelmüller. "Introducing Fermionic Link Models." In: *arXiv preprint arXiv:2111.00300* (2021).

[Ban+13] Debasish Banerjee, FJ Jiang, Philippe Widmer, and Uwe-Jens Wiese. "The (2 + 1)-d U(1) quantum link model masquerading as deconfined criticality." In: *Journal of Statistical Mechanics: Theory and Experiment* 2013.12 (2013), P12010.

[Ban+14] Debasish Banerjee, Michael Bögli, CP Hofmann, F-J Jiang, Philippe Widmer, and U-J Wiese. "Interfaces, strings, and a soft mode in the square lattice quantum dimer model." In: *Physical Review B* 90.24 (2014), p. 245143.

[BFR18] Daniel G Barci, Eduardo Fradkin, and Leonardo Ribeiro. "Bosonization of Fermi liquids in a weak magnetic field." In: *Physical Review B* 98.15 (2018), p. 155146.

[BO00] Daniel G Barci and Luis E Oxman. "Universal transverse conductance between quantum Hall regions and (2+ 1) D bosonization." In: *Nuclear Physics B* 580.3 (2000), pp. 721–738.

[Bar+00] Daniel G Barci, Cesar A Linhares, AF De Queiroz, and JF Medeiros Neto. "Functional bosonization of nonrelativistic fermions in 2+ 1 dimensions." In: *International Journal of Modern Physics A* 15.29 (2000), pp. 4655–4679.

[Bar72] John Bardeen. *Banquet speech. NobelPrize.org*. Nobel Prize Outreach AB 2022. Tue. 29 Mar 2022. Dec. 1972. URL: `https://www.nobelprize.org/prizes/physics/1982/wilson/speech/`.

[BCS57] John Bardeen, Leon N Cooper, and John Robert Schrieffer. "Theory of superconductivity." In: *Physical review* 108.5 (1957), p. 1175.

[Bar+14a] Edwin Barnes, EH Hwang, RE Throckmorton, and S Das Sarma. "Effective field theory, three-loop perturbative expansion, and their experimental implications in graphene many-body effects." In: *Physical Review B* 89.23 (2014), p. 235431.

[Bar+14b] Edwin Barnes, EH Hwang, RE Throckmorton, and S Das Sarma. "Effective field theory, three-loop perturbative expansion, and their experimental implications in graphene many-body effects." In: *Physical Review B* 89.23 (2014), p. 235431.

[BT04] CD Batista and SA Trugman. "Exact ground states of a frustrated 2d magnet: Deconfined fractional excitations at a first-order quantum phase transition." In: *Physical review letters* 93.21 (2004), p. 217202.

[Bay62] Gordon Baym. "Self-consistent approximations in many-body systems." In: *Physical review* 127.4 (1962), p. 1391.

[BK61] Gordon Baym and Leo P Kadanoff. "Conservation laws and correlation functions." In: *Physical Review* 124.2 (1961), p. 287.

[BR+22] Carlos L Benavides-Riveros, Lipeng Chen, Sebastián Mantilla, and Stefano Pittalis. "Excitations of Quantum Many-Body Systems via Purified Ensembles." In: *arXiv preprint arXiv:2201.10974* (2022).

[Ben+18] Y Benhouria, I Bouziani, I Essaoudi, Abdelmajid Ainane, and Rajeev Ahuja. "Quantum Monte Carlo study of dynamic magnetic properties of nano-graphene." In: *Journal of Magnetism and Magnetic Materials* 460 (2018), pp. 223–228.

[BF33] John D Bernal and Ralph H Fowler. "A theory of water and ionic solution, with particular reference to hydrogen and hydroxyl ions." In: *The Journal of Chemical Physics* 1.8 (1933), pp. 515–548.

[BM11] Rafi Bistritzer and Allan H MacDonald. "Moiré bands in twisted double-layer graphene." In: *Proceedings of the National Academy of Sciences* 108.30 (2011), pp. 12233–12237.

[Blo33] Felix Bloch. "Bremsvermögen von Atomen mit mehreren Elektronen." In: *Zeitschrift für Physik* 81 (1933), pp. 363–376.

[BDZ08] Immanuel Bloch, Jean Dalibard, and Wilhelm Zwerger. "Many-body physics with ultracold gases." In: *Reviews of modern physics* 80.3 (2008), p. 885.

[Boe+62] Hans-Peter Boehm, A Clauss, G Fischer, and U Hofmann. "Surface properties of extremely thin graphite lamellae." In: *Proceedings of the fifth conference on carbon*. Vol. 1. Pergamon Press New York, NY, USA. 1962, pp. 73–80.

[Bog58] NN Bogoljubov. "On a new method in the theory of superconductivity." In: *Il Nuovo Cimento (1955-1965)* 7.6 (1958), pp. 794–805.

[Bon87] Jill C Bonner. "Generalized Heisenberg quantum spin chains." In: *Journal of Applied Physics* 61.8 (1987), pp. 3941–3946.

[Boy+16] DL Boyda, VV Braguta, MI Katsnelson, and MV Ulybyshev. "Many-body effects on graphene conductivity: Quantum Monte Carlo calculations." In: *Physical Review B* 94.8 (2016), p. 085421.

[Bra+16] Barry Bradlyn, Jennifer Cano, Zhijun Wang, MG Vergniory, C Felser, Robert Joseph Cava, and B Andrei Bernevig. "Beyond Dirac and Weyl fermions: Unconventional quasiparticles in conventional crystals." In: *Science* 353.6299 (2016), aaf5037.

[BH20] Steven T Bramwell and Mark J Harris. "The history of spin ice." In: *Journal of Physics: Condensed Matter* 32.37 (2020), p. 374010.

[Cao+18] Yuan Cao, Valla Fatemi, Shiang Fang, Kenji Watanabe, Takashi Taniguchi, Efthimios Kaxiras, and Pablo Jarillo-Herrero. "Unconventional superconductivity in magic-angle graphene superlattices." In: *Nature* 556.7699 (2018), pp. 43–50.

[CRS17] Andrea Cappelli, Enrico Randellini, and Jacopo Sisti. "Three-dimensional topological insulators and bosonization." In: *Journal of High Energy Physics* 2017.5 (2017), pp. 1–50.

[CMS08] Claudio Castelnovo, Roderich Moessner, and Shivaji L Sondhi. "Magnetic monopoles in spin ice." In: *Nature* 451.7174 (2008), pp. 42–45.

[CNF95] AH Castro Neto and Eduardo H Fradkin. "Exact solution of the Landau fixed point via bosonization." In: *Physical Review B* 51.7 (1995), p. 4084.

[CNF94a] AH Castro Neto and Eduardo Fradkin. "Bosonization of Fermi liquids." In: *Physical Review B* 49.16 (1994), p. 10877.

[CNF94b] AH Castro Neto and Eduardo Fradkin. "Bosonization of the low energy excitations of Fermi liquids." In: *Physical review letters* 72.10 (1994), p. 1393.

[CNPF06] AH Castro Neto, Pierre Pujol, and Eduardo Fradkin. "Ice: a strongly correlated proton system." In: *Physical Review B* 74.2 (2006), p. 024302.

[CN+09] AH Castro Neto, Francisco Guinea, Nuno MR Peres, Kostya S Novoselov, and Andre K Geim. "The electronic properties of graphene." In: *Reviews of modern physics* 81.1 (2009), p. 109.

[Cha05] Claudio Chamon. "Quantum glassiness in strongly correlated clean systems: An example of topological overprotection." In: *Physical review letters* 94.4 (2005), p. 040402.

[Cha+13] AtMa Chan, Taylor L Hughes, Shinsei Ryu, and Eduardo Fradkin. "Effective field theories for topological insulators by functional bosonization." In: *Physical Review B* 87.8 (2013), p. 085132.

[CW97] Shailesh Chandrasekharan and U-J Wiese. "Quantum link models: A discrete approach to gauge theories." In: *Nuclear Physics B* 492.1-2 (1997), pp. 455–471.

[CMV14] Igor Olegovich Cherednikov, Tom Mertens, and Frederik F Van der Veken. *Wilson lines in quantum field theory*. De Gruyter, 2014.

[Chi+10] Cheng Chin, Rudolf Grimm, Paul Julienne, and Eite Tiesinga. "Feshbach resonances in ultracold gases." In: *Reviews of Modern Physics* 82.2 (2010), p. 1225.

[Cho+19] Youngjoon Choi, Jeannette Kemmer, Yang Peng, Alex Thomson, Harpreet Arora, Robert Polski, Yiran Zhang, Hechen Ren, Jason Alicea, Gil Refael, et al. "Electronic correlations in twisted bilayer graphene near the magic angle." In: *Nature Physics* 15.11 (2019), pp. 1174–1180.

[CS16] Monique Combescot and Shiue-Yuan Shiau. *Excitons and Cooper Pairs: Two Composite Bosons in Many-body Physics*. Oxford University Press, 2016.

[CTV12] Vladimir Cvetkovic, Robert E Throckmorton, and Oskar Vafek. "Electronic multicriticality in bilayer graphene." In: *Physical Review B* 86.7 (2012), p. 075467.

[Dir72] Paul AM Dirac. "The scientific work of Georges Lemaître." In: *Potificiae Acad. Sci* 36 (1972), pp. 67–83.

[Eli+11] DC Elias, RV Gorbachev, AS Mayorov, SV Morozov, AA Zhukov, P Blake, LA Ponomarenko, IV Grigorieva, KS Novoselov, F Guinea, et al. "Dirac cones reshaped by interaction effects in suspended graphene." In: *Nature Physics* 7.9 (2011), pp. 701–704.

[ED79] JP Elliott and PG Dawber. *Symmetry in Physics, Volume 1 and 2*. Macmillan, 1979.

[Fra13] Eduardo Fradkin. *Field theories of condensed matter physics*. Cambridge University Press, 2013.

[Fra+04] Eduardo Fradkin, David A Huse, Roderich Moessner, Vadim Oganesyan, and Shivaji L Sondhi. "Bipartite rokhsar–kivelson points and cantor deconfinement." In: *Physical Review B* 69.22 (2004), p. 224415.

[Fra+17] Fabio Franchini et al. "An introduction to integrable techniques for one-dimensional quantum systems." In: (2017).

[Frö53] H Fröhlich. "Superconductivity and lattice vibrations introduction to a discussion." In: *Physica* 19.1-12 (1953), pp. 755–764.

[Fuc+10] JN Fuchs, F Piéchon, MO Goerbig, and G Montambaux. "Topological Berry phase and semiclassical quantization of cyclotron orbits for two dimensional electrons in coupled band models." In: *The European Physical Journal B* 77.3 (2010), pp. 351–362.

[Gaz+13] Gustavo Gazzola, AL Cherchiglia, LA Cabral, MC Nemes, and Marcos Sampaio. "Conductivity of Coulomb interacting massless Dirac particles in graphene: Regularization-dependent parameters and symmetry constraints." In: *EPL (Europhysics Letters)* 104.2 (2013), p. 27002.

[Gei11] Andre K Geim. "Random walk to graphene." In: *International Journal of Modern Physics B* 25.30 (2011), pp. 4055–4080.

[Gia03] Thierry Giamarchi. *Quantum physics in one dimension*. Vol. 121. Clarendon press, 2003.

[Gil12] Robert Gilmore. *Lie groups, Lie algebras, and some of their applications*. Courier Corporation, 2012.

[GM14] Michel JP Gingras and Paul A McClarty. "Quantum spin ice: a search for gapless quantum spin liquids in pyrochlore magnets." In: *Reports on Progress in Physics* 77.5 (2014), p. 056501.

[GV05] Gabriele Giuliani and Giovanni Vignale. *Quantum theory of the electron liquid*. Cambridge university press, 2005.

[Goe11] MO Goerbig. "Electronic properties of graphene in a strong magnetic field." In: *Reviews of Modern Physics* 83.4 (2011), p. 1193.

[Gol+16] VML Durga Prasad Goli, Suryoday Prodhan, Sumit Mazumdar, and S Ramasesha. "Correlated electronic properties of some graphene nanoribbons: A DMRG study." In: *Physical Review B* 94.3 (2016), p. 035139.

[GGV94] J González, F Guinea, and MAH Vozmediano. "Non-Fermi liquid behavior of electrons in the half-filled honeycomb lattice (A renormalization group approach)." In: *Nuclear Physics B* 424.3 (1994), pp. 595–618.

[Haa11] Jeongwan Haah. "Local stabilizer codes in three dimensions without string logical operators." In: *Physical Review A* 83.4 (2011), p. 042330.

[HL16] Imre Hagymási and Örs Legeza. "Entanglement, excitations, and correlation effects in narrow zigzag graphene nanoribbons." In: *Physical Review B* 94.16 (2016), p. 165147.

[Hal05] FDM Haldane. "Luttinger's theorem and bosonization of the Fermi surface." In: *arXiv preprint cond-mat/0505529* (2005).

[Hal94] Frederick Duncan Michael Haldane. "Luttinger's Theorem and Bosonization of the Fermi Surface." In: *Proceedings of the International School of Physics "Enrico Fermi", Course CXXI: "Perspectives in Many-Particle Physics"*. Ed. by R. Broglia and JR Schrieffer. North Holland, Amsterdam, 1994, pp. 207–216. URL: arXivpreprintcond-mat/0505529.

[Har+97] Mark J Harris, ST Bramwell, DF McMorrow, TH Zeiske, and KW Godfrey. “Geometrical frustration in the ferromagnetic pyrochlore $Ho_2Ti_2O_7$.” In: *Physical Review Letters* 79.13 (1997), p. 2554.

[Hem80] JL van Hemmen. “A note on the Diagonalization of Quadratic Boson and Fermion Hamiltonians.” In: *Zeitschrift für Physik B Condensed Matter* 38.3 (1980), pp. 271–277.

[HJV08] Igor F Herbut, Vladimir Juričić, and Oskar Vafek. “Coulomb interaction, ripples, and the minimal conductivity of graphene.” In: *Physical review letters* 100.4 (2008), p. 046403.

[HFB04] Michael Hermele, Matthew PA Fisher, and Leon Balents. “Pyrochlore photons: The U (1) spin liquid in a S= 1 2 three-dimensional frustrated magnet.” In: *Physical Review B* 69.6 (2004), p. 064404.

[HAMS19] Jonah Herzog-Arbeitman, Sebastian Mantilla, and Inti Sodemann. “Solving the quantum dimer and six-vertex models one electric field line at a time.” In: *Physical Review B* 99.24 (2019), p. 245108.

[Hoo78] Gerard ’t Hooft. “On the phase transition towards permanent quark confinement.” In: *Nuclear Physics B* 138.1 (1978), pp. 1–25.

[Hor81] D Horn. “Finite matrix models with continuous local gauge invariance.” In: *Physics Letters B* 100.2 (1981), pp. 149–151.

[HKM94] A Houghton, H-J Kwon, and JB Marston. “Stability and single-particle properties of bosonized Fermi liquids.” In: *Physical Review B* 50.3 (1994), p. 1351.

[HKM00] A Houghton, H-J Kwon, and JB Marston. “Multidimensional bosonization.” In: *Advances in Physics* 49.2 (2000), pp. 141–228.

[HM93] A Houghton and JB Marston. “Bosonization and fermion liquids in dimensions greater than one.” In: *Physical Review B* 48.11 (1993), p. 7790.

[IM14] Ikuo Ichinose and Tetsuo Matsui. “Lattice gauge theory for condensed matter physics: ferromagnetic superconductivity as its example.” In: *Modern Physics Letters B* 28.22 (2014), p. 1430012.

[İW53] Erdal İnönü and Eugene P Wigner. “On the contraction of groups and their representations.” In: *Proceedings of the National Academy of Sciences* 39.6 (1953), pp. 510–524.

[Isa+99] ED Isaacs, A Shukla, PM Platzman, DR Hamann, B Barbiellini, and CA Tulk. “Covalency of the hydrogen bond in ice: A direct X-ray measurement.” In: *Physical Review Letters* 82.3 (1999), p. 600.

[JO01] John David Jackson and Lev Borisovich Okun. “Historical roots of gauge invariance.” In: *Reviews of Modern Physics* 73.3 (2001), p. 663.

[Jia+22] Yanyu Jia, Pengjie Wang, Cheng-Li Chiu, Zhida Song, Guo Yu, Berthold Jäck, Shiming Lei, Sebastian Klemenz, F Alexandre Cevallos, Michael Onyszczak, et al. “Evidence for a monolayer excitonic insulator.” In: *Nature Physics* 18.1 (2022), pp. 87–93.

[Kat12] Mikhail I. Katsnelson. *Graphene: Carbon in Two Dimensions*. Cambridge University Press, 2012. DOI: `10.1017/CBO9781139031080`.

[KSV19] Jun Yong Khoo and Inti Sodemann Villadiego. "Shear sound of two-dimensional Fermi liquids." In: *Physical Review B* 99.7 (2019), p. 075434.

[KW88] YS Kim and Eugene P Wigner. "Cylindrical group and massless particles." In: *Special Relativity and Quantum Theory*. Springer, 1988, pp. 387–391.

[Kle16] Hagen Kleinert. *Particles and quantum fields*. world scientific, 2016.

[Kog79] John B Kogut. "An introduction to lattice gauge theory and spin systems." In: *Reviews of Modern Physics* 51.4 (1979), p. 659.

[KS75] John Kogut and Leonard Susskind. "Hamiltonian formulation of Wilson's lattice gauge theories." In: *Physical Review D* 11.2 (1975), p. 395.

[Koh64] Walter Kohn. "Theory of the insulating state." In: *Physical Review* 133.1A (1964), A171.

[Kot+12] Valeri N Kotov, Bruno Uchoa, Vitor M Pereira, F Guinea, and AH Castro Neto. "Electron-electron interactions in graphene: Current status and perspectives." In: *Reviews of Modern Physics* 84.3 (2012), p. 1067.

[LMM11] Claudine Lacroix, Philippe Mendels, and Frédéric Mila. *Introduction to frustrated magnetism: materials, experiments, theory*. Vol. 164. Springer Science & Business Media, 2011.

[LCR96] Pak Wo Leung, King Chuen Chiu, and Karl J Runge. "Columnar dimer and plaquette resonating-valence-bond orders in the quantum dimer model." In: *Physical Review B* 54.18 (1996), p. 12938.

[Li+12] Jian Li, Ivar Martin, Markus Büttiker, and Alberto F Morpurgo. "Marginal topological properties of graphene: a comparison with topological insulators." In: *Physica Scripta* 2012.T146 (2012), p. 014021.

[Li+08] ZhiQuan Li, Eric A Henriksen, Zhifang Jiang, Zhao Hao, Michael C Martin, Phaly Kim, Horst Ludwig Stormer, and Dimitri N Basov. "Dirac charge dynamics in graphene by infrared spectroscopy." In: *Nature physics* 4.7 (2008), pp. 532–535.

[Lie67] Elliott H Lieb. "Residual entropy of square ice." In: *Physical Review* 162.1 (1967), p. 162.

[Lud+94] Andreas WW Ludwig, Matthew PA Fisher, R Shankar, and G Grinstein. "Integer quantum Hall transition: An alternative approach and exact results." In: *Physical Review B* 50.11 (1994), p. 7526.

[Lut79] A Luther. "Tomonaga fermions and the Dirac equation in three dimensions." In: *Physical Review B* 19.1 (1979), p. 320.

[Lut60] JM Luttinger. "Fermi surface and some simple equilibrium properties of a system of interacting fermions." In: *Physical Review* 119.4 (1960), p. 1153.

[Mak+08] Kin Fai Mak, Matthew Y Sfeir, Yang Wu, Chun Hung Lui, James A Misewich, and Tony F Heinz. "Measurement of the optical conductivity of graphene." In: *Physical review letters* 101.19 (2008), p. 196405.

[MS20] Sebastian Mantilla and Inti Sodemann. “Bosonization of the Q= 0 continuum of Dirac fermions.” In: *Physical Review B* 102.12 (2020), p. 121103.

[MM56] Takeo Matsubara and Hirotsugu Matsuda. “A Lattice Model of Liquid Helium, I.” In: *Progress of Theoretical Physics* 16.6 (Dec. 1956), pp. 569–582.

[MM57] Hirotsugu Matsuda and Takeo Matsubara. “A Lattice Model of Liquid Helium, II.” In: *Progress of Theoretical Physics* 17.1 (Jan. 1957), pp. 19–29.

[MAF07] Edward McCann, David SL Abergel, and Vladimir I Fal’ko. “Electrons in bilayer graphene.” In: *Solid state communications* 143.1-2 (2007), pp. 110–115.

[Mer89] N. David Mermin. “What’s wrong with this pillow?” In: *Physics Today* 42.4 (1989), p. 9.

[Mis08] EG Mishchenko. “Minimal conductivity in graphene: Interaction corrections and ultraviolet anomaly.” In: *EPL (Europhysics Letters)* 83.1 (2008), p. 17005.

[MR11a] R Moessner and KS Raman. *Introduction to Frustrated Magnetism, volume 164 of Springer Series in Solid-State Sciences, chapter Quantum Dimer Models*. 2011.

[MTS04] R Moessner, Oleg Tchernyshyov, and Shivaji Lal Sondhi. “Planar pyrochlore, quantum ice and sliding ice.” In: *Journal of statistical physics* 116.1 (2004), pp. 755–772.

[MR11b] Roderich Moessner and Kumar S Raman. “Quantum dimer models.” In: *Introduction to Frustrated Magnetism*. Springer, 2011, pp. 437–479.

[Mon+09] Claude Monney, Hervé Cercellier, Florian Clerc, Corsin Battaglia, EF Schwier, Clement Didiot, Michael Gunnar Garnier, Hans Beck, Philipp Aebi, Helmut Berger, et al. “Spontaneous exciton condensation in 1 T-TiSe 2: BCS-like approach.” In: *Physical Review B* 79.4 (2009), p. 045116.

[MDF15] E Mostaani, ND Drummond, and VI Fal’Ko. “Quantum Monte Carlo calculation of the binding energy of bilayer graphene.” In: *Physical review letters* 115.11 (2015), p. 115501.

[Nag99] Naoto Nagaosa. *Quantum field theory in condensed matter physics*. Springer Science & Business Media, 1999.

[Nai+08] Rahul Raveendran Nair, Peter Blake, Alexander N Grigorenko, Konstantin S Novoselov, Tim J Booth, Tobias Stauber, Nuno MR Peres, and Andre K Geim. “Fine structure constant defines visual transparency of graphene.” In: *Science* 320.5881 (2008), pp. 1308–1308.

[Nov+04] Kostya S Novoselov, Andre K Geim, Sergei V Morozov, De-eng Jiang, Yanshui Zhang, Sergey V Dubonos, Irina V Grigorieva, and Alexandr A Firsov. “Electric field effect in atomically thin carbon films.” In: *science* 306.5696 (2004), pp. 666–669.

[Nov+05] Kostya S Novoselov, Andre K Geim, Sergei Vladimirovich Morozov, Dingde Jiang, Michail I Katsnelson, Irina V Grigorieva, Sergey V Dubonos, and Alexandr A Firsov. "Two-dimensional gas of massless Dirac fermions in graphene." In: *nature* 438.7065 (2005), pp. 197–200.

[Oak+18] Tom Oakes, Stephen Powell, Claudio Castelnovo, Austen Lamacraft, and Juan P Garrahan. "Phases of quantum dimers from ensembles of classical stochastic trajectories." In: *Physical Review B* 98.6 (2018), p. 064302.

[Orl92] Peter Orland. "Exact solution of a quantum gauge magnet in 2+1 dimensions." In: *Nuclear Physics B* 372.3 (1992), pp. 635–653.

[OR90] Peter Orland and Daniel Rohrlich. "Lattice gauge magnets: Local isospin from spin." In: *Nuclear Physics B* 338.3 (1990), pp. 647–672.

[Par+04] Belén Paredes, Artur Widera, Valentin Murg, Olaf Mandel, Simon Fölling, Ignacio Cirac, Gora V Shlyapnikov, Theodor W Hänsch, and Immanuel Bloch. "Tonks–Girardeau gas of ultracold atoms in an optical lattice." In: *Nature* 429.6989 (2004), pp. 277–281.

[Pau35] Linus Pauling. "The structure and entropy of ice and of other crystals with some randomness of atomic arrangement." In: *Journal of the American Chemical Society* 57.12 (1935), pp. 2680–2684.

[Pau53] Linus Pauling. "A theory of ferromagnetism." In: *Proceedings of the National Academy of Sciences of the United States of America* 39.6 (1953), p. 551.

[PH58] Linus Pauling and Roger Hayward. *No More War!* Liberty book club. Dodd, Mead, 1958. URL: `https://books.google.de/books?id=ncmxf-iyYoQC`.

[PS95] Michael E Peskin and Daniel V Schroeder. *An Introduction to Quantum Field Theory (Boulder, CO*. 1995.

[Pet92] Henry Petroski. *The pencil: A history of design and circumstance*. Alfred a Knopf Incorporated, 1992.

[Pol87] Aleksandr Michajlovič Polyakov. *Gauge fields and strings*. Taylor & Francis, 1987.

[Pol06] Alexios P Polychronakos. "Bosonization in higher dimensions via noncommutative field theory." In: *Physical review letters* 96.18 (2006), p. 186401.

[Pre17] Michael Pretko. "Subdimensional particle structure of higher rank U(1) spin liquids." In: *Physical Review B* 95.11 (2017), p. 115139.

[PMR19] Suryoday Prodhan, Sumit Mazumdar, and S Ramasesha. "Correlated electronic properties of a graphene nanoflake: coronene." In: *Molecules* 24.4 (2019), p. 730.

[PC09] International Union of Pure and Applied Chemistry. *IUPAC Compendium of Chemical Terminology – The Gold Book*. 2009. URL: `http://goldbook.iupac.org/`.

[RPM08] Arnaud Ralko, Didier Poilblanc, and R Moessner. "Generic mixed columnar-plaquette phases in Rokhsar-Kivelson models." In: *Physical review letters* 100.3 (2008), p. 037201.

[Ram+99] Arthur P Ramirez, A Hayashi, Robert Joseph Cava, R Siddharthan, and BS Shastry. "Zero-point entropy in 'spin ice'." In: *Nature* 399.6734 (1999), pp. 333–335.

[RK88] Daniel S Rokhsar and Steven A Kivelson. "Superconductivity and the quantum hard-core dimer gas." In: *Physical review letters* 61.20 (1988), p. 2376.

[Rot12] Heinz J Rothe. *Lattice gauge theories: an introduction*. World Scientific Publishing Company, 2012.

[RF04] Erich Runge and Peter Fulde. "Charge degrees of freedom in frustrated lattice structures." In: *Physical Review B* 70.24 (2004), p. 245113.

[Ryd96] Lewis H Ryder. *Quantum field theory*. Cambridge university press, 1996.

[Sch18] John Robert Schrieffer. *Theory of superconductivity*. CRC press, 2018.

[Set06] Girish S Setlur. "Bosonization and quantum hydrodynamics." In: *Pramana* 66.3 (2006), pp. 575–588.

[SMP04] Nic Shannon, Grégoire Misguich, and Karlo Penc. "Cyclic exchange, isolated states, and spinon deconfinement in an XXZ Heisenberg model on the checkerboard lattice." In: *Physical Review B* 69.22 (2004), p. 220403.

[SS09] Daniel E Sheehy and Jörg Schmalian. "Optical transparency of graphene as determined by the fine-structure constant." In: *Physical Review B* 80.19 (2009), p. 193411.

[Sla41] John C Slater. "Theory of the transition in KH2PO4." In: *The Journal of Chemical Physics* 9.1 (1941), pp. 16–33.

[SF12] Inti Sodemann and Michael M Fogler. "Interaction corrections to the polarization function of graphene." In: *Physical Review B* 86.11 (2012), p. 115408.

[SM20] J. Spence and E. Malone. *Observations, anecdotes, and characters, of books and men. Arranged with notes by E. Malone*. John Murray, 1820.

[Sun+22] Bosong Sun, Wenjin Zhao, Tauno Palomaki, Zaiyao Fei, Elliott Runburg, Paul Malinowski, Xiong Huang, John Cenker, Yong-Tao Cui, Jiun-Haw Chu, et al. "Evidence for equilibrium exciton condensation in monolayer WTe2." In: *Nature Physics* 18.1 (2022), pp. 94–99.

[Syl06] Olav F Syljuåsen. "Plaquette phase of the square-lattice quantum dimer model: Quantum Monte Carlo calculations." In: *Physical Review B* 73.24 (2006), p. 245105.

[TK14] S Teber and AV Kotikov. "Interaction corrections to the minimal conductivity of graphene via dimensional regularization." In: *EPL (Europhysics Letters)* 107.5 (2014), p. 57001.

[TK18] S Teber and AV Kotikov. "Field theoretic renormalization study of interaction corrections to the universal ac conductivity of graphene." In: *Journal of High Energy Physics* 2018.7 (2018), pp. 1–22.

[Tom50] Sin-itiro Tomonaga. "Remarks on Bloch's method of sound waves applied to many-fermion problems." In: *Progress of Theoretical Physics* 5.4 (1950), pp. 544–569.

[Tre+08] Paolo E Trevisanutto, Christine Giorgetti, Lucia Reining, Massimo Ladisa, and Valerio Olevano. "Ab Initio G-W Many-Body Effects in Graphene." In: *Physical review letters* 101.22 (2008), p. 226405.

[UJ21] Masafumi Udagawa and Ludovic Jaubert. *Spin Ice*. Springer, 2021.

[Val58] JG Valatin. "Comments on the theory of superconductivity." In: *Il Nuovo Cimento (1955-1965)* 7.6 (1958), pp. 843–857.

[VHF15] Sagar Vijay, Jeongwan Haah, and Liang Fu. "A new kind of topological quantum order: A dimensional hierarchy of quasiparticles built from stationary excitations." In: *Physical Review B* 92.23 (2015), p. 235136.

[Von68] Franz Vonessen. "Heisenberg, Werner:" Das Naturgesetz und die Struktur der Materie"(Book Review)." In: *Philosophischer Literaturanzeiger* 21 (1968), p. 150.

[VKG10] Maria AH Vozmediano, MI Katsnelson, and Francisco Guinea. "Gauge fields in graphene." In: *Physics Reports* 496.4-5 (2010), pp. 109–148.

[Wal47] Philip Richard Wallace. "The band theory of graphite." In: *Physical review* 71.9 (1947), p. 622.

[Wen04] Xiao-Gang Wen. *Quantum field theory of many-body systems: from the origin of sound to an origin of light and electrons*. Oxford University Press on Demand, 2004.

[Wie13] U-J Wiese. "Ultracold quantum gases and lattice systems: quantum simulation of lattice gauge theories." In: *Annalen der Physik* 525.10-11 (2013), pp. 777–796.

[Wil74] Kenneth G Wilson. "Confinement of quarks." In: *Physical review D* 10.8 (1974), p. 2445.

[Wil96] Kenneth G Wilson. *Banquet speech. NobelPrize.org*. Nobel Prize Outreach AB 2022. Tue. 29 Mar 2022. Dec. 1996. URL: https://www.nobelprize.org/prizes/physics/1982/wilson/speech/.

[Xue+04] Kuan-Hong Xue, Fei-Fei Tao, Wei Shen, Chun-Jian He, Qiao-Ling Chen, Li-Jun Wu, and Yi-Mei Zhu. "Linear carbon allotrope - carbon atom wires prepared by pyrolysis of starch." In: *Chemical Physics Letters* 385.5 (2004), pp. 477–480. ISSN: 0009-2614. DOI: https://doi.org/10.1016/j.cplett.2004.01.007. URL: https://www.sciencedirect.com/science/article/pii/S000926140400034X.

[Yan57] Chen-Ning Yang. *Nobel Lecture. NobelPrize.org*. Nobel Prize Outreach AB 2022. Tue. 29 Mar 2022. Dec. 1957. URL: https://www.nobelprize.org/prizes/physics/1957/yang/lecture/.

[YY66a] Chen-Ning Yang and Chen-Ping Yang. "Ground-state energy of a Heisenberg-Ising lattice." In: *Physical Review* 147.1 (1966), p. 303.

[YY66b] Chen-Ning Yang and Chen-Ping Yang. "One-dimensional chain of anisotropic spin-spin interactions. I. Proof of Bethe's hypothesis for ground state in a finite system." In: *Physical Review* 150.1 (1966), p. 321.

[YY66c] Chen-Ning Yang and Chen-Ping Yang. "One-dimensional chain of anisotropic spin-spin interactions. II. Properties of the ground-state energy per lattice site for an infinite system." In: *Physical Review* 150.1 (1966), p. 327.

[YY66d] Chen-Ning Yang and Chen-Ping Yang. "One-dimensional chain of anisotropic spin-spin interactions. III. Applications." In: *Physical Review* 151.1 (1966), p. 258.

[Yos13] Beni Yoshida. "Exotic topological order in fractal spin liquids." In: *Physical Review B* 88.12 (2013), p. 125122.

[Zei11] Eberhard Zeidler. *Quantum Field Theory III: Gauge Theory: A Bridge between Mathematicians and Physicists*. Springer Science & Business Media, 2011.

[Zha+21] Xu Zhang, Gaopei Pan, Yi Zhang, Jian Kang, and Zi Yang Meng. "Momentum space quantum monte carlo on twisted bilayer graphene." In: *Chinese Physics Letters* 38.7 (2021), p. 077305.

[ZCR15] Erez Zohar, J Ignacio Cirac, and Benni Reznik. "Quantum simulations of lattice gauge theories using ultracold atoms in optical lattices." In: *Reports on Progress in Physics* 79.1 (2015), p. 014401.

[Zyl+20] P.A. Zyla et al. "Review of Particle Physics." In: *PTEP* 2020.8 (2020). and 2021 update, p. 083C01. DOI: `10.1093/ptep/ptaa104`.

ERKLÄRUNG

Hiermit versichere ich, Sebastián Felipe Mantilla Serrano, dass ich die vorliegende Arbeit ohne unzulässige Hilfe Dritter und ohne Benutzung anderer als der angegebenen Hilfsmittel angefertigt habe; die aus fremden Quellen direkt oder indirekt übernommenen Gedanken sind als solche kenntlich gemacht. Die Arbeit wurde bisher weder im Inland noch im Ausland in gleicher oder ähnlicher Form einer anderen Prüfungsbehörde vorgelegt. Diese Arbeit wurde unter der wissenschaftlichen Betreuung von Prof. Dr. Inti Sodemann und Prof. Dr. Roderich Moessner am Max-Planck-Institut für Physik komplexer Systeme in Dresden angefertigt. Ich erkläre hiermit, dass keine früheren erfolglosen Promotionsverfahren stattgefunden haben. Ich erkenne die Promotionsordnung der Fakultät für Mathematik und Naturwissenschaften der Technische Universität Dresden an.

Dresden, Deutschland, Juni 2022

Sebastián Felipe Mantilla Serrano

COLOPHON

This document was typeset using the typographical look-and-feel `classicthesis` developed by André Miede and Ivo Pletikosić. The style was inspired by Robert Bringhurst's seminal book on typography *"The Elements of Typographic Style"*. `classicthesis` is available for both LaTeX and LyX:

`https://bitbucket.org/amiede/classicthesis/`